The Microwave Effect

Non-thermal effects of microwave radiation in solid state chemistry

Graeme R. Robb

PhD – The University of Edinburgh – 2003

"I mean, after all; you have to consider we're only made out of dust. That's admittedly not much to go on and we shouldn't forget that. But even considering, I mean it's a sort of bad beginning, we're not doing too bad. So I personally have faith that even in this lousy situation we're faced with we can make it. You get me?"

Philip K. Dick

The Three Stigmata of Palmer Eldritch.

For Nicola.

Without you, I am nothing.

Abstract

Microwaves are frequently used as a method of heating: in the chemistry laboratory, in industry and in the home. In many aspects microwave heating can be regarded as behaving as conventional modes of heating. However, there are important differences that can lead to specific *microwave effects*. These effects can be exploited to useful purpose, for example enhanced rates of certain reactions, but first they must be more fully understood. Microwaves are commonly used for a number of solid state reactions, including sintering of ceramics, drying of materials and ionic substitution reactions. It is for such solid state processes that some of the most interesting effects are observed; yet these are presently amongst the most poorly understood.

Diffraction is arguably the most incisive technique for the probing of solid state processes. To observe specific effects of microwave radiation it is necessary to perform *in-situ* diffraction experiments. Here are detailed microwave applicators, modified for such a purpose. Simple phenomena, such as thermal expansion and phase transitions were observed for diverse materials (aspirin, silver iodide, β"-alumina and barium titanate) under the influence of microwave heating. Furthermore, the use of *in*-situ diffraction as a method of temperature measurement is investigated. Some of these materials show unexpected effects when heated with microwaves, including anomalously large thermal expansion, the lowering of the phase transition temperature and a reduction in atomic displacement parameters. A consistent model has been proposed to explain these effects in terms of interactions of the electric field with a low-energy transverse optic phonon mode. The model only applies to materials possessing such a mode and no anomalous effects are observed otherwise. Barium titanate is a seemingly more complicated material and a strong electron-phonon interaction, resulting in local ordering may account for further anomalies.

Another application of microwaves is the synthesis of nanoparticles using a microwave-induced plasma. This is an established technique, yet its application is limited to species with a volatile precursor. Here the technique is extended and design apparatus for use with a precursor in an aerosol, allowing the use of non-volatile, cheap precursor compounds

Contents

Acknowledgements

Throughout the three years that have gone into my PhD and the production of this thesis, I feel I have had enormous support from those around me. My supervisor, Andrew Harrison, has always been there to help and encourage, excepting (of course) when he's in Japan, or Australia, or some other far-flung destination. Nonetheless he was always there (if by 'there' you include email) and was always available when I needed him. Gavin Whittaker's enthusiastic help was always appreciated. Somehow he could get anything to work – with enough prodding, hitting and, occasionally, a well-structured modification. Much of the experimental work would never have taken place without his input.

The various other PhD students, post-docs and visitors I encountered in lab 79 have all helped me out from time to time, so thank you: Vin Bondah-Jagalu, Marcela Pina-Sandoval, Lisa Yule, Keith Pettigrew, Douglas Youngson, Gareth Oakley, Keith Grant, Kenji Kamashima, Clare Peters, Satish Tiwary and Gui-Hua Wang. Far too many undergraduates to list have passed through these portals, so I limit my thanks to Rada Djangazov, Daniel Blake, and Lucy Spackman, all of whom I worked with directly. Lastly, special thanks to Emma Martin, an honorary lab 79-er, who was a great help throughout.

As you may soon come to realise, there is a lot of specialised equipment (designed by Gavin and myself) involved in much of the experimental work and it is a testimony to the skill of the mechanical and electrical workshops of the school of chemistry that such equipment could be made and maintained (most of the time).

For some of the more complex aspects of my work, I decided to tap other people's brains rather than risk tiring my own. Two of the people I tapped were Philip Camp (chemistry) and Alistair Bruce (physics). Both were supremely helpful (and interested), giving up some of their precious time to help me along.

I would also like to thank Chick Wilson, Richard Ibberson and Kevin Knight (of the ISIS Facility at the Rutherford Appleton Laboratory), and Mark Roberts and Ian Harvey (of the

Synchrotron Radiation Source at the Daresbury Laboratory). All these people were involved in different experiments at central facilities and made the whole process much easier.

Money is always important, so it is appropriate that I thank the University of Edinburgh, which found it in its heart to fund me throughout this work. Also thanks to the RSC who paid for me to go to various conferences.

Perhaps more important than any scientific contribution is the support and sustenance I received from family and friends. They have always been there for a chat and a few beers. Thanks guys, you know who you are. I also want to thank the wonderful people at id software, the makers of Doom, which helped keep me sane during those long months of writing-up.

Finally, and most importantly, a huge thanks to my wife Nicola without whose daily love, support and encouragement, this thesis would never have seen the light of day. Thanks for putting up with this for so long.

Publications

"*In situ* neutron diffraction studies of single crystals and powders during microwave irradiation", A. Harrison, R. Ibberson, G. R. Robb, A. G. Whittaker, C. C. Wilson and D. Youngson, *Faraday Discuss.*, 2003, **122**, 363-369.

"Instrumentation for in situ diffraction of materials under microwave radiation", A. Harrison, G. R. Robb and A. G. Whittaker, in *Proceedings of the Third World Congress on Microwave and Radio Frequency Applications*, 2002, Sydney, *in press*

"Temperature-resolved, *in-situ* powder X-ray diffraction of silver iodide under microwave irradiation", G. R. Robb, A. Harrison and A. G. Whittaker, *PhysChemComm*, 2002, **5** (19), 135-137

"*In-situ* monitoring of temperature in a microwave- heated ceramic material", A.G. Whittaker, G.R. Robb and R. Ibberson, *ISIS experimental report*, 2001, RB:12599

"Microwave reactor for in-situ X-ray diffraction measurements. Evidence of non-thermal effects in silver iodide", G. R. Robb, R. Djangazov, A. G. Whittaker and A. Harrison, in *Proceedings of the Second International Conference on Microwave Chemistry*, 2000, ed. A. Gourdenne, Antibe – Juan-les-Pins, AMPERE: 291-294.

Introduction

The 'Microwave Effect' of the title is a term frequently mentioned by microwave chemists. Whilst some are sceptical as to its existence, others are resolutely convinced that it is real. Whichever group is correct, it is important to be clear about what is meant by a 'microwave effect'. One definition is any phenomenon that occurs with microwave heating but not with other, conventional forms of heating. This definition is rather too broad in scope to deal with here in a satisfactory manner, and includes a variety of processes resulting from the volumetric nature of microwave heating (such as accelerated heating rates). In this thesis, therefore, I am primarily concerned with *non-thermal* processes induced by the presence of microwaves, i.e. those processes that result from some other characteristic of microwaves beyond simply being a means to heat matter. The focus has further been limited to solid-state materials, as these have been shown to have interesting interactions with microwaves in the past.

However, in order to investigate these phenomena it is essential to understand the fundamental nature of microwaves and their interactions with substances. Therefore, the opening chapter discusses how electromagnetic microwave energy is transformed into heat in the various forms of matter. This is followed by a comprehensive review of effects specific to microwaves (both thermal and non-thermal) in the literature, particularly in relation to solid materials. For a greater understanding, it is important to consider the mechanisms and technology involved in microwave heating. Chapter 1 is therefore rounded off by a discussion of these issues. In addition, these matters are important for the design and building of microwave applicators for research, which is a large part of the work that shaped this thesis. The following chapters then outline the theories upon which this work is based and the experimental procedures employed.

The experimental investigations, which form the bulk of this thesis, are described in Chapters 4 to 8. Each chapter discusses a different material and describes the research from the choice of material and initial design of microwave equipment through to the results and a discussion of these. The chapters are presented in chronological order as this seemed logical and serves to preserve the discovery process and incremental improvements in equipment as the work progressed.

Finally, Chapter 9 deals with the slightly tangential subject of nanoparticles synthesis using microwave induced plasma. This is another process where microwaves can have significant benefits over other methods. Though the work never came to fruition, great steps were made in the design of apparatus for the process and the project will hopefully be picked up again at some point in the future.

1 Microwaves

1.1 Microwave heating

Microwaves are used to heat everything from food, through wood pulp to microgram quantities of chemicals in the pharmaceutical industry.[1] In order to understand some of the processes observed it is necessary to consider the fundamental nature of microwaves and their interactions with matter, both in terms of thermal processes and the possibility of non-thermal interactions. This chapter discusses the different mechanisms by which heating can occur with microwaves, provides a review of microwave-specific effect reported in the literature and introduces some of the technologies involved in microwave heating and how these might be incorporated into scientific devices for research.

Microwaves are part of the electromagnetic spectrum, encompassing the region between infrared and radio frequency waves, and having wavelengths between 1 mm and 1 m.[1] A microwave possesses both an electric and a magnetic field component. In free space (i.e. vacuum and far from conducting objects, relative to the wavelength), these components are orthogonal to one another and perpendicular to the direction of propagation, as illustrated in Figure 1.1. Note that there is no field component in the direction of propagation; thus the wave is transverse electromagnetic (TEM) as all the field components are transverse to the direction of travel.

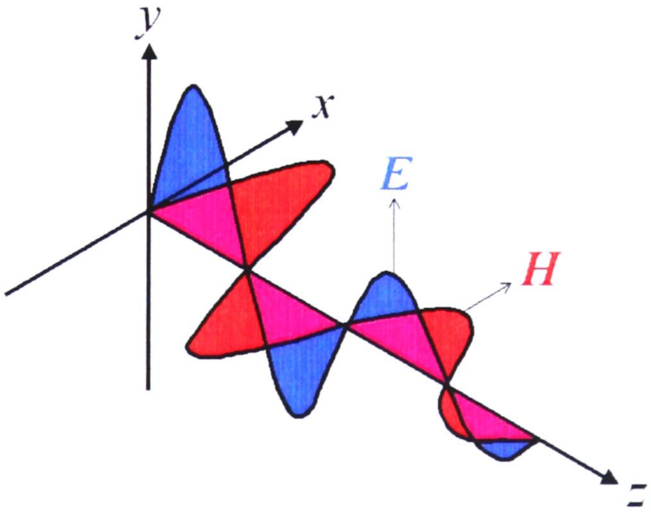

Figure 1.1 - Perspective illustration of plane-wave components, where z is the direction of propagation.

Microwaves interact with matter through a variety of mechanisms, depending on, amongst other things, the physical state, the dielectric properties and consequently the temperature of the material. There are two heating processes of primary important to the majority of solid and liquid substances.[2] *Dielectric heating* is the process that occurs when dipolar components of a material move to align themselves with the alternating field. *Conduction heating* arises when a material behaves as a poor electrical conductor in the microwave field: the material posessing a finite resistivity and consequently generating heat. Two further heating mechanisms are also possible. *Interfacial heating* occurs in inhomogeoeous materials with conducting inclusions dispersed through an insulating medium. The final heating mechanism is though the creation of a *microwave-induced plasma* (MIP) and is a separate case from the others in that it operates in the gas phase and frequently at sub-atmospheric pressures. When considering microwave heating effects, it is the electric component which is of primary interest. However, it should be noted that similar mechanisms can operate where the magnetic field can interact with, and cause heating in magnetic materials

1.1.1 Dielectric heating

For a material to heat via the dielectric heating mechanism it must be one which contains either permanent or induced dipoles that, when placed between two electrodes, acts similarly to a capacitor, i.e. the material allows a charge to be stored and no dc conductivity is observed. Induced polarisation can be the result of finite displacement of charges or rotation of dipoles in the electric field and should not be confused with conduction effects, which result from net translation of charges under the applied electric field. Consider then the simplest model for a dielectric material under the conditions of microwave heating: a parallel plate capacitor,[3] the capacitance of which is given by:

$$C = \frac{A\varepsilon_0\varepsilon^*}{d} \tag{1.1}$$

where A is the area of one plate, ε_0 is the absolute permittivity of free space, ε^* is the relative permittivity of the capacitor material (also referred to as the dielectric constant) and d is the spacing between the plates. The relative permittivity, ε^*, has real and imaginary parts (where i denotes the component 90° out of phase from the real part).

$$\varepsilon^* = \varepsilon' - i\varepsilon'' \quad \textbf{(1.2)}$$

The real part, ε', relates to the response of the material to a static field, whilst the imaginary quantity, ε'', is necessary to describe the material's response to a fluctuating field.[3] Simple ac theory shows that for a capacitor of value C connected to a sinusoidal electrical power source of RMS voltage V and angular frequency ω, a current I will be drawn such that:

$$I = iV\omega C \quad \textbf{(1.3)}$$

In other words, the current is out of phase with the sinusoidal voltage by 90°. Substitution of Equations (1.1) and (1.2) into (1.3) gives:

$$I = V\omega \frac{\varepsilon_0 A}{d}(i\varepsilon' + \varepsilon'') \quad \textbf{(1.4)}$$

The first term in parentheses shows the current in phase-quadrature with the voltage, as with a lossless capacitor. However, the second term is in-phase with the voltage and therefore represents power dissipation. The energy not used to drive the current is lost as heat: this is the basis of microwave dielectric heating.[3] Materials which heat well under microwave irradiation are often described as 'lossy', where 'lossiness' is quantified by ε'' (at a given microwave frequency), or more commonly by the dielectric loss angle, δ. This is defined as the angle by which the resultant current differs from the ideal (i.e. zero power dissipation) 90° phase angle, relative to the voltage.[2]

$$\delta = \tan^{-1}\left(\frac{\varepsilon''}{\varepsilon'}\right) \quad \textbf{(1.5)}$$

The relative permittivity, and hence the loss angle, are frequency dependant:[3] the dependence of ε' and ε'' being governed by the Debye equations:

$$\varepsilon' = \varepsilon'_{\infty} + \frac{\left(\varepsilon'_{0} - \varepsilon''_{\infty}\right)}{\left(1 + \omega^{2}\tau^{2}\right)} \qquad \textbf{(1.6)}$$

$$\varepsilon'' = \frac{(\varepsilon'_{0} - \varepsilon''_{\infty})\omega\tau}{(1 + \omega^{2}\tau)} \qquad \textbf{(1.7)}$$

where ε'_{∞} and ε'_{0} are defined as the high frequency and static dielectric constants, and where ω is the rotation frequency of polarisation build-up and τ is the corresponding relaxation time characteristic of the material. Clearly, the choice of microwave frequency, ω, will have an impact on the heating efficiency (or lossiness).

One of the substances most commonly heated with microwaves is water. Applications range from domestic microwave ovens, which cook food by heating the water content, to industrial-scale drying processes.[1, 4] One may therefore expect a microwave frequency to be chosen for these applications whereby the lossiness for water is a maximum. It is surprising to discover that this is far from true (Figure 1.2).

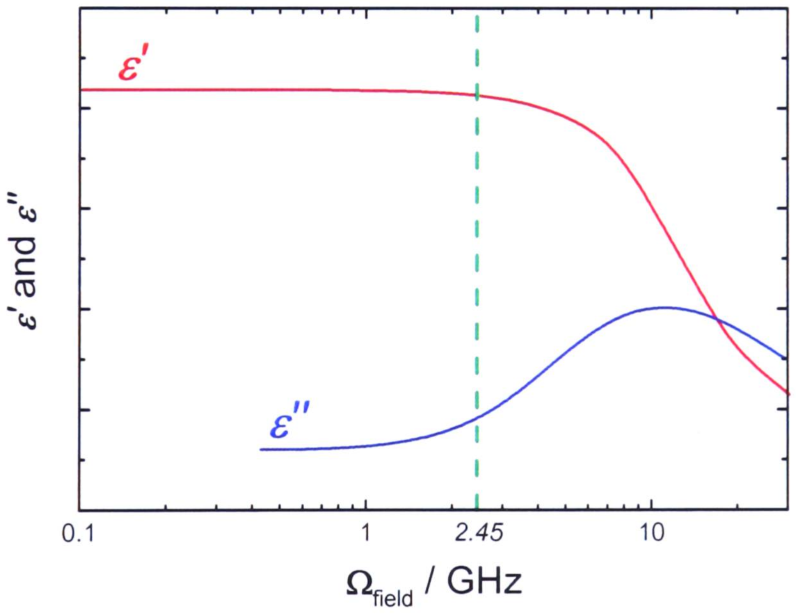

Figure 1.2 - Variation of relative permittivity, with electric field frequency for water (298 K). The standard industrial and commercial microwave frequency (2.45 GHz) is indicated.[2]

The frequency chosen (and the one to which all heating applications are limited, to avoid interfering with communications bandwidths) is 2.45 GHz[†]. The maximum heating efficiency for water, however, would be closer to 10 GHz. The explanation is related to the practical use of microwave heating. At 10 GHz water would absorb microwave power strongly; the majority of the available power would therefore be absorbed in the surface layer and could not penetrate the interior. In practice, this would mean food became cooked on the outside, but remained raw in the centre. The choice of frequency away from the maximum absorption avoids this problem. This introduces another important concept in microwave heating: the penetration depth. It is defined as the depth in the material at which the power flux has fallen to 1/e of its surface value. A good measure of the penetration depth, D_p,[3] is given (with an error of up to 10%) by:

$$D_p \approx \frac{\lambda_0 \sqrt{\varepsilon'}}{2\pi\varepsilon''} \qquad \textbf{(1.8)}$$

where λ_0 is the field wavelength in free-space. At 2.45 GHz the penetration depth is increased to a practical value, but heating efficiency is reduced. This problem is overcome by placing the object to be heated inside a resonant cavity. Microwaves are reflected from the walls of the cavity allowing multiple passes through the object and maximising the amount of power that can be absorbed.

In water, the origin of the absorption is the rotation of molecular dipoles to align themselves with the electric field.[2] Many liquids will heat by a similar process, the only criteria being the possession of a permanent dipole and a reasonable match between the frequency of microwave radiation and the characteristic relaxation time of the dipole.[1] The molecular dipoles are therefore in a constant state of mechanical oscillation at microwave frequencies and heating occurs through friction (i.e. interactions between molecules). The total polarisation, α_t, of a material may be written as the sum of its components.[2]

[†] It should be noted that the frequencies chosen for microwave heating, often designated ISM 'industrial, scientific and medical' frequencies, are the result of historical evolution and were developed in the period 1930 to 1970, before microwave heating had developed significantly.

$$\alpha_t = \alpha_e + \alpha_a + \alpha_d + \alpha_i \tag{1.9}$$

where α_e is the polarisation resulting from the displacement of electrons, α_a resulting from the displacement of nuclei, α_d resulting from reorientation of dipoles and α_i resulting from interfacial effects. In the case of water, polarisation results principally from the reorientation of polar molecules under the influence of the electric field. For the majority of solid materials, molecular fragments are not free to rotate (hence, water-free ice is not a good absorber of microwaves). Instead, the electric field couples with charged particles and induces transient dipoles through local distortions.[2]

The time scale for the movements of charges (α_e and α_a) is very much smaller than that for microwave field oscillations.[5, 6] The two processes cannot interact directly. Instead, the energy of electron and ion oscillations is converted, via a series of processes, to the energy of lattice vibrations (phonons). Electron oscillations induce periodic distortion of the lattice potential that modify the phonon spectrum, forcing it away from equilibrium. Equilibrium then re-establishes itself via anharmonic interactions between phonons. The time scale of the latter process determines the amount of energy stored as non-equilibrium excitation.[5]

An important mechanism in the converting of energy from the microwave field into heat in solids is through multi-phonon interactions.[5, 6] The most common is the three-wave mixing process, as illustrated in Figure 1.3. The energy of a photon corresponds with the difference in energies of two phonons, the result being the excitation of a higher energy phonon. The importance of this will be discussed at some length in later chapters.

From conservation of energy and momentum, it follows that the sum of the frequencies, ω, and the wavevectors, $\mathbf{k}$, of the interacting vibrations are conserved. There is some debate, however, as to the effectiveness of this mechanism in solid materials.[5] This heating route dominates only in the lower temperature regime. At temperatures high enough to activate mass-transport, conduction heating effects dominate.[6]

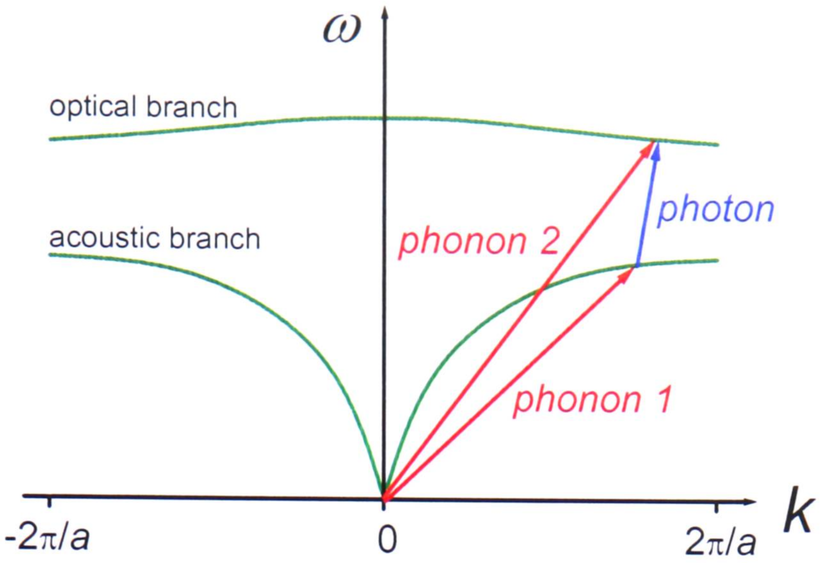

Figure 1.3 – multi-phonon interaction leading to the excitation of a higher energy phonon. The photon and phonons are shown as vectors in frequency, *ω*, and wavevector, *k*, whilst *a* is the lattice parameter.

1.1.2 Conduction heating

Conduction heating can act alone or in conjunction with dielectric heating. In pure water, dielectric losses dominate; however, the presence of dissolved salt greatly increases the conduction effects. Sufficient concentrations of salt may cause conduction heating to dominate the dielectric effects. The expression for the relative permittivity, Equation (1.2), may be adapted to take account of these conduction losses:[3]

$$\varepsilon^* = \varepsilon'_\infty + \frac{(\varepsilon'_0 - \varepsilon''_\infty)}{(1 + i\omega\tau)} - \left(\frac{i\sigma}{\omega\varepsilon'_0}\right) \qquad \textbf{(1.10)}$$

where σ is the conductivity of the material. For solid materials and high temperature processing, conduction losses are of primary importance.[7] The electric field frequency (GHz) is slow on the time scale of ionic and electronic motion (THz). The result is that these charged particles will move in phase with the electric field.[3] As the field is sinusoidal in nature, there is no net particle flow in a purely homogeneous material.

The magnitude of this effect is proportional to the number of charge carriers (ions and electrons) free to couple with the electric field. This is obviously a temperature dependent quantity and at higher temperatures the bonds between ions in ionic crystals are significantly weakened, and the electrons in covalent materials begin to populate the conduction band. This results in a rapid increase in microwave absorption and heating rate. For example, the conductivity of alumina (amongst the least absorbing materials at room temperature) increases with temperature as electrons are promoted into the conduction band from the O(2p) valence band.[2] This results in an increase in the loss angle, δ, as illustrated in Figure 1.4 for alumina and a number of other ceramic materials that exhibit similar behaviour.

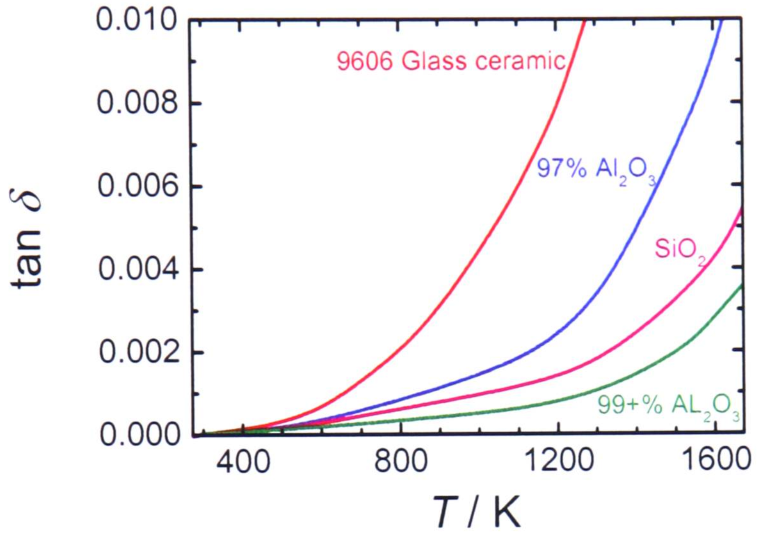

Figure 1.4 - Increase in the dielectric loss angle with temperature for a range of ceramic materials.[2]

This sharp rise in lossiness can result in uncontrolled heating up to the decomposition temperature of the material. This effect is commonly known as *thermal runaway* and can be troublesome in microwave applications, as it is self-sustaining.[2] That is, an increase in temperature results in the material becoming more lossy, which in turn results in a further increase in temperature, and so on.

At room temperature metals already have a significant number of electrons in the conduction band and consequently the charges couple extremely well with microwave radiation: so well in fact, that the penetration depth is greatly reduced (of the order of 50 μm). In practice, this means that most of the microwave energy is reflected by the surface, rather than absorbed in the bulk. The reflection coefficient (fraction of reflected power), R, can be characterised:[3]

$$R = \frac{1-\sqrt{2\varepsilon'[1+\sqrt{1+(\tan\delta)^2}\,]}+\varepsilon'\sqrt{1+(\tan\delta)^2}}{1+\sqrt{2\varepsilon'[1+\sqrt{1+(\tan\delta)^2}\,]}+\varepsilon'\sqrt{1+(\tan\delta)^2}} \qquad \textbf{(1.11)}$$

Surface currents are induced by the electric field, though in a perfectly conducting metal these do not result in any absorption. Consequently, metal can be used to construct a resonant cavity (microwave applicator) that contains the microwaves in the vicinity of the sample, greatly increasing the efficiency of heating. Care must be taken, however, in the design of a microwave device. It is normal to construct such devices from smooth metal surfaces. However, sharp edges or vertices result in electric field stresses and voltage breakdown can occur, ionising gas in the vicinity and resulting in burn damage. Accordingly, microwave devices (such as domestic microwave ovens) have rounded edges in order to avoid such damage.[3]

In practice, heating can occur in metals even without the presence of sharp edges. Surface defects such as scratches and corrosion can result in absorption. Metal powder or thin foil heats extremely rapidly, having a much greater surface area than bulk metal itself.

1.1.3 Heterogeneous materials

In practical microwave processing, most materials are heterogeneous. For example, the processing of ceramics at all stages remains a two-component mixture of grains and voids between these grains. Other examples include metal-ceramic composites, commonly used to produce hard metal machine tools, and wet paper, a solid matrix impregnated with water, dried rapidly by microwaves.

A number of theories have been developed to describe heterogeneous materials as they undergo microwave heating.[2, 8] If the two components of the mixture are sufficiently similar (in terms of conductivity) and the non-uniformity is small in relation to the radiation wavelength, it is possible to use an averaged description of the electromagnetic field interaction with the material. The material is therefore treated as homogeneous, with calculated values for the effective dielectric permittivity, ε_{eff}, which takes the same role as the permittivity in a homogeneous material. The effective properties depend on the constituent materials, the relative proportions and the size and shape of the particles composing the mixture. Amongst the most popular descriptions are the Maxwell-Garnet theory (MGT) and the effective medium approximation (EMA).[8] The MGT describes a host material containing spherical inclusions of another material. The theory gives good agreement with experimental results, providing the concentration of inclusions is low so that particles of the inclusion material do not interact. However, it breaks down at higher concentrations where the choice of one component as a host material becomes unjustified. In such cases, the EMA provides a better description. In this methodology, both components are considered as inclusions into a host material that is the effective medium whose properties are sought. Further details are beyond the scope of the discussion here, but may be found elsewhere.[8]

When conductive material (e.g. a metal) is embedded in a low-loss host (an insulator) an altogether different heating mechanism can operate. The oscillating electromagnetic field may drive strong currents at the surface of the conducting inclusions, resulting in interfacial polarisation, α_I, as mentioned in Equation (1.9). This phenomenon is described by Maxwell-Wagner theory (MWT). The simplest model is a dispersion of conducting spheres through an insulating medium. Experimentally this has been achieved by incorporating up to 3% of approximately spherical particles of semi-conducting copper phthalocyanine into paraffin wax.[9] This effect has been shown to be much greater than conduction heating, in certain cases and depending upon particle size, and is also frequently termed induction heating.

1.1.4 Interaction with gases

Gases are significantly less dense than other forms of matter and consequently individual molecules are much further apart and ideally do not interact. Microwave spectroscopy makes use of this and the fact that microwave frequencies coincide with those of the transitions between rotational energy levels of gas phase molecules. Unlike the condensed phases, energy levels in the gas phase are quantised. Consequently, the rotational spectrum is a series of sharp lines representing the transitions between various energy states, E_J, defined by the relationship:

$$E_J = \frac{J(J+1)h^2}{8\pi I^2} \tag{1.12}$$

where J is the rotational quantum number, h is Planck's constant and I is the moment of inertia of the molecule. Microwave rotational spectroscopy, though only observed for molecules with a permanent or induced dipole, is an extremely useful technique for identifying molecules and calculating bond angles in the gas phase.

Microwaves of sufficient power act on low-pressure gases in a very different way. Rather than coupling with a molecular dipole and exciting rotational motion, a powerful microwave field can couple directly with the valence electrons, ionising gaseous atoms and molecules to create free ions and electrons: a microwave-induced plasma (MIP).[2, 10] Ions, due to their greater mass, remain essentially unaffected by the electric field, whilst the electrons are rapidly accelerated. These reactive particles oscillate with the field and will inevitably collide with other species in the reactor. The plasma is sustained by collisions between electrons and heavier, neutral species (normally the carrier gas), which tend to increase the number of electrons. This process can be elastic – in which case there is no net change in kinetic energy – or inelastic. Inelastic collisions can result in excited internal states of the heavier particle, or even ionisation to create new charged species. However, the energy supplied to an electron by the electric field is insufficient by itself to induce ionisation and an electron must first undergo other collisional processes to increase its own energy before this can happen. After ionisation the original electron remains free but with little energy and starts the build-up process again.

Overall, the electron energies can be described by a Boltzmann-like distribution where only the high-energy tail of the distribution has sufficient energy to ionise the gas molecules. Propagation of the plasma is limited by other collisions, which consume free electrons. These can be either with cations present in the plasma or with the walls of the reactor. Energy is transferred from the microwaves to the electrons and then on to the heavier particles. Finally the energy is given up to the surroundings, either by collision with the reactor walls or by radiative emission (often in the visible part of the spectrum). Details of the energy distributions in argon plasmas are presented in a paper by Junck and co-workers.[10]

The plasma can be broadly divided into two regions. The first is the *active zone* and is the area where the microwaves are focussed. This region is dominated by charged species and comprises 'hot' plasma. Outside this region, there are fewer ions and electrons (as the distance from the centre of the active zone is much greater than the mean free path). Excited atoms, molecules and radicals dominate. This *afterglow* region is cooler than the active zone and some useful chemistry can be performed in this 'cold' plasma.[11, 12] Plasmas are frequently used for the deposition of films via CVD (chemical vapour deposition)[4] or the synthesis of nanoparticles (crystallites with maximum diameter in the nanometre range).[13-16] The advantage of MIP over other methods of generating plasma is the relatively cold afterglow region. This can avoid damaging substrates and limits particle growth, facilitating the creation of smaller particles.

1.2 Microwave specific effects

A quick inspection of the literature on microwave chemistry will reveal a variety of papers reporting improved rates, yields, or product quality for reactions performed with microwave radiation as a heat source.[17-21] The physical processes behind these claims can be broadly separated into two categories. The first is enhancements based upon the volumetric or specific nature of microwave heating. The second concerns the non-thermal effects of an alternating electromagnetic field on a material, especially for solid state processes.

1.2.1 Volumetric heating

One of the fundamental differences between microwave and conventional heating is the way in which heat is supplied to the material. For microwave heating, power is supplied at a constant rate and the temperature rises linearly with time, assuming dielectric properties remain constant and that heat losses to the surroundings are negligible. By contrast, the temperature of a material in a conventional oven rises asymptotically towards the oven temperature and cannot exceed it. The 'temperature' of a microwave oven is a meaningless concept, as the temperature of the material may in practice continue to rise well above that of the oven walls or the air inside the oven, as long as power is applied. This demonstrates one of the primary advantages of microwave heating: efficiency. Conventional ovens must heat the oven walls, the air inside the oven, the sample holder and the sample; microwave ovens need only heat the sample. For industrial ovens, the power efficiency, defined as the proportion of microwave power dissipated as heat in the sample, can be as high as 95%.[3]

Though not heated by microwaves, the surroundings do play an important secondary role in terms of surface heating and cooling. In conventional ovens a sample must be heated from the surface, through to the centre. The rate of temperature increase is limited by the thermal conductivity of the sample and, until thermal equilibrium is attained, the centre of the sample will always be cooler than the surface. A system such as this takes a long time to re-attain equilibrium in response to a change in oven temperature. By its nature, microwave heating heats the whole sample at the same rate (assuming the sample is small in relation to the penetration depth). It therefore maintains a homogeneous temperature and responds quickly to changes in the applied power, termed *inertia-less* heating.[3] It is therefore feasible to have *in-situ* temperature control with a fast feedback control loop. A small caveat to this is the effect of surface cooling on the sample. Though the sample is heated uniformly, it may cool quickly at the surface. Many industrial processes used a combined system, therefore, to ensure the surroundings are at the same temperature as the surface.[3]

In practice, there are a number of factors that complicate this idealised view of 'uniform' microwave heating. Heat dissipation in the sample is only approximately uniform and is affected by concentration gradients and microstructure of the material. Furthermore, penetration depth is often of the order of the sample size; the field will therefore be attenuated by absorption as it passes through the material and will tend to absorb more strongly at the surface (this is, of course, offset by surface cooling effects). Finally, for most materials the dielectric permittivity is a strong function of temperature and effective control is hampered by the risk of thermal runaway, as discussed in Section 1.1.2.

In chemical synthesis, the inverse temperature profile has been exploited in order to superheat reaction solvents. The boiling of a liquid requires two things: sufficient energy to break all intermolecular forces and a nucleation point at which bubbles of gas may form. Nucleation points may be added (e.g. boiling chips or salt) the walls of the reaction vessel, or small gas bubbles in the solvent. An unstirred, conventionally heated sample will be hottest at the outside with a temperature gradient towards a cooler centre. The solvent will begin to boil when the surface region reaches the necessary temperature. The centre, however, can remain below this temperature. With microwave heating, the temperature profile is inverted. Heating is uniform, but surface cooling (the reaction vessel would be chosen so as it did not heat with microwaves) would make the surface region colder. To make the liquid boil it is necessary to heat the surface region to the boiling temperature, at which point the temperature at the centre could be several degrees above the boiling point i.e. the liquid is superheated (Table 1-1).

The result is that reactions may be performed under solvent reflux, but at significantly higher temperatures, resulting in increased reaction rates.[22] For example, the Knoevenagel reaction of acetophenone with ethyl cyanoacetate was shown to have a rate enhancement of 2.5 times under reflux, though for like-temperature comparisons no increase was observed.[23]

Table 1-1 - Nucleation limited boiling points of selected organic solvents in a microwave oven compared with conventional heating. [2]

SOLVENT	NUCLEATION LIMITED BOILING POINT / K	CONVENTIONAL BOILING POINT / K	DIFFERENCE / K
Water	377	373	4
Methanol	358	337	21
Ethanol	376	355	21
Acetone	354	329	25
Tetrahydrofuran	354	339	15

The inverse temperature profile has also been exploited in solid state chemistry. The synthesis of some ceramics goes via a self-propagating, high-temperature synthesis (SHS) route, e.g. the formation of silicon carbide from the elemental precursors.[24] The reaction is initiated by the introduction of a heat source to the compacted reactants and a combustion wavefront then spreads rapidly through the material, generating the product. The problem with conventional methods is that the initiation step must be performed at the surface. The result is often incomplete conversion and undesirable product morphologies. Microwaves can be used to preferentially heat the centre of the sample and initiate the reaction at this position, resulting in a more uniform product and interesting product morphology, e.g. whiskers.[24] If desired, it is perfectly possible to create a non-uniform microwave field and thus selectively heat a specific area of a sample. The methodology of this is discussed in more detail in Section 1.3.

Another non-thermal effect of microwaves is to produce different product ratios. An example of this is the Diels-Alder reaction of 3,6-dimethoxy-β-dihydrothebaine with excess methylvinylketone. This synthesis strongly favours the formation of the polymerisation product under conventional conditions. In contrast, the same reaction under microwave heating produces much more of the desired adduct (Figure 1.5), with a correspondingly smaller amount of the unwanted polymeric material,[25] presumably as a consequence of the altered reaction conditions produced when microwave heating is employed.

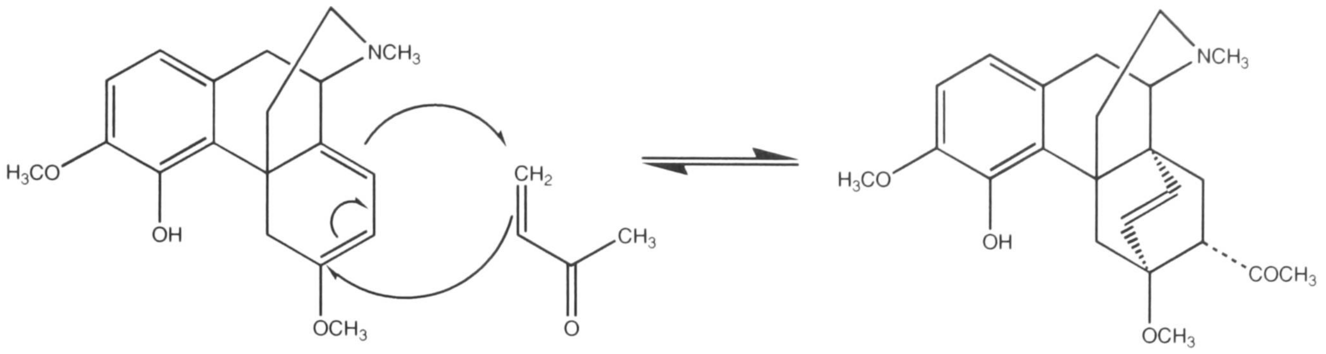

Figure 1.5 – Diels-Alder reaction of 3,6-dimethoxy-β-dihdrothebaine with methylvinylketone.

1.2.2 Selective heating

It has been shown (in the preceding section) that microwaves are specific, in that they only heat the sample, not necessarily the container or the surroundings. This can be extended to allow the use of microwaves to heat low-loss materials. The simple addition of a high loss susceptor (either as a support for the material or as a powder dispersed through the material) will, when irradiated with microwaves, introduce a heat source into the immediate vicinity of the sample. Logically, it should then be possible to formulate a reaction where only some of the components will heat with microwaves. A simple example is the choice of a non-polar, solid matrix with a polar reactant or reactants dispersed through it. The microwave field selectively heats the reactant molecules and reaction may proceed without the need to heat the bulk material to a significant degree. In reactions where there are competing processes, it may be possible to selectively excite a molecule, or part of a molecule, thereby favouring one particular route.[26]

For example, it has been proposed that the coupling of the microwave field with certain molecules in solution can generate molecular agitation, but without inducing reaction. Chen and co-workers have shown such an effect in the synthesis of refractory *β*-branched amino acids.[27] The increase in molecular agitation at the same mean temperature appears to promote the synthesis reaction by a factor of 4-8, depending on reaction conditions.

In the solid state, similar techniques can be used, for example, to selectively heat a metal catalyst, but not the support material.[28-30] Microwaves may be used to dry water from mesoporous materials,[31-34] or to remove guest molecules from zeolites without destroying the framework of the material.[35] An increasingly popular application is dry organic chemistry.[36-

[41] This involves carrying out a reaction on a solid support phase, using microwaves to heat the organic molecules, but leaving the solid phase cold. This has the advantage of being a solvent free process, reducing harmful VOC (volatile organic chemical) emissions, and the solid phase may be recycled for reuse.

1.2.3 Mass transport effects

High temperature processing of solids is an important area of microwave application and includes, amongst other things, sintering of ceramic compacts to create ceramic pieces of desirable physical and mechanical properties, namely hardness, strength and durability.[5, 7, 42-47] High temperatures are necessary in order to activate the mass transport phenomena responsible for grain fusion and growth. However, heating by conventional means can be very expensive and, in order to maintain uniform temperature throughout the sample, slow heating and cooling cycles are required, resulting in extended process time. Microwave heating can present benefits, not only in terms of heating efficiency, but also enhanced rate of reaction as a result of an increase in mass transport rate.[48, 49]

Mass transport in the solid phase implies diffusion of some species through the structure. One of the most important, yet simple, mechanisms in crystalline solids is vacancy diffusion. Vacancy formation requires energy, U, to deform the lattice, but results in an increase in the entropy, S. The vacancy concentration at equilibrium is thus dependent upon the temperature and the stresses acting on the crystal body (since these affect U). The concentration is established from the minimum in the free energy, A, at a given temperature (where A is the Helmholtz free energy).

$$A = U - TS \tag{1.13}$$

The vacancy concentration is generally small so that any interaction between vacancies is negligible, making the application of the ideal gas theorem possible. It is therefore convenient to consider transport of vacancies rather than diffusion of atoms. The vacancy diffusion coefficient, D, is proportional to the probability of atom transfer into a neighbouring vacant lattice site:[50]

$$D \propto a^2 \nu_0 \exp\left(-\frac{\Delta A}{kT}\right) \qquad \textbf{(1.14)}$$

where a is the lattice parameter, ν_0 is the vibration frequency of the atom and k is Boltzmann's constant. On inspection, Equation (1.14) has an Arrhenius-like formulation, that is, diffusion is a thermally activated process that becomes significant when the temperature exceeds some critical value determined by the activation energy.

Sintering of a ceramic is well described by this vacancy diffusion model.[19, 21] At high temperatures, several processes compete; control of these processes is the key to improved product quality. Diffusion can take place via a number of pathways, including at the surface, at the grain boundary and through the bulk. Diffusion at the surface and grain boundaries can lead to the formation of rigid 'necks' between grains, opposing densification.[51] It is well known that inhibition of surface diffusion at the initial stages of densification favours a higher quality product. Rapid attainment of sintering temperature promotes bulk diffusion over surface diffusion (surface heating is favoured by conventional heating) reducing the formation of rigid neck structures between grains. Furthermore, when microwave heating is used to produce a uniform temperature profile, thermal stresses are reduced and the ceramic is less likely to develop cracks and related problems. In later stages of the sintering process microwaves appear to help to limit grain growth. Re-crystallisation and subsequent grain growth is the main obstacle for the fabrication of nanostructured ceramics. Yet, it can be accomplished routinely using microwave heating leading to enhanced mechanical properties.[5, 49]

Although there is no doubt that microwave heating can lead to denser, stronger and harder ceramic work pieces, there is some debate as to why. It is thought that the microwave field is responsible not only for heat dissipation, but also for increased ion mobility. It has been established that microwave sintering can be performed at a lower temperature than conventional sintering.[49] Applying Equation (1.14) would lead to the conclusion that the activation energy must therefore be reduced under microwave heating and diffusion occurs via a lower energy route.[50] However, this seems an unlikely proposition as the activation energy is largely determined by intrinsic material characteristics such as the atomic bonds and structure of the compound. Some significant work by two groups: Booske, Cooper and

Freeman,[50, 52] and Rybakov and Semenov[53] dispute the diminished activation energy theory. One of the key experiments has been the measurement of ionic conductivity of various halide salts in response to applied microwave power. The experimental system is simple. A salt crystal is mounted between two electrodes, over which a dc bias voltage, *V*, is applied and the current, *I*, measured. Sample temperature is controlled by resistive heating tape and pulsed microwave radiation is incident on the crystal (Figure 1.6).

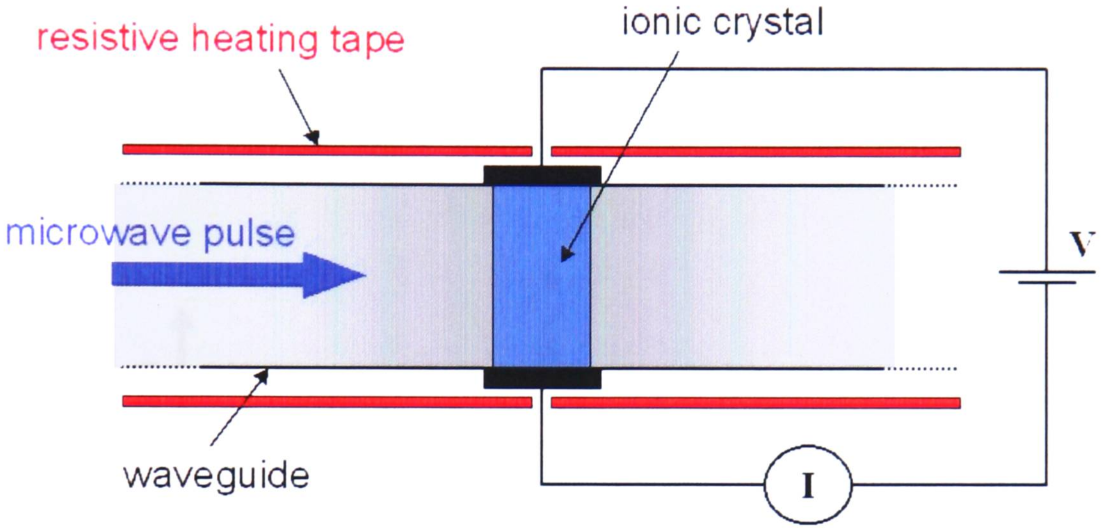

Figure 1.6 - Schematic illustration of the configuration used to observe microwave field effects on ionic currents in halide salt crystals.

The experiment was designed to distinguish whether microwaves effectively lowered the activation energy for mass transport or whether the microwave field provided an additional force for mass transport. These two effects were resolved by performing experiments with different values of bias voltage and applied microwave power. It was found that upon varying the bias voltage the increase in ionic current during a pulse was independent of *V*. Furthermore, with no dc voltage bias applied, finite current was measured during microwave pulses. This points to the microwave field acting as an additional and separate force for mass transport of ions. It was also shown that the microwave-induced part of the ionic current scaled with the square of the microwave field intensity, suggesting a non-linear interaction.

Another very interesting piece of work has been performed by Whittaker and co-worker.[54] By making use of plane-polarised microwave radiation they were able to show the directional nature of the enhanced diffusion. The experiment design was simple: a compressed pellet of $YbBa_2Cu_3O_7$ was embedded inside a larger pellet of the iso-structural material, $YBa_2Cu_3O_7$. The resulting pellet was placed in a mono-mode microwave resonator, arranged so that the electric field was plane-polarised, and irradiated for a period of several days. Elevated temperatures (~850 K) were employed to ensure that mass transport processes were also activated thermally. At the end of this period the sample was sliced, polished and examined using X-ray fluorescence on a scanning electron microscope. They showed that diffusion of yttrium into the ytterbium structure was greater parallel to the electric field than perpendicular to it, Figure 1.7. This evidence, together with that from the previous example, suggests that microwaves themselves provide a force for mass transit and do not affect the activation energy for the process.

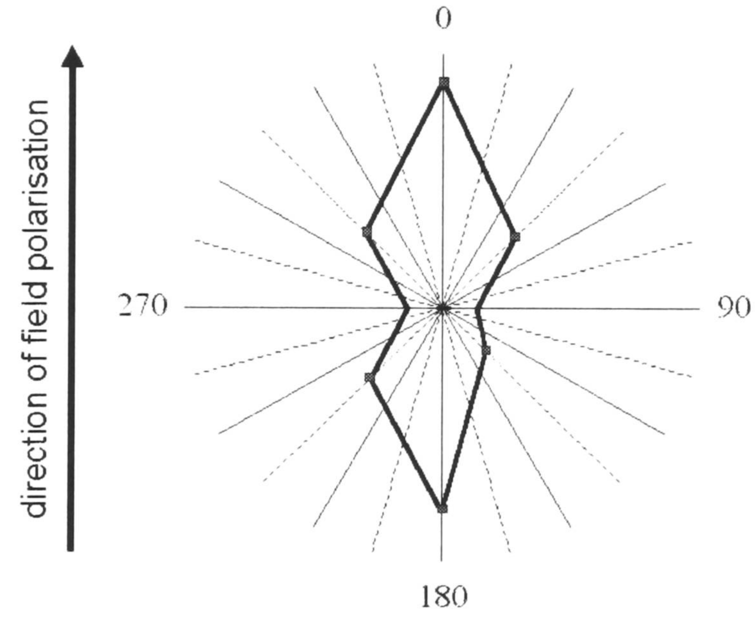

Figure 1.7 - Polar plot of relative diffusion coefficient of yttrium under microwave irradiation (Y/$YbBa_2Cu_3O_7$, 5 days, ~850 K) as a function of angle.

There are two leading theories to explain the enhanced ion diffusion, which we will term "non-equilibrium excitations" and "ponderomotive effects".[50] It should be noted that though these theories are different in essence, they are not mutually exclusive and the true mechanism may include aspects of both.

The excitement of particular phonons has already been touched upon in Section 1.1.2. For excitation to occur in this manner the energy of a microwave-frequency photon must correspond to the difference in energy between two phonons:[5]

$$\omega_{field} = \omega_{phonon\,1} - \omega_{phonon\,2} \tag{1.15}$$

where, due to the conservation of energy and momentum, the sums of frequencies, ω, and wavevectors, $\mathbf{k}$, of the interacting vibrations are conserved. This drives the energy distribution away from equilibrium. The theory of non-equilibrium excitations supposes that the rate at which the system is driven away from equilibrium is greater than the rate of energy redistribution. Under these non-equilibrium conditions, some lattice vibrations will have more energy than usual for a given temperature, which may result in increased probability for atoms to diffuse into adjacent vacancies. The magnitude of this effect has yet to be fully investigated, though Bykov, Rybakov and Semenov have performed some calculations in order to provide an estimate.[5] The calculations show that the fraction of total energy in the system (for a model ionic material) stored as non-equilibrium excitations is about 10^{-10}. They therefore conclude that the contribution of non-equilibrium excitation processes have an insignificant contribution to mass transport. However, real materials may behave differently from their ideal model.

The other popular theory is that of the ponderomotive force (PMF). The ponderomotive theory is based on considerations from plasma physics. Transport effects are manifest as a result of gradients in charge mobility (e.g. near surfaces and boundaries), rather than as a consequence of gradients in the radiation field intensity (as with gas plasma). The theory is complex and requires non-linear perturbation analysis of three fundamental equations: the mass transport equation for mobile ions, the continuity equation and Gauss's Law. Details of this analysis are beyond the scope of this work and can readily be found elsewhere.[6, 52, 53, 55] The theory is simplified by the consideration of vacancy diffusion, rather than atomic diffusion. In crystalline solids, the microwave field acts on electrically charged vacancies. In ponderomotive theory the vacancy flux ($\mathbf{J}$), resulting from either a concentration (C) gradient (∇C) or an electric potential gradient ($\mathbf{E}= -\nabla V$), is described by:

$$\mathbf{J} = -D\nabla C + \frac{DCq\mathbf{E}}{kT} \tag{1.16}$$

where D is the diffusion coefficient and q is the effective charge. The vacancy flux contains two components: *diffusion* and *drift* (the two terms on the right side of Equation (1.16) respectively). The drift term is due to the applied field and even in comparatively weak electromagnetic fields, it exceeds the characteristic value of the diffusion component. However, since the microwave field is oscillatory, the time-averaged effect on vacancy flux would be zero. Non-zero interactions can only result from non-linear rectification of the ionic currents. These tend to occur at surfaces, boundaries and interfaces. It has been shown that currents up to 80° out of phase can be rectified at the interface, resulting in a non-zero drift flux.[19, 51] The direction of flux is the same for both positively and negatively charged vacancies, which means that a transport of neutral mass occurs. Generally the mobility of positive and negative vacancies is different and a net charge transport has also been observed. The final result for the net drift vacancy flux (responsible for mass transport) can be presented as the product of effective mobility and the average volumetric force.

$$\langle \mathbf{J} \rangle = \frac{D_+ D_-}{D_+ + D_-} \langle \rho_{sc} \mathbf{E} \rangle \qquad \textbf{(1.17)}$$

Where ρ_{sc} is the space charge density ($= |q_+|N_+ - |q_-|N_-$). Generally, the magnitude of the ponderomotive force can be assessed from the 'pressure' of the electromagnetic field, $\mathbf{E}^2/8\pi$. For typical microwave applications (field strength of the order of 10^3 Vcm^{-1}) the radiation pressure is as low as 0.1 Pa, significantly lower than that normally required to influence mass transport phenomena by electromagnetic field pressure.[56] However the action of the microwave field seems to be effectively amplified. Part of the reason for this is that the effect is applied directly to a relatively small number of mobile vacancies. Thus, it can be shown that the equivalent stress induced by the ponderomotive action exceeds the radiation pressure by a large factor, $C_0/C \geq 10^5$ (where C is the concentration of vacancies and C_0 is the concentration of atoms in the solid).[5] In addition, the microwave field can have a localised effect at surfaces and grain boundaries, where vacancy concentrations are highest.[51] Rectification of currents across boundaries between particles can result in large amplification of the microwave field.

A recent study has used computer modelling to calculate the electric field in and around spherical particles.[51] Figure 1.8a shows focussing of the field in the neck region between two particles, whilst Figure 1.8b shows that the field is most intense immediately adjacent to the outer circumference of the neck and that the field in the neck region is tilted away from 45° and rectified towards the inter-particle axis. Amplification up to three orders of magnitude can occur in this region, with respect to the particle-averaged field. This is particularly relevant to microwave enhanced sintering of ceramic materials since the mass transport processes that result in densification occur predominantly within this neck region, suggesting the role of ponderomotive forces is especially relevant.

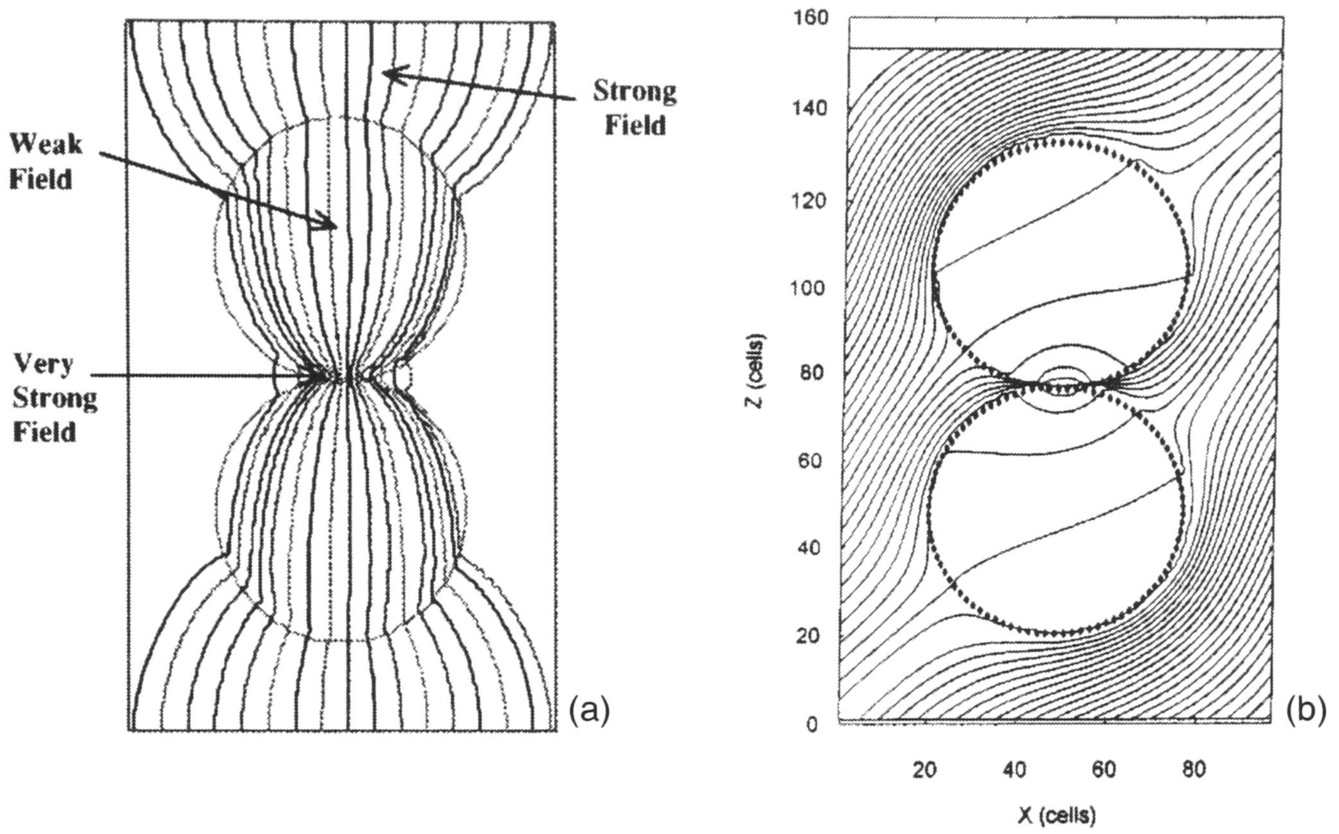

Figure 1.8 – Calculated electric field in spherical particles. (a) electric field in the neck region between two particles, field-lines shown. (b) equipotential contours in the vicinity of the interparticle contact zone when the applied field (2.45 GHz) is is aligned 45° to the axis joining the particles.[51]

1.2.4 Biological effects

The effects and dangers of exposure to microwave-frequency radiation, such as that emitted by mobile phones, is a matter of some concern. Though the emitted power of a typical mobile phone handset (0.5-1 W) is far too small to result in any significant heating, there is a question as to what the chronic effect of regular, low-level exposure is. Governments in various parts of the world have issued regulations and guidelines for the use of mobile phones. However, these limitations are frequently based only on the well-understood heating effects of microwaves, owing to the dearth of information concerning non-thermal effects. A report commissioned for the UK government,[57] for example, recommended a precautionary approach to the use of mobile phones and a lowering of exposure limits, but admits to there being little peer-reviewed scientific evidence to support this. Given the lack of scientific evidence concerning long-term exposure any limitations are effectively arbitrary. However, a few studies have been published which are the first to begin to look at the problem from a scientific basis.

It has been shown, by de Pomerai and co-workers, that heat-shock proteins (HSPs) are produced in response to overnight exposure of nematode worms to low-level microwave radiation.[58] HSPs are induced in most organisms by adverse conditions, such as heat or toxins, that cause harm to cellular proteins. They act as chaperones to help repair the damaged proteins. Though no heating was observed in their sample, HSP production would correspond to a rise in temperature of 3K. It was proposed that microwaves induce the production of HSPs through a non-thermal route. This could be through disruption of weak bonds that control protein conformation, enhanced production of reactive oxygen species (known to induce an HSP response), or by interference with the relevant cell-signalling pathways. Further work by the same group has shown that exposure to microwaves can have distinct effects on the growth and maturation of these nematode worms.[59] Both factors are enhanced significantly by microwave irradiation, yet mild heat treatment (a rise of 3 K) has the opposite effect. This work is further evidence that a non-thermal mechanism operates.

Recent work by Leszczynski and co-workers on *in-vitro* human endothelial cells has shown the same sort of effect.[60] Transient changes were noted in a number of proteins, including HSPs amongst others. It has been put forward that chronic expression of HSPs, resulting from the regular use of mobile phones, may ultimately lead to cancer formation in humans,[61] but as yet the hypothesis remains untested.

Despite evidence of non-thermal microwave effects, a more critical analysis is perhaps required. The studies mentioned above all state that no temperature rise had been observed. Yet, it has previously been shown (Section 1.2.2) that microwave heating can be extremely selective and local hotspots may not be sufficiently large to affect the average temperature.[62] This, of course, could still be classified as a microwave-specific effect as it is not a consequence of heating from a conventional source. Obviously, more work needs to be done to clarify these issues.

In summary, there are several examples of microwaves having non-thermal effects on biological tissue. However, there remains no evidence that this translates into deleterious health effects for humans. More quantitative evidence will be required before conclusive evidence can be gained. Studies of protein conformation and vibrations are perhaps one route to discovering the fundamental effects of microwave irradiation on biological systems. However, the complexity of biological materials and the relative difficulties in performing common structural analyses, such as X-ray diffraction (poor scattering from light elements and amorphous samples or solutions) have prevented such studies from being successful.

1.3 Microwave transmission theory

The previous two sections have shown how microwaves can heat and affect matter, yet the efficiency of heating or magnitude of this effect can be greatly affected by the means in which microwaves are brought into the vicinity of the sample. These considerations become even more important when attempting to design equipment to measure and quantify the effect of microwaves upon a material. It is essential therefore to understand the technologies used to transmit, emit and focus microwaves onto their target.

Though microwaves are part of the electromagnetic spectrum, their long wavelength means that it is impractical to manipulate them in the same manner as, for example, visible light, i.e. lenses, mirrors, etc.[†] Instead of a beam of photons, microwaves are treated more as a wave and as such the components for transmitting microwaves are much like those used for electricity transmission. Open wires, coaxial cables and parallel plates are all capable of transmitting microwaves in the elementary TEM mode, as in free-space transmission (Chapter 1.1). Waveguides are also very useful for microwave transmission and have the advantage of being able to operate in different electromagnetic modes, depending on their dimensions.

Although microwaves may be sent along open (non-coaxial) wires, the traditional view of this practice, i.e. power transmission along a pair of conductors, breaks down at microwave frequencies. The physical separation between conductors is a significant part of a wavelength, so at a distant point there is a phase difference between components of field due to the conductors. Energy is radiated wastefully into space and effective power transmission is not achieved. Closed waveguides (rectangular or circular cross-section tubing) are used instead as they behave as a transmission line at lower frequency in many important aspects. Energy does not escape from the waveguide, and the power is transmitted efficiently.

[†] By in large this discussion deals with the most commonly used frequencies, having wavelengths of the order of centimetres, however an exception to this statement occurs for high-frequency microwaves where their short wavelength will allow the use of lenses, mirrors, etc, to a limited degree.

1.3.1 Coaxial cable transmission

A coaxial line is shielded, unlike an open wire, and so will not radiate strongly. It can be a rigid section or, commonly, a flexible cable. This flexibility is advantageous in many low power (< 1 kW) applications, facilitating transmission where there is no room for larger waveguides. A coaxial line, in its simplest form, is a conducting tube of circular cross-section and constant diameter with a conducting element at the centre, also circular in cross-section. The line operates in the TEM mode and ideally does not radiate heavily. The electric field is a set of radial vectors, normal to the surfaces of the inner and outer conductors. The characteristic inductance, capacitance and resistivity of the line are dependent upon the diameter of the inner conductor, b, and the bore of the outer conductor, a. The maximum field intensity, $E_{\max}$, occurs at the surface of the inner conductor[3] and is given by:

$$E_{\max} = \frac{|V|}{b\ln(b/a)} \qquad \textbf{(1.18)}$$

where V is the voltage between the inner and outer conductor. For constant outer radius and $E_{\max}$, the power flow is a maximum when $a/b = 1.65$. The attenuation of power, however, is unavoidable and is the main drawback of coaxial lines. For a perfect coaxial line, attenuation is only significant at higher power levels (> 1 kW) but in reality, surface roughness, contamination and work hardening all contribute to appreciable attenuation and heating of the transmission line at even low power levels. The greatest problem, inherent to all coaxial cabling, is that the mechanical support for the inner conductor (small dielectric discs) attracts dust electrostatically and will eventually cause surface arcing and voltage breakdown between the inner and outer conductors. Bending the cable only serves to exacerbate the problem. Repeated bending results in micro-fractures in the conductor surfaces and is another potential source of power dissipation.

Another issue is the transition between coaxial lines and waveguides or applicators. The currents in coaxial lines are high, especially within the inner line, where the current density is greatest. Less than perfect contact at the waveguide interface can result in severe conduction heating and eventual oxidation.[3] This leads to micro-arcing and may precipitate voltage breakdown. Generally, coaxial lines should only be used for low-power applications and over short lengths where their compact size and flexibility give them distinct advantages.

1.3.2 Parallel plate transmission

Parallel plates behave in a similar way to parallel wires. They radiate significantly and are not an effective means of power transmission. They do find use as a special case of microwave applicator, however. Two parallel plates will behave much like a simple capacitor. In dc operation a parallel electric field exists between the two plates away from the edges (Figure 1.9).

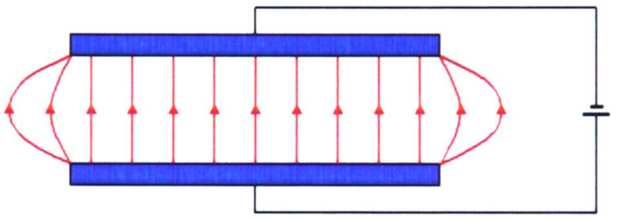

Figure 1.9 - A simple, parallel-plate capacitor with dc voltage across the terminals. Electric field lines are indicated by directional arrows.

When an ac voltage power supply is attached to the terminals of a capacitor, the capacitor will go into a charge-discharge cycle. The direction of the field between the plates will oscillate back and forth. Similarly, when parallel plates are attached to a microwave power source a field is established between them (Figure 1.10). The field oscillates with time at the microwave frequency.

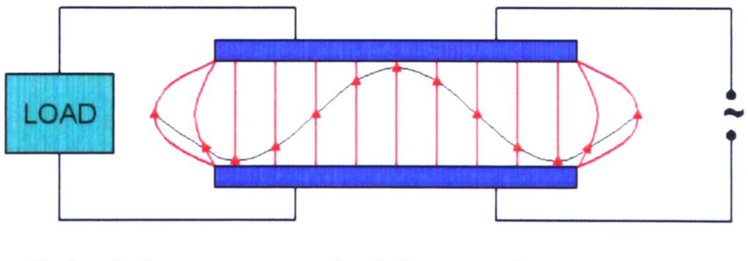

Figure 1.10 – Parallel plates connected to a microwave power source. Electric field lines are indicated by directional arrows. The circuit is terminated in a load where excess power is dissipated. The relative phase is also indicated

It should be noted that the field lines bend at the edges of the plates. This can be a problem in microwave transmission as it can cause field stresses that, with sufficient applied potential, can result in voltage breakdown and arcing. For this reason, radius bends are frequently used in microwave transmission lines.

If a sample material is placed between the plates, it will experience a microwave field acting upon it. The field will be plane-polarised normal to the plate surfaces with its magnitude oscillating with the field.[3] Most of the microwave power is not absorbed by the sample material and, in order to prevent the wave reflecting and causing the formation of a standing wave, the circuit is terminated with a high-loss load, generally water. In many respects, the open, parallel plate system behaves in the same manner as the closed, rectangular waveguide system (Section 1.3.3). The main difference is that the two open sides of parallel plates will radiate strongly, decreasing efficiency. Thus, the field experienced by the sample is highly uniform (away from the plate edges), but is less intense than can be achieved using a resonant cavity.

1.3.3 Waveguide transmission

In almost every industrial and commercial microwave oven, waveguides have an essential role in conveying power from the generator to the load. The heating chamber itself is often based on waveguide technology. An interested reader will find a complete discussion on waveguides by Meredith.[3] As opposed to open wires, parallel plates and coaxial cables, waveguides support several modes of transmission. There are two differential equations, which describe two important classes of wave propagating in the waveguide. They are derived in rectangular co-ordinates (*x*,*y*,*z*), where *z* is the axis of propagation.

$$\frac{\partial^2 H_z}{\partial x^2}+\frac{\partial^2 H_z}{\partial y^2}+k^2 H_z=0 \qquad \textbf{(1.19)}$$

$$\frac{\partial^2 E_z}{\partial x^2}+\frac{\partial^2 E_z}{\partial y^2}+k^2 E_z=0 \qquad \textbf{(1.20)}$$

where $k^2 = \omega^2\mu_0\varepsilon_0 + \gamma^2$, $\gamma = \alpha + i\beta$, α is the attenuation constant and β is the phase constant (equal to $2\pi/\lambda_0$). Propagating waves based on Equation (1.19) are designated H modes, or more commonly TE (transverse electric) modes, as the magnetic field has only an axial component, H_z, and there is no axial electric field (E_z=0). Only transverse electric fields (E_x and E_y) are possible for these modes, hence the TE label. Similarly for Equation (1.20), propagating wave solutions have an axial component of electric field, E_z, with H_z=0. These are designated E or TM modes.

Attenuation in waveguides is almost entirely due to conduction heating in the walls. The magnitude of the heat dissipation in the walls depends on the material chosen for waveguide construction. Aluminium is the material of choice in industrial applications (due to its low-attenuation and relatively low cost), whilst copper and brass are often used in laboratory equipment (due to their ease of machining). Other materials, such as stainless steel, can be used when high temperatures are required, but attenuation in these materials is higher. Attenuation is increased by surface roughness, micro-fissures or corrosion.

1.3.3.1 Rectangular waveguides

A rectangular waveguide is a tube of rectangular cross-section. The internal dimensions are designated a (broad face, parallel with x-axis) and b (narrow face, parallel with y-axis), see Figure 1.11.

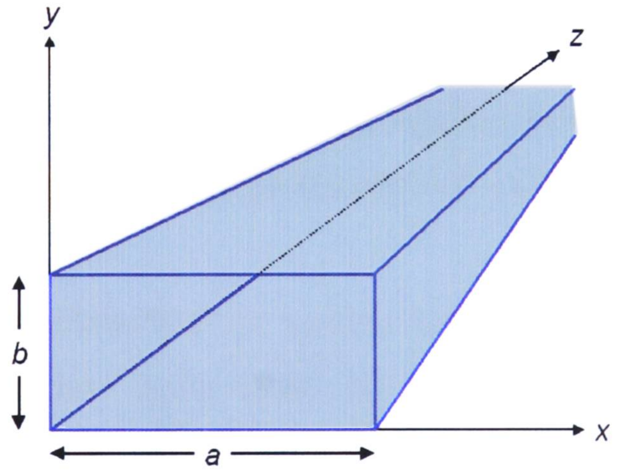

Figure 1.11 - Rectangular waveguide co-ordinate system, with broad-face (*a*) and narrow face (*b*).

The boundary conditions for the waveguide are the same as any conductor. Assuming perfect conductivity, the electric field tangential to the walls must be zero, E_{tan}=0. The magnetic field normal to the walls is also zero, H_{norm}=0. Solution of field equations applying these boundary conditions leads to a number of different modes, characterised by values of *m* and *n*.

For TE modes *m* and *n* are positive integers greater than or equal to zero. (Note, only one can be zero to avoid the trivial solution of all-zero fields.) The modes are labelled $TE_{m,n}$. The integers *m*,*n* indicate the number of sinusoidal half cycles of intensity existing within the waveguide: *m* along the *x*-axis, *n* along the *y*-axis. Clearly, the simplest mode is the TE_{10}, having a single half-wave in the electric field across *a* and a constant value across *b*, see Figure 1.12.

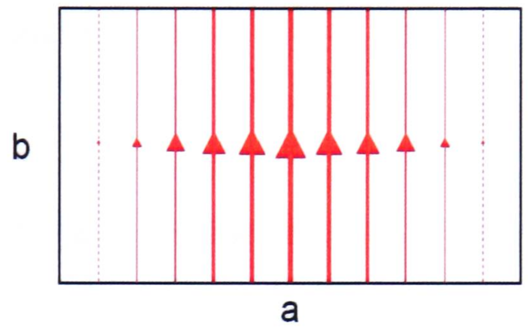

Figure 1.12 - Electric field in the TE_{10} mode: transverse section across waveguide.

Equally, there are a number of $TM_{m,n}$ modes, where *m* and *n* are integers greater than zero. Hence the lowest order TM mode is TM_{11}, i.e. one half-wave of magnetic field across both the *a* and *b* dimensions, maximum field intensity being at the centre of the waveguide. TM modes are of less interest in relation to heating applications, as the normal mechanisms involve only the electric field and TE modes are deemed more useful.

The particular mode or combination of modes that operate in a given waveguide is determined by the dimensions. Each mode has a cut-off wavelength, λ_c, which is the maximum wavelength that will propagate in a given waveguide, for a given mode.

$$\left(\frac{2}{\lambda_c}\right)^2 = \left(\frac{m}{a}\right)^2 + \left(\frac{n}{b}\right)^2 \qquad \textbf{(1.21)}$$

For microwaves with $\lambda > \lambda_c$ the field intensity will be rapidly attenuated and the wave will not propagate. Clearly, Equation (1.21) can also be used to calculate minimum waveguide dimensions for a particular microwave frequency and a particular mode. Appropriate choice of waveguide dimensions can be used to select a single mode, i.e. the lowest order mode, TE_{10}. Substitution of m=1 and n=0 into Equation (1.21) shows that the cut-off wavelength for this mode, $\lambda_c=2a$. Thus in order for a waveguide to propagate its width must be at least half the free-space wavelength. Applications where only the TE_{10} mode is selected operate in the mono-mode regime. Though important in theoretical studies, mono mode ovens have the disadvantage of distinct troughs and peaks in the electric field intensity. In multi-mode ovens (where several modes operate) the superposition of all the modes tend to average out the field strength so that heating of a body is more even.

The microwave wavelength inside the guide, λ_g, is not the same as in free space and is generally longer than its free-space counterpart, λ_0. For the fundamental TE_{10} mode, λ_g is given by:

$$\frac{1}{\lambda_g^2} = \frac{1}{\lambda_0^2} - \frac{1}{\lambda_c^2} \qquad \textbf{(1.22)}$$

The guide wavelength, λ_g, increases as λ_0 approaches λ_c. This is an important consideration in the design of microwave heating applications as it will effect the positioning of field maxima.

1.3.3.2 Circular waveguides

The use of circular waveguides is generally limited to specialised heating applications. The reason for this is that for the fundamental mode (analogous to the TE_{10} mode in rectangular waveguides) the plane of polarisation may twist, causing phase mismatch and power loss. Circular waveguides are therefore not used for transmission, but they do find applications as heating ovens. Like rectangular waveguides, circular waveguides support both TE and TM modes, each with its individual cut-off wavelength, λ_c. The calculation of λ_c is a more complicated process than for rectangular geometry. It is sufficient to know that for the lowest order mode, TE_{11}, the cut-off wavelength, $\lambda_c=3.413a$, where a is the internal radius of the circular waveguide. For fixed-frequency applications, the cut-off diameter (equal to $2a_c$) is often a more useful quantity and is equal to $0.5860\lambda_0$. Tubular sections with a diameter that is less than this value can be used as chokes, i.e. an open tube with high attenuation rate, which microwaves cannot significantly penetrate. Chokes have an important role in allowing the safe introduction of probes into the hot reactor zone whilst preventing microwave leakage.

1.3.3.3 Waveguide bends

In practice, waveguide dimensions are frequently chosen to allow only the fundamental TE_{10} mode to operate, avoiding resonance and impedance-matching problems. Attenuation and conduction losses are reduced for larger waveguide dimensions, hence as large a size of waveguide as possible, whilst avoiding higher order modes, is desirable. In practice, dimensions of ~25% less than the cut-off dimensions for higher order modes are used otherwise discontinuities, such as bends and twists, are liable to excite higher order modes.

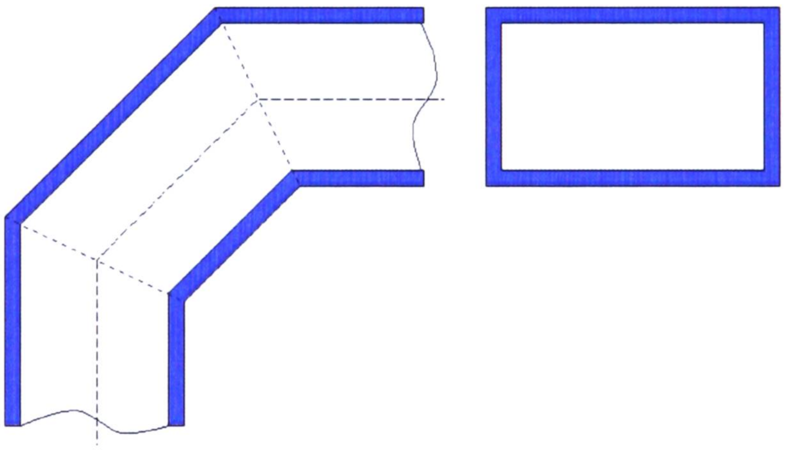

Figure 1.13 - E-plane, 3-section bend of a rectangular waveguide, also known as a mitre bend, in plan (left) and cross-section (right).

Incorporation of bends is inevitable in most practical uses of waveguides. Large radius bends create negligible reflection, but are inconvenient. Small radius bends are also excellent in principle, but are difficult to manufacture to the required level of accuracy. Mitre bends are the preferred method, are cheap to fabricate and, when designed well, will give low resultant reflection. Mitre bends are designed with an intermediate section of waveguide $\lambda_g/4$ long, measured along the centre-line of the broad face, joined between two straight sections. This gives two mis-matched zones where the reflections are equal and spaced apart $\lambda_g/4$ so that they cancel. It is preferable to have an odd number of sections in the bend, giving an even number of junctions, whose reflections cancel out in pairs. Bends can be either E-plane (where the side walls of a rectangular waveguide remain in the same plane, Figure 1.13) or H-plane (where the broad walls remain in the same plane).

1.3.3.4 Waveguide – coaxial interface

Low power microwave transmission frequently employs coaxial cabling (for spatial considerations) yet transmission from the generator is via a waveguide and microwave applicators are often based on waveguide technology. Hence, an interface is required in order to facilitate joining of one form of transmission to another. Conceptually this is simple: add a conducting element to the centre of a waveguide (insulated from the walls), connect this to the inner conductor of a coaxial line and connect the walls of the waveguide to the outer sheath (all connections having high conductivity). This is not a perfect solution and a significant proportion of the power is reflected. Nonetheless, for low power applications it is adequate. The design can be improved by the avoidance of sharp edged pieces and the matching of conductor diameter of the coaxial line with waveguide diameter.

For a coaxial to waveguide transmission, such as would be used in a microwave applicator, it is important to have an idea of the resultant field created. Field lines in a coaxial line are radial about the central conductor. On termination of that conductor the field lines fan out from the end towards the side walls, before regaining the regular waveguide mode, Figure 1.14.

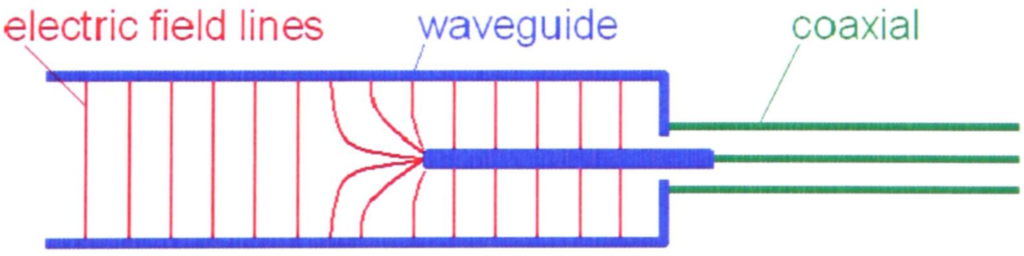

Figure 1.14 - Coaxial - waveguide interface showing the electric field lines in the waveguide.

1.3.4 The microwave applicator

A microwave applicator can be defined as the volume in which microwave energy is dissipated as heat in the sample. This can be simply part of the transmission system (parallel plate or waveguide) in which case the transmission line will terminate in a load. This is acceptable for high-loss samples or where efficiency is not of prime concern. However, low-loss samples will not generally absorb enough energy to heat in a single pass. A complete description of the theories outlined here is presented in reference 20.

In order to improve efficiency the sample can be placed in a resonant cavity. These are often based on waveguide principles, but are short-circuited at one or both ends. The microwaves will be reflected from these short circuits, making multiple passes through the sample until the energy is dissipated as heat in the sample (and in the walls). The incident and reflected travelling waves interfere with one another and result in the formation of a standing wave.

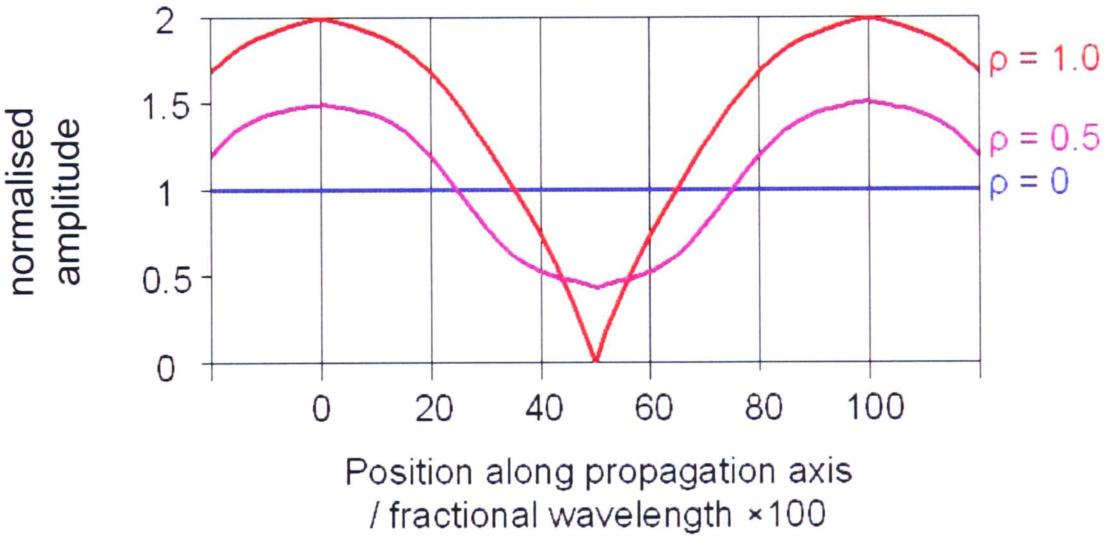

Figure 1.15 - Standing wave pattern for single reflection from terminating short circuit in a waveguide.

Consider the simplest example of a single reflection from a short-circuited end of a waveguide. Regarding the waves as vectors, the forward wave remains fixed along the propagation axis, but the vector representing the reflected wave rotates along this axis. The normalised vector sum representing the standing wave (stationary in position with time) varies from a maximum of $(1+|\rho|)$ to a minimum of $(1-|\rho|)$, where ρ is the reflection coefficient ($0<\rho<1$ with $\rho=1$ representing complete reflection). In general the resultant voltage can be readily calculated:

$$V_{res} = \sqrt{1 + |\rho|^2 + 2|\rho|\cos(-2\beta z)} \tag{1.23}$$

When ρ is small, the resultant varies approximately sinusoidally with position, but as ρ→1.0 it can be seen (Figure 1.15) that the resultant varies quite slowly with displacement, around the maximum value of the resultant, but rapidly near the minimum. The resultant field pattern has a wavelength equal to half the radiation wavelength, with minima and maxima spaced $\lambda/4$ apart (in a waveguide λ_g must be considered).

An important measure in quantifying the effects of resonance is the voltage standing-wave ratio (VSWR) defined as the voltage maximum divided by the voltage minimum. The minima and maxima are readily measurable using a probe travelling along the axis of propagation. The reflection coefficient can then be calculated.

$$\rho = \frac{\text{VSWR} - 1}{\text{VSWR} + 1} \tag{1.24}$$

Reflected waves can cause damage to the microwave power source. In order to avoid this a circulator[3] is used between the generator and the applicator. A circulator is analogous to a one-way mirror and will allow the output power from the generator to pass through, but will redirect any reflected power into a dummy load. Typically the dummy load is water and, with a knowledge of the heat capacity and flow rate of water in and out of the load, or a microwave detector in the water load, the power dissipated there can be calculated, thus revealing the proportion of the power dissipated in the sample.

1.3.5 Tuning devices

For small samples it is desirable to position the sample at a maximum of the field intensity to maximise heating efficiency. As the field pattern is a function of temperature, it is impractical to have to move the sample during irradiation. Altering the field pattern with tuning devices is preferable. The simplest such device is a sliding short circuit. This takes the form of an adjustable screw attached to the end-plate short-circuiting a waveguide. The length of the resonant cavity may effectively be altered, thus changing the positioning of the maxima. The only difficulty in constructing such a device is the need to maintain electrical conductivity whilst allowing it to slide.

If the nature of the application makes this impractical, another method is to use a multi-screw tuner.[3] This type of tuner can be fairly crude and consists of a set of, typically, 3 or 4 screws projecting into the centre of the broad face of a rectangular waveguide. Each screw provides a variable, capacitive susceptance whose amplitude is a function of the insertion into the waveguide. The difficulty is that adjacent screws interact with each other, making reliable tuning a difficult process. Moreover, the screws tend to heat up due to the high currents and micro-arcing in the thread. Generally they are only practical at low power levels (< 1 kW), where their relative cheapness is the chief advantage.

Commercially available multi-stub tuners have improved significantly over the basic design. They use smooth rods rather than screws, avoiding the detrimental effects associated with the screw thread. They can also be automated, using sophisticated coding, to continually adjust the tuning of the wavefunction and centre the field maximum on the sample.[63, 64]

1.3.6 Temperature measurement during microwave heating

One of the greatest problems encountered when examining a reaction occurring under microwave heating is the measurement of temperature. The various methods of temperature measurement can be broadly classified as either *in-situ*[65-67] or *ex-situ*,[68-70] i.e. measurements can be performed either during microwave irradiation or the microwave power must be turned off before a measurement can be taken. This later approach has some advantages, chiefly that the microwave field cannot interact with the thermometer used and thus relatively inexpensive, non-specialised thermometers may be used. However, the obvious disadvantage is that the sample will have cooled by a small but possibly significant amount before the measurement can be taken.[69] Indeed, the very act of placing a thermometer (at room temperature) into a heated sample may well be sufficient to cause measurable cooling. Furthermore, *ex-situ* methods become impractical if access to the sample is restricted (e.g. during x-ray or neutron diffraction collection).

Thus *in-situ* temperature measurement is desirable during many microwave experiments. However, this is not a straight-forward undertaking. Two of the most common methods of temperature measurement, i.e. thermocouples and mercury or alcohol-filled thermometers, are generally incompatible with the requirements of microwave heating applications. Both will interact directly with the microwave field and give rise to spurious readings. It is therefore necessary to use more specialised measurement devices.

Shielded Thermocouples

This is perhaps the least expensive and consequently most common method of *in-situ* temperature measurement for use in microwave applications. A thermocouple is essentially a pair of wires joined with a welded tip such that the current flowing in the device varies as a function of temperature.[71] However, as the current is being measured the reading will be extremely susceptible to interference from other electromagnetic fields, such as microwaves, see Figure 1.16.

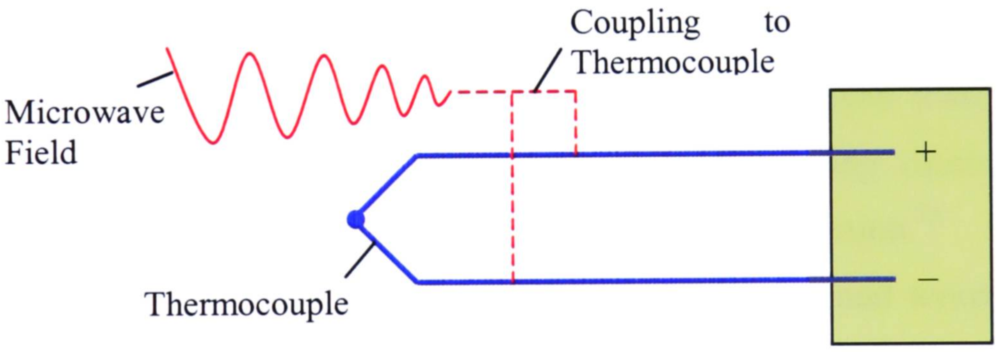

Figure 1.16 - Noise generation in a thermocouple through coupling with a microwave field.

A shielded thermocouple attempts to solve this problem by surrounding the thermocouple in a conducting, earthed sheath, which should prevent microwaves from interacting directly with the thermocouple wires.[66, 67, 72] However, even when shielded, thermocouples are not without their problems. The addition of the shield can make a thermocouple bulky,[73] which is unsuitable for small samples and can result in a temperature lag between the sample and the probe. Furthermore, though the thermocouple should be shielded from direct interaction with the field, the shield itself may act as an antenna (much like a tuning screw does) and be heated directly by the field thus giving spurious results. It has been shown that the presence of a shielded thermocouple in a microwave furnace can locally distort the electromagnetic field, conduct heat away from the sample, induce thermal instabilities and microwave breakdown, and lead to serious measurement errors.[74] Thus for applications that require greater reliability alternative methods must be employed.

Infrared Sensors

Infrared (IR) sensors measure the flux of IR radiation emitted from a body and converts this to a temperature. They have the advantage over thermocouples in that they are *non-contact* or *remote* measurement devices. As such they cannot be affected by the microwave radiation. IR sensors are common, particularly in the bench-top, small-volume reactors that are frequently used in organic synthesis work. However, these sensors have distinct drawbacks in that they are generally set up to measure the temperature at the surface of the vessel. This temperature will significantly underestimate the true temperature of the bulk of a sample (by as much as 30K) owing to the inverse temperature profile of microwave-heated solvents.[65, 73]

In solid state applications an IR pyrometer can be calibrated to record the temperature of a particular material of interest. IR pyrometers have been employed with great success in catalyst chemistry, for example.[48, 62] Similarly thermal-imaging cameras can measure surface temperature and have the advantage of spatial resolution.[75] In this way the temperature profile across the entire sample may be observed and temperature gradients across the sample are clear. The disadvantage of these instruments is that they can only measure surface temperature, unlike a contact probe that may be embedded in a sample or solution.

Other similar methods that rely on optical measurements include the measurement of the position of a materials absorption edge.[76] This was found to have distinct advantages in chemical vapour deposition applications where a gradual build up of material on the reactor's viewing ports would obscure IR pyrometry measurements.

Atypical Thermometers

Thermometers, based on the simple principle of thermal expansion, can be used inside a microwave reactor, if a suitable microwave-transparent medium can be found. Xylene (an apolar liquid) thermometers have been used with some success.[2] Another option is to use a gas thermometer with the temperature being proportional to the pressure as read by a pressure transducer.[77] This is an effective method from room temperature up to 500 K, greater than the liquid range of xylene. However, both these methods require careful calibration in order to achieve accurate results and, owing to the necessary size, they will tend to exhibit temperature lag relative to the sample, especially for small volumes.

Fibre Optic Thermometers

Thermometers based on optical fibres are relatively expensive compared with thermocouples, yet they are seen as the 'gold standard' of temperature measurement in the presence of electromagnetic fields.[73] Fibre optic thermometers depend on either of two principles: fluoroptic thermometry or absorption shift of semiconductor crystals.

Fluoroptic thermometers use a phosphor (magnesium fluorogermanate activated with tetravalent manganese) as the temperature sensing element. The material fluoresces in the deep-red region of the spectrum when excited with ultraviolet or blue-violet radiation. The rate of decay in the emission is a function of temperature (e.g., 5 ms at 73 K, 0.5 ms at 723 K). Measuring the rate of afterglow decay allows an indirect determination of the temperature.[71]

A fibre optic sensor based on absorption shift of semiconductor crystals relies on the temperature-dependent light absorption/transmission characteristics of gallium arsenide (GaAs). A feature of this material is that as its temperature increases its transmission spectrum shifts to higher wavelength. The position of the absorption shift indicates the temperature of the sensor.[78]

In either case the sensing material must be glued to the end of a fibre optic cable and sheathed in a protective sleeve. The sensor may thus be put in direct contact with sample and can measure the interior temperature rather than the surface temperature, giving it distinct advantages over infrared sensors. Furthermore, as no metal is used in its construction and all materials are chosen so as to eliminate interactions with electromagnetic fields, fibre optic temperature probes are the most accurate means of measuring bulk sample temperature. They have fast response times (owing to the small mass of the sensor) and have accuracy generally comparable to thermocouples (in field free conditions). However, they do have one distinct disadvantage in that they are far less durable than thermocouples. The fibre optic cable may be easily nicked or snapped, preventing the device from working. Furthermore, the necessity of gluing the sensor in place imposes a maximum working temperature for the device (typically around 500 K), above which the glue will decay. Nonetheless, where experimental conditions permit, fibre optic thermometers are the most accurate method of temperature measurement in a microwave field.[71, 73]

2 Structure of Solid Materials

2.1 Crystal structure

This chapter introduces several important concepts useful in the understanding of the following experimental work. Crystallography was the major technique employed in the investigations of the materials in the thesis and is described here in some detail. The dynamics of the solid-state are also introduced before being applied in later discussions of the experimental results. For more detail on the topics covered in this section I would direct the reader to some excellent material by Ladd and Palmer[79] and Schwarzenbach.[80]

Solids can be classified as either crystalline or non-crystalline, where crystalline solids are those with an atomic structure based on a regular repeating pattern. Many important materials, for example, glass, plastics, wood and bone, are poorly ordered on the atomic scale and are non-crystalline. However, the fundamentals of how these non-crystalline materials behave are poorly understood. It is instructive, therefore, to limit discussion to crystalline materials where the concepts are well established and more easily modelled mathematically. Even limited to only crystalline materials, an enormous range of different properties are exhibited: insulators, conductors, semi-conductors or superconductors; opaque or transparent; soft or brittle; magnetic or nonmagnetic. These properties can be understood with reference to the atomic crystal structure.

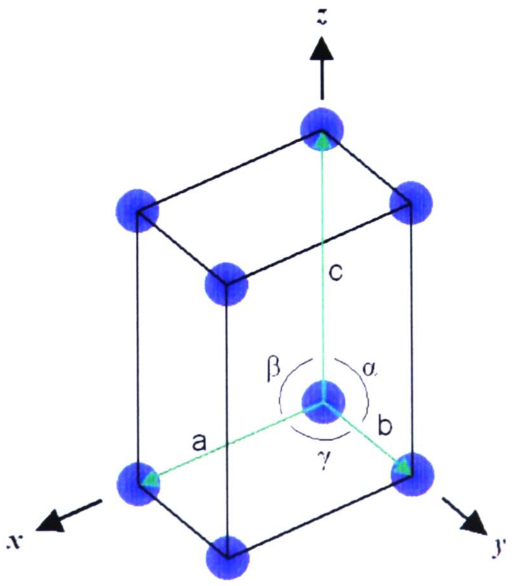

Figure 2.1 - Crystallographic axes and unit cell for a three-dimensional crystal lattice.

A crystal can be defined by its *crystal lattice*: a set of identical points in space, i.e. a theoretical observer at one point would see an identical view to an observer at any other point. The lines joining a point with three of its nearest neighbours can then define a set of co-ordinate axes, where the x, y and z-axes are not co-planar. The distance and direction of the nearest lattice points along the x, y and z-axes are specified by the vectors **a**, **b**, and **c** respectively. The crystal lattice is therefore completely defined by the lengths of **a**, **b** and **c** and the angles α, β and γ between them (Figure 2.1). The positions of all lattice points are reached by drawing all possible vectors of the form:

$$\mathbf{r} = u\mathbf{a} + v\mathbf{b} + w\mathbf{c} \qquad (u,\ v \text{ and } w \text{ are integers}) \qquad \textbf{(2.1)}$$

from the origin. This is true no matter what the choice of origin and shows the translational invariance of the crystal. Therefore a crystalline material is one that possesses a crystal lattice of this kind.

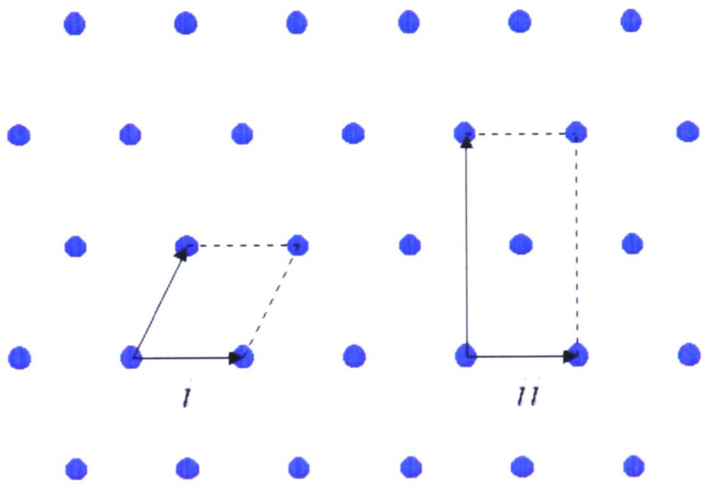

Figure 2.2 - Two-dimensional lattice showing *(i)* primitive and *(ii)* non-primitive unit cells.

The lattice vectors also define the *unit cell* of a crystal. The shape defined by the three vectors (called a parallelopiped) is the unit cell and is the basic repeat unit for the crystal (solid lines in Figure 2.1). The entire crystal can be replicated from the unit cell, transformed through translation. In many cases the lattice is such that there is a choice of more than one possible unit cell. Figure 2.2 illustrates this for a two-dimensional lattice. The primitive unit cell (*i*) has the minimum possible volume, whereas (*ii*) has twice the volume and is defined on a centred rectangular lattice. It is consequently a non-primitive unit cell.

Crystal lattices will contain symmetry properties other than translational invariance. Bravais deduced that three-dimensional crystal lattices could be classified into one of fourteen possible types, according to the symmetry it possesses.[79] The fourteen Bravais lattices (as they became known) contain only one, two, three, four or six-fold rotation axes.

Once the crystal lattice has been determined and used to identify a suitable set of axes and unit cell, the description of the crystal structure is completed by specifying the contents of the unit cell. A group of atoms is associated with each lattice point such that the entire structure is generated. This group of atoms is known as the *basis*. The position of an atom can be defined by the vector, **r**, as described by Equation (2.2).

$$\mathbf{r} = x\mathbf{a} + y\mathbf{b} + z\mathbf{c} \tag{2.2}$$

Each atom can then be identified uniquely by an element type and a vector, **r**. The atom is said to be at position (x,y,z) where x, y and z are fractions of the dimension of the unit cell in the directions of the corresponding axes. If atoms in a unit cell are symmetry related, only one need be specified where the symmetry is stated. Taking symmetry of the basis as well as the lattice into consideration allows any crystal to be sorted into one of 32 point symmetry groups and one of 230 possible space symmetry groups (or simply space groups).[79]

It is possible to identify sets of equally spaced parallel planes within a crystal lattice. Two examples of lattice planes are illustrated in Figure 2.3 for a two dimensional lattice. The density of lattice points on each plane is the same for a given set and all lattice points are contained on each set of planes. Planes of lattice points, such as these, play an important role in the physics of diffraction from crystals.

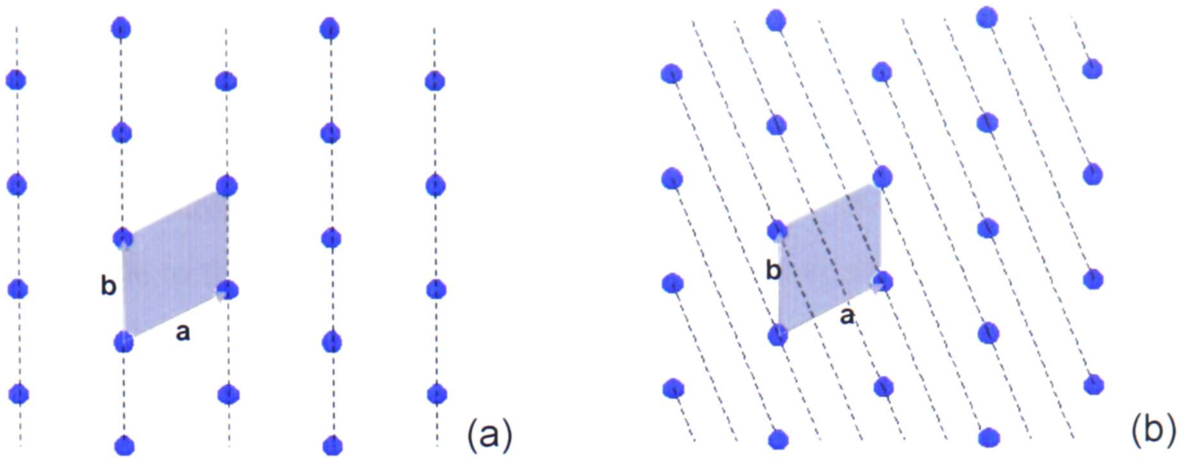

Figure 2.3 - (a) the [1 0] set of planes on a two-dimensional lattice. (b) the [3 1] set of planes on a two-dimensional lattice.

In order to identify the different sets of planes, a set of Miller indices are assigned to each set. In three dimensions a set of planes is referred to by the Miller indices [*h k l*], where all are integers. The indices are defined in such a way that the plane intercepts with **a**, **b** and **c** at 1/*h*, 1/*k* and 1/*l* respectively. Notice in Figure 2.3a that the intercept with the **b** vector is infinite; the Miller index is thus zero. Negative intercepts are indicated by a bar over the corresponding index. The $[\bar{h}\,\bar{k}\,\bar{l}]$ set of planes is however identical to the [*h k l*] set. An alternative method of identification of the Miller indices is to count the number of planes that cut each vector, **a**, **b** and **c**, excluding at the origin itself. Take Figure 2.3b as an example. The **a** vector is crossed by 3 different planes, the **b** vector by a single plane; the Miller indices are therefore [3 1].

Often in crystals, different sets of planes may be related by lattice symmetry and thus be equivalent from an atomic point of view. For example, in crystals of cubic symmetry the vectors **a**, **b** and **c** are equal in magnitude and mutually perpendicular. The sets of planes [1 0 0], [0 1 0] and [0 0 1] are symmetry related and are said to be of the form {1 0 0}, where the curly brackets indicate all planes equivalent by symmetry are included. It is often necessary to specify a direction in a crystal. This can be done using a similar method, by specifying the vector, $\mathbf{r} = u\mathbf{a} + v\mathbf{b} + w\mathbf{c}$. The direction is generally referred to as the [*u v w*] direction. The vector **r** and the plane defined by [*h k l*] = [*u v w*] are perpendicular to one another.

2.2 Crystallography

The subject of crystallography is introduced in this section. A wealth of supplementary material is available to the interested reader in the reference works of Ladd and Palmer[79] and Schwarzenbach.[80]

The structure of crystalline matter can be probed using radiation of wavelength comparable to the atomic separations being investigated, which is of the order of 1 Å (1×10^{-10} m). X-rays, neutrons and electrons can all be generated with the appropriate energies, though X-rays are by far the most commonly used method. A crystal behaves as a three-dimensional diffraction grating for X-rays. In an optical experiment, the spacing of the lines of a grating can be deduced from the separation of diffraction maxima; the relative intensities of different orders can give information about the structure of lines on the grating. In an exactly similar way, measurement of the separation of X-ray diffraction maxima from a crystal allows us to determine the size of the unit cell, and study of the relative intensities can be used to give information about the unit cell contents.

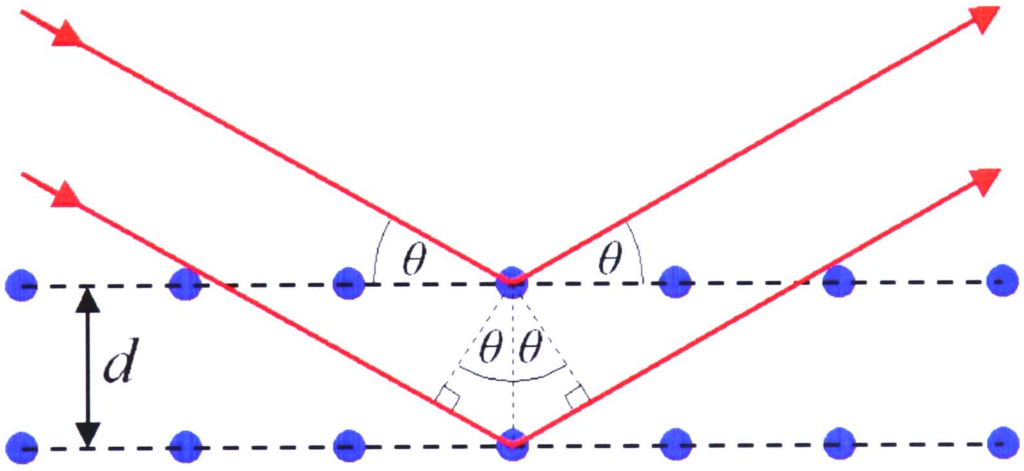

Figure 2.4 - Scattering from successive planes is in phase if the path difference, $2d\sin\theta$ is an integral number of wavelengths, $n\lambda$.

The relationship between diffraction maxima and the spacing between adjacent planes in the crystal was first determined by Bragg. Consider X-rays incident at a glancing angle, θ, on to a set of crystal planes, as in Figure 2.4. Scattering occurs and the X-ray is deflected through an angle 2θ. The X-ray will be similarly scattered from adjacent planes. For constructive interference between scattered beams the path length difference must be an integral number of wavelengths, stated formally as *Bragg's Law.*

$$n\lambda = 2d\sin\theta \tag{2.3}$$

For conditions where the path length is a non-integral number of wavelengths, it can be shown that the diffraction intensity will be zero. Consider if the scattered beams (often referred to as reflections) from the first and second planes were completely out of phase. The result would be that the two would interfere destructively and cancel. Similarly, if the reflections from the first two planes were only 1% out of phase, then the scattered beams from the first and 101st planes would cancel each other out. Thus, as long as a crystal is sufficiently large to have sufficient lattice planes, reflections will always cancel out except in the special case where Bragg's law is satisfied.

The Miller indices of a plane are used to describe the reflection from that plane. Thus the reflection from the [1 1 1] set of planes is the [1 1 1] reflection. Solutions of Bragg's law where $n > 1$ are termed the nth order reflection. However, a less cumbersome notation is commonly used. Rather than stating, "the 3rd order reflection of the [1 1 1] planes," it is described as the [3 3 3] reflection.

The *positions* of diffraction maxima tell us about the crystal lattice, but in order to get information about the unit cell contents the *relative intensity* of these maxima must be studied. Consider a simple ionic crystal, such as caesium chloride, where both ions are mono-valent and the structure has a simple unit cell, as illustrated in Figure 2.5.

For the condition of constructive interference in the [1 0 0] plane (layers of Cs ions) then scattering from the Cl ions (exactly half-way between the [1 0 0] planes) will be in anti-phase and the observed intensity will depend upon the difference between f_{Cs} and f_{Cl}. Similarly, the reflection from the [2 0 0] plane (half the d-spacing of the [1 0 0]) will have both Cs and Cl ions lying on the plane and scatter from both ions will interfere constructively. The observed intensity will therefore depend on the sum of f_{Cs} and f_{Cl}. In this way the relative intensities of different reflections can be used (with knowledge of the scattering cross-sections for the atoms) to gain information on the unit cell contents.

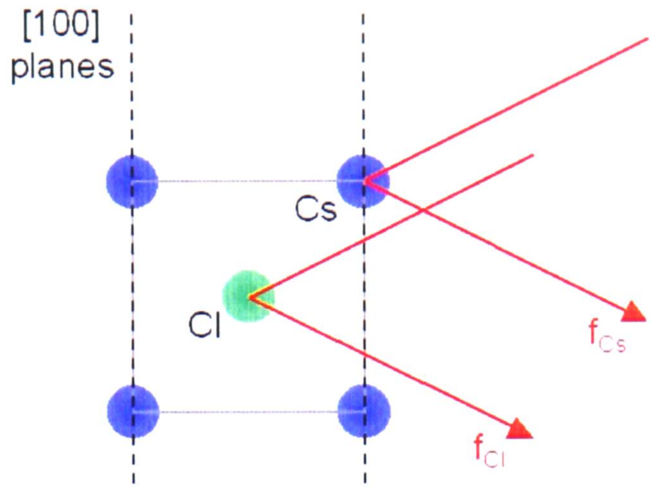

Figure 2.5 - Crystal structure of CsCl viewed in the *x*-*y* plane. The scattering intensities (f) for individual atoms are shown.

Formally, the effect of atomic structure factors, f_j, are combined in the structure factor of the unit cell:

$$F(\boldsymbol{\kappa}) = \sum_j f_j \exp(-i\boldsymbol{\kappa} \cdot \mathbf{r}_j) \tag{2.4}$$

where **r** is a direct lattice vector, as defined in Equation (2.2), and **κ** is a reciprocal lattice vector. The reciprocal lattice is that in which the wavevector **k** exists (Section 2.3). The reciprocal lattice is a set of points for which:

$$\boldsymbol{\kappa} = h\mathbf{A} + k\mathbf{B} + l\mathbf{C} \tag{2.5}$$

where **A**, **B** and **C** are the reciprocal equivalents of **a**, **b** and **c** on the direct lattice.

The structure of a crystalline material is calculated from the electron density, atoms being placed at points of high electron density. The electron density ρ at a given point depends on the structure factor summed over the crystal, F_0. For centro-symmetric space groups, Equation (2.4) can be simplified and electron density is governed by Equation (2.6), where V is the volume.

$$\rho(x,y,z) \propto \tfrac{1}{V}\sum_{hkl} \pm |F_o(hkl)| \cos[2\pi(hx+ky+lz)] \qquad \textbf{(2.6)}$$

There is a problem, in that the phase of the structure factor is unknown. Various techniques exist in order to solve this problem and software exists to routinely perform this calculation and solve crystal structures. However, in order to solve a structure from scratch a single crystal is required in order to gain sufficient data. For real materials, single crystals cannot always be found or grown. In such cases, powders may be utilised.

Diffraction from powders represents a significant reduction in the information content of the data. Rather than the positions of diffraction maxima as a function of angle in three dimensions about the crystal, the data are collected as a function of angle in only one dimension. The crystallites in the powder are randomly oriented. This has the effect of superimposing all data with the same *d*-spacing, e.g. the [1 0 0], the [0 1 0] and the [0 0 1] reflections of a cubic lattice would all be superimposed. *Ab initio* structure solution is essentially impossible for all but the simplest of structures. Instead, powder diffraction is used for phase identification and refinement of known structures. A typical powder X-ray diffraction pattern is shown in Figure 2.6.

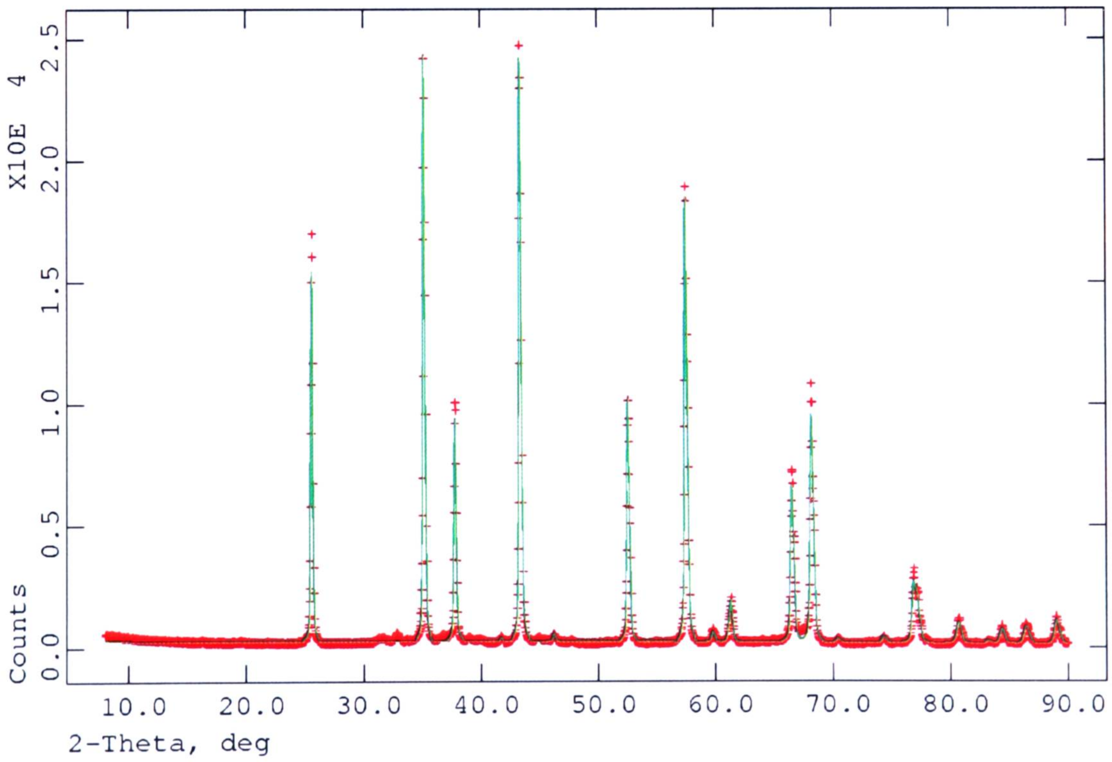

Figure 2.6 - Powder X-ray diffraction pattern of α-alumina, using Cu K_α radiation.

Theoretically, the peaks should be simple lines, but in practice they will have finite width. Contributions to peak broadening include instrumental limitations, slight structural variations and particle size. In order for the Bragg law to hold true the crystal must be a large enough to contain sufficient lattice planes so that for every non-integer value of n in Bragg's law (Equation (2.3)) there is a plane that is exactly out of phase. Scherrer broadening occurs when this is not the case and is the result of small crystallites. The degree of broadening is governed by the Scherrer equation:

$$\beta = \frac{k\lambda}{D\cos\theta} \tag{2.7}$$

where β is the peak width at half-maximum, k is the Scherrer constant (~1), λ is the radiation wavelength, D is the mean crystallite diameter and θ is the Bragg angle. The effect is greater at high angle due to the inverse cos θ dependence.

2.3 Crystal dynamics

In this section the concept of crystals as dynamic systems is introduced. Information on crystal dynamics may be found in a number of books including the excellent texts of Hook and Hall[81] and Kittel.[82]

So far, atoms in a crystal have been considered stationary objects. However, this assumption conflicts with the Heisenberg uncertainty principle, in that it is not possible to know accurately both the position and momentum of a particle. Thus, even at a temperature approaching absolute zero the atoms in a crystal will vibrate about their equilibrium positions. The energy they possess as a result of this zero point motion is the zero point energy. A potential well governs the position of an atom about its equilibrium position. The form of this potential is complex and would require knowledge of the wavefunctions and the energies of the electrons within the crystal. Fortunately, this calculation can be avoided by the use of a few simplifications. The form of the potential well can be described as harmonic; a good approximation for small amplitude vibrations. Figure 2.7 shows, for displacement along their mutual axis how the potential energy of two atoms vary with displacements from the equilibrium separation. The harmonic potential is a good description of the base of the potential well.

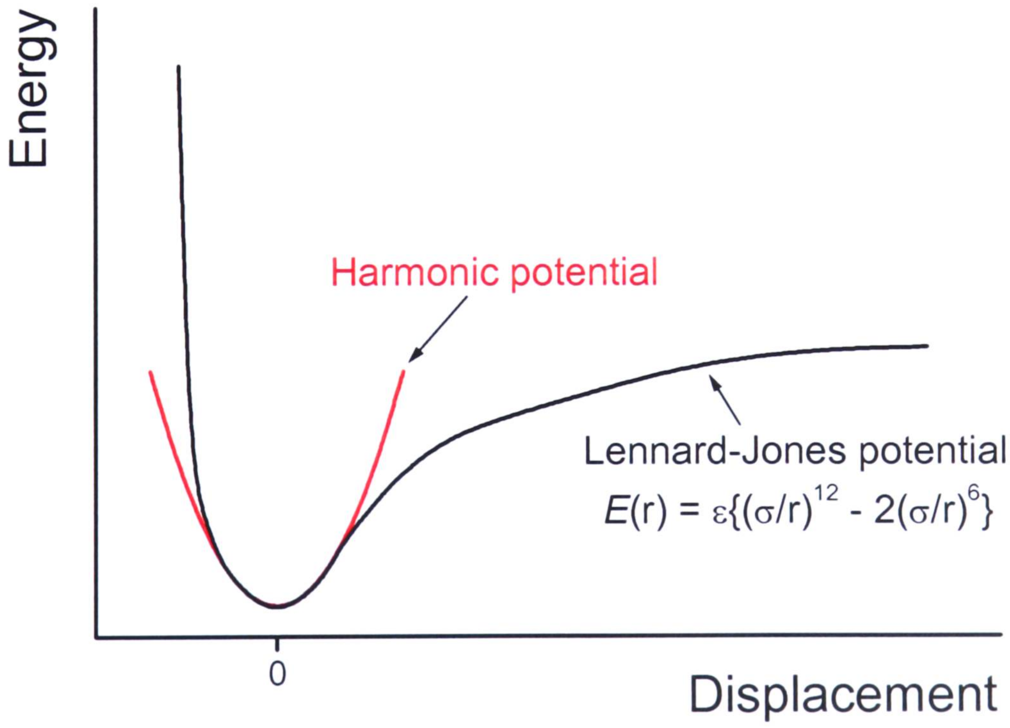

Figure 2.7 - The Leonard-Jones potential for the interaction of two atoms and the harmonic approximation, valid in the small amplitude limit.

2.3.1 Lattice vibrations

Consider a simple one-dimensional model of a solid. A row of identical atoms, with mass M and whose equilibrium positions are separated by a distance a, are connected by means of inter-atomic forces of the form shown in Figure 2.7. The interaction energy, $V(r)$, between nearest neighbours of separation r may, for small deviations of r from its equilibrium value a, be expanded as a Taylor series about $r = a$.

$$V(r) = V(a) + \frac{(r-a)^2}{2}\left(\frac{\mathrm{d}^2V}{\mathrm{d}r^2}\right)_{r=a} + \frac{(r-a)^3}{6}\left(\frac{\mathrm{d}^3V}{\mathrm{d}r^3}\right)_{r=a} + \ldots \tag{2.8}$$

Note there is no linear $\left(\frac{dV}{dr}\right)_{r=a}$ term as the first derivative of V must vanish at the equilibrium spacing where V is a minimum. In the harmonic approximation the higher order terms can be ignored. Curtailing the series at the second order term gives a potential much like that of a spring with force constant, K:

$$K = \left(\frac{\mathrm{d}^2V}{\mathrm{d}r^2}\right)_{r=a} \tag{2.9}$$

Hence the force that one atom exerts on another is $K(r - a)$. Returning to the one-dimensional chain of atoms, consider the forces acting on the nth atom, somewhere in the middle of the chain. If we call the displacement $(r - a)$ of this atom u_n, then the forces acting are:

(i) $K(u_n - u_{n-1})$ from the spring on its left, and

(ii) $K(u_{n+1} - u_n)$ from the spring on its right

Equating the total force (difference of i and ii) with the products of mass and acceleration gives:

$$M\ddot{u}_n = K(u_{n+1} - 2u_n + u_{n-1}) \tag{2.10}$$

If we apply periodic boundary conditions (valid as the motion of atoms in the middle of a long chain will be independent of what occurs at the chain ends) then the equations of motion of all atoms are of this form, regardless of the value of n. A solution to this, in which all atoms vibrate with the same amplitude, is:

$$u_n = A\exp[i(kx_n^0 - \omega t)] \tag{2.11}$$

where $x_n^0 = na$ is the undisplaced position of the nth atom. Substitution of Equation (2.11) into Equation (2.10) and simplifying gives the relationship between frequency, ω, and wavevector, k, for a one-dimensional chain of atoms.

$$\omega^2 M = 4K\sin^2\left(\tfrac{1}{2}ka\right) \tag{2.12}$$

Figure 2.8 shows this dispersion relation over a range of k values. The maximum value for a sine term is 1, thus the maximum frequency is $2(K/M)^{1/2}$. This is known as the cut-off frequency for the lattice. Notice that n has cancelled out of the equation so that the equations of motion of all atoms lead to the same algebraic relation between ω and k. This shows that the trial function is a valid solution of Equation (2.10).

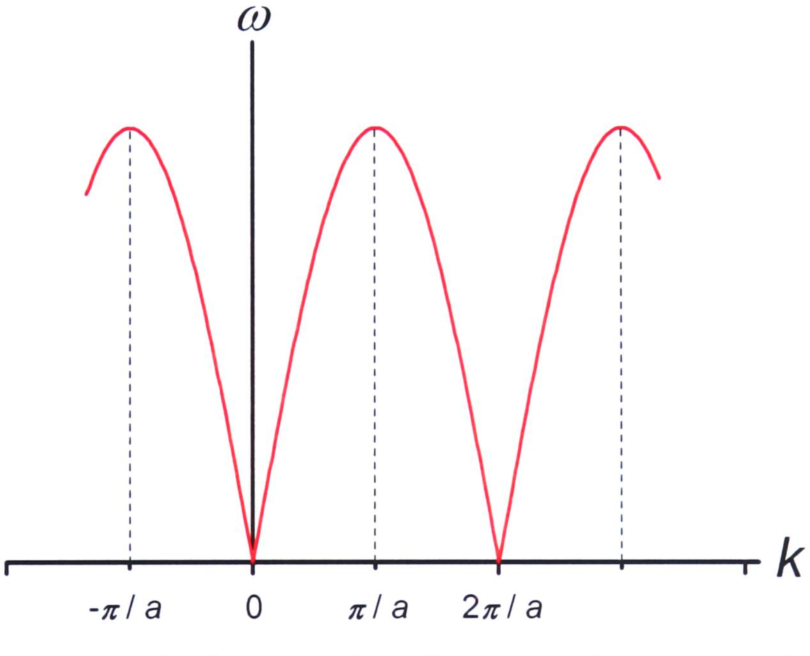

Figure 2.8 - Normal mode frequencies for a chain of identical atoms in the harmonic approximation.

It should be noted that the modes arrived at in this manner refer to a collection of coupled harmonic oscillators all moving together. If one atom were to start vibrating it will not continue with constant amplitude, but transfer energy to its neighbours. Solutions of the type given in Equation (2.11) are called *normal modes* and comprise coherent, coupled oscillations of atoms. In the harmonic approximation these normal modes are not however coupled to each other. Different values of k (as shown in Figure 2.8) correspond to the same values of frequency ω and group velocity ($d\omega/dk$). If periodic boundary conditions are applied to a chain of N atoms, such that $u_n = u_{N+n}$, then there must be an integral number of wavelengths in our chain, i.e. $Na = p\lambda$. Hence:

$$k = \frac{2\pi}{\lambda} = \frac{2\pi p}{Na} \tag{2.13}$$

where p is an integer. There are N possible k values in a range $2\pi/a$ of k; conventionally taken as the range $-\pi/a < k \leq \pi/a$. k values outside this range have no physical significance.

Consider now a chain made up of two atoms, of mass M_1 and M_2, connected by identical springs of spring constant K. This is the simplest model of an ionic crystal, and although the nearest neighbour interaction implicit in this model are a poor representation of the much longer range forces in ionic crystals, the model does reproduce the qualitative features of the lattice vibrations in ionic solids. If we employ the same solution as before, two equations are required, one for each atom type:

$$u_n = A\exp\left[i(kx_n^0 - \omega t)\right] \qquad \text{mass} = M_1 \tag{2.14}$$

$$u_n = \alpha A\exp\left[i(kx_n^0 - \omega t)\right] \qquad \text{mass} = M_2 \tag{2.15}$$

where the term α is a complex number giving the relative amplitude and phase. Substitution back into Equation (2.10) gives two algebraic equations for frequency as a function of wavevector.

$$\omega^2 M_1 = 2K\left[\alpha\cos\left(\tfrac{1}{2}ka\right) - 1\right] \tag{2.16}$$

$$\omega^2 M_2 = 2K\left[\cos\left(\tfrac{1}{2}ka\right) - \alpha\right] \tag{2.17}$$

When ω is plotted as a function of k there are two solutions to the equation and two branches on the graph (Figure 2.9). Once again, the physically significant range of wavevectors is $-\pi/a < k \leq \pi/a$ and adding any multiple of $2\pi/a$ to k does not alter the atomic displacements

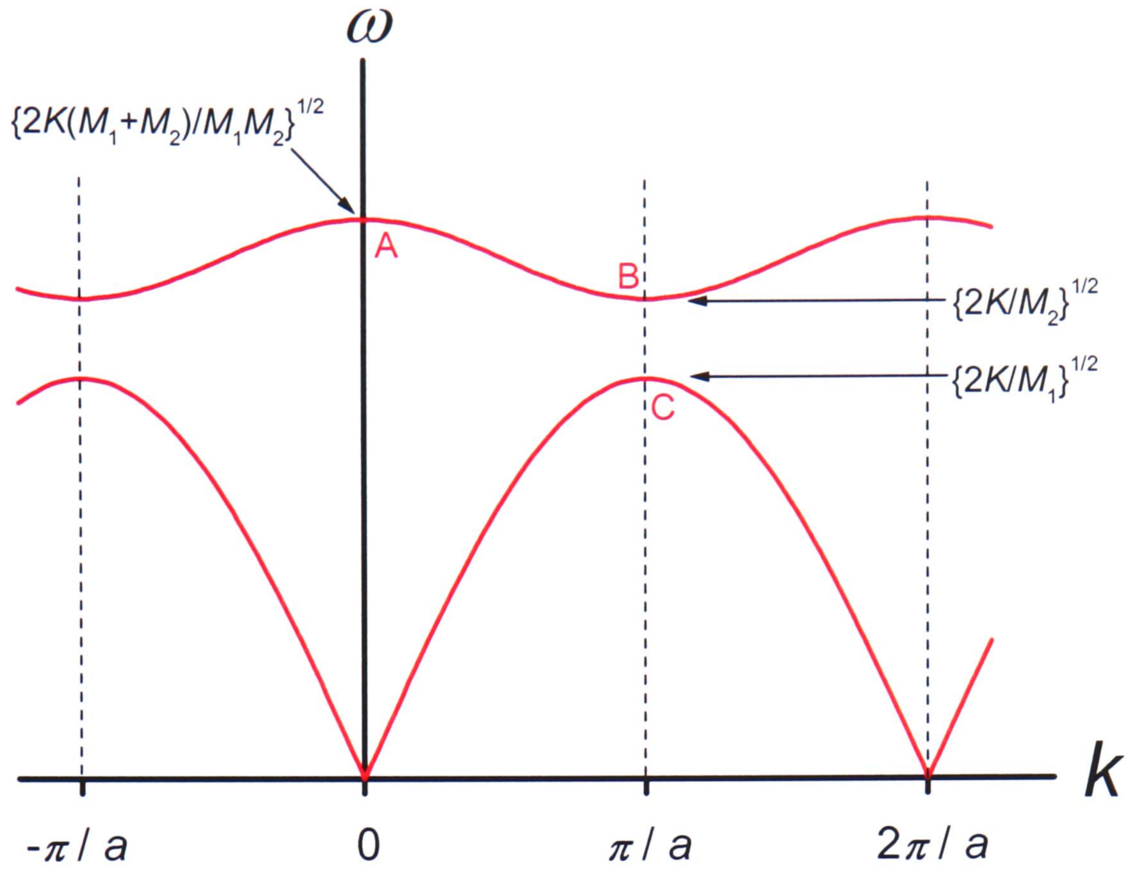

Figure 2.9 - Normal mode frequencies of a chain of two types of atom. At A the two types are oscillating in anti-phase with their centres of mass at rest; at B the lighter mass (M_2) is oscillating and M_1 is at rest; at C, M_1 is oscillating and M_2 is at rest.

The two branches are both periodic in k with period $2\pi/a$. Only one of the branches has the limiting form of sound waves at long wavelength ($\omega/k \rightarrow$constant as $k \rightarrow 0$). This branch, the lower branch on Figure 2.9, is consequently known as the *acoustic branch*. The other branch is called the *optical branch* because as $k \rightarrow 0$ the vibrations of the two types of atoms are in anti-phase and the resulting charge oscillations in an ionic crystal give strong coupling to electromagnetic waves at the frequency of point A in Figure 2.9.

The vibration modes for a one-dimensional crystal concern motion along the crystal axis only. These are longitudinal modes as motion and propagation are in the same direction. Consider now a wave propagating in a three-dimensional crystal. There can be a *longitudinal* mode (vibrations along the z direction), as in the one-dimensional case, and in addition there can be two *transverse* modes (corresponding to atomic motion in the x and y directions). Taking into account the extra dimensionality, many of the qualitative features of the one-dimensional model are retained in three-dimensional ionic crystals. In crystals containing only one crystallographically unique atom, there are three branches in the dispersion relation; all of which are acoustic in form. For a solid with two different atoms in the primitive unit cell there are three acoustic branches and three optical branches. The general result for a unit cell containing N atoms is three acoustic branches and $3(N\text{-}1)$ optical branches.

2.3.2 Phonons

The theory in the previous section deals with the mechanics of lattice vibrations in an entirely classical way: the normal modes are independent and harmonic. The transition to quantum theory is easily made by supposing that a lattice vibration of frequency ω will behave like a simple harmonic oscillator and will thus be restricted in the energy values it can possess.

$$\varepsilon_n = (n + \tfrac{1}{2})\hbar\omega \qquad \textbf{(2.18)}$$

Equation (2.18) represents a series of equally spaced energy levels. Thus, it may be considered that the ε_n state is constructed by adding n 'excitation quanta' (of energy $\hbar\omega$) to the ground state. In the context of electromagnetic radiation these 'excitation quanta' are termed *photons*. In an analogous way, quanta of excitation in lattice vibrations, of energy $\hbar\omega$, are termed *phonons*.[81] Normal modes are plane waves extending throughout the crystal, and correspondingly phonons are not localised particles; the uncertainty principle demanding that, as the momentum ($\hbar\mathbf{k}$) is exact, the position cannot be known. However if we consider waves with a spread of $\mathbf{k}$ values it is possible to construct a relatively localised wave-packet. Such a wave-packet represents a fairly localised phonon moving with group velocity $d\omega/d\mathbf{k}$. Phonons can therefore be treated as localised particles within the limits of the uncertainty principle. Note also that phonons, like photons, are a type of boson and will conform to Bose-Einstein statistics.

2.3.3 Density of states

In the discussions concerning one-dimensional crystals, it was seen that the periodic boundary condition meant that the allowed wavevectors were given by:

$$k = \frac{2\pi p}{Na} = \frac{2\pi p}{L} \qquad \textbf{(2.19)}$$

where p is an integer and $L=Na$ is the length of the crystal. The allowed k values are therefore uniformly spaced with a density $\rho_R(k)$ such that the number of values in the range $k \rightarrow k+\mathrm{d}k$ is given by:

$$\rho_R(k)\mathrm{d}k = \frac{L}{2\pi}\mathrm{d}k \qquad \textbf{(2.20)}$$

To calculate an energy by summing over normal modes a different expression is required. The density of states *per unit frequency range*, $g(\omega)$, is defined such that the number of modes with frequency $\omega \rightarrow \omega+\mathrm{d}\omega$ *is* $g(\omega)\mathrm{d}\omega$. An area of the dispersion relation graph can be defined as the dn modes that have frequency $\omega+\mathrm{d}\omega$ and wavevector $k+\mathrm{d}k$. Thus:

$$\mathrm{d}n = \rho_R(k)\mathrm{d}k = g(\omega)\mathrm{d}\omega \qquad \textbf{(2.21)}$$

Rearrangement of this equation for $g(\omega)$ and substituting in Equation (2.12) for a chain of identical atoms yields the result:

$$g(\omega) = \frac{2N}{\pi}\left(\frac{4K}{M} - \omega^2\right)^{-\frac{1}{2}} \qquad \textbf{(2.22)}$$

The density of states diagram is shown in Figure 2.10. Notice that it tends to infinity as the cut-off frequency $2(K/M)^{-\frac{1}{2}}$ is approached from below, because the group velocity ($\mathrm{d}\omega/\mathrm{d}k$) tends to zero there. It should also be noted that this is the result taking account of the dispersion of sound at wavelengths comparable to the atomic spacing; otherwise the density of states would have a constant value over the frequency range.

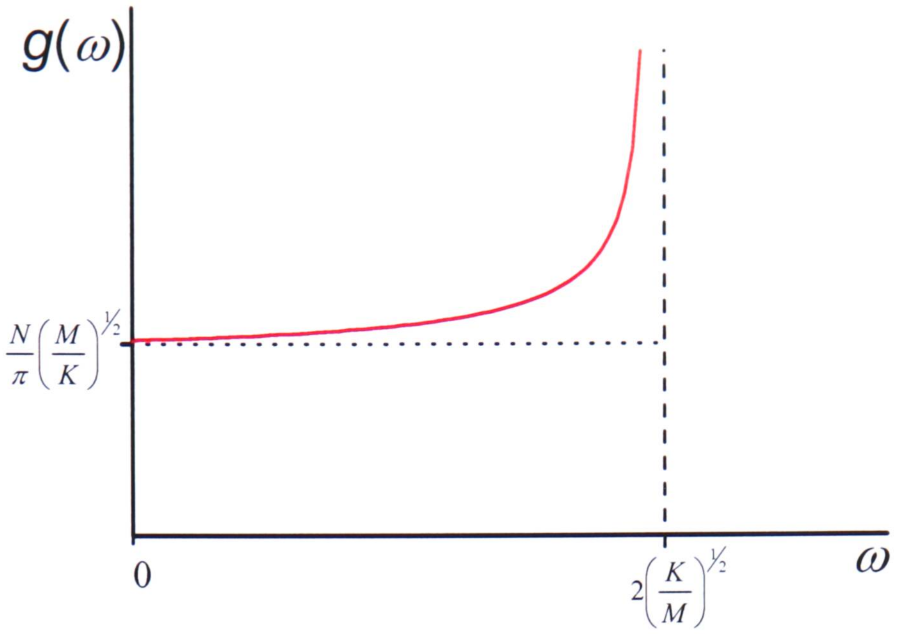

Figure 2.10 - Density of states for a chain of identical atoms, in the harmonic approximation.

In three dimensions the explanation is similar. Consider a cubic lattice of side L and volume $V=L^3$ with periodic boundary conditions. Equation (2.19) can be applied to the allowed **k**-values for the three dimensions independently, such that:

$$k_x = \frac{2\pi p}{L} \qquad k_y = \frac{2\pi q}{L} \qquad k_z = \frac{2\pi r}{L} \tag{2.23}$$

where p, q and r are integers. Thus the allowed **k**-values lie on a simple cubic lattice in **k**-space (reciprocal space) of side $2\pi/L$. The density of allowed running wave **k** values in a spherical shell ($\mathrm{d}^3\mathbf{k}$) of **k**-space is:

$$\rho_{\mathrm{R}}(\mathbf{k})\mathrm{d}^3\mathbf{k} = \frac{V}{8\pi^3}\mathrm{d}^3\mathbf{k} = g(k)\mathrm{d}k \tag{2.24}$$

where $g(k)$ is a new density of states function, defined as the number of states per unit *magnitude* of k (in the one dimensional case $g(k)$ and $\rho(k)$ are identical because the volume element in k-space is just $\mathrm{d}k$). Consequently, if ω is a function only of the magnitude of **k** and $\mathrm{d}\omega$ is the frequency range corresponding to the wavevector range $\mathrm{d}k$, then we obtain the result of Equation (2.25), analogous to Equation (2.22).

$$g(\omega) = g(k)\frac{dk}{d\omega} = \frac{Vk^2}{2\pi^2}\frac{dk}{d\omega} \tag{2.25}$$

The density of states must be evaluated, using Equation (2.25), for each branch of the dispersion relation and then the total density of states obtained by summing over all the branches. This theory is, of course, an oversimplification of a real ionic crystal and measured density of states will differ appreciably from those calculated from this method. The differences arise through three main effects:

(i) Dispersion of sound lowers the cut-off frequency and causes a rise in the density of states just below it (as in the one-dimensional example).

(ii) The variation of cut-off wavevector with crystallographic orientation blurs the sharp cut-off in the density of states so that the actual maximum frequency is raised somewhat.

(iii) The theory here takes no account of atomic structure, only lattice structure. It is therefore of no surprise that the measured density of states will generally present more features than would be calculated. An example is shown in Figure 2.11.

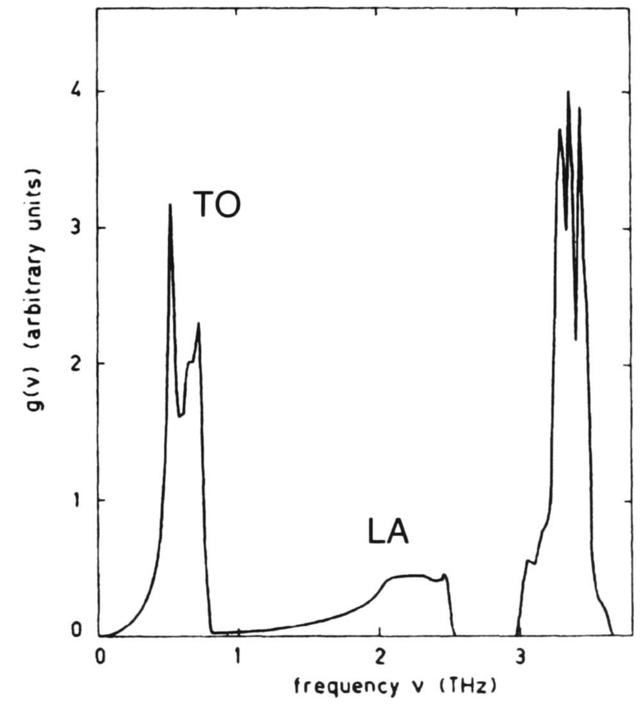

Figure 2.11 - Density of states for the β polymorph of silver iodide (discussed in more detail in a later section). The shape of three distinct branches is shown. Reproduced from work by Bühler *et al.*[83]

2.3.4 Anharmonic effects

Up until this point, atomic thermal motion has been treated as harmonic but that is only an approximation to the base of the atomic potential. A real crystal resists compression to below its equilibrium volume more than it resists expansion: a consequence of the shape of the potential shown in Figure 2.7. This is a departure from Hooke's law, which defines the action of simple harmonic motion, and is one of a number of properties of real crystals not predicted in the harmonic approximation. Such properties are termed *anharmonic* effects.

Consider, once again, Equation (2.8): the Taylor expansion describing atomic motion about its equilibrium position. In the harmonic approximation this was curtailed at the second-order term. The inclusion of third and higher order terms may be used to describe the anharmonic modulation of this motion. One of the major consequences of anharmonicity is coupling between modes. In terms of phonons, this can be thought of as a collision and accompanying energy transfer. Collisions will effectively limit the thermal conductivity associated with the flow of phonons. In the harmonic approximation the phonons do not interact and, in the absence of boundaries, lattice defects and impurities (which also scatter phonons), the thermal conductivity is infinite.

Thermal expansion of solid matter is something familiar from everyday experience, e.g. wooden floorboards expand and contract depending on the room temperature. However, in the harmonic approximation, no mater how much energy is put into lattice vibrations, the equilibrium position is constant owing to the symmetrical potential surface. In order to explain thermal expansion, anharmonic effects must be considered. The volume coefficient of thermal expansion β is defined:

$$\beta = \frac{1}{V}\left(\frac{\partial V}{\partial T}\right)_P \tag{2.26}$$

where V is the volume. The linear coefficient of thermal expansion is then simply $\beta/3$. In the harmonic approximation the frequencies of lattice modes are independent of volume, but this dependence is introduced by the inclusion of anharmonic terms to describe the potential.

The degree of anharmonicity can be evaluated from this dependence in the form of the *Gruneisen parameter*, γ:

$$\gamma = -\frac{d(\ln\omega)}{d(\ln V)} \tag{2.27}$$

The calculation of γ assumes that all mode frequencies have the same volume dependence. That this is not the case is clear from the existence of *soft modes* in some crystalline solids. A soft mode is one for which anharmonicity causes the frequency to vanish at a certain finite temperature. When this happens the atomic displacement associated with the mode becomes time-independent and a permanent displacement of the atom occurs. Typically this will involve a zero-wavevector (infinite wavelength) transverse optic mode and in this case the unit cell is subject to the same change, providing the mechanism for a phase transition from one crystal structure to another, at this temperature. Such a transformation is referred to as a *displacive phase transition*. In such cases the higher temperature phase will have greater symmetry. In ionic solids the opposite displacement of positive and negative ions associated with a zero-wavevector transverse optic mode results in the lower temperature phase possessing a permanent electric dipole. A material possessing these characteristics is *ferroelectric* – the electric analogue of ferromagnetic materials.

2.3.5 The Debye-Waller factor

The previous discussion on crystallography, in Section 2.2, assumed atoms were stationary on the crystal lattice. Now we see that that is not the case and that in reality atoms oscillate about a mean position. However, though random thermal motion removes the periodicity of the structure at any given instant, the previous discussions are not invalidated. Experimental observations show that (neglecting thermal expansion) reflection positions are unchanged by temperature; only the intensity is modified. A rise in temperature is generally accompanied by a reduction in diffraction intensity. For an explanation, consider a modification to Equation (2.2) to include a time dependent atomic displacement parameter $\mathbf{u}$ in the vector describing atomic position.

$$\mathbf{r}(t) = \mathbf{r} + \mathbf{u}(t) \tag{2.28}$$

The structure factor of the unit cell over j atoms is now defined:

$$F(\boldsymbol{\kappa}) = \sum_j f_j \exp(-i\boldsymbol{\kappa}\cdot\mathbf{r}_j)\langle\exp(-i\boldsymbol{\kappa}\cdot\mathbf{u})\rangle \tag{2.29}$$

where <...> represents the thermal average. Evaluation of this function can be used to express the observed diffraction intensity in terms of the theoretical intensity associated with a stationary atom I_0.

$$I = I_0 \exp\left(-\tfrac{1}{3}\langle u^2\rangle\kappa^2\right) \tag{2.30}$$

where the exponential term is known as the Debye-Waller factor. Here $\langle u^2\rangle$ is the mean square displacement of an atom. For anisotropic motion $\langle u^2\rangle$ is commonly expressed as the anisotropic displacement tensor with components U^{ij}, as Equation (2.31).

$$\langle u^2\rangle = U^{11}l_1^2 + U^{22}l_2^2 + U^{33}l_3^2 + 2U^{12}l_1l_2 + 2U^{13}l_1l_3 + 2U^{23}l_2l_3 \tag{2.31}$$

where l_i denotes the cosine of the angle between the polarisation of the vibration and the reciprocal axis i. The components, U^{ij}, are commonly referred to as the atomic displacement parameters or ADPs. The intensity lost from coherent scattering is expressed as diffuse scattering.

It should be noted that it can be difficult to differentiate between thermal motion of atoms and small degrees of static disorder in the equilibrium position of the atom. In the latter case the system can be more accurately modelled by the use of a larger unit cell to describe the different atom positions, or by two (or more) atoms around the same site, set with fractional occupancy. However this requires forward knowledge of the static disorder and its nature. In practice it can be simpler to allow the effect to be integrated with the thermal motion and accounted for in this manner. In crystal structure refinement, the atomic displacement parameters can therefore be a measure of both thermal and static disorder.

3 Structural techniques

3.1 Diffraction techniques

The experimental techniques used throughout this thesis are introduced in this chapter. Crystallography, in its various forms, is discussed in the first section and is the primary measurement technique employed throughout Chapters 4 to 8. The second section deals with some of the more specialised techniques used in the study of nanoparticles. These techniques were employed for the work covered in Chapter 9.

The probing of chemical reactions is the method by which we can find out more about the processes occurring. By careful examination of the reactants and products and their respective energies (e.g. vibrations, electronic excitations and translation energy), educated guesses can be made concerning the intervening time. Spectroscopy, in its many and varied forms, is a useful tool for making these measurements. However, for processes occurring in the solid state there are additional complications. Spectroscopic techniques work either in transmission or in reflection, but absorption for most forms of spectroscopic radiation is so strong for solids that transmission does not occur, and reflective measurements may only probe surface phenomenon. Solid state processes, such as ion-diffusion, sintering of ceramic particles and drying reactions, are bulk phenomena and in order to study them a bulk measurement technique must be employed. The most incisive technique for probing solid state structure is diffraction. Diffraction methods employ penetrating radiation, such as high-energy X-rays or neutrons. The data collected is a sum over the entire sample (in the radiation beam) and can be employed to investigate single crystals or micro-crystalline powders.

In order to more fully elucidate a reaction, quenching and analysis of intermediate species can be used to see several snapshots of the reaction over time. The closer together the snapshots are, the less interpolation is required between snapshots and a clearer picture of the reaction is obtained. However, there is always some doubt as to whether the species studied in the quenched reaction mixture are truly a fair representation of the reaction as a whole. There is always a possibility that the reaction may continue, or that quenching itself may cause another reaction to come to the fore. Furthermore, dynamic effects that only occur under the conditions of the reaction, such as atomic vibrations, cannot be observed by this method. It is far better then to examine the reaction *in-situ*. Observation of a reaction in this manner is far less likely to affect the course of the reaction and the observer can achieve superior time-resolution, or even continuous monitoring in some cases.

In-situ diffraction with X-rays or neutrons is therefore the desired technique for the examination of solid state reactions. With sufficiently good data, it can provide information on phase, structure, atomic thermal vibrations, particle size and the degree of crystallinity of a sample.

3.1.1 X-ray diffraction

By far the most commonly used form of diffraction is X-ray diffraction.[79, 80] Not only is the technique sufficiently powerful for structure solution of many single crystals, but also the X-ray source is comparatively small and instruments are relatively affordable. The standard source of X-rays is an 'X-ray tube'. This is a construction of glass and metal that produces electrons by passing an electrical current through a wire filament and accelerates them to a high velocity by an electrical potential of the order of 50,000 volts across a few millimetres. A water-cooled metal block absorbs these high-energy electrons. Most of the kinetic energy is converted to heat and wasted, but a small proportion generates X-rays through interaction with the metal nuclei. If an electron in a core atomic orbital is ionised, an electron from a higher energy orbital can take its place, producing a photon with wavelength defined by the energy difference ($\lambda = hc/\Delta E$). Several such transitions are possible and the output spectrum has several sharp lines. The most intense line may be selected by use of a monochromator crystal; only the selected wavelength is diffracted at the correct angle to pass through the slit to reach the sample. The most commonly used target materials are copper and molybdenum, whose most intense lines (K_α) have wavelengths of 1.54184Å and 0.71073Å respectively.

There are two general types of diffraction instrument. The first type is primarily for single-crystals and collects the diffraction data on either a 2-dimensional detector, such as an image plate, which does not move during detection or a single-point detector that travels round the sample in 3 dimensions. In either case high-quality data can be obtained. The second type is used primarily for powders and thin films. The sample is placed on a sample plate and mounted at the centre of the instrument (Figure 3.1).

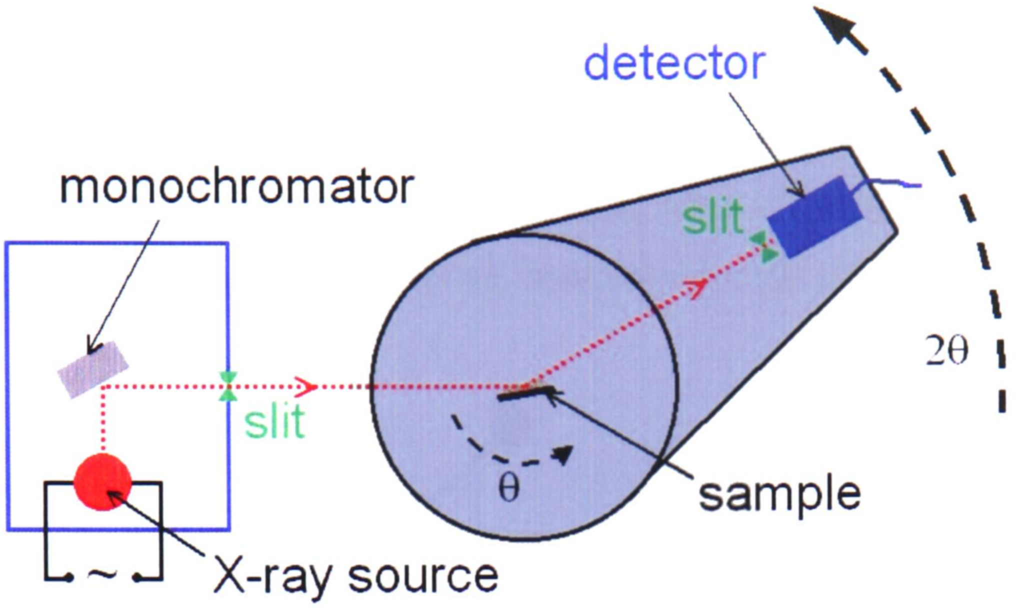

Figure 3.1 - Schematic of an X-ray powder diffractometer, with *θ/2θ* geometry and X-ray tube source.

The position of the source is kept constant, whilst the detector rotates around the sample position. The angle between the incident beam and the detector is 2θ. The sample also rotates, with half the rate of the detector (i.e. angle is θ). A pattern of diffraction intensity versus 2θ is recorded, which can be related to the d-spacing via the Bragg equation. It is this latter type of diffractometer that is of more interest here as, in the main, the samples being studied are powders and this geometry generally provides superior angle resolution.

3.1.2 Synchrotron radiation

Powder diffraction measurements using a Cu K_α X-ray are for practical purposes insufficiently intense to fully elucidate the details of more complex crystal structure; or to extract more accurate detail, such as thermal parameters. Therefore, in order to improve the resolution of the data and the speed of the measurement high-intensity synchrotron radiation may be used.[84, 85] Measurements of this type were performed at the Synchrotron Radiation Source (SRS), at the Daresbury Laboratory in the UK.

The general operation of a synchrotron is shown in Figure 3.2. A packet of electrons is created, accelerated to relativistic speeds in the booster ring and then injected into the storage ring. The storage ring has straight sections joined by bends. Large dipole (bending) and quadrupole (focussing) electromagnets are used to change the course of the electrons at corners. Accelerating electrons round these corners results in the emission of radiation cones with narrow wavelength distribution anywhere between infrared and gamma rays depending on the magnetic field, see Figure 3.3. At the SRS there are a series of such magnets around a ring of approximately 96 metres circular path. At each corner of the ring the emitted photons pass out of the storage ring, down a beam-line, to an experimental station.

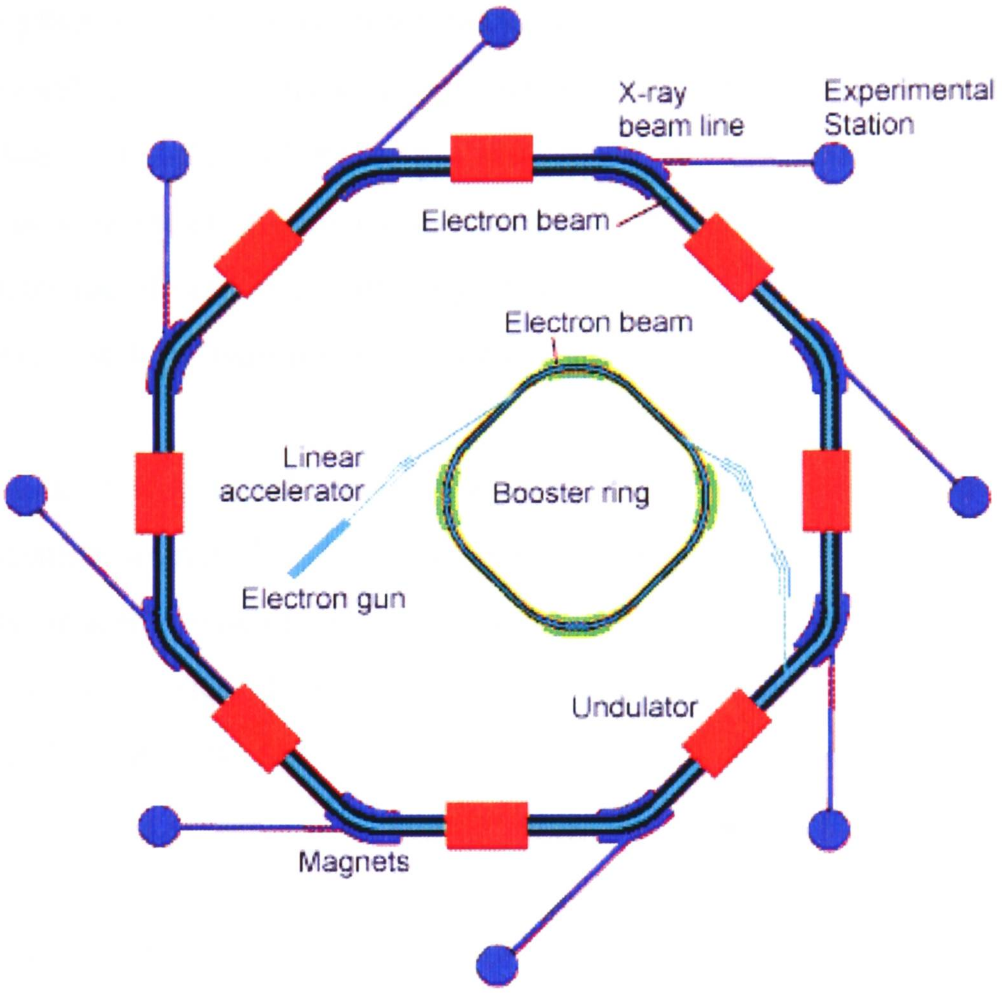

Figure 3.2 - A generic storage ring synchrotron X-ray source, such as exists at the Synchrotron Radiation Source (SRS), Daresbury.

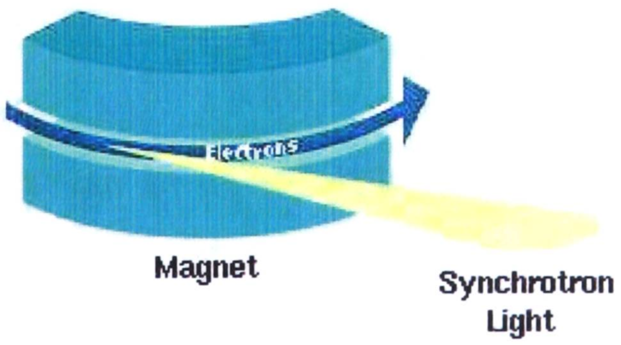

Figure 3.3 - Emission of synchrotron radiation as the electron packet is accelerated by the magnetic field.

The nature of the storage ring is such that the electron beam will be ribbon-like, that is that the vertical distribution is greater than the horizontal. Typically, however, beam-lines use monochromators[84] with horizontal slits and obtaining a useful flux through the monochromator exit slits requires that the photon beam have a small vertical size and angular divergence so that most of the flux from the source can pass through the narrowed entrance slits. Crystallography experiments, especially those with small crystals and large unit cells, also place a premium on brightness, since it is necessary to match the incident beam to the crystal size while maintaining sufficient angular resolution to resolve closely spaced diffraction spots. Optical methods cannot focus the beam to increase the brightness (flux per unit area) without increasing divergence of the beam. Likewise, apertures can reduce beam size and divergence, but only at the cost of flux. The solution is to place insertion devices,[84] such as *undulators* or *wigglers*, on the straight sections, see Figure 3.2.

Undulators provide a way to take maximum advantage of the intrinsic brightness of the synchrotron-radiation source. The magnetic structure of a common (planar) undulator is an array of closely spaced vertically oriented dipole magnets of alternating polarity. As the electron beam passes longitudinally through the array, its trajectory oscillates in the horizontal plane. Owing to the relatively weak field, the radiation cones emitted at each bend in the trajectory overlap, giving rise to a constructive interference effect that results in one or a few spectrally narrow peaks (a fundamental and harmonics) in a beam that is highly collimated in both the horizontal and vertical directions; that is, the beam has a high spectral brightness. Tuning of the wavelengths of the harmonics is by means of mechanically adjusting the vertical spacing (gap) between the pole tips. Wigglers are similar to undulators but generally have higher fields and fewer dipoles, with the result that they produce a continuous spectrum with a higher flux and a spectrum that extends to shorter wavelengths than bend magnets.

Consequently an electron current can be created with packets of known size, shape and energy, and can be used to create an X-ray beam of known size, shape and energy. Monochromators and slits can then be used to select parts of the white X-ray beam for use in diffraction experiments, amongst others.

3.1.3 Neutron diffraction

As an alternative to X-rays, high-flux neutrons can be used to perform diffraction measurements. Neutron diffraction is fundamentally different from X-ray diffraction, in that the neutrons are diffracted from the atomic nuclei rather than by electron density, as is the case for X-rays. This means that neutrons give information about atomic positions directly, rather than indirectly locating the atoms at the centres of electrons. It also means that scattering cross-section is not proportional to atomic number: many lighter atoms may be detected which are more difficult to observe using X-rays, and different isotopes may be distinguished.

The energy and momentum of neutrons can be matched to typical values found in matter, with wavelengths between ~0.02Å and 20Å. The main advantages they have over X-rays are that they have a magnetic moment and can therefore probe magnetic structure, and neutrons have a larger penetration depth than X-rays (owing to the weak interactions involved) and can be used to probe further into the interior of a bulk sample.

Production of neutrons, however, is not a simple process. A very high flux is required to take measurements and the only ways of creating such a flux are within a nuclear reactor or using a large particle accelerator. The most efficient way of producing neutrons from an accelerator is spallation. The ISIS Facility (Rutherford Appleton Laboratory, Oxfordshire, UK) is one such spallation source.[86] A synchrotron is used to accelerate protons to high speed: a current of ~200μA, 800MeV is produced. The protons are sent down a track to a heavy metal target where they interact, via radioactive decay processes, to create neutrons (~2×10^{16} neutrons per second). Lead, tantalum, titanium and uranium are all used as they have desirable properties as a spallation target:

- high atomic weight for improved neutron yield
- high density for increased brightness
- high melting point, high thermal conductivity, chemically inert and resistant to radiation damage, all of which prolongs the life of the target material
- low absorption cross-section for thermal neutrons
- high scattering cross-section

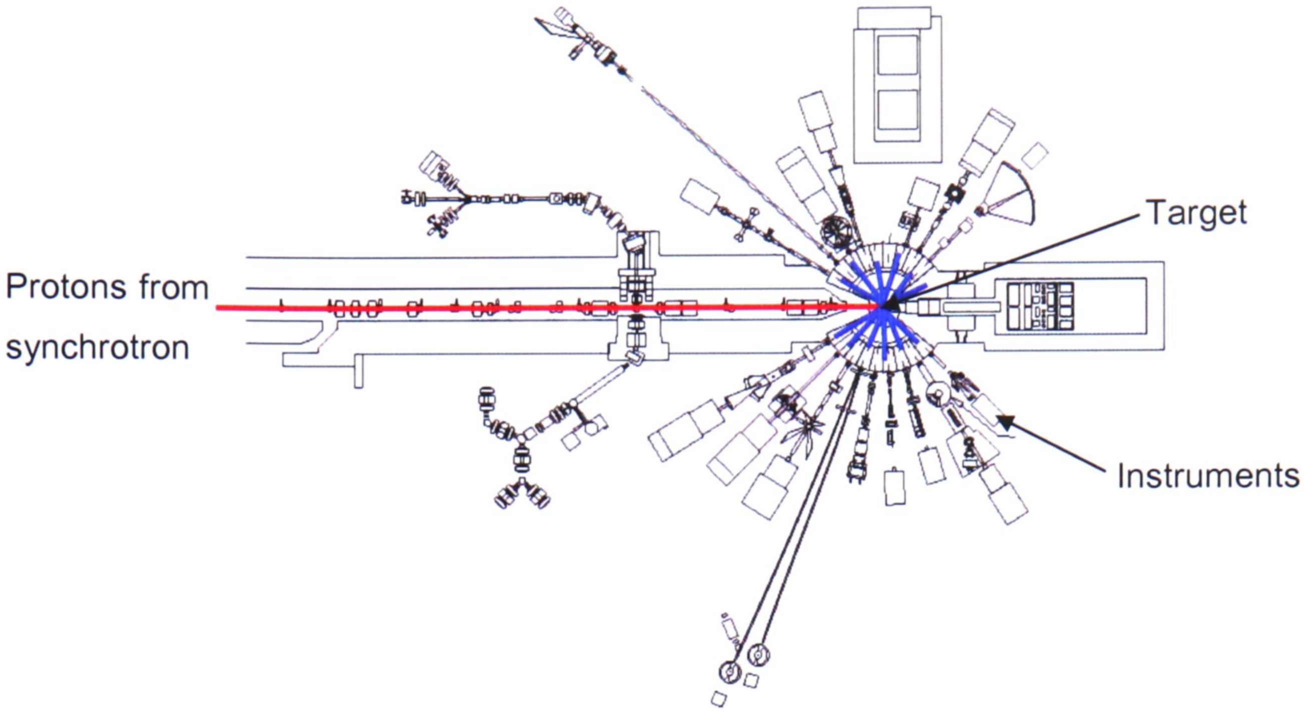

Figure 3.4 - Plan of the instrument hall at the ISIS Facility. Instruments are situated radially about the tantalum target. Figure reproduced from the 2001 annual report of the ISIS Facility. [86]

Spallation results in a broad range of neutron energies, peaking at around 1 MeV. Much of this range is too great for diffraction and spectroscopy instruments. Moderators are employed to scatter fast neutrons (~1 MeV) from the target, slowing them down to energies required for the neutron instruments (typically between 1 eV and 1 meV).[86] The extra energy is transferred to the atoms of the moderator. Moderators and reflectors are used to send neutrons of the correct energy to beam-lines for each neutron instrument.

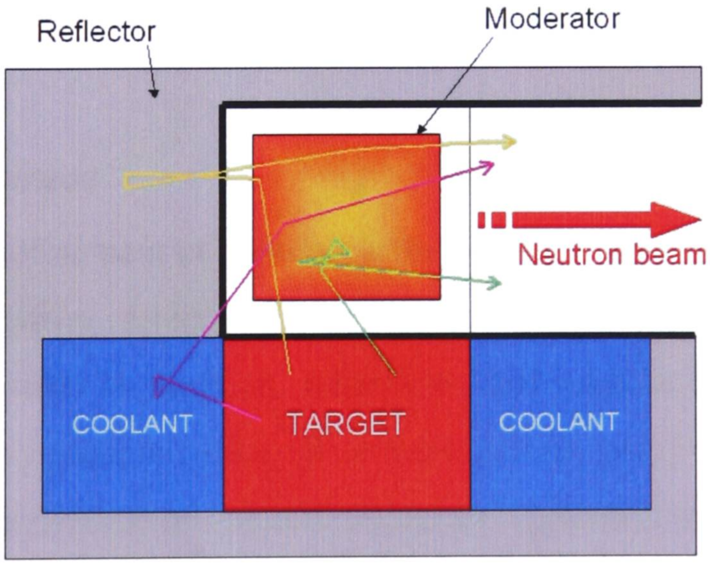

Figure 3.5 - Schematic of the target assembly of a spallation source, showing how reflectors and moderator are used to create the neutron beam.

The resultant neutron beam is pulsed in nature (largely owing to the fact that the proton synchrotron beam is pulsed). Various devices, including moderators (modifying neutron energies) and choppers (which 'chop' out unwanted neutron energies) are employed in the beam-line for each instrument, ensuring only neutrons of appropriate energy are allowed to pass.

3.1.4 Structure refinement of powders

For diffraction from micro-crystalline powder, as opposed to single crystals, there is insufficient information in the data for complete structure solution using current techniques. Instead, it is advantageous to refine the structure from a known starting point, that is usually the space group and approximate atom positions.[79, 80] These are often available from a database and even when the exact structural composition of the sample is unknown, it is usually possible to identify it by a search of the database using the powder diffraction pattern as a fingerprint of the sample. Many solid materials of interest to a materials chemist have been studied at some time or another and crystal structures are known for these. In cases where the material has not been studied previously, the correct structure can frequently be deduced by comparison with similar materials.

Having obtained the correct general structure, it is then possible to accurately determine such parameters as unit cell size, atomic positions and atomic displacement parameters (ADPs) as well as other parameters of the sample, such as the average particle size, and information on impurity phases.

3.1.4.1 Rietveld refinement

The main problem with refinement of powder diffraction data is reflections with the same *d*-spacing but different relative directions (e.g. 002 and $00\bar{2}$) coincide. Furthermore, as reflections have finite width in practice, reflections with similar *d*-spacing will overlap, causing broadening or asymmetric peaks. It is therefore necessary to resolve such profiles into contributions from individual sets of reflections and apportion the integrated intensity of the complex line shape into components from those reflections. Additionally, incoherent scattering gives rise to background noise, which can be fitted to an empirical function.

Improved instrumentation has allowed higher resolution, but cannot always resolve peaks completely. Rietveld refinement was developed primarily to deal with this problem.[87, 88]

H. M. Rietveld produced the first algorithm to assign the integrated intensity of peaks in a powder profile to a set of contributing reflections in 1966.[89] This development was facilitated by the growing capabilities of computers at that time. The original program was designed to analyse powder neutron diffraction data by exploiting the apparently Gaussian peak shape of the reflections in this type of data. Several factors affect the peak shape, including instrument resolution and the nature of the crystallites. However, it was found that, for a reactor source, the peak shape could be approximated by a Gaussian function. Thus the contribution to the intensity at a given angle, θ_n, due to a reflection centred at θ_{hkl} is given by the Gaussian function:

$$I(\theta_n) = \sqrt{\frac{4\ln(2)}{H_{hkl}\pi}} \exp\left(\frac{-4\ln(2)(2\theta_n - 2\theta_{hkl})^2}{H_{hkl}^2} \right) \tag{3.1}$$

where H_{hkl} is the full-width at half-maximum (FWHM) of the Bragg reflection with Miller indices *hkl*. The H_{hkl} values depend on the mosaic spread of both the crystals used in the monochromator and the crystallites in the sample.

The creation of more powerful computers has since allowed the program to be extended to allow the refinement of the peak profile.[88, 90] The angular dependence of H_{hkl} for a Gaussian diffraction peak can be described by the expression:

$$H_{hkl}^2 = U \tan^2 \theta_{hkl} + V \tan \theta_{hkl} + W \tag{3.2}$$

where U, V and W are the half-width parameters, which may be varied in the course of refinement. The refinement process utilises a non-linear least-squares fitting program and though originally designed for powder neutron diffraction data, it has now been expanded to cater for X-ray diffraction data by including a suitable peak profile function.[91] From these humble beginnings the Rietveld method has grown in popularity and complexity; it is now routinely used as a powerful tool in structural refinement. Several texts are available to explain the complexities and further advances of the technique.[87]

The peak profile function given in Equations (3.1) and (3.2) works well for medium to low resolution neutron diffraction data, but higher resolutions or X-ray diffraction experiments produce asymmetric peaks, not well fitted by a simple Gaussian function. A convolution of Gaussian (G) and Lorentzian (L) expressions is necessary. This is given by the pseudo-Voigt function,[92]

$$I(\theta_n) = \eta L + (1 - \eta)G \tag{3.3}$$

where the weighting factor, η, can be refined as a linear function of 2θ, i.e.

$$\eta = NA + NB(2\theta) \tag{3.4}$$

where NA and NB are the refinable variables.

3.1.4.2 The generalised structure analysis system

The generalised structure analysis system (GSAS)[92] is one of a number of computer programs available that use the Rietveld method to refine powder diffraction data. It is amongst the most popular owing to its versatility: it can be used for data collected from X-ray diffractometers and neutron diffractometers and can be used to refine magnetic structure in the case of the latter. More recently a new interface (EXPGUI)[93] has been created for Microsoft Windows, facilitating rapid refinement and ease of use.

Several different peak profile functions are incorporated within GSAS. These are designed for use with data from specific instrument types and are discussed thoroughly in the GSAS manual. Specific profile functions used in the course of this thesis are described in the Appendix (page A2).

3.1.4.3 Quantifying the quality of fit

When refining the data from powder diffraction studies many parameters may be refined simultaneously. These parameters include those that define the background, peak shape, structure, lattice, thermal parameters and absorption. The effectiveness of the resulting fit is quantified by the *R*-factors: R_p the *pattern R*-factor and R_{wp} the *weighted-profile R*-factor (see the GSAS[92] manual for more information on the weighting scheme):

$$R_p = \sum_n \frac{\left| I^n_{obs} - I^n_{calc} \right|}{\sum_n I^n_{obs}} \qquad (3.5)$$

$$R_{wp} = \sqrt{\frac{\sum_n w_n \left(I^n_{obs} - I^n_{calc} \right)^2}{\sum_n w_n \left(I^n_{obs} \right)^2}} \qquad (3.6)$$

where I^n_{obs} and I^n_{calc} are the observed and calculated intensities of all *n* data points. As the calculated model grows more like the observed pattern, the *R*-factors tend to be minimised.

The overall 'goodness of fit' parameter, χ^2, is defined in a similar manner except that it also depends on the number of observables (N_{obs}), variables (N_{var}) and constraints (N_{cons}) applied in the refinement:

$$\chi^2 = \frac{\sum_n w_n \left(I^n_{obs} - I_{calc} n \right)^2}{N_{obs} - N_{\mathrm{var}} + N_{cons}} \qquad (3.7)$$

Refinement continues until the values of χ^2 and the *R*-factors are minimised and the calculated profile is seen to fit the observed reflections as well as possible.

3.2 Studying nanoparticles

In the previous section, it was seen that diffraction is a powerful technique, applicable to macroscopic objects, such as single crystals, down to microscopic objects such as a collection of crystallites in a powder. However, below the order of micrometers diffraction becomes difficult. Particles become so small that they may not contain sufficient unit cells for Bragg's Law to hold. Furthermore as particles become small the surface to bulk ratio increases and the regular crystal structure can become distorted. For these particles in the nanometre length regime (nanoparticles) alternative analysis techniques must be employed.

The synthesis of nanoparticles is one potential application of microwave radiation. Nanoparticles have been found to be very interesting from a chemical perspective as they exhibits a range of intriguing physical and chemical attributes. Due to their small size they have a high surface to bulk atom ratio: surface effects cannot be ignored – as they can be with larger particles – and the material's properties are modified accordingly. One of the problems with this field of chemistry is that because the particles are so tiny, it proves difficult to 'see' them or measure their properties. Nonetheless, a few techniques have proved particularly useful in their study.

3.2.1 Electron microscopy

Both *Scanning Electron Microscopy* (SEM) and, the related technique, *Transmission Electron Microscopy* (TEM) have been used to good effect in the study of nanoscale particles.[94] With modern TEM it is possible to achieve resolutions of as little as 0.5 nm. In comparison, SEM can only achieve resolutions of the order of 10 nm. One may wonder, therefore, at the popularity of SEM in the study of nanoparticles and other samples of similar dimension. Ease of sample preparation compared with TEM may be one reason. However, the most appealing aspect of SEM, and its main advantage over TEM, is its depth of field. Variations in the topography of a three-dimensional sample are clearly rendered and the created image contains a greater amount of information in a readily interpretable form. The depth of field is illustrated in Figure 3.6. A sample is placed, in focus, a distance Q from the lens. The depth of field is thus the limit to which the sample can be displaced from this position and remain in electron optical focus, distances Q' and Q". Thus a surface viewed at Q' or Q" is viewed as a disc of confusion rather than a point. The disc's radius, *r* (equal to $d\alpha$ in the limit of small α), determines the resolution of the instrument.

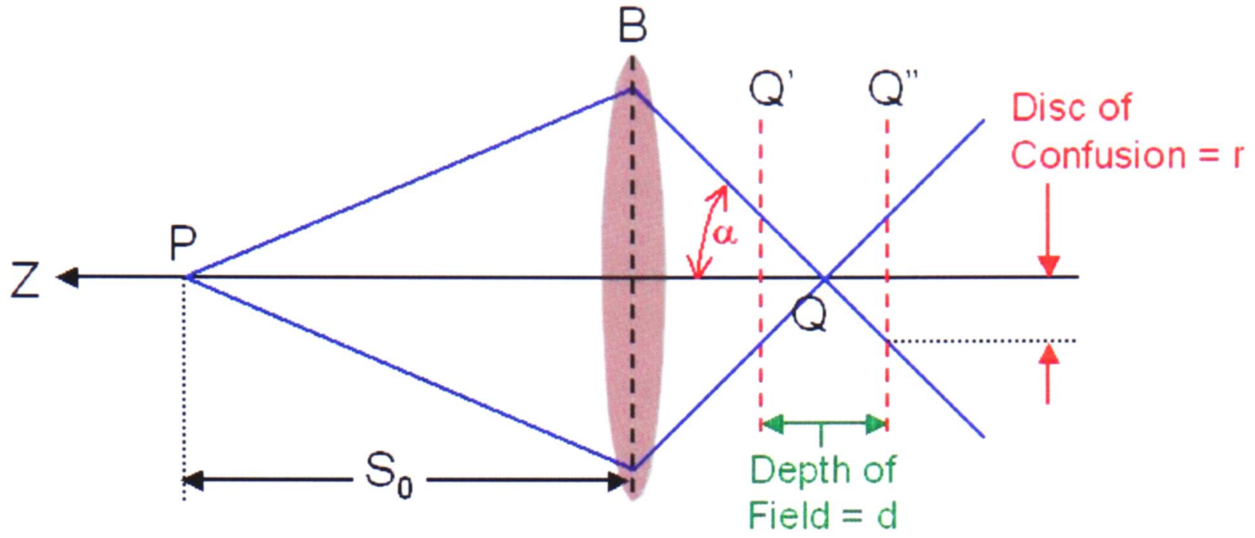

Figure 3.6 - Schematic drawing showing depth of field for a typical electron optics system used in SEM and how it relates to the disc of confusion.

At comparable magnification the depth of field of a SEM instrument is over 100 times greater then that of a light microscope – an enormous advantage in viewing objects with rough surfaces. It should be noted, however, that at high magnification the depth of field must be compromised in order to improve the resolution. This can be done by decreasing the spot size of the incident beam, thus reducing α.

A scanning electron microscope uses an electron gun to fire a beam of electrons (with energies in the range 1-50 eV) at the sample. A large number of interactions are possible between the sample and the primary electrons: the production of secondary electrons, back-scattering of electrons, emission of characteristic and continuum X-rays, Auger electrons and photons of various wavelengths are all possible – the emission volume depending both on the beam energy and on the atomic number of elements in the sample. The primary effect is the elastic and inelastic scattering of electrons. Elastic scattering results from interaction between primary electrons and an atomic nucleus in the sample. The result is a change in direction for the electron, but very little change in energy. The scattering angle for these is relatively large and is detected only as background.

Inelastic scattering results from primary electrons interacting with both the nucleus and the bound electrons in the sample. The primary electron will lose energy in the coulomb field of the atom as it approaches, emitting the energy as white (continuum) X-ray radiation. If the moving electron encounters a bound electron it results in the ejection of a secondary electron. This secondary electron will have an energy less than the incident electron. If it is produced at the surface of the sample (within 10 nm) and has energy greater than the surface barrier energy (2-6 eV) then the electron escapes the surface and is detected by the SEM. It is the detection of these secondary electrons that gives the information required for the micrograph. Sweeping the beam raster-fashion across the surface completes the entire image. Images produced using SEM are clear and give a good feel for the three-dimensional topography of the sample, the size of the nanoparticles and their morphology

3.2.2 Energy dispersive X-ray spectroscopy

Energy Dispersive X-ray (EDX) spectroscopy is a very closely related technique to electron microscopy. So much so that it is generally incorporated within the same instrument, requiring only the use of a different detector.

As in SEM, an electron gun is used to create a beam of electrons that impinges on the sample. The same processes occur as previously described. The process of interest is observed when an inelastic interaction between a nucleus and the primary electron occurs. The moving electron loses energy equivalent to the binding energy of the K, L or M shells of the atom. This results in the emission of a characteristic X-ray that can be detected by EDX, but that is not used in SEM. Alternatively, an Auger electron may be ejected without the emission of a photon and cannot be detected. This emission occurs simultaneously with the scattering of secondary electrons (detected in SEM) but requires a different collector and a longer collection time, as the emission volume is much smaller.

The characteristic X-ray emission can be used to qualitatively identify individual elements in a sample. This is remarkably effective for heavier elements, with computer programmes now capable of quickly matching spectra with a database of emission characteristics. However, as the scattering efficiency is dependent upon the atomic mass, lighter elements (up to fluorine) have weaker responses and consequently are not so readily observed. Recent improvements involving the use of diffracting crystals with large inter-planar spacings have enabled long wavelength X-rays, emitted from lighter elements (lithium to fluorine) to be detected. However, this modification is relatively modern and is generally not standard on older equipment. Furthermore, though the instrument may be calibrated to give quantitative results for heavy elements, this cannot be done with lighter elements owing to the larger errors involved. It can only be used to tell which elements are present, not their proportions.

Nonetheless, the technique is still extremely useful as it can be targeted at small (μm size) areas and used to construct an elemental map of the sample. It is also non-destructive and can be run in conjunction with SEM analysis.

3.2.3 Diffraction from nanoparticles

As discussed previously, X-ray powder diffraction is the most commonly used technique when dealing with any solid sample. The limitations of this technique, as applied to nanoparticles, are that the sample must be crystalline - amorphous samples will not generally give a useful pattern. It requires extremely good quality data in order to provide any information on particle size (Scherer peak broadening can give a good estmate of particle size up to tens of nanometres, see Section 2.2) and can only present data describing an average of the entire sample and cannot focus on individual particles. Moreover, small quantities of nanoparicles are frequently insufficient to obtain a diffraction pattern.

A less widespread technique, though very useful for the examination of nanoscale particles, is electron diffraction. Commonly used for small gas-phase molecules, it can also be applied to surfaces to give some idea of the internal crystal structure of small groups of particles. The technique measures concentrations of the elastically scattered primary electrons from an electron gun (similar to the setup used for SEM). The resulting pattern is a series of concentric rings of varying brightness. This pattern is unique for a given structure, though variations in intensity are possible due to deformations and defects imposed by the small particle sizes. The technique has, for example, been used to identify which polymorph dominates in certain iron oxide nanoparticles[21]. With good instrumentation this approach may be applied to individual nanoparticles. The pattern of spots and their intensities can be examined in the same fashion as single-crystal X-ray diffraction. However, this technique is limited to crystalline nanoparticles.

4 Aspirin

Previous chapters have introduced how microwave radiation may heat various different types of material, that there are possible microwave-specific effects and how these processes may be followed by the use of *in-situ* measurements, particularly diffraction. This chapter, and those following, describe detailed experiments employing these techniques in order to investigate if the proposed mechanisms for microwave heating in solid state materials are applicable. In this manner any non-thermal effects (the so-called 'microwave effect') may be revealed from detailed measurements of the crystal structures involved.

Careful consideration of appropriate material for each experiment was undertaken. In each case a potential interaction for microwave radiation was identified beforehand (such as a flexible part of the molecule or a weakly bound ion) and with each experiment the information learned from the previous was used to inform the next, evolving the experimental design and equipment at each stage. For this investigation the molecule *aspirin* was chosen. It has both a relatively simple crystal structure and a wealth of structural studies relating to its dynamics facilitating the interpretation of the data.

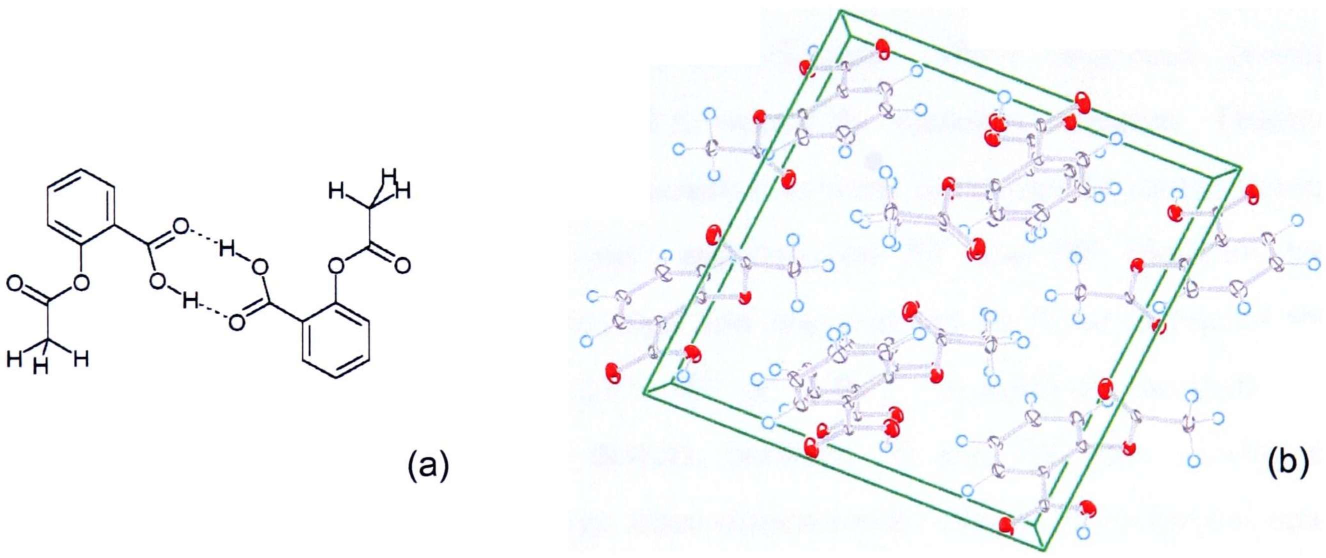

Figure 4.1 – (a) molecular structure of aspirin, showing dimer formation, and (b) crystal structure of aspirin ($P2_1/c$), showing unit cell (viewed down c-axis).

Acetylsalicylic acid (a painkiller, marketed as aspirin) has a well-studied crystal structure, both by X-ray[95] and neutron diffraction[96, 97]. Several interesting temperature dependent features have been noted in the range 20-300K. Among these are enhanced thermal parameters (which contribute to the atomic displacement parameters, or ADPs) for the hydrogen atoms of the terminal methyl group and for the hydrogen atom involved in the carboxylic acid dimeric hydrogen bond (Figure 4.1). For the former, large ADPs are the result of libration of the methyl group;[96, 98, 99] whilst the latter effect is of specific interest here, in that determination of the thermal parameters for this atom show clear evidence that increasing temperature allows the anharmonicity of the potential to be directly observed.

This clear temperature-dependent behaviour makes it an ideal candidate for structural analysis under microwave heating. It was hoped that details of the atomic displacement parameters may demonstrate the existence of 'preferential' redistribution of energy, if such should exist. Therefore, a single-crystal neutron-diffraction study was undertaken on the SXD instrument at the ISIS facility at the Rutherford Appleton laboratory (RAL).[‡]

4.1 Applicator Design

Instrument station SXD is situated on beam line S3, with the sample positioned 8 m from the moderator (ambient water, poisoned with Gadolinium at a depth of 2 cm). The maximum beam diameter of SXD is 15 mm, though this may be reduced with B_4C apertures. A resolution of approximately 1% can routinely be achieved. Three large-area, position-sensitive ZnS-scintillation detectors were used to record the scattered radiation. Detectors one and two may be rotated about the sample position in order to change 2θ for the detector centre between 90° and 130° (detector one) and between 50° and 90° (detector two). Detector three is located opposite detectors one and two and can be fixed in one of three positions (2θ for the detector centre at -55°, -90° or -125°). In addition the distance to sample can be varied for the first two detects, between 70 and 500 mm. Using this arrangement it is possible to access a large three-dimensional volume of reciprocal space. This makes SXD especially powerful in applications involving surveys of reciprocal space, such as phase transitions, incommensurate structures (i.e. not fully crystalline) and subtle changes in thermal parameters.[96, 101] There are also advantages in applications where sample orientation may be restricted.

[‡] This experiment has previously been described, albeit in a preliminary fashion, in a thesis by Douglas Youngson.[100] Greater detail is provided here, particularly as regards interpretation.

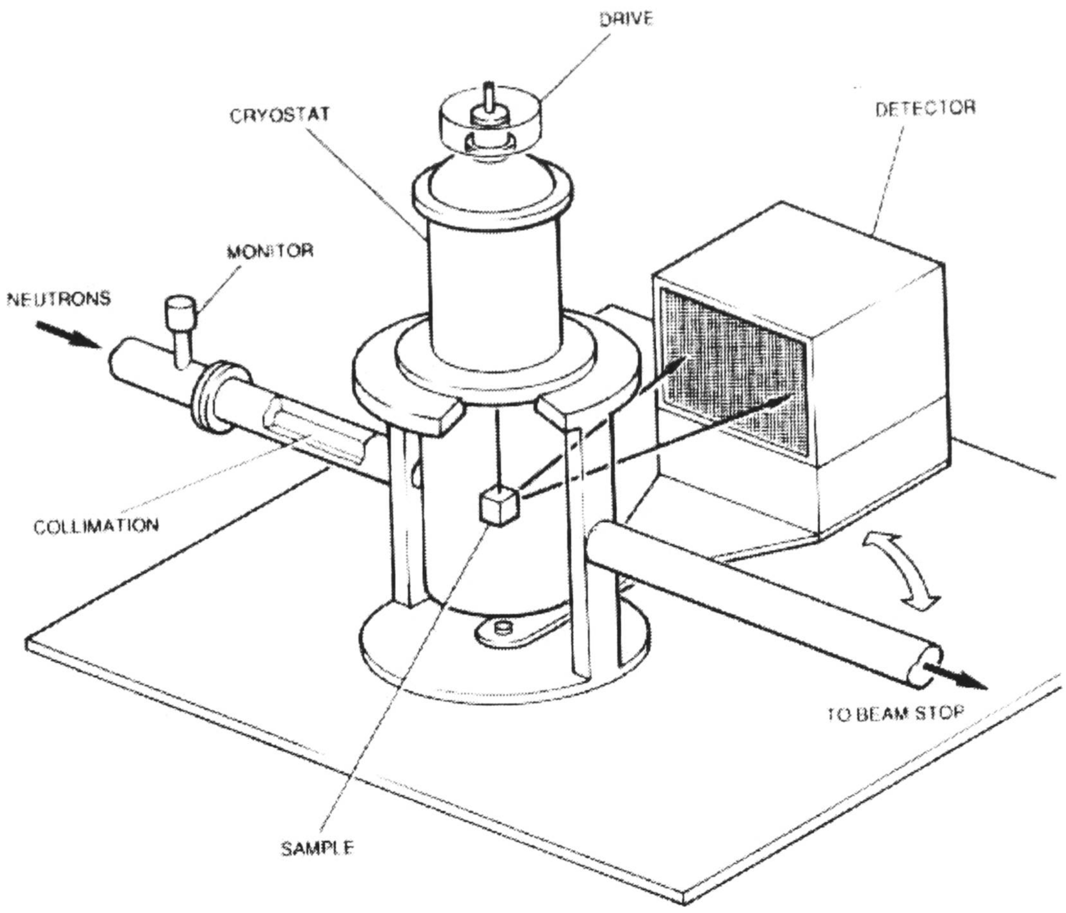

Figure 4.2 - Schematic of the SXD sample environment under normal cryogenic operation.

During the experiment a CCR cryostat was employed in order to access the required temperatures. The cryostat was capable of producing precisely defined, invariant temperatures in the sample tank, between 1.5 K and 300 K. Consequently, for this experiment heating and cooling power was provided by the cryostat, not the microwaves. The tails of the cryostat (Vanadium) were modified to provide reliable sample rotation and to minimise unwanted scatter. Furthermore, the sample tank was evacuated prior to data collection in order to prevent scatter from the air.

Single crystals are generally mounted on a pin and positioned in the radiation beam. However, metal pins would disrupt the microwave field in the vicinity of the sample. Therefore, the aspirin crystal was mounted on a custom-made aluminium nitride sample pin, using Kapton tape. Not only is the ceramic material aluminium nitride transparent to microwaves, but it has high thermal conductivity, thus allowing the maximum degree of temperature control by conventional methods.[102]

The sample space at SXD was limited and space had to be allowed for the cryostat in addition to the detectors themselves. Transmitting microwaves to the sample under these restrictions via tubular waveguides was impractical. Waveguides have minimum dimensions for propagation of microwaves, which for rectangular guide is $\lambda/2$ across the broad face (minimum 61 mm at 2.45 GHz) and for circular guides is $\lambda/1.7$ in diameter (minimum 72 mm at 2.45 GHz). These sizes were too large to introduce into the SXD sample chamber and an alternative method had to be employed. There are no size restrictions for waveguides where transverse electromagnetic (TEM) waves can propagate. Thus, we were able to use coaxial lines to transmit microwaves from the generator to the sample. Parallel-plate waveguides were used to bathe the sample (between the plates) in the microwave field. To prevent the formation of standing waves and reflected waves, which could potentially damage equipment, excess power was dumped into a water load external to the sample chamber. The custom-made apparatus is shown in Figure 4.3.

A commercial 0-1 kW variable power microwave source (ASTeX 5-1000) was used to deliver microwaves (2.45 GHz) into the sample tank via a flexible 200 W coaxial cable and vacuum feed-through. Microwaves are then transmitted from the coaxial line to a parallel plate waveguide (made from Vanadium – low neutron scattering cross-section) straddling the sample crystal. The plates are fixed at a constant separation with 10 mm wide PTFE spacers, placed so as not to interfere with the incident or scattered beam. The electric field at the sample should therefore be uniform, polarised normal to the plates.

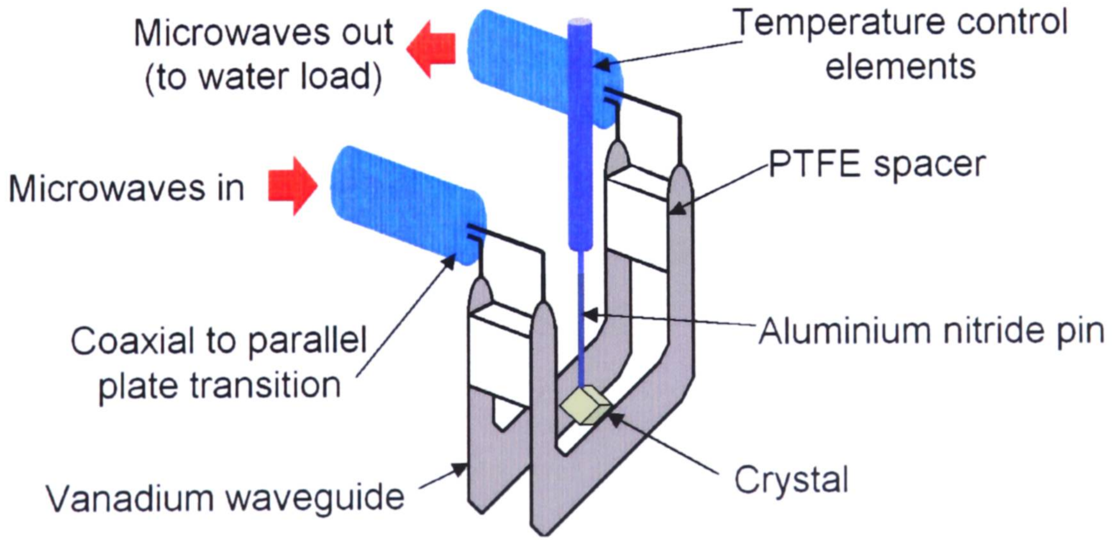

Figure 4.3 - Schematic representation of the sample arrangement and microwave applicator.

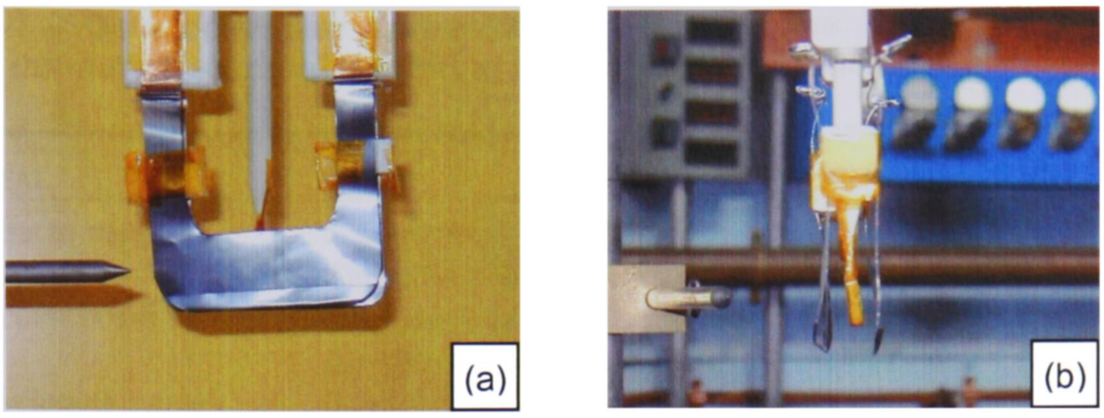

Figure 4.4 - Parallel-plate applicator for the irradiation of aspirin, from (a) front, and (b) side.

4.2 Experimental

The aspirin crystal was prepared prior to the experiment by dissolving aspirin in acetone. The resulting solution was left in a lightly stoppered sample vial and allowed to evaporate over a period of 5 days. A crystal of dimensions $8\times4\times1.5$ mm^3 was produced. Diffraction data on this crystal was collected under several sets of conditions (Table 4-1).

The spatial constraints imposed by the microwave apparatus made it necessary to remount the crystal several times in order to obtain a reasonably representative data set to allow the necessary refinement of atomic thermal parameters. Data were recorded in the presence and absence of a microwave field. During irradiation, microwave power was held at 50 W throughout. Temperature control was achieved by cooling the sample pin, which in turn controlled the temperature at the crystal. A total of 8 data frames, each containing data from two detectors, were collected: 4 in each of two crystal orientations, achieved by remounting the crystal. Exposure times for each frame varied from around 60 to 180 minutes. The intensities were extracted and reduced to structure factors using standard SXD procedures[101] and the refinement was performed using SHELXL-97,[103] refining on F^2. C.C. Wilson, the SXD instrument scientist, performed all refinements.

Table 4-1 - Data collection and refinement parameters for the single crystal neutron diffraction study of Aspirin under microwave irradiation.

INSTRUMENTAL			
Diffractometer	SXD neutron time-of-flight Laue diffractometer		
Detectors	Three, 64 x 64 element, 3×3 mm pixel, scintillator PSDs		
Detector position	Detector 1: $2\theta_c=125°$, $L_2=150$ mm; Detector 2: $2\theta_c=55°$, $L_2=190$ mm; Detector 3: $2\theta_c=95°$, $L_2=110$ mm		
Wavelength range	0.5-5.0 Å		
SAMPLE			
Compound	Aspirin ($C_9H_8O_4$)		
Molecular Weight	180.16		
Crystallising solvent	Acetone		
Crystal size	8 x 4 x 1.5 mm^3		
DATA COLLECTION			
Crystal symmetry	Monoclinic ($P2_1/c$)		
Z	4		
Unit cell (100K)	a=11.233, b=6.544, c=11.231, β=95.89		
Data	8 data frames at each temperature		
REFINEMENT			
T / K	100	200	300
Observed Refs	3971	3611	2794
Unique Refs I>2σ(I)	1151	877	625
R_{int}	0.068	0.078	0.085
Absorption coefficient	$\mu(cm^{-1}) = 0.80 + 0.75\lambda$		
Refined parameters	190 for full anisotropic refinement		

4.3 Results

The data obtained are unfortunately somewhat limited, owing to the spatial constraints of the apparatus and limited time on the instrument. Nonetheless, there was sufficient to allow anisotropic refinement of the atomic displacement parameters, though these refinements result in a rather low data/parameter ratio. Data at 100 K, both in the presence and absence of microwaves, were sufficiently good to allow full anisotropic refinement. Data at 200 K and 300 K could only be refined with isotropic thermal parameters, but in addition we have data from a previous study of aspirin at 300 K with anisotropic ADPs,[96] which can be used as a benchmark 'microwaves off' data set.

Table 4-2 shows a selection of the structural data calculated. The data here represents the most reliable data sets where the data at 300 K is the result from previous experiment.[96] The equivalent isotropic ADP has been listed for ease of comparison. However, the essential points are more clearly distinguished from a thermal ellipsoid diagram of the molecule, see Figure 4.5.

Table 4-2 - Refined values of U^{eq} for atoms in aspirin with conventional heating at 100, 200 and 300 K and with microwave heating (50 W) at 100 K. Labelling of atoms as in previous structural studies on aspirin and indicated in the text.

	NO MICROWAVES			MICROWAVES
T/K	100	200	300	100
a/Å	11.233	11.233	11.416	11.233
b/Å	6.544	6.544	6.598	6.544
c/Å	11.231	11.231	11.483	11.231
β/°	95.89	95.89	95.6	95.89
V/Å^3	762.58	762.58	670.81	762.58
U^{eq}/Å^2				
C1	0.011717	0.020437	0.022550	0.029963
C2	0.011957	0.021117	0.038453	0.033197
C3	0.017763	0.028620	0.048660	0.040730
C4	0.020130	0.029817	0.051037	0.043270
C5	0.017727	0.029043	0.046740	0.035577
C6	0.015973	0.025770	0.041377	0.036917
C7	0.011543	0.021263	0.037220	0.030143
C8	0.013920	0.022433	0.044713	0.035090
C9	0.021590	0.032927	0.062563	0.048163
O1	0.020387	0.029960	0.050937	0.044363
O2	0.021220	0.033840	0.051753	0.044963
O3	0.013650	0.022733	0.042373	0.032583
O4	0.025073	0.039167	0.060673	0.049127
H1	0.034827	0.046817	0.082880	0.062020
H2	0.033687	0.050300	0.073500	0.066477
H3	0.040343	0.046950	0.072340	0.057767
H4	0.031363	0.043323	0.068200	0.053293
H5	0.059453	0.073377	0.113440	0.101673
H6	0.085200	0.161223	0.167093	0.146717
H7	0.075087	0.123933	0.174443	0.140967
H8	0.030670	0.049227	0.076183	0.070010
$R(F)$	0.0957	0.0954	0.0873	0.1302
w$R(F^2)$	0.237	0.243	0.218	0.268
G of F (S)	1.468	1.424	1.398	1.452

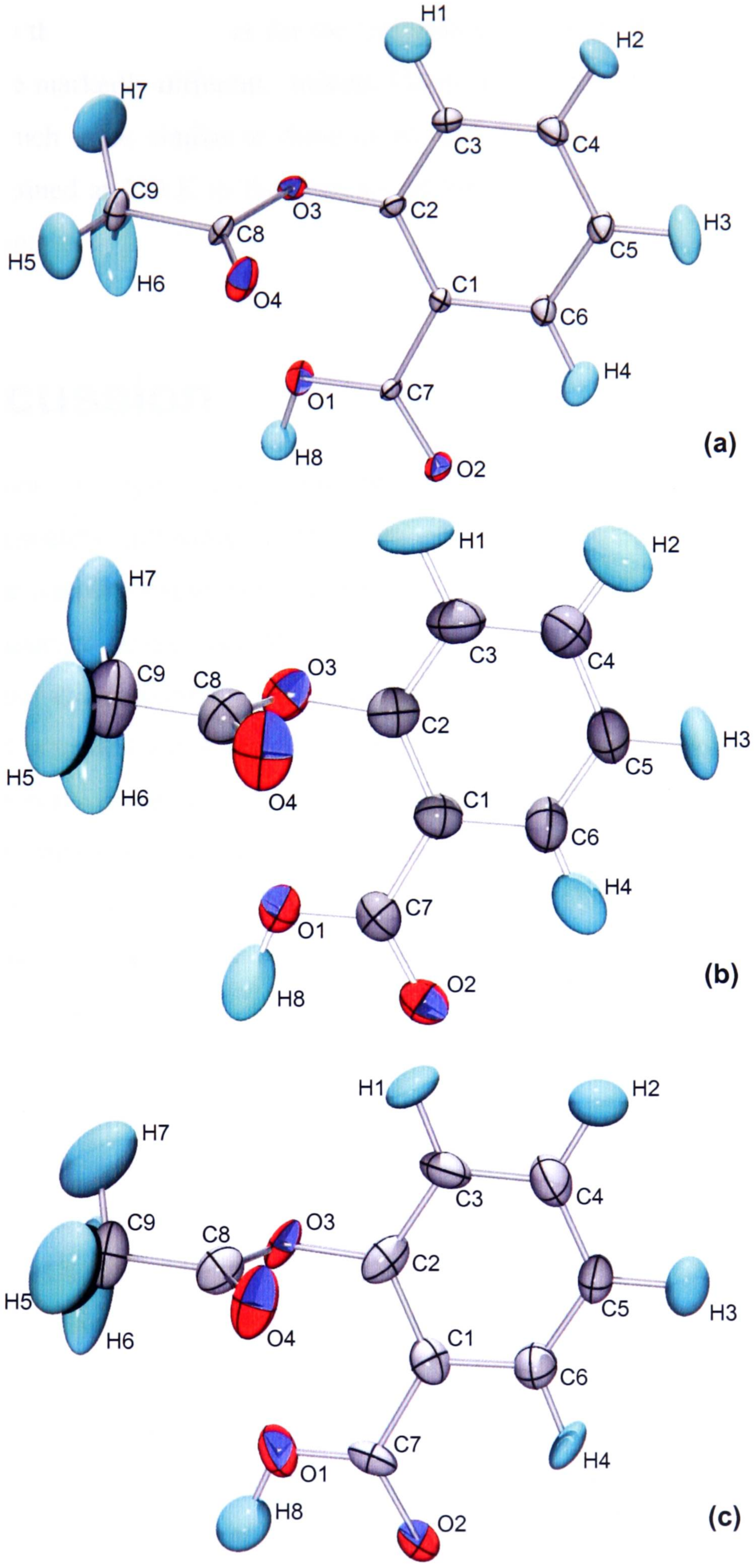

Figure 4.5 - Aspirin structure showing atomic thermal ellipsoids from crystal structure determination: (a) at 100 K, (b) at 300 K, and (c) at 100 K with 50 W microwave field.

It is clear that the thermal parameter for the 'microwave on' and 'microwave off' data sets taken at 100 K are markedly different. Indeed, Figure 4.5 plainly illustrates that the thermal parameters are much more similar to those of the 300 K, conventionally heated structure. The structure obtained at 200 K in the presence of microwaves shows a similar increase in thermal parameters.

4.4 Discussion

Closer examination of Figure 4.5 reveals that the thermal ellipsoids of all atoms are increased approximately uniformly, so that they closely resemble the 300 K data without microwaves. The simplest explanation therefore is that the aspirin crystal is hotter than the temperature measured. Experimentally this can be explained by the method in which temperature control is maintained. The conduction path from the sample to the cold head of the CCR cryostat is made by thin aluminium strips to the pin, then along the pin itself. One possibility is that in the presence of microwaves the aspirin crystal would heat preferentially, but that the heat introduced into such a small mass would have a negligible effect on the temperature measurement in the CCR. However, is it plausible that a temperature gradient of several hundred Kelvin could exist? If not then this must point to the existence of a non-thermal microwave effect.

The work by Whittaker and co-workers[54] has shown that in a plane-polarised microwave field, anisotropic diffusion may be induced. It is thought that in the present case the plane-polarised microwave field may show itself as enhanced vibrations along the field polarisation axis. Unfortunately, the necessary remounting of the crystal between frames will have superimposed any such effects and Figure 4.5 shows no such directional enhancement. Any such enhancements would apparently take place along multiple vectors, best fitted through anisotropic displacement. Neither are there any apparent vibrational enhancements of the hydrogen atoms of the terminal methyl group, or for the hydrogen atom involved in the carboxylic acid dimeric hydrogen bond. There is therefore no evidence to suggest a non-equilibrium distribution of energies. Furthermore, Booske and co-workers have predicted that any non-thermal effects would be less pronounced in single-crystals rather than polycrystalline samples,[50] owing to the role of microstructure in microwave heating, thus making observation of an effect that much more difficult.

The experiment has shown the specific nature of microwave heating, but ambiguities in the recorded temperature and due to the superposition of data due to remounting the crystal have made it difficult to draw further conclusions. Since the completion of this experiment SXD has been upgraded and is now equipped with a bank of detectors which completely fill the solid angle. New data collection procedures are also possible, which will allow full three-dimensional data sets to be obtained from a vertically mounted single crystal.[104] The use of more efficient cooling, such as a cryogenic gas stream, and a more reliable method of temperature measurement, such as contact probes or thermal imaging, would significantly improve the experimental procedure and may produce far more useful and interesting results.

Single crystal diffraction (by this method) is not ideal for the study of the effect of microwaves on crystal structure. The necessity to reorient the sample in the middle of data collection negates any directional effect the microwave field may have on the structure or vibrations. Temperature monitoring remote from the sample is ineffective for microwaves, where the heating effect is local. Improvements in data collection and temperature control may enable this experiment to be repeated in the future with clearer results.

5 Silver iodide

Silver iodide is an attractive material to study as not only does it have a relatively well-understood, simple crystal structure, but it is a solid-state, ionic conductor at ambient temperatures. Furthermore, it has a readily accessible phase transformation (420 K), introducing another aspect to the research. This experiment also introduced a new reactor design: one for use with X-rays rather than neutrons, and therefore of more practical value where neutrons are a scarce (and expensive) resource. The development of this applicator is discussed in detail.

5.1 Applicator design

Though neutrons do present one solution to the problem of performing diffraction measurements inside a microwave applicator, the production of neutrons is expensive and time on such instruments is limited. Therefore, efforts have been directed at designing a microwave applicator compatible with the requirements of X-ray diffraction, and specifically a commercially available, powder X-ray diffractometer with a sealed-tube Cu K_α source.

In order for a microwave applicator to heat successfully, it must have a continuous, conducting interior surface. It is therefore necessary to use a metal with low electrical resistivity, frequently aluminium or brass. Though microwave radiation containment is paramount, holes are allowed as long as the hole is of narrow diameter with respect to the microwave wavelength (122 mm at 2.45 GHz). The cut-off wavelength, λ_c, for the lowest order mode (TE_{11} in a cylindrical waveguide) determines the maximum wavelength that will propagate. Equally, the cut-off diameter determines the maximum bore dimension that will prevent propagation. Thus the maximum hole diameter is 36 mm at λ_c = 122 mm; smaller than this and the field intensity diminishes extremely rapidly so that only a short collar on the outside of the hole is necessary to prevent any leakage whatsoever. However, for a complete 2θ scan a hole consisting of an arc with ~180° coverage about the sample position is desirable for maximum beam intensity. This is far too large to be successfully accommodated in this manner.

An alternate solution is to use a 'window' material. For example, in neutron diffraction Vanadium is frequently used for sample containment as it has a low coherent neutron-scattering cross-section and its diffraction pattern is simple, any vanadium reflections being easily identified and accounted for. For X-ray diffraction, the material with the best balance of electrical conductivity and X-ray transparency is beryllium. However, beryllium is a difficult material to use. It tends to form extremely toxic oxides and the machining involved in making the applicator would create large amounts of harmful dust. Therefore, an alternative material was used: aluminium. Though aluminium has a larger X-ray scattering cross-section than beryllium, it does have desirable physical properties, that is, high conductivity, it is easily shaped and readily available as thin films. It was consequently chosen for the 'window' material in the applicator. To prevent significant attenuation of the X-ray radiation, only a thin layer of aluminium foil was used. Foil of ~10 μm thickness (Aldrich) was found to be a sufficiently good conductor, whilst allowing the passage of X-rays.

Rather than place the entire microwave generator inside the shielded cabinet surrounding the diffractometer, microwaves were introduced into the applicator via a 1m length of coaxial cable (with copper conductor). The advantages of this are that the control mechanism remains outside and can be adjusted in the midst of an experiment, and the size of the hole to be cut in the cabinet is minimised, for safety considerations. The design of the applicator is shown in Figure 5.1.

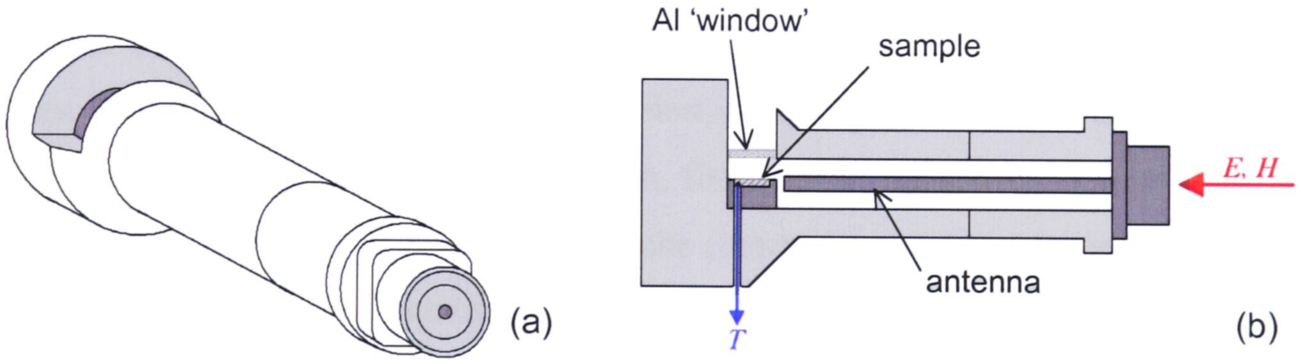

Figure 5.1 - Prototype applicator for in-situ X-ray diffraction during microwave heating. (a) Perspective. (b) Schematic, showing port for temperature probe, incoming microwave radiation at the coaxial port and central antenna to re-emit microwaves.

Externally, the applicator is 154 mm in length and 31 mm diameter across the main length of the barrel. The internal barrel is 112 mm long, by 20 mm diameter. The antenna is 104 mm long and 7 mm diameter. The slot cut across the applicator to admit X-rays is a full 180° arc and is 10 mm across. In this slot sits the aluminium window. In order that we might have the ability to change the material used as the 'window' a frame was constructed to support the foil (2 mm thick), which has the result of reducing the actual window size to 6 mm by ~140°. This frame was held in position by screws and was readily removed to allow access to the sample and replacement of the foil. The cylindrical design means that X-rays pass through the foil normal to the surface, minimising scatter from the foil itself. The construction material was brass, apart from the coaxial port and antenna (stainless steel), the aluminium foil window and the microwave-transparent, ceramic sample holder (Shapal™). The larger end of the applicator (drawn to the left in Figure 5.1b) was designed to attach to the goniometer head of a Philips PW X'pert powder diffractometer.

The narrow bore of the applicator is less than the cut-off diameter for 2.45 GHz microwaves (36 mm). However, the introduction of a conducting element (the antenna) into the cavity turns what would be a circular choke into a coaxial waveguide with efficient transmission properties. The antenna reaches to within a few millimetres of the sample. The dimensions of sample are kept deliberately short so as to minimise the effect of field gradient and therefore temperature gradient over the sample.

The applicator was first tested to ensure that it would heat the sample effectively. A substance already known to be a good microwave susceptor, i.e. powdered graphite, was used in this experiment. A temperature probe was used to record the sample temperature. However, the ceramic sample holder, as detailed in Figure 5.1, had not been constructed at this early stage of development; instead a thin, flat ceramic plate was used with the sample sitting on top. The fibreoptic temperature probe (Nortech) sat on the underside of the plate and therefore measured a temperature probably significantly less than that of the sample, due to the temperature gradient through the thermally insulating plate. This experiment proved successful with rapid heating of the order of 10 K per second, even at a relatively low power output of 100 W. It was noted at this stage that some minor heating did occur in the co-axial cable, but this was not significant. Microwave containment was assessed using a Sairem hand-held, microwave survey meter (sensitive to ~0.1 mW/cm^2). No microwave leakage was detected from the reactor.

Having ensured that the applicator was effective at heating the sample, it was then tested to guarantee that diffraction measurements could be taken effectively. For this test, a sample of alumina (α-Al_2O_3, Aldrich, 99.9%) was used. Powder X-ray diffraction patterns were recorded on the Philips X'pert diffractometer for $10° < 2\theta < 65°$ with a step-size of 0.02° and collection rate of 4 seconds per step. The sample was placed in the sample holder (now constructed), inserted into the applicator and placed on the goniometer. Histograms were made with the foil window in place and absent. A comparison of measurements is shown in Figure 5.2.

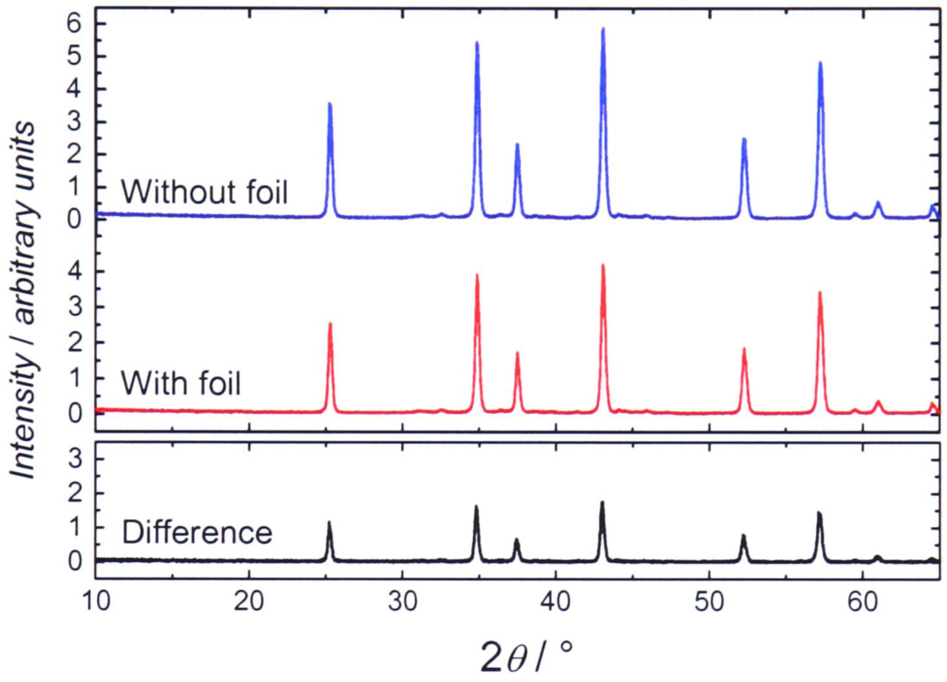

Figure 5.2 - Diffraction patterns of alumina showing effect of Al foil window.

It is clear that the only difference between the diffraction pattern with the foil, and without, is a slight decrease in intensity, due to the attenuation of the X-ray flux as it passes through the foil. Measurements made through the foil show ~70% the intensity of the same measurement made in the absence of the foil.

5.2 Experimental

The applicator was mounted on the goniometer head of a Philips X'pert powder diffractometer. The sample, silver iodide, was placed in the sample holder and when in position, the sample was aligned with the aluminium foil window, the X-ray source and the detector. A fibre-optic temperature probe was inserted into the port (as shown in Figure

5.1b) and was ensured to be in direct contact with the sample (located near the centre of the sample). Temperature was then recorded using a Nortech Fibronic NoEMI-TS series fluoroptic thermometer (precision of ± 0.1 K). The thermometer had previously been calibrated by a co-worker (A. G. Whittaker). The coaxial cable (copper conductors, 1 m long, rated 200 W) was connected to the applicator and through a small hole in the roof of the safety enclosure, out to the microwave generator (ASTeX S-1000, 2.45 GHz, 0-1000 W variable power source). The hole was shielded with additional lead plating and no X-ray leakage was detected. The apparatus is shown in Figure 5.3.

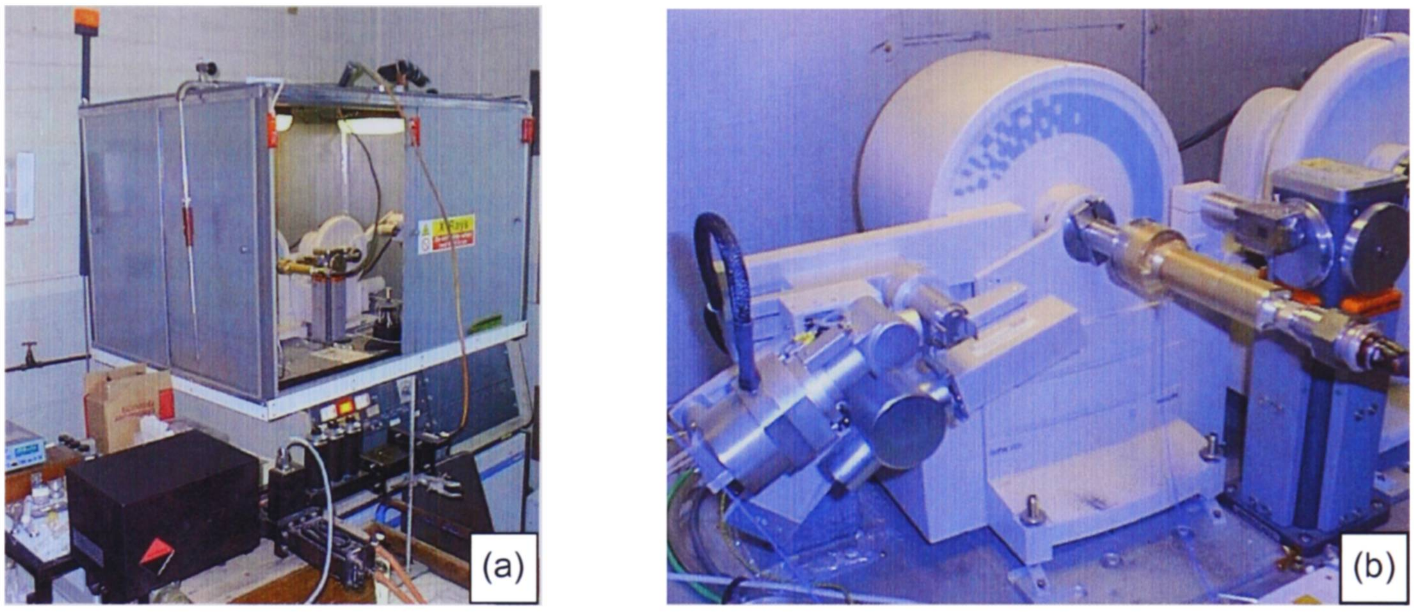

Figure 5.3 - Inside the safety enclosure (a), the microwave applicator, attached to the goniometer (b). The fibre-optic cable can just be seen exiting the underside of the applicator.

For each measurement, the temperature was monitored and the heating rate of the sample controlled by altering the power output of the generator in the range 50-200 W and by adjusting the field pattern in the applicator using a three-stub tuner. Small adjustments of the field pattern were necessary throughout, as the dielectric properties of the sample and applicator are a function of temperature. A reasonably steady temperature rise of about one Kelvin per minute was achieved. In order to achieve good time and temperature resolution, a relatively narrow angle range was studied.

Silver iodide is an ionic conductor with relatively simple structure. It was chosen for this study for several reasons.

(i) The simple structure makes powder diffraction analysis much easier and other parameters, such as atomic displacement parameters, can be determined accurately.

(ii) Enhanced ion mobility has been reported as a result of microwave irradiation[52, 53, 55] and our hypothesis is that the effect may be more pronounced in a system where ions are already quite mobile.

(iii) There is a well documented[105-107] phase change at approximately 420 K from the *β*-polymorph (wurtzite structure, space group $P6_3mc$) to the more-dense *α*-polymorph (body-centre cubic structure, space group $Im\bar{3}m$) with a corresponding sharp increase in conductivity and ion mobility.

(iv) The phase change temperature was accessible using the fluoroptic thermometer (maximum temperature, 473 K).

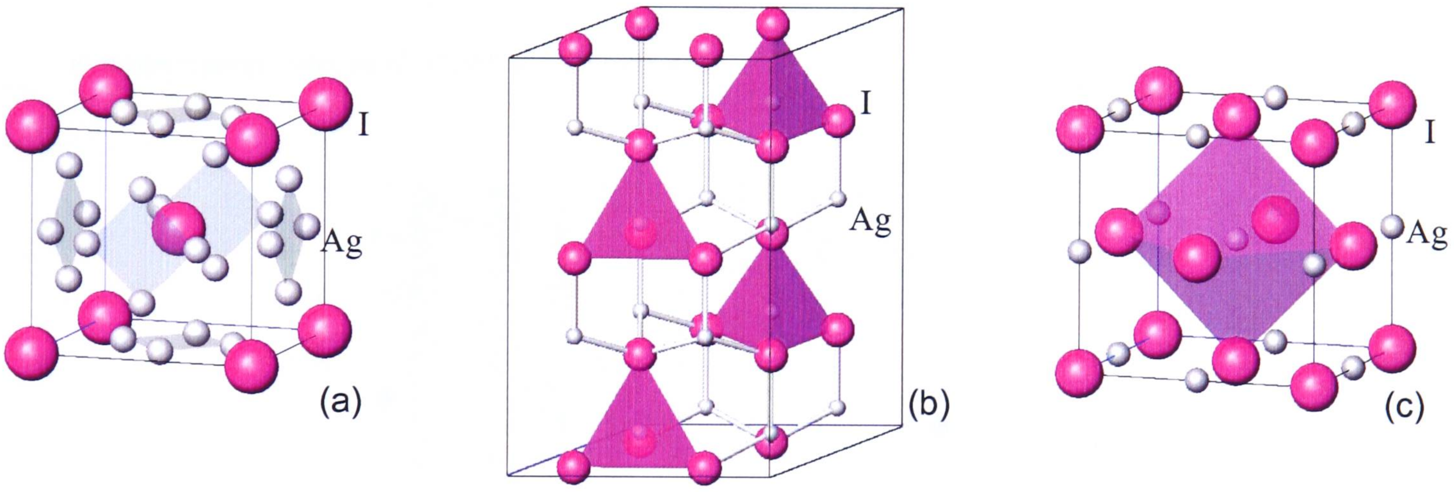

Figure 5.4 - Structure types of silver iodide (Ag=smaller diameter, I=larger diameter). (a) the superionic *α*-AgI, *bcc* structure. Silver ion positions are disordered and the statistical occupancy of each site is $^1/_6$. (b) *β*-AgI, wurtzite structure (2×2×2 unit cells). (c) *γ*-AgI, zinc-blend structure. Often exists in syntaxy with *β*-AgI.

Structural studies of silver iodide are slightly complicated in that the room-temperature material (other than pure single crystals) generally contains a proportion of the meta-stable polymorph *γ*-AgI. *γ*-AgI has a zinc-blend, *fcc* structure and is the result of cubic stacking faults in the *β*-AgI structure. Maskasky[105] has shown that pure crystals of the *β*-phase only transform to the superionic *α*-phase at 435 K. However, on cooling a mixed *β*/*γ* phase is formed at 420 K and the material no longer exhibits the raised phase transition temperature. The large difference in density between the α and β/γ phases is responsible for the creation of these stacking faults and the corresponding reduction in transition temperature.

Silver iodide (AgI) samples were prepared by grinding with a pestle and mortar to ensure a fine consistency. Purification was impractical (extensive handling being undesirable as AgI is light sensitive and will decompose to silver and iodine on prolonged exposure to daylight) and unnecessary, as the supplied purity (99%, Aldrich) was sufficient for this purpose.

5.3 Results

In the course of the experiment, microwave power and sample-temperature were recorded at frequent intervals (approximately every two minutes). Powder X-ray diffraction (PXRD) measurements were performed at approximately 10 K intervals. The power and temperature profiles are shown in Figure 5.5. Note, maintaining a constant temperature during data collection would be preferred, yet this proved extremely difficult. Thus a constant temperature ramp was employed throughout.

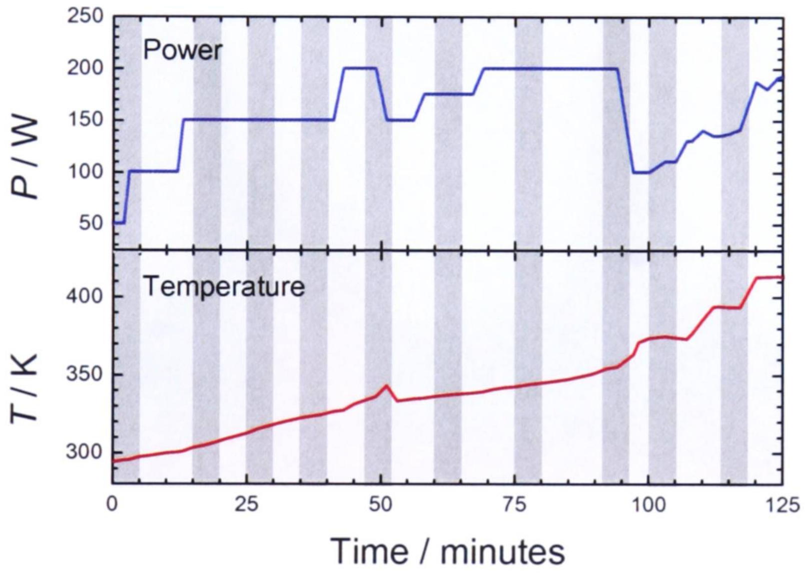

Figure 5.5 - Variation of power and temperature in course of experiment. Grey bands indicate that a diffraction measurement was performed over this time period.

There were two occasions in the experiment where temperature began to rise rapidly: at 51 minutes and again at 97 minutes. On each of these occasions, a sharp cracking sound was heard. At once, the power was turned down to a lower level until the noise ceased. It was noted that the coaxial cable became very hot at points during the experiment and, afterwards, charring was observed at the cable-waveguide connections. It is thought that these connections are the limiting factor in experiments using this apparatus. They are points of electrical field stress, which – at sufficient power – can cause micro-arcing, oxidation and eventually voltage breakdown.

In Figure 5.5 the series of PXRD measurements are shown as grey bands. Each of these bands represents a 5 minute measurement for 41° < 2θ < 48°, with a step size of 0.02° and measurement rate of 0.5s per step. Examples of these patterns, one from each of the lower temperature, β-AgI phase and the higher temperature, α-AgI phase, are shown in Figure 5.6. There are three reflections of interest in this range: reflections at 42.5° (*103*) and 46.2° (*112*) belong to the β-AgI phase, whilst the broader reflection at 43.5° (*211*) belongs to the α-AgI phase. The signal has a significant level of noise and some settling of the sample has occurred during the experiment (resulting in optical misalignment and splitting of the diffraction peak – as observed for the α-AgI phase in Figure 5.6). Nonetheless, the diffraction peaks are clearly resolved and unambiguous.

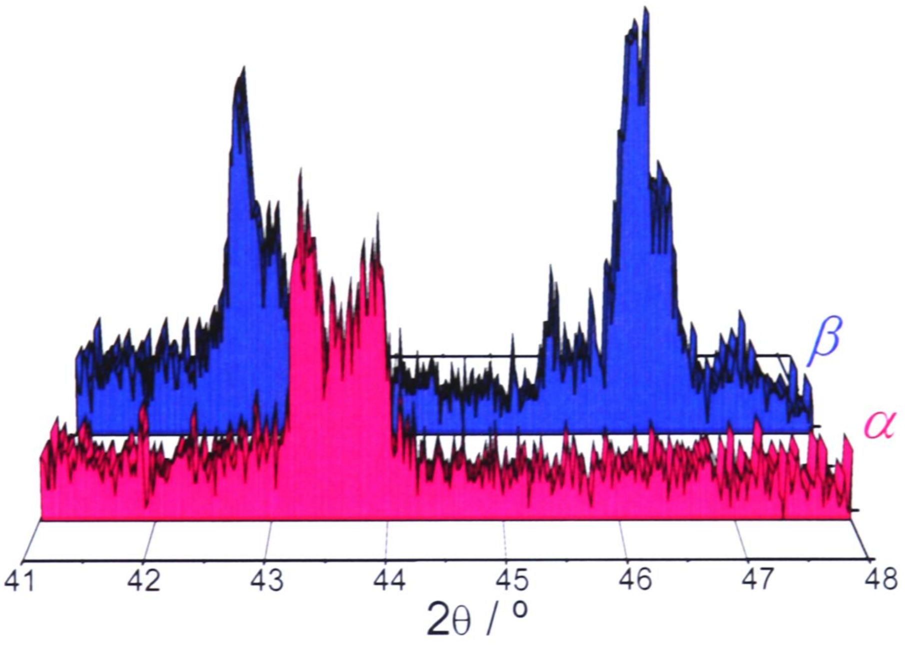

Figure 5.6 - Diffraction patterns for α-AgI and β-AgI, over the range 41° < 2θ < 48°.

Experimental data (X-ray scattering intensity) was measured for this experiment as a function of angle and as a function of temperature. Therefore, it is sensible to plot the results in three dimensions. In order to do this the data was first converted into a matrix using Microcal Origin 5.0. A 20×20 grid of intensity was created using the correlation method, with a search radius of 2 and a smoothing factor of 0.8. Vertical elements show the range of temperatures; horizontal elements show the angle range. The result can be plotted (Figure 5.7) as a contour map to clearly show the phase transition temperature.

Figure 5.7 shows that with increasing temperature, the peak intensity for the *β*-AgI peaks falls off rapidly as the phase transition temperature is approached. At the same time, the new peak, from the α-AgI phase, rapidly increases in intensity. Figure 5.7 clearly shows the phase transition occurs at approximately 370 K, with an estimated error of 10 K. This is about 50 K below the accepted literature value of 420 K. Such a large discrepancy cannot easily be explained in conventional terms. The sample was small with respect to the microwave penetration depth, hence the microwave field at the sample would be relatively uniform. It is difficult to predict the exact nature of the field pattern within the sample itself, owing to complex microstructure in the grains. Therefore, though efforts have been taken to avoid this, it is perfectly possible that temperature gradients exist in the sample. Nonetheless, diffraction measures bulk properties and there are no signs of the *α* and *β* phases co-existing at any point outside the transition temperature range.

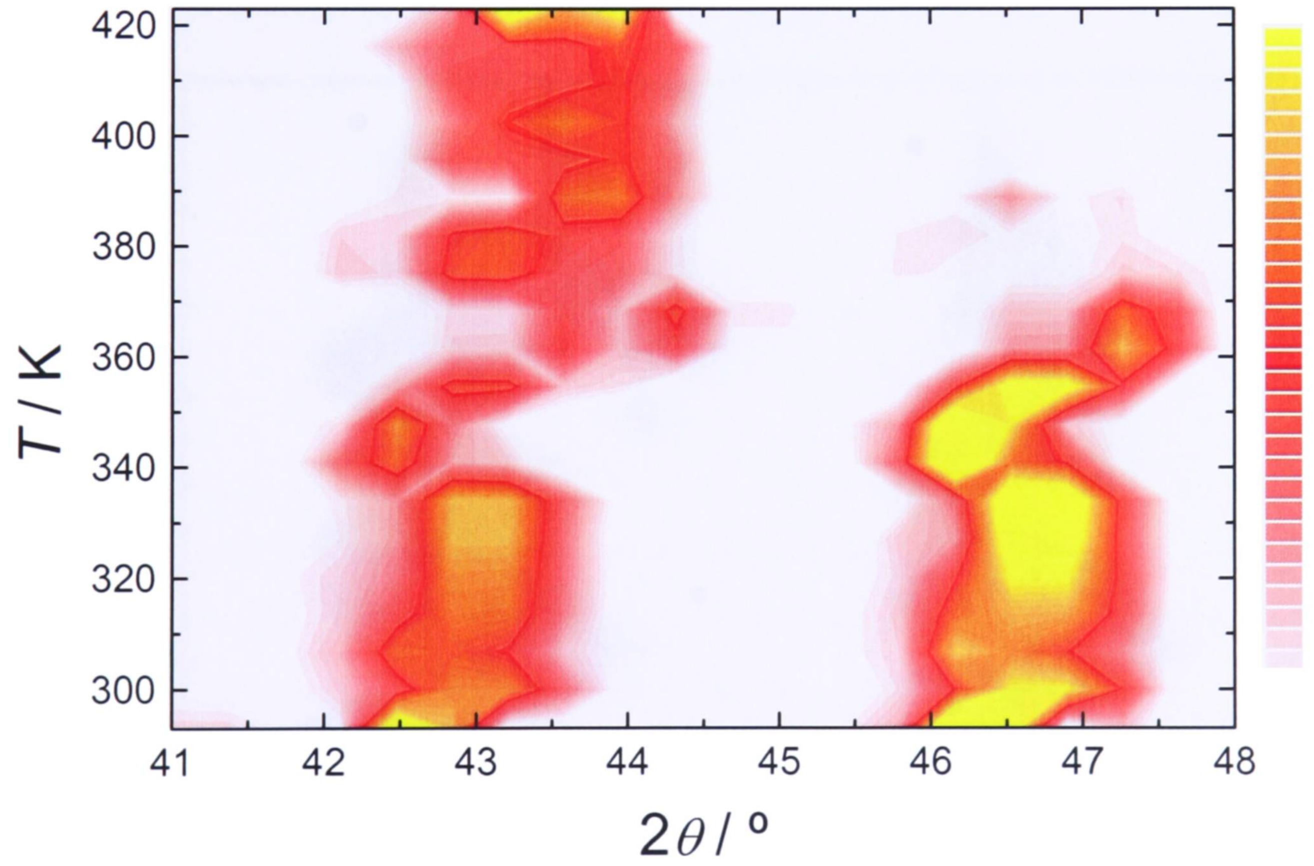

Figure 5.7 - Contour map showing variation of Bragg peak intensity (41°<2*θ*<48°) with temperature for silver iodide heated by microwave irradiation. The phase-transition temperature is 370K ±10K.

In order to ensure a fair comparison, the same measurement was performed using convection heating (Steinel HG4000, 273-1073 K heat gun). The hot air was blown down a copper tube and directed towards the open end of the applicator (the applicator is opened by unscrewing at the centre join – see Figure 5.1 – and removing the section attached to the antenna). The temperature of the sample was increased in this manner until the phase transition was reached. Note that a new sample of AgI was used (no previous heating history) and the temperature was much easier to control in this experiment and so a better temperature resolution was achieved.

The data were transformed into three dimensions and are plotted in Figure 5.8. The calculated phase transition temperature is 412K with an estimated error of 2K. This is below the established literature value, but the difference could be accounted for by the presence of the γ-AgI phase resulting from cubic stacking faults.[105] These act as nucleation points for phase transformation and the higher the proportion of γ-AgI, the lower the transition temperature. The difference is certainly not so great as to throw into doubt the anomalously low temperature of the phase transition under microwave heating.

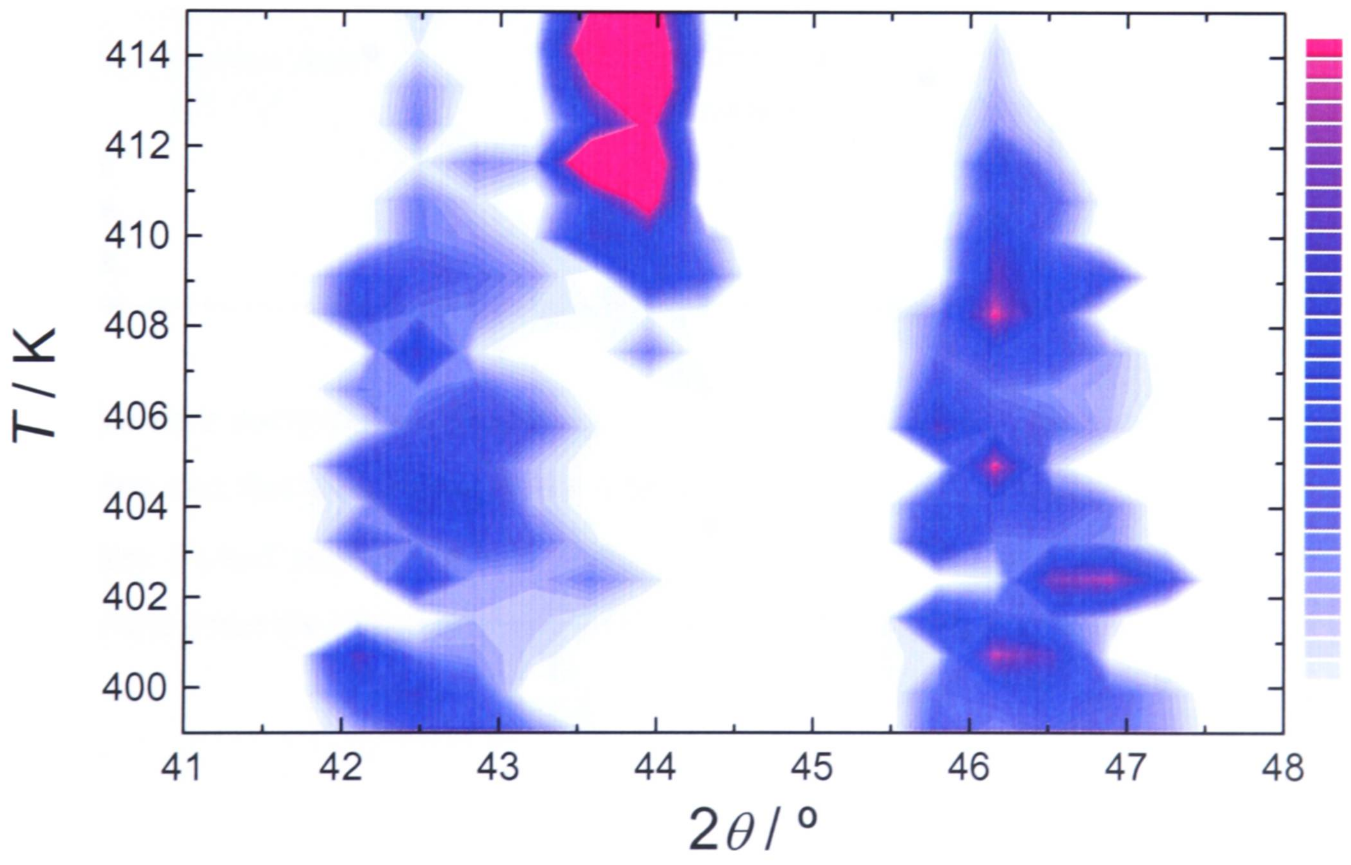

Figure 5.8 - Contour map showing variation of Bragg peak intensity (41°<2θ<48°) with temperature for silver iodide heated by microwave irradiation. The phase-transition temperature is 412K ±2K.

Powder X-ray diffraction measurements were also performed over a much wider angle range (20° < 2θ < 60°) with a slower collection rate (4s per 0.02° step) for better signal to noise. However, the data collected in this manner was not ideal for structure refinement. As mentioned earlier, the sample tends to settle during the course of an experiment (due to changing density of the sample) and consequently moves out of optical alignment with the X-ray beam and detector. The result was changed intensities and split peaks, both of which prohibit accurate structure refinement. The optimised parameters for data collected at 353 K are given in Table 5-1, whilst the corresponding diffraction pattern is shown in Figure 5.9.

Table 5-1 – Optimised crystallographic data for silver iodide at 353 K, using prototype applicator and conventional heating.

PHASE	β-AgI	γ-AgI
Space Group	$P63mc$	$F\bar{4}3m$
Phase Fraction (%)	68.5(17)	31.5(17)
$a = b$ / Å	4.5983(9)	6.5094(12)
c / Å	7.526(2)	6.5094(12)
V / Å^3	137.81(5)	275.82(9)
Ag *position vector*	{⅓, ⅔, 0}	{0, 0, 0}
U^{eq} / Å^2	-0.016(12)	-0.06(3)
I *position vector*	{⅓, ⅔, 0.62(2)}	{¼, ¼, ¼}
U^{eq} / Å^2	-0.074(6)	-0.05(3)
χ^2	4.383	
R_{wp}	0.2780	
R_p	0.2162	

The difference curve illustrated in Figure 5.9 shows that the structural model is not a good fit to the data and that therefore accurate structural data cannot be obtained. However, the data does show a small peak at 1.63 Å. This reflection is absent for α-AgI but present for γ-AgI, thus showing that the zinc-blend structure is present in the current sample.[105]

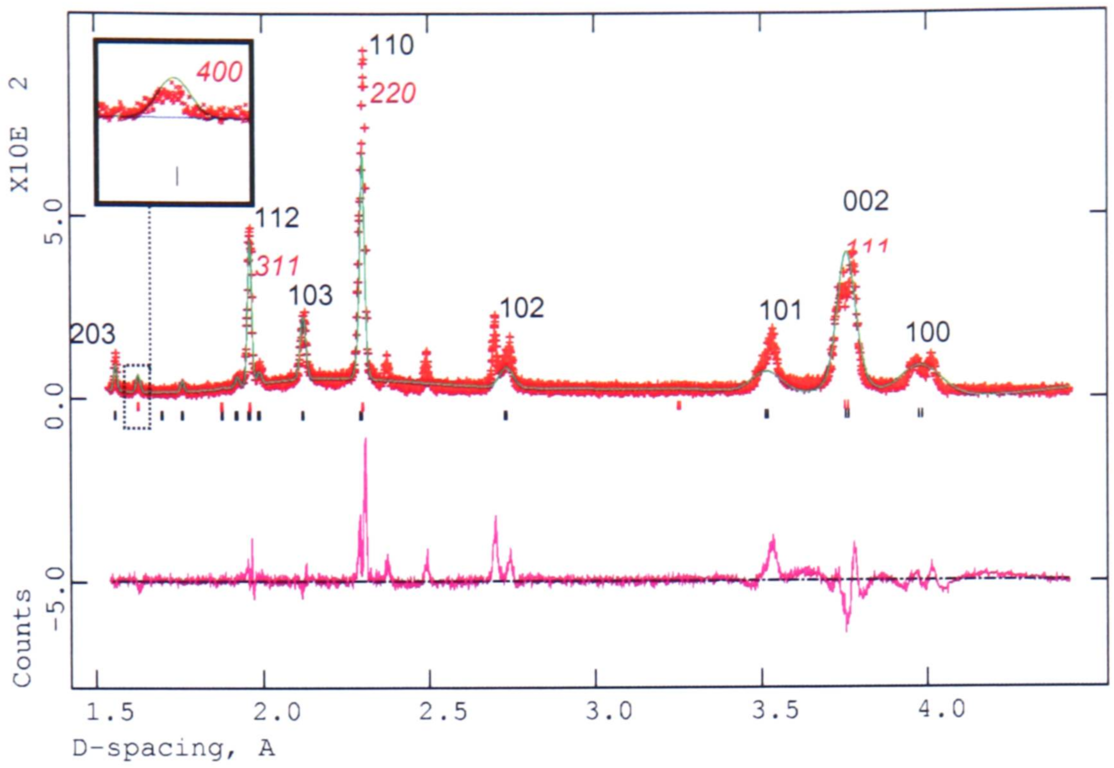

Figure 5.9 - Powder X-ray diffraction pattern of silver iodide at 353 K, using prototype applicator and conventional heating. Crosses show the experimental data, the line through them is the refined structural model, the line below is the calculated difference. Reflections are shown with tickmarks and *hkl* labels for β-AgI and for γ-AgI (the latter in italics). Box shows the unique γ-AgI [*400*] reflection.

Another problem was overheating of the apparatus. A circulator was present just before the magnetron and protects it from reflected power. Unfortunately the coaxial cable was not protected in a similar manner and suffered both forward and reflected TEM waves. Most of the magnetron's power output, in fact, was reflected from the applicator, as the sample will have absorbed only a fraction of the available power. Most of the power loss in the system therefore occurred at the junctions between waveguide and cable, and cable and applicator. These heated up significantly in the course of an experiment and imposed a practical maximum experiment time of around 2 hours. This was too short a period to obtain a PXRD measurement sufficient for accurate structure refinement.

5.4 Discussion

The bold result from this experiment is that the β-AgI to α-AgI phase transformation goes at a much lower temperature under microwave heating than under convection (surface) heating. Firstly, errors in experimental procedure must be eliminated as a possible cause. The data shown here are from the third such investigation of microwave heating of silver iodide. All experiments used a fresh AgI sample and show the same depression in the transition temperature. This data set, though, has significantly greater temperature resolution, making it possible to define the transition temperature more accurately. Temperature measurement is another possible source of error. Though the fluoroptic thermometer is itself accurate, thought must be given to whether the temperature being reported is representative of the sample as a whole. This is a difficult question, particularly as regarding a sample with high surface area, such as a powder. Studies have shown that microwave field intensity is concentrated at surfaces, defects, and other micro-structural features.[6, 51] It is therefore difficult to predict details of the field pattern within the sample. However, it is not known if this will be a significant effect across the width of the sample (small relative to the radiation wavelength). Heat will be rapidly spread by conduction so that any temperature gradients are minimised. Generally then, temperature equilibration occurs sufficiently rapidly in such a small sample that any inhomogeneities in the electric field are inconsequential.

Furthermore, if a large (~50 K) temperature gradient did exist within the sample, then the X-ray diffraction results (which are averaged over the whole sample) would be expected to show the persistence of the β-AgI phase up to at least 412K (transition temperature observed for conventional heating). They do not. Therefore, though 'hot-spots' may be possible within the sample, their effect would be averaged out by the nature of the measurement. The measured temperature may therefore deviate from the average sample temperature, but by an amount less than the quoted error in the phase transition temperature, that is 10 K. Furthermore, if high temperature gradients do exist then, imagining the worst-case scenario, the measured temperature would correspond to the coldest part of the sample. Yet at 380 K, Figure 5.7 shows that the sample as a whole retains none of the β-AgI phase. Thus, despite ambiguity in the recorded temperature it can be conclusively stated that the phase change goes at a significantly lower temperature under microwave heating. Hence, the cause of the change in transition temperature is very likely to be a real physical phenomenon rather than an artefact of the experimental design.

In order to interpret the result it is necessary to consider exactly how microwave heating works. Its nature is very different to conventional modes of heating. Normally heat is provided through convection, conduction or radiative processes. The energy comes as a broad spectrum, chiefly in the infrared region, and a broad range of vibrational modes is excited, according to the Bose-Einstein distribution. With microwave radiation, energy is supplied with a specific frequency. The frequency does not correspond to a particular phonon mode of a solid, these having typical frequencies in the terahertz region, but interacts via a multi-phonon process to activate a small number of phonon modes, e.g.

$$\omega_{field} = \omega_{phonon_1} - \omega_{phonon_2} \tag{5.1}$$

Energy is redistributed over the phonon density of states via phonon-phonon coupling, which is a consequence of anharmonicity in the crystal. The speed of redistribution depends on how dense the phonon states are and the degree of coupling between phonons.

The phonon density of states has been calculated by Bührer and Brüesch for the wurtzite-type phase of silver iodide, and has been shown to be in good agreement with experimental results.[83] Their calculated phonon dispersion curves (taken from the 1978 paper) are shown in Figure 5.10.

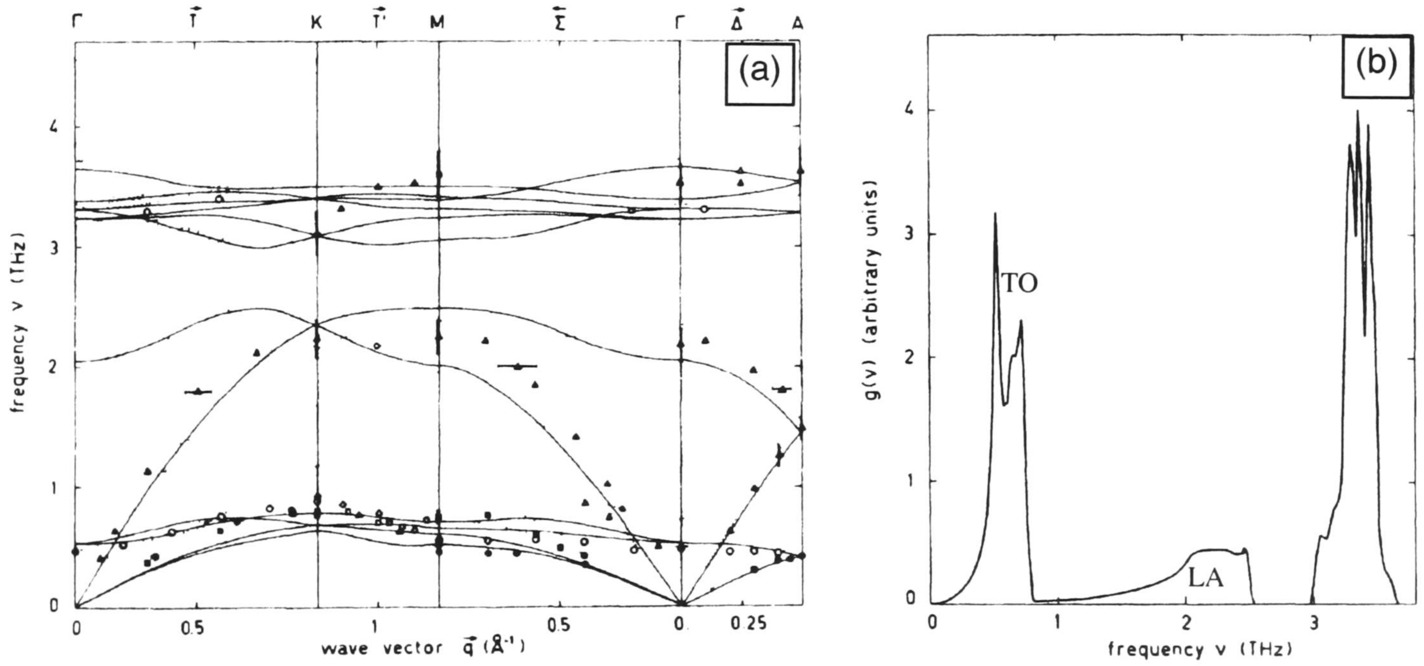

Figure 5.10 – (a) Calculated phonon dispersion curves for β-AgI. Dotted lines: rigid-ion model; solid lines: valence-shell model. (b) Frequency distribution for phonons calculated with the valence-shell model.[83]

Figure 5.10a shows that the phonon spectrum is dominated by strong anharmonic effects (many nodes at which the phonons couple), characteristic of all silver halides.[83] β-AgI has several low-lying transverse optic (TO) modes which behave as largely decoupled from the remainder of the phonon spectrum. It is these modes that give the major contribution to the thermal motion because they have a high density of states (Figure 5.10b) and are easily thermally activated due to the low energy of around 500 MHz. In terms of microwave heating, this low-lying band of closely related TO modes should allow facile multi-phonon interactions with the microwave field. Furthermore, owing to the large separation between TO and higher frequency bands it may prove a more difficult process to redistribute this energy quickly. This may result in a non-classical distribution of energies within the phonon spectrum. Another important point is that the silver ion performs most of the movement in these low-energy modes. Though lighter, the silver atom is smaller and it is this movement that leads to the formation of Frenkel defects in the structure and allows ionic conduction of the silver ions to take place.[83]

The nature of the β-α phase change in silver iodide has been studied in some depth.[83, 105-109] Bührer and Brüesch[83] postulate that the phase change is driven by entropy (an order-disorder transition). In the β-AgI phase, Frenkel defects are formed thermally, the ionic conductivity is therefore a function of temperature. However, as the defect concentration increases with temperature, restorative forces oppose the formation of more defects, limiting the increase in entropy. Transformation into the α-AgI phase results in many more vacant sites and a statistical distribution of silver ions across them.

However, Yoshiasa and co-workers propose that the aforementioned low-lying TO mode is responsible not only for large Ag ion movements, but also for small I ion displacements which lead directly into the phase transformation (displacive).[108] As was previously stated, the silver iodide system is highly anharmonic. Anharmonicities in atom vibrations increase as the temperature approaches the phase transition. The low energy TO modes are primarily bending modes, with apical Ag-I bond angles changing significantly. This movement is accompanied by small changes in the apical Ag-I bond length, see Figure 5.11.

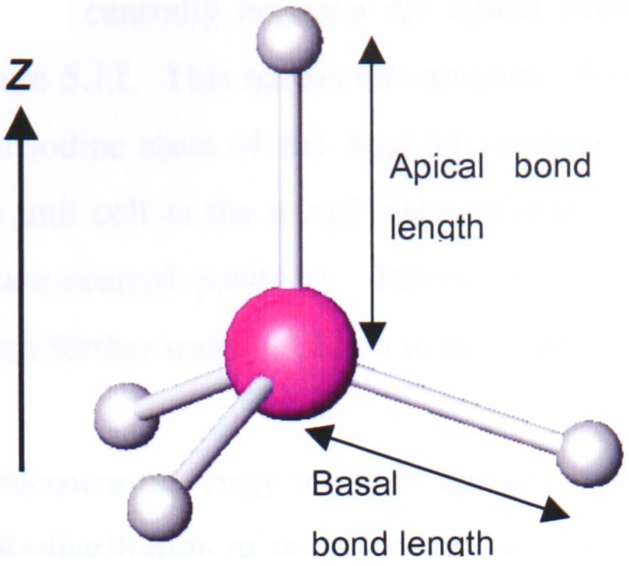

Figure 5.11 - Ag_4I tetrahedron showing apical bond (parallel with z-axis) and three basal bonds (nearly perpendicular with z-axis).

At temperatures significantly lower than the phase transition, the apical Ag-I bond is observed to be longer than the ideal structure would suggest, owing to a large covalent component in the bonding. This bond length becomes equal to the basal bond-lengths on heating and as the phase transition is approached the apical Ag-I distance becomes shorter whilst the three basal Ag-I distances become slightly larger.

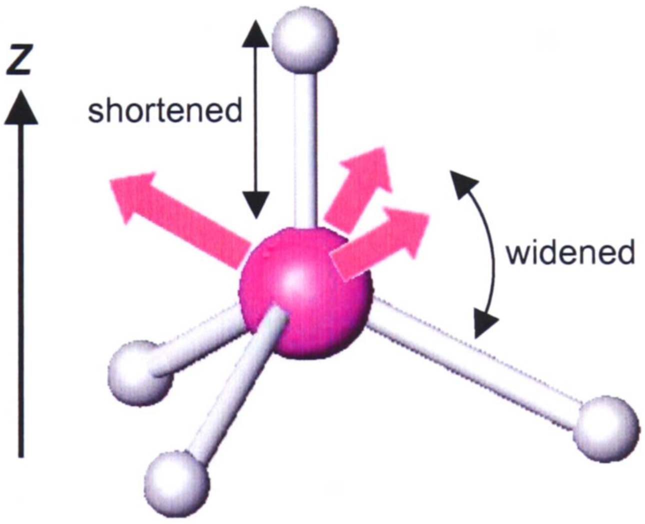

Figure 5.12 - Ag_4I tetrahedron, showing deformation of β-AgI phase as temperature approaches 413 K. Arrows show increased vibration of iodine atom in the anti-bonding directions.

This structure change can be explained by anharmonicity in the atomic thermal vibrations, especially for the iodine atom, as demonstrated by Yoshiasa.[108] As the anharmonic effect increases, it is observed that the magnitudes of iodine displacement are greater in three of the anti-bonding directions (i.e. centrally between the apical bond and any two of the basal bonds), as shown in Figure 5.12. This makes the structure closer to the *bcc* arrangement of α-AgI, where the central iodine atom of the Ag_4I tetrahedron in the β-AgI phase takes the role at the corner of the unit cell in the α-AgI phase (Figure 5.4(a)), whilst the three basal silver atoms takes up face-centred positions. Hence, the increase in anharmonic thermal motion is consistent with a further transformation to the superionic α-phase.

The hypothesis is that microwave energy interacts directly with low-lying TO modes via a multi-phonon process. Redistribution of this energy is slow with respect to the rate at which energy goes into the system from the microwave field and a non-classical distribution of internal energies is the result. The phase transition occurs when enough energy is in the relevant mode to promote the structural change (be that through the creation of sufficient interstitial Ag ions, or through displacement of I ions). However, the average internal energy in the system is lower than at the equivalent point during conventional heating. Hence, the temperature measured is lower. Further work is necessary in order to test this theory. Individual atomic displacement parameters (ADPs) would be particularly useful. This level of accuracy, however, is beyond the scope of this technique.

6 β"-Alumina

Having had some success studying silver iodide, an archetypal ionic conductor, it was decided to investigate other *superionic* materials for the effects of microwave irradiation. One such material, possessing one of the greatest levels of ionic conductivity at ambient temperatures is the *β*"-alumina family: structural variants of *β*-alumina. For this experiment we were fortunate to be allocated time on a synchrotron source and thus make use of the higher X-ray flux. A similar design of reactor to that used for silver iodide was employed, the differences being described in a section below.

β-alumina, in its ordinary form, is a non-stoichiometric compound with an excess of sodium, corresponding to the formula

$$[\mathrm{Al}_{11}\mathrm{O}_{16}]\text{-}[\mathrm{O}\text{-}\mathrm{Na}_{(1+x)}]\text{-}\mathrm{O}_{x/2}$$

where x refers to the excess sodium ($0.25 < x < 0.30$). Its structure is hexagonal, with an alternating spinel block (first parentheses) and a loosely bound plane containing the sodium ions. This plane is associated with the low activation energy, two-dimensional diffusion of sodium ions and is the origin of the high ionic conductivity and its temperature dependence. There are two such formula units per unit cell, as shown in Figure 6.1. The sodium ions are distributed over three sites, widely referred to as the Beevers-Ross (BR), anti-Beevers-Ross (aBR), and mid-oxygen (mO) sites,[110] as detailed in Figure 6.2. Surplus electric charge is balanced by extra oxygen ions residing in interstitial mid-oxygen positions and are associated with an adjacent Frenkel defect in the spinel block. A family of similar aluminates is obtained by exchanging the usual sodium ions for another univalent cation (for example, potassium or silver) or by varying the composition.

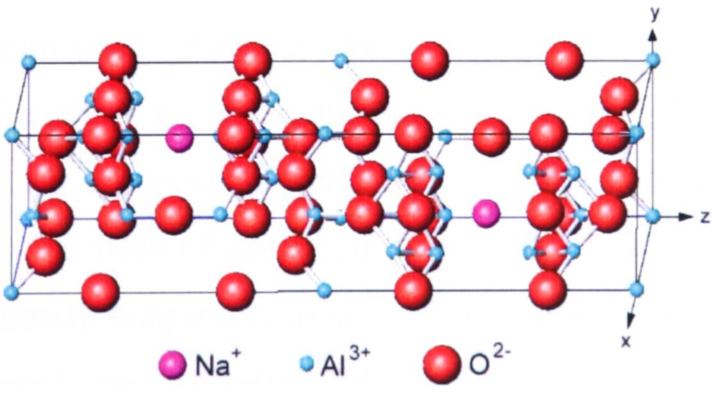

Figure 6.1 - Crystal structure of stoichiometric sodium *β*-alumina. Layers containing sodium ions are clearly visible.

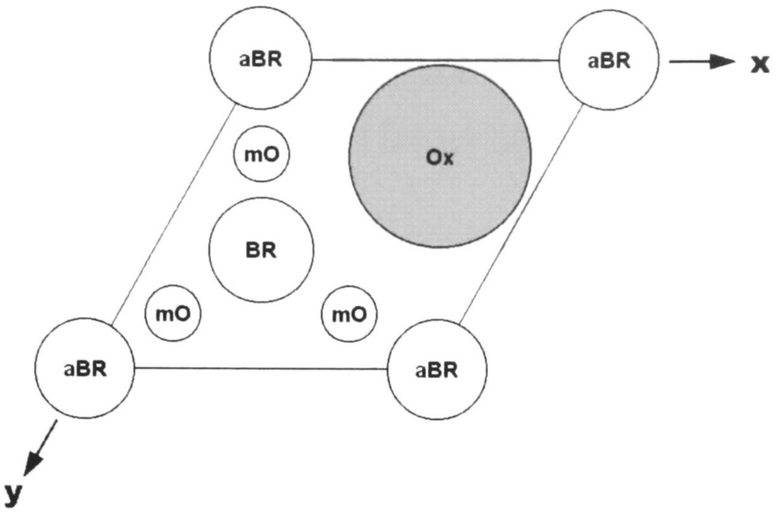

Figure 6.2 - The different sites in the conducting plane: Beevers-Ross (BR), anti-Beevers-Ross (aBR) and mid-oxygen (mO).

For higher conducting ion concentrations, an alternative compensation mechanism can act where the electrical charge is balanced by substitution of Al^{3+} with Mg^{2+} ions. This can be in addition to the usual interstitial oxygen mechanism, or even completely replace it. Such is the case for the commercially used solid electrolyte, the most common example of which is β''-alumina, a rhombohedral variant of the more usual β-structure. The β'' designation was coined by Yamaguchi and Suzuki[111] who reserved the β' designation for another variant of β-alumina which has failed to be observed since. Nonetheless, the term has now been adopted. The structure of sodium β''-alumina is shown in Figure 6.3. The structure again consists of spinel blocks separated by loosely packed layers of sodium and oxygen, but contains three formula units per unit cell. The structural formula is of the type:

$$[Al_{11-y}O_{16}Mg_y]\text{-}[O\text{-}Na_{(1+x+y)}]\text{-}O_{x/2}$$

where x refers to the excess conducting ions compensated by interstitial oxygens, and y those compensated by magnesium ions. Towards the upper limits of sodium ion concentration these values are found to be $x \approx 0$, $y \approx 1.7$ compared with the upper limit of $x \approx 1.3$ for the β-polymorph. The fact that the compensation mechanism is dominated by the substitution of aluminium by magnesium has been of great help in structural studies where the mechanism of ionic conductivity is greatly simplified, as the BR and aBR sites in β-alumina, on which the sodium ions are located, are crystallographically equivalent in β''-alumina. Another important difference is that the conducting ions are not strictly planar in β''-alumina and instead form a 'conduction slab' of finite width. It should be noted that the β and β'' variants co-exist by syntaxy, though the material can be made significantly richer in one phase over the other. During synthesis, excess sodium will favour the β'' variant.

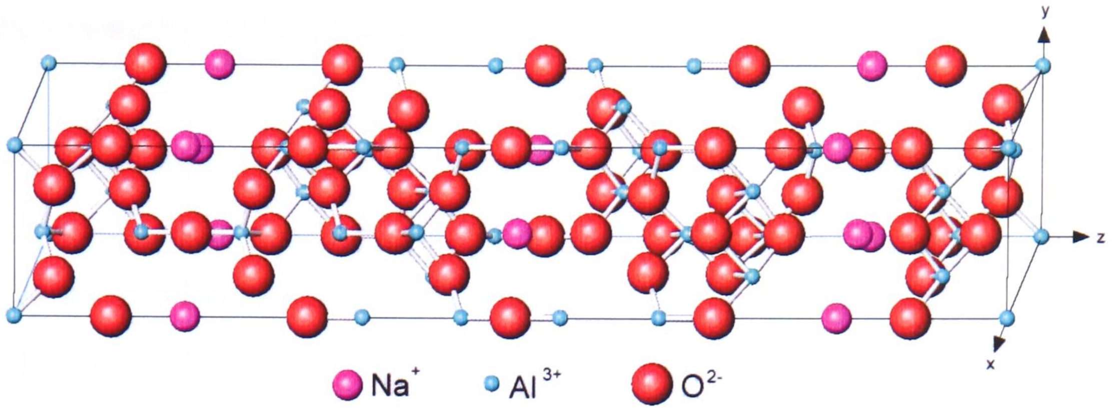

Figure 6.3 - Crystal structure of sodium β''-alumina. Structure incorporates extra sodium ions in the layers between spinel blocks.

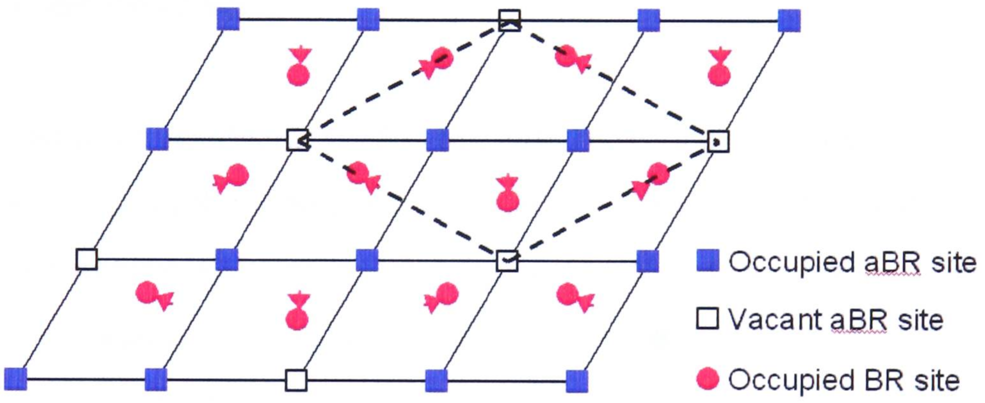

Figure 6.4 - Ordering of the vacant sites in the conducting plane of β"-alumina. The solid line is average unit cell, dotted line is 2-D supercell and arrows show the displacement of Na ions from ideal positions to form clusters around vacant aBR sites.

For this study, sodium β''-alumina and silver β''-alumina were used, as accurate structure determinations exist for both and they exhibit some intriguing deviations from the idealised structure. Boilot and co-workers[110, 112, 113] have undertaken a number of structural studies on these and related β''-alumina compounds (and it is their models on which later Rietveld refinements are based). They have shown for most β''-aluminas, including sodium β''-alumina (β''_{Na}) that the conducting ion distribution comprises a two-dimensional, hexagonal supercell (Figure 6.4) and that there is consequently an additional conducting ion site located near a mid-oxygen position, see Figure 6.2. Modelling of this site significantly improves the fit of the model to the data.

Boilot also showed that there is a general correlation across the β"-aluminas between three properties of the material:

(i) the coherence length ($\xi_{||}$): a measure of ion-ion correlation in the conducting plane,
(ii) the thickness of the conduction slab (E), and
(iii) the resistivity of the material (ρ).

That is, as E increases, $\xi_{||}$ and ρ will increase and the ionic conductivity ($\sigma = 1/\rho$) will decrease. However, β''_{Ag}-alumina seems to be an exception in the β"-alumina family. Modelling of an additional silver ion position is not beneficial to the structure refinement process. Moreover, despite having amongst the smallest conduction slab thickness across the series (0.19 Å compared with 0.39 Å for β''_{Na}), and the shortest coherence length (~10 Å compared with ~70 Å for β''_{Na}), β''_{Ag} has much higher resistivity than the rest of the series. Boilot[112] puts this down to three-dimensional, inter-planar ion-ion correlation owing to the covalent character of the Ag-O bond.

With well documented ionic conductivity, β"-aluminas seem a good prospect for study. This experiment, therefore, is to probe whether microwave irradiation will enhance the mobility of the ions in the conduction slab, using powder X-ray diffraction. β''_{Na} is typical of the family, but disordered sodium ion positions may prohibit satisfactory refinement. β"Ag, on the other hand, has a more ordered structure and will probably give a better fit, but has poor ionic conductivity and may not show the phenomenon. Hopefully these compounds will give clearer results than silver iodide. Rather than a sudden onset of conductivity when the phase moves from a low temperature crystalline state to a high temperature conducting sublattice liquid (as in the case of AgI), the β"-aluminas have a continuous increase in properties across a broad temperature range.

6.1 Applicator Design

The measurement was performed on Station 9.1 at the Synchrotron Radiation Source (SRS), Daresbury Laboratory. Station 9.1 houses a general-purpose powder X-ray diffraction facility, which was set up for flat-plate, powder sample geometry. The beam passes through a water-cooled aperture (to reduce beam size) and then through a silicon [111] channel-cut monochromator. This was used to produce a monochromatic X-ray beam of wavelength 1.000 Å. The beam then travels through an adjustable aperture that controls the size of the beam at the sample. A small (0.09%) λ/3 harmonic also exists in the beam, but should not significantly interfere with measurements. The radiation source is a 5 Tesla wiggler, situated 15m from the monochromator. The instrument itself is a vertically scattering diffractometer as shown in Figure 6.5. The sample plate axis was set to a fixed angle, ω, of 5.00°. The instrument has high sensitivity and angular resolution (up to 0.001°) and a well-defined peak-profile. Diffraction patterns were recorded between 11° and 50° in 2*θ*, with a resolution of 0.01° (approximately equivalent to a d-spacing range of 1.20 to 5.20 Å).

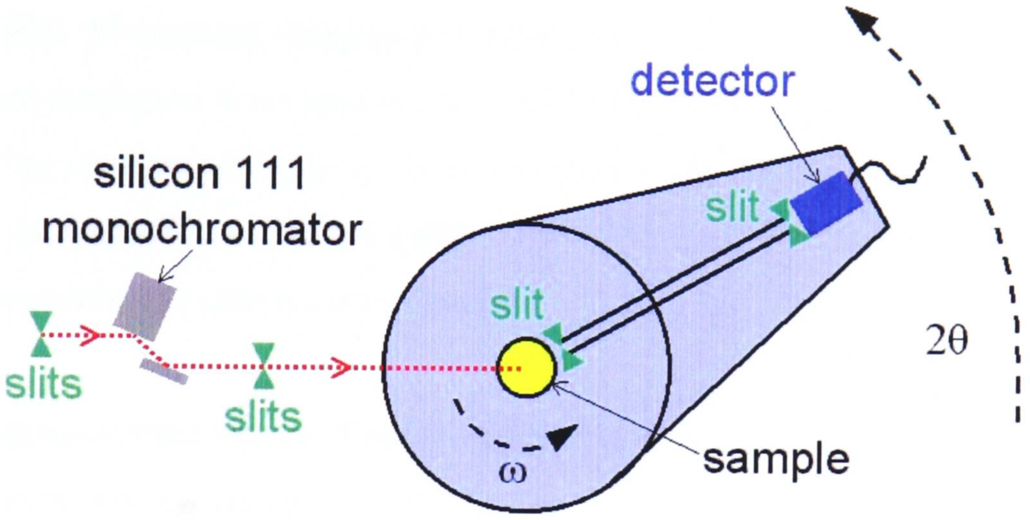

Figure 6.5 - Station 9.1 at the SRS, showing the powder diffractometer and 2*θ* detector.

Microwave heating was performed using a similar design to that used for silver iodide. The applicator is shown in Figure 6.6. It has an internal diameter of 103 mm and a length of 120 – 160 mm, varied by the use of a moveable short-circuit. A slot was cut across the applicator to allow the passage of X-rays. This was covered with aluminium foil during microwave heating to present a continuous, conducting surface. The sample was placed as loose powder onto an insulating, ceramic post (Macor) at the centre of the applicator and aligned with the foil window and the incident X-rays. Microwaves were introduced into the heating chamber via an antenna of length 34 mm (immediately below the sample, see Figure 6.6), and connected through a 2 metre, copper-based, flexible coaxial cable (maximum rating 200 W) to an externally controlled microwave source (commercial 0 – 1 kW variable power, ASTeX 5-1000 operating at a frequency of 2.45 GHz).

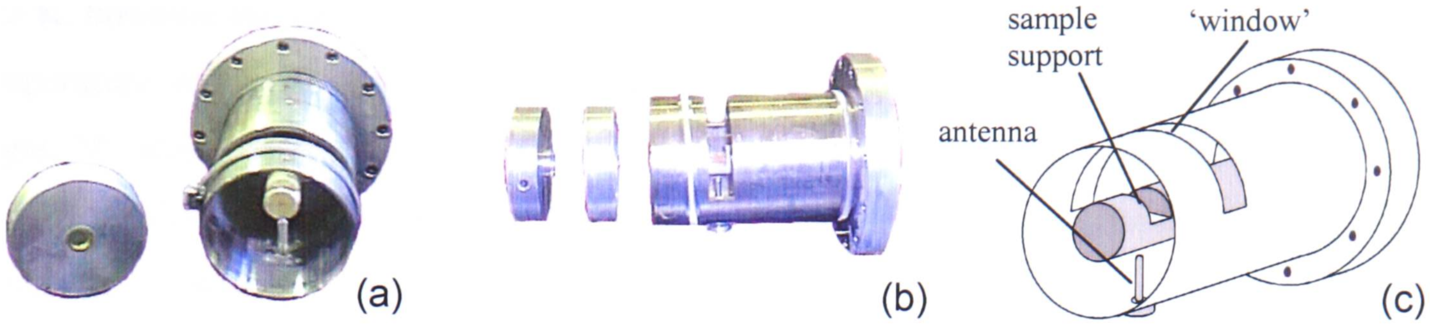

Figure 6.6 - Apparatus for use with station 9.1 at the SRS, shown end-on (a), side-on (b) and schematic (c).

6.2 Experimental

Samples of silver β''-alumina (magnesium stabilised) and sodium β''-alumina (magnesium stabilised) were purchased from Ionotec Inc. These samples are commercial grade and have 95% purity. The remaining 5% is the silver or sodium β-alumina polymorph, respectively. Samples were heated either by conventional means (a hot air gun clamped in position) or by combined microwave and conventional heating.

Temperature measurement was performed using a fibre-optic thermometer (Nortech Fibronic NoEMI-TS series, with precision of 0.1 K) in contact with the sample. The thermometer had been previously calibrated by a co-worker (A. G. Whittaker). The temperature was sent to a PC, which controlled the power output and could be used to automatically maintain a steady sample temperature by adjusting the power between 0 and 200 W throughout. The volume of the applicator is much greater than the previous design (used with silver iodide), therefore in order to minimise the heated space and maximise the efficiency of heating, the empty space was filled with glass-wool insulation (transparent to microwaves). Nonetheless, it was found to be necessary to provide additional heating to the sample with the hot air gun (via a length of copper tubing) in order to reach the required temperature range.

6.3 Results

For each sample two experimental runs were performed, one with microwaves and one without microwaves. The temperature was kept the same in both cases: 456 K for silver β''-alumina and 523 K for sodium β''-alumina. The target temperature for both samples was

523 K, however the silver β"-alumina sample heated less well with microwaves and a lower temperature was used instead. Histograms were recorded as diffraction intensity against angle, 2θ. Refinements were performed using the Rietveld method, on a desktop PC running the GSAS (Generalised Structure Analysis System) suite of programs,[92] with EXPGUI (MS Windows compatible interface).[93]

A typical synchrotron instrument parameter file is supplied with GSAS and this was used when refining the data. The form of instrument parameters is much the same as for a copper K_α source with some minor differences. Firstly, only one radiation wavelength was used and the value was not associated with any element's *K*-edge. A polarisation term was necessary to account for the fact that synchrotron radiation is generally polarised. Finally, the profile function was a simpler version of the multi-term Simpson's rule integration employed previously. Asymmetry and sample shift terms can be assumed to be zero, owing to the superior optics and calibration of the instrument and sample stage. In practise, Lorentzian broadening terms could also be ignored, as their effect was negligible.

The same refinement procedure was followed for all data. The model was firstly fitted to the β"-alumina structure, with refined cell parameters, atom positions and isotropic ADPs. Six parameters were used in the background function, a cosine Fourier series. The next layer of complexity was introduced by adding the β-alumina structure (isotropic ADPs) at approximately 5%. The number of background parameters was increased to 12 and the model fitted. Atomic displacement factors for the β"-alumina phase were made anisotropic and the number of background parameters increased to 24. Finally, the fractional occupancy of the mobile ion sites and the profile function were allowed to refine. Structure refinements for β"-alumina and β"-alumina are in Sections 6.3.1 and 6.3.2, respectively.

For the two measurements made on the same sample, the chemical composition and profile function coefficients should be the same. Therefore, these values (which were very similar anyway) were reset to their calculated mean values, thus facilitating more meaningful comparison between conventional and microwave heating. It was noted that structural and thermal parameters for the conducting ions were highly correlated in all the refinements. Therefore, these parameters were fitted in an alternating fashion until the final stages of the fitting process. Furthermore, the aluminium and magnesium ions that share the same site had highly correlated parameters and were therefore restricted to the same values of position and ADP. In the final refinement, all structure parameters, except for the chemical composition and profile function, were allowed to refine and a minimum χ^2 was reached. Following this method reduced the probability of finding of false minima during refinement.

6.3.1 Sodium β"-alumina

The structural model for β''_{Na}-alumina used in the refinement was that proposed by Boilot and co-workers[110] (space group $R\bar{3}m$). The structure of the minority β_{Na}-alumina phase was that proposed by England and co-workers,[114] (space group $P6_3/mmc$). Note that this is the structure of the ion-rich, non-stoichiometric β-alumina and has two sodium ion positions in the conducting plane.

The refinement of sodium β''-alumina met a snag immediately as there appeared to be 'extra' lines in the diffraction pattern. These lines did not correspond to any of the reflections for β''_{Na} or β_{Na}. There were two realistic possibilities:

(i) The extra lines were due to some impurity, the sample holder, the cell or some other effect peculiar to the instrument.

(ii) The extra lines were due to a structural distortion, not allowed for by the space group being used. If this were the case, a different space group would need to be used.

Examining the histogram shows that there are at least five discrepancies between the data and the model. These are highlighted in Figure 6.7 and Table 6-1.

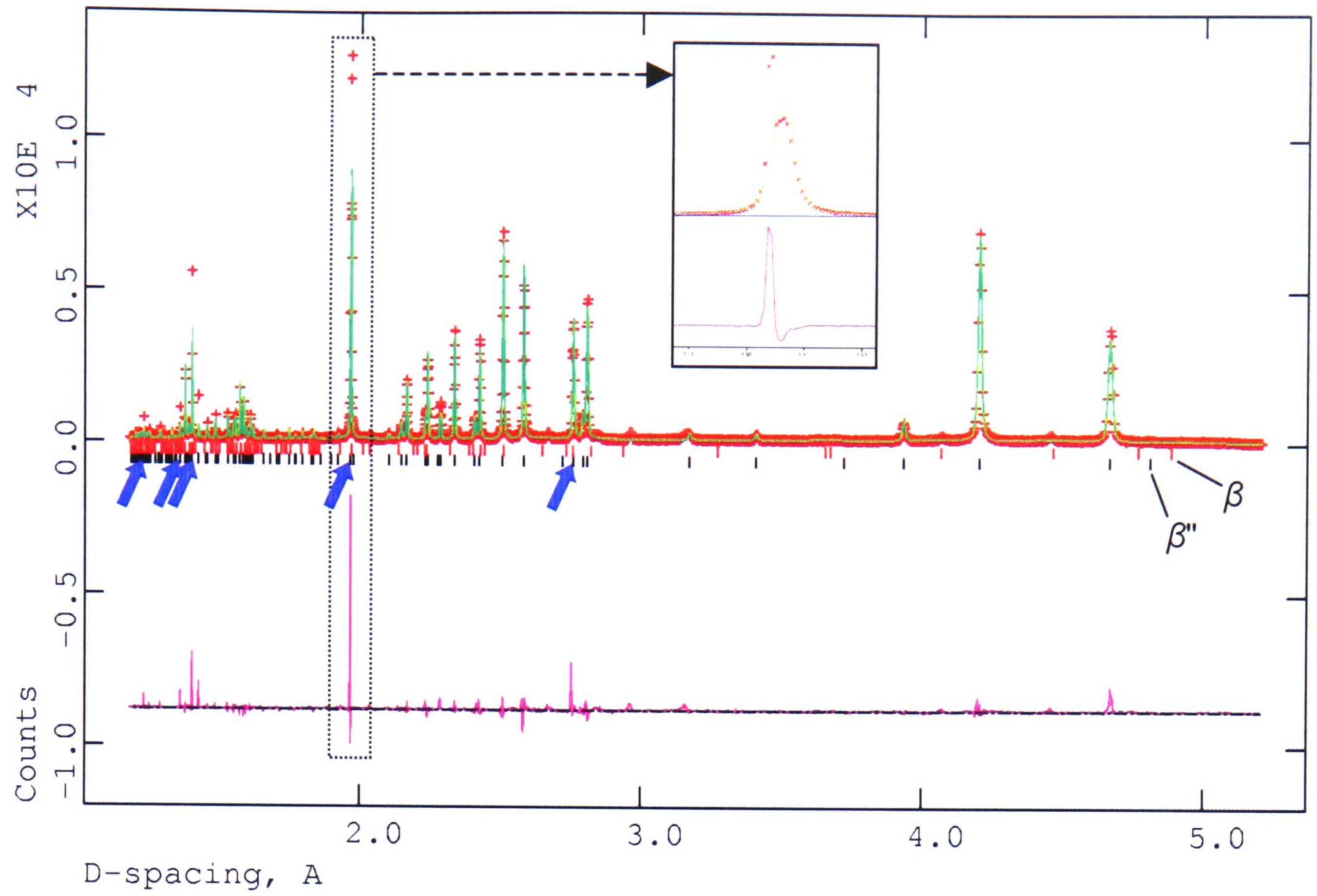

Figure 6.7 - Histogram for β''_{Na}-alumina (no microwaves, 523 K). Upper part of the diagram shows the collected data (crosses) and the fitted structural model (line through the points). Tick marks showing reflections for β''_{Na} and minority phase, β_{Na} are shown. The lower part shows the difference between the data and the fitted model. Arrows indicate anomalous reflections. The box shows the [*2 0* $\overline{10}$] reflection and extra peak in more detail.

Table 6-1 - Discrepancies between data and model for sodium β''-alumina.

d-SPACING / Å	2θ / °	CLOSEST REFLECTION FOR β''_{NA}
1.232	47.88	[*3 1 11*]
1.361	43.09	[*2 2 6*]
1.402	41.78	[*2 2 0*]
1.966	29.48	[*2 0* $\overline{10}$]
2.756	20.89	[*1 0 10*]

Though the extra peaks next to the [*1 0 10*] and [*2 0* $\overline{10}$] reflections are significantly more intense than the others, there appears to be no relation between the anomalous peaks and the Miller indices of the closest β''_{Na} reflection. Fortunately, access to another diffraction instrument, the HRPD station at ISIS (Rutherford Appleton Laboratory), was scheduled for shortly after this measurement and the opportunity was taken to compare this high-resolution

X-ray diffraction measurement with a high-resolution neutron diffraction measurement. Complete details of this experiment are given in Chapter 7. The information presented here is sufficient to allow comparison with the synchrotron X-ray diffraction data.

A sample of β''_{Na}-alumina, from the same source, was heated to 473 K in a Vanadium can using a conventional furnace. A parallel beam of neutrons was used to perform the diffraction measurement. The resulting time-of-flight (TOF) diffraction pattern was recorded on a bank of back-scatter detectors. Histograms were recorded between 30 and 120 ms (approximately equivalent to a d-spacing range of 0.70 to 2.45Å). Measurements from this instrument cover a narrower range of d-spacing than station 9.1, but are of very high-resolution. Refinement was performed using GSAS[92] and EXPGUI,[93] as with the synchrotron data with the exception that the peak profile function is much more rigorously defined for HRPD and is therefore not open to refinement to the same degree. Further details of the HRPD instrument, peak profile and refinement can be found in Chapter 7. The final structural model is shown in Table 6-2, whilst the fit of the structural model to the measured diffraction pattern is shown in Figure 6.8.

Table 6-2 - β''_{Na}-alumina at 473 K, by neutron diffraction (HRPD): including positional and thermal parameters and fractional occupancy. a = 5.61727(13)Å, c = 33.5113(9)Å. χ^2 = 1.272, R_p = 0.0464, R_{wp} = 0.0574

NAME	POSITIONAL PARAMETERS			ANISOTROPIC DISPLACEMENT PARAMETERS ×100/Å²						FRAC
	x	y	z	U^{11}	U^{22}	U^{33}	U^{12}	U^{13}	U^{23}	
Al(1)	0.1601(18)	0.320(4)	0.9293(5)	-0.5(3)	-0.2(5)	5.3(7)	-0.1(3)	-0.6(4)	-1.3(9)	1
Al(2)	0	0	0.3517(9)	1.3(5)	1.3(5)	5.4(17)	-0.6(3)	0	0	0.6725
Mg(1)	0	0	0.3502(9)	1.3(5)	1.3(5)	5.4(17)	-0.6(3)	0	0	0.3275
Al(3)	0	0	0.4506(5)	-0.6(4)	-0.6(4)	-1.6(8)	-0.3(2)	0	0	1
Al(4)	0	0	0	-1.7(8)	-1.7(8)	12(4)	-0.8(4)	0	0	1
O(1)	0.1629(14)	0.3258(28)	0.2343(3)	-0.1(2)	0.4(4)	2.8(4)	0.2(2)	0.2(2)	0.4(4)	1
O(2)	0.1597(11)	0.3194(23)	0.0348(2)	1.3(3)	2.4(6)	0.3(4)	1.2(3)	-0.6(3)	-1.2(5)	1
O(3)	0	0	0.0985(5)	1.8(5)	1.8(5)	1.8(10)	0.9(2)	0	0	1
O(4)	0	0	0.2950(4)	0.1(5)	0.1(5)	-0.4(7)	0.0(2)	0	0	1
O(5)	0	0	0.5	4.1(9)	4.1(9)	0.3(13)	2.1(5)	0.00	0.00	1
Na(1)	0	0	0.7973(27)	15(7)	15(7)	1.1(47)	7.3(33)	0.00	0.00	0.3400
Na(2)	-0.014(33)	-0.03(7)	0.8303(20)	27(10)	80(49)	-5.0(27)	40(25)	5(6)	10(12)	0.1616

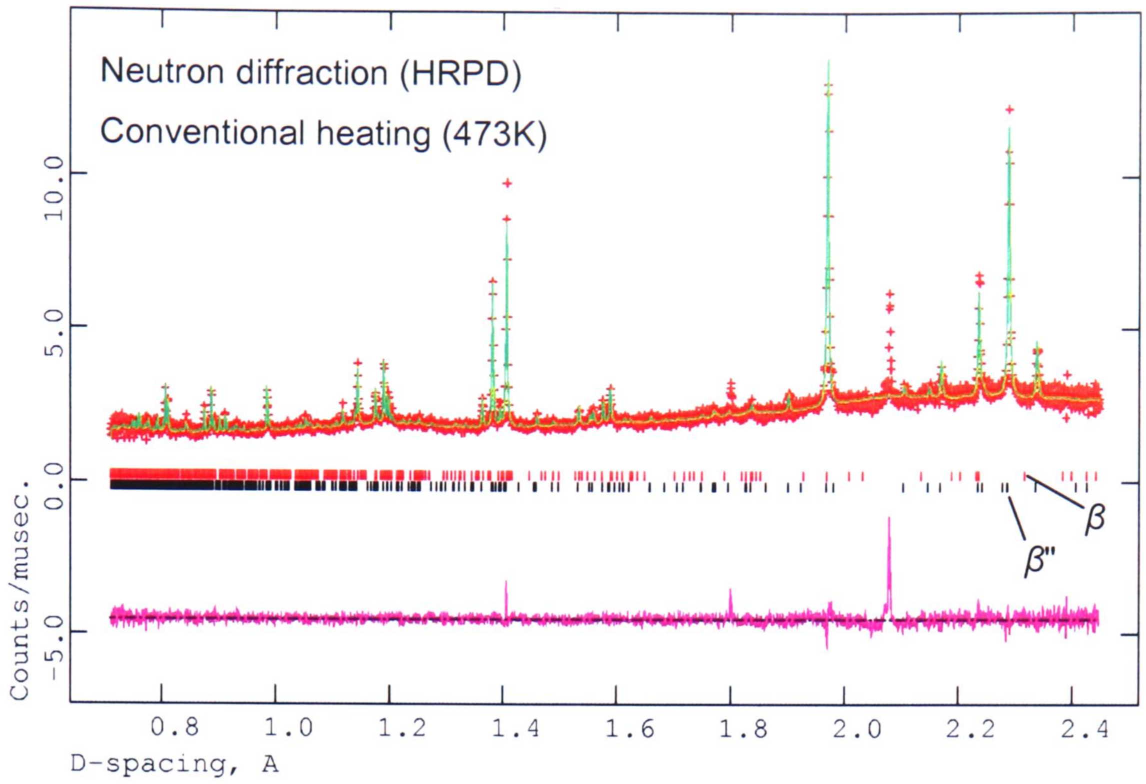

Figure 6.8 - Histogram for β''_{Na}-alumina (neutron diffraction, 473 K). Upper part of the diagram shows the collected data (crosses) and the fitted structural model (line through the points). Tick marks showing reflections for β''_{Na} and minority phase, β_{Na} are shown. The lower part shows the difference between the data and the fitted model.

Examination of Figure 6.8 reveals that the anomalous peak-splitting and extraneous shoulders shown in Figure 6.7 are absent in the neutron diffraction pattern. As the resolution of the HRPD instrument is at least equal to that of station 9.1, it seems safe to assume that the effect, if it were real, would be detected by neutron diffraction also. It is therefore assumed from now on that these extra peaks are artefacts of the experiment and data referring to them will be excised from the refinements. Two peaks remain in the pattern taken at HRPD (1.80Å and 2.08Å) and are not accounted for by the structural model. These are in reasonable agreement with the accepted values for Vanadium (in the sample container) and are disregarded.

Returning to the measurements performed at station 9.1 and having excluded the anomalous data from the synchrotron X-ray diffraction refinements, the structural model was found to give a good fit to the data. The only difficulty with the refinement was in fitting the fractional occupancy of the mobile ion sites. The model seemed quite insensitive to the value, and therefore the value arrived at by Boilot was used and fixed in value. The phase composition was therefore:

$[Al_{10.345}O_{16}Mg_{0.615}]\text{-}[O\text{-}Na_{1.795}]$

Summaries of the structural models, for both conventional and microwave/conventional heating, are given in Table 6-3 and Table 6-4, whilst Figure 6.9 and Figure 6.10 show a comparison of the model and the measured diffraction patterns after the final fitting cycle. Complete data for both phases are found in the Appendix (pages A9-A14). Note that GSAS limits ADPs to a maximum value of 0.8Å^2 and this is reflected in some of the data. The proportions of the elements present is in agreement with those supplied by the manufacturer.

Table 6-3 - β''$_{Na}$-alumina at 523 K (conventional heating only), by synchrotron X-ray diffraction: including positional and thermal parameters and fractional occupancy. a = 5.61018(9)Å, c = 33.4767(5)Å. χ^2 = 5.021, R_p = 0.1001, R_{wp} = 0.1381.

NAME	POSITIONAL PARAMETERS			ANISOTROPIC DISPLACEMENT PARAMETERS ×100/Å^2						FRAC
	x	y	z	U^{11}	U^{22}	U^{33}	U^{12}	U^{13}	U^{23}	
Al(1)	0.1666(4)	0.3331(8)	0.92918(7)	4.9(2)	5.9(2)	3.9(2)	3.0(1)	-0.1(1)	-0.2(2)	1
Al(2)	0	0	0.34864(17)	4.7(3)	4.7(3)	8.7(7)	1.1(1)	0	0	0.6725
Mg(1)	0	0	0.34864(17)	4.7(3)	4.7(3)	8.7(7)	1.1(1)	0	0	0.3275
Al(3)	0	0	0.45013(14)	4.0(3)	4.0(3)	4.4(5)	2.0(1)	0	0	1
Al(4)	0	0	0	4.2(3)	4.2(3)	3.9(5)	2.1(2)	0	0	1
O(1)	0.1708(6)	0.3417(13)	0.23476(17)	3.8(3)	2.6(4)	7.8(4)	1.3(2)	-0.8(2)	-1.7(4)	1
O(2)	0.1470(5)	0.2939(11)	0.03491(13)	4.7(3)	6.5(4)	1.7(4)	3.3(2)	1.1(2)	2.2(4)	1
O(3)	0	0	0.09510(24)	7.5(4)	7.5(4)	0.2(7)	3.7(2)	0	0	1
O(4)	0	0	0.29494(27)	1.9(5)	1.9(5)	6.2(8)	0.9(3)	0	0	1
O(5)	0	0	0.5	9.0(8)	9.0(8)	-5.4(8)	4.5(4)	0	0	1
Na(1)	0	0	0.7868(47)	80(14)	80(14)	77(25)	40(7)	0	0	0.3400
Na(2)	0.0606(25)	0.121(5)	0.8292(6)	4.2(16)	24(5)	-2.4(8)	11(3)	3.6(10)	7.3(21)	0.1616

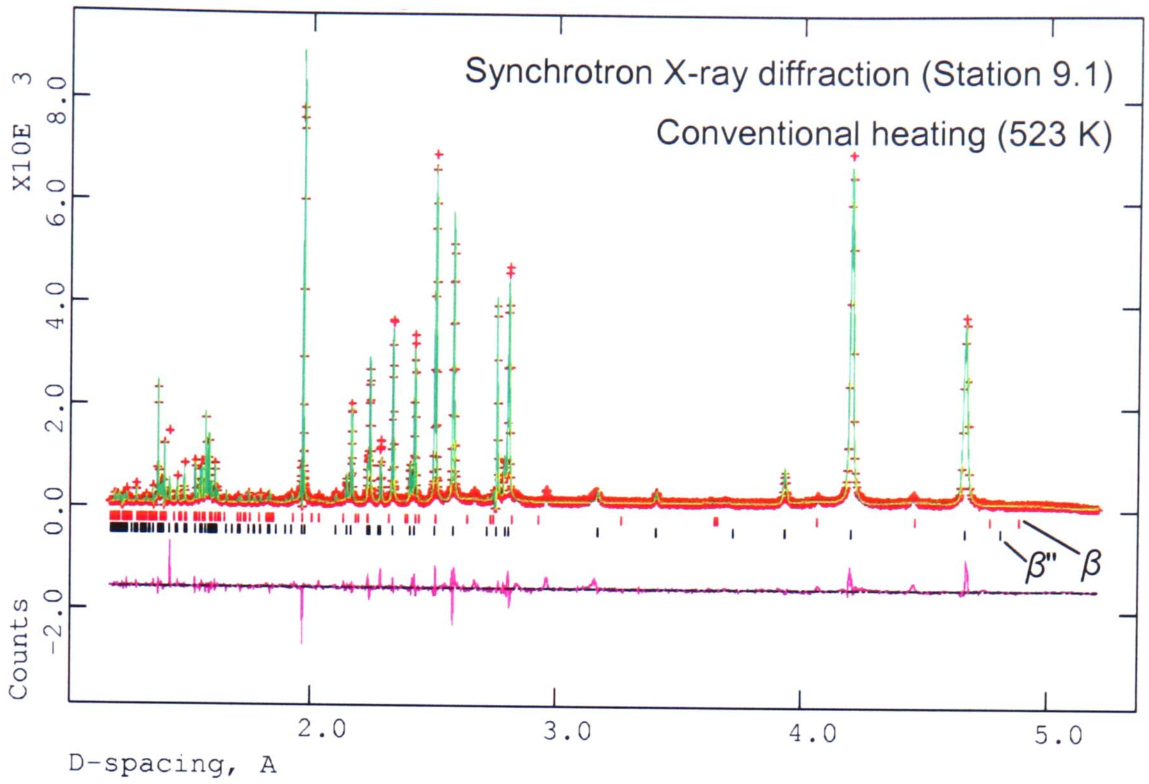

Figure 6.9 - Histogram for β''_{Na}-alumina (synchrotron X-ray diffraction, 523 K by conventional heating only). Upper part of the diagram shows the collected data (crosses) and the fitted structural model (line through the points). Tick marks showing reflections for β''_{Na} and minority phase, β_{Na} are shown. The lower part shows the difference between the data and the fitted model.

Table 6-4 - β''_{Na}-alumina at 523 K (microwave/conventional heating), by synchrotron X-ray diffraction: including positional and thermal parameters and fractional occupancy. a = 5.61029(9)Å, c = 33.4722(6)Å. χ^2 = 4.294, R_p = 0.1036, R_{wp} = 0.1423.

NAME	POSITIONAL PARAMETERS			ANISOTROPIC DISPLACEMENT PARAMETERS $\times 100/\text{Å}^2$						FRAC
	x	y	z	U^{11}	U^{22}	U^{33}	U^{12}	U^{13}	U^{23}	
Al(1)	0.1664(4)	0.3327(8)	0.92905(8)	4.8(2)	5.8(2)	3.6(2)	2.9(1)	-0.1(1)	-0.3(2)	1
Al(2)	0	0	0.34892(18)	4.5(3)	4.5(3)	8.6(7)	1.0(1)	0	0	0.6750
Mg(1)	0	0	0.34892(18)	4.5(3)	4.5(3)	8.6(7)	1.0(1)	0	0	0.3250
Al(3)	0	0	0.45017(14)	4.2(3)	4.2(3)	3.9(5)	2.1(1)	0	0	1
Al(4)	0	0	0.000000	3.6(3)	3.6(3)	4.3(6)	1.8(2)	0	0	1
O(1)	0.1709(7)	0.3417(13)	0.23489(17)	3.9(3)	3.0(4)	7.0(4)	1.5(2)	-1.2(2)	-2.4(4)	1
O(2)	0.1469(6)	0.2938(11)	0.03493(13)	4.6(3)	6.0(4)	1.3(4)	3.0(2)	1.0(2)	2.0(4)	1
O(3)	0	0	0.09487(26)	7.4(4)	7.4(4)	1.1(7)	3.7(2)	0	0	1
O(4)	0	0	0.29496(27)	1.7(5)	1.7(5)	5.6(8)	0.9(3)	0	0	1
O(5)	0	0	0.500000	9.1(8)	9.1(8)	-5.1(9)	4.5(4)	0	0	1
Na(1)	0	0	0.7890(48)	80(14)	80(14)	74(24)	40(7)	0	0	0.3400
Na(2)	0.0614(26)	0.123(5)	0.8291(6)	4.5(17)	23(5)	-3.6(8)	10(3)	2.6(9)	5.2(18)	0.1616

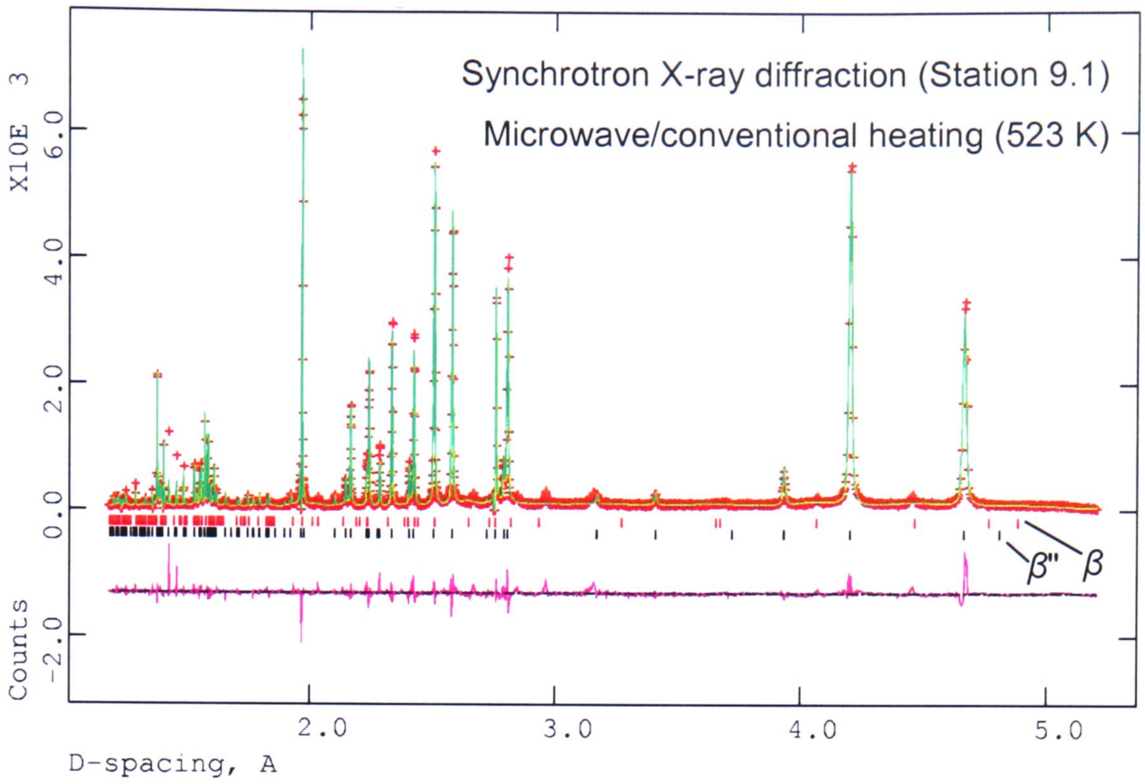

Figure 6.10 - Histogram for β''_{Na}-alumina (synchrotron X-ray diffraction, 523 K by microwave/ conventional heating). Upper part of the diagram shows the collected data (crosses) and the fitted structural model (line through the points). Tick marks showing reflections for β''_{Na} and minority phase, β_{Na} are shown. The lower part shows the difference between the data and the fitted model.

The differences between the two data sets are minimal. Differences in ion mobility should initially be observed in the atomic displacement parameters. These are summarised, for the major components, in Figure 6.11. Differences are limited and are all within one standard deviation (error bar). Therefore, no general trend can be observed for which form of heating gives the larger ADPs. Both sodium atoms show much larger ADPs than the other atoms, as expected for these relatively mobile ions; this is particularly true in the plane of conduction. Any possible difference between the two heating methods is presumably masked by the relative degree of disorder in the sodium ion positions. Perhaps the more localised structure of β''_{Ag}-alumina will show any differences more clearly.

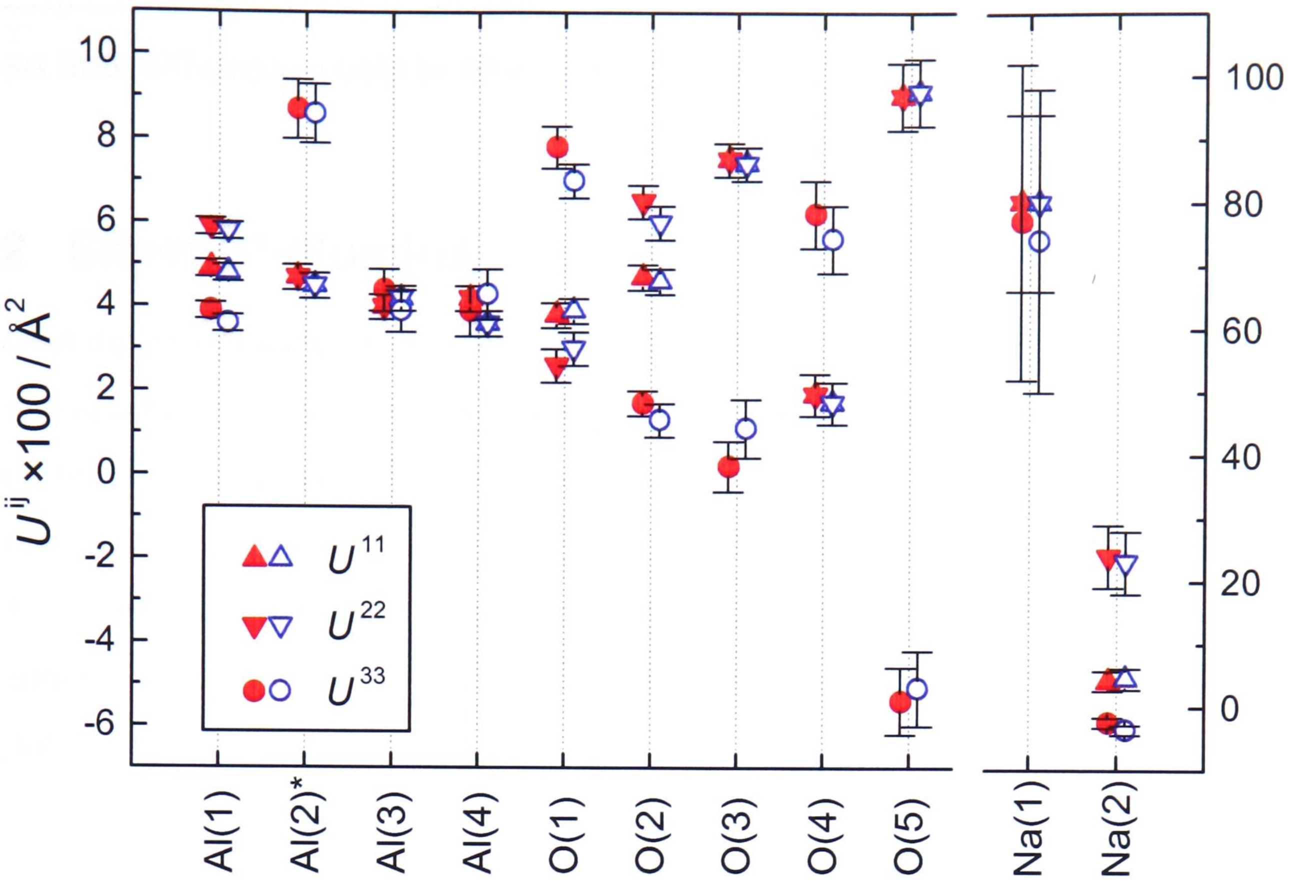

Figure 6.11 - Major atomic displacement parameters for β"$_{Na}$-alumina for both conventional heating (solid) and microwave heating (open). U^{11} and U^{22} are the thermal parameters in the plane of conduction, U^{33} is perpendicular to the plane of conduction. The Al(2)* position is also the Mg(1) position.

The thickness of the conduction slab, E, can be calculated for both heating methods. It is defined for the sodium ions as the deviation in the z positional parameter from the idealised position, as stated in Equation (6.1), where E is the conduction slab thickness (Å), z_{MI} is the z positional parameter of the mobile ions (greatest deviation from ideal) and c is the unit cell edge length (Å).

$$E = |0.8333 - z_{MI}| \times 2c \qquad \textbf{(6.1)}$$

The conduction slab thickness, E, for conventional heating is 3.1Å (±0.3), whilst it is 3.0Å (±0.3) for the microwave-heated sample. The difference between these two values is negligible. There seems to be very little structural difference between these two heating methods. If the material had been affected anomalously by microwave irradiation, it would be expected that conventional heating would show a greater value for E, and hence mobile ions would be less free to move (resistivity, ρ, is proportional to E). Though conductivity measurements have not been performed on this powdered material, the evidence here suggests little difference would be observed between conventional and microwave heating.

6.3.2 Silver β"-alumina

The structural model used for β''_{Ag}-alumina (space group R$\bar{3}$m) was that proposed by Boilot and co-workers.[113] Unlike the sodium analogue, β''_{Ag}-alumina has only one localised position for conducting ions. Furthermore, there appears to be inter-planar correlation in the positions of the silver ions though the spinel blocks. As a result, the conducting ions are more localised and less mobile than found for other β''-alumina materials. A minor phase of β_{Ag}-alumina is also present. The structural model used is that of Roth[115, 116] (space group $P6_3/mmc$).

Exactly the same fitting procedure was used here as for β''_{Na}-alumina. Also as before, several anomalous extra peaks and shoulders were observed. On examination, these appear to be in approximately the same places as they are observed in β''_{Na}-alumina, lending credibility to the theory that these extra features are some artefact of the sample preparation or the cell itself. When these peaks are excised from the data, the models are observed to refine well. The chemical composition of the majority phase was refined without difficulty, owing to the less complex structure here. The phase composition was therefore:

$$[Al_{10.267}O_{16}Mg_{0.733}]\text{-}[O\text{-}Ag_{1.733}]$$

Summaries of the structural models, for both conventional and microwave/conventional heating, are given in Table 6-5 and Table 6-6. Comparisons of measured diffraction patterns and model data for these are shown in Figure 6.12 and Figure 6.13 respectively. Complete data for both phases are found in the Appendix (pages A15-A21).

Table 6-5 - β''_{Ag}-alumina at 456 K (conventional heating only), by synchrotron X-ray diffraction: including positional and thermal parameters and fractional occupancy. a = 5.61351(8) Å, c = 33.3795(6) Å. $\chi^2 = 2.574$, $R_p = 0.0813$, $R_{wp} = 0.1059$.

NAME	POSITIONAL PARAMETERS			ANISOTROPIC DISPLACEMENT PARAMETERS ×100/Å²						FRAC
	x	y	z	U^{11}	U^{22}	U^{33}	U^{12}	U^{13}	U^{23}	
Al(1)	0.1656(6)	0.8344(6)	0.92817(11)	1.3(2)	1.3(2)	3.3(3)	0.6(2)	0.9(1)	-0.9(1)	1
Al(2)	0	0	0.35101(24)	0.5(4)	0.5(4)	6.7(8)	-1.0(2)	0	0	0.633(9)
Mg(1)	0	0	0.35101(24)	0.5(4)	0.5(4)	6.7(8)	-1.0(2)	0	0	0.367(9)
Al(3)	0	0	0.45137(22)	-1.3(4)	-1.3(4)	5.6(6)	-0.6(2)	0	0	1
Al(4)	0	0	0	0.6(5)	0.6(5)	0.6(8)	0.3(2)	0	0	1
O(1)	0.1658(8)	0.8342(8)	0.23524(18)	-1.4(4)	-1.4(4)	3.6(6)	-1.5(4)	0.2(3)	-0.2(3)	1
O(2)	0.1541(8)	0.8459(8)	0.03482(16)	2.9(5)	2.9(5)	-1.3(5)	1.6(5)	-1.3(2)	1.3(2)	1
O(3)	0	0	0.10099(28)	0.6(6)	0.6(6)	-3.6(8)	0.3(3)	0	0	1
O(4)	0	0	0.29801(41)	1.1(9)	1.1(9)	3.6(14)	0.6(5)	0	0	1
O(5)	0	0	0.5	5.5(12)	5.5(12)	-9.0(12)	2.8(6)	0	0	1
Ag(1)	0.021(7)	0.979(7)	0.83087(11)	9.3(9)	9.3(9)	0.4(2)	2.0(13)	1.3(7)	-1.3(7)	0.289(3)

Table 6-6 - β''_{Ag}-alumina at 456 K (microwave/conventional heating), by synchrotron X-ray diffraction: including positional and thermal parameters and fractional occupancy. a = 5.61307(8) Å, c = 33.3754(6) Å. $\chi^2 = 2.406$, $R_p = 0.0855$, $R_{wp} = 0.1121$.

NAME	POSITIONAL PARAMETERS			ANISOTROPIC DISPLACEMENT PARAMETERS ×100/Å²						FRAC
	x	y	z	U^{11}	U^{22}	U^{33}	U^{12}	U^{13}	U^{23}	
Al(1)	0.1585(5)	0.8415(5)	0.92830(11)	1.0(2)	1.0(2)	2.9(3)	0.8(2)	-0.4(2)	0.4(2)	1
Al(2)	0	0	0.34872(26)	-3.3(3)	-3.3(3)	9.5(9)	-2.9(2)	0	0	0.633(9)
Mg(1)	0	0	0.34872(26)	-3.3(3)	-3.3(3)	9.5(9)	-2.9(2)	0	0	0.367(9)
Al(3)	0	0	0.45029(21)	-0.5(4)	-0.5(4)	2.5(6)	-0.2(2)	0	0	1
Al(4)	0	0	0	-1.4(4)	-1.4(4)	7.5(10)	-0.7(2)	0	0	1
O(1)	0.1624(7)	0.8376(7)	0.23541(17)	-3.5(3)	-3.5(3)	3.6(6)	-3.7(3)	0.7(3)	-0.7(3)	1
O(2)	0.1613(7)	0.8387(7)	0.03381(15)	3.8(5)	3.8(5)	-2.6(4)	4.8(5)	1.5(2)	-1.5(2)	1
O(3)	0	0	0.10220(25)	-0.1(6)	-0.1(6)	-6.3(7)	-0.1(3)	0	0	1
O(4)	0	0	0.29434(38)	2.1(9)	2.1(9)	-2.0(10)	1.1(4)	0	0	1
O(5)	0	0	0.5	2.3(10)	2.3(10)	-9.0(11)	1.2(5)	0	0	1
Ag(1)	0.029(5)	0.971(5)	0.83128(10)	10.8(15)	10.8(15)	-0.5(2)	5.6(5)	1.8(5)	-1.8(5)	0.289(3)

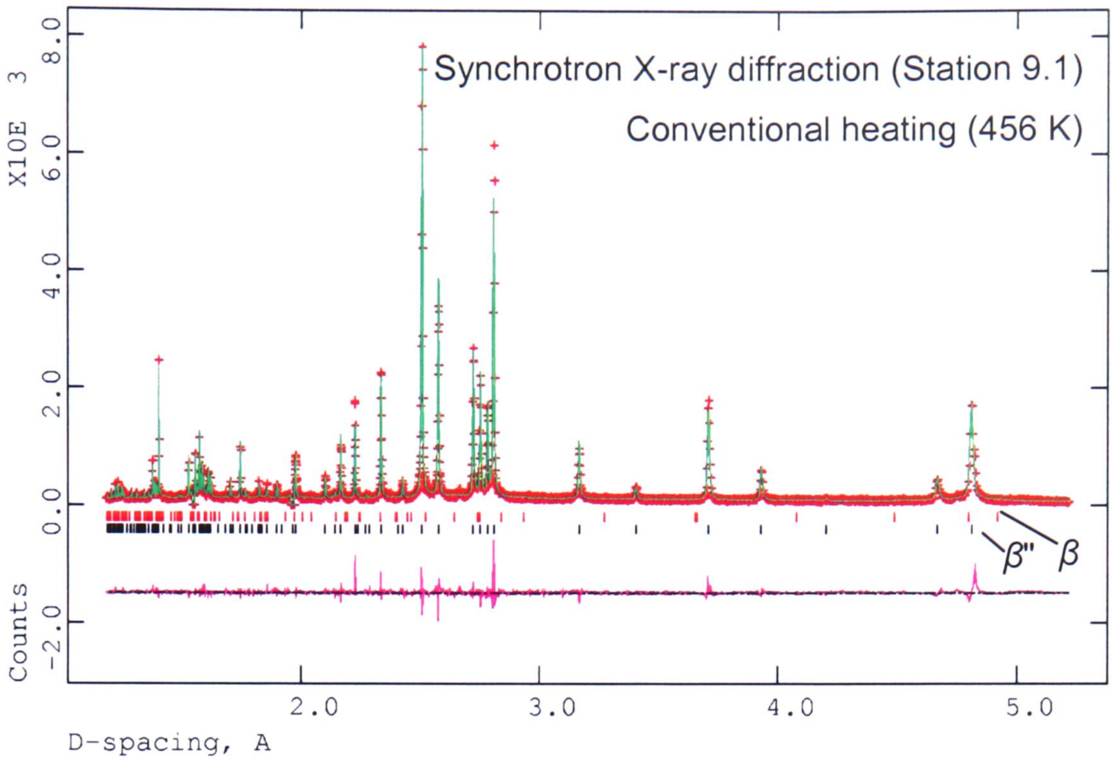

Figure 6.12 - Histogram for β"$_{Ag}$-alumina (synchrotron X-ray diffraction, 456 K by conventional heating only). Upper part of the diagram shows the collected data (crosses) and the fitted structural model (line through the points). Tick marks showing reflections for β"$_{Ag}$ and minority phase, β$_{Ag}$ are shown. The lower part shows the difference between the data and the fitted model.

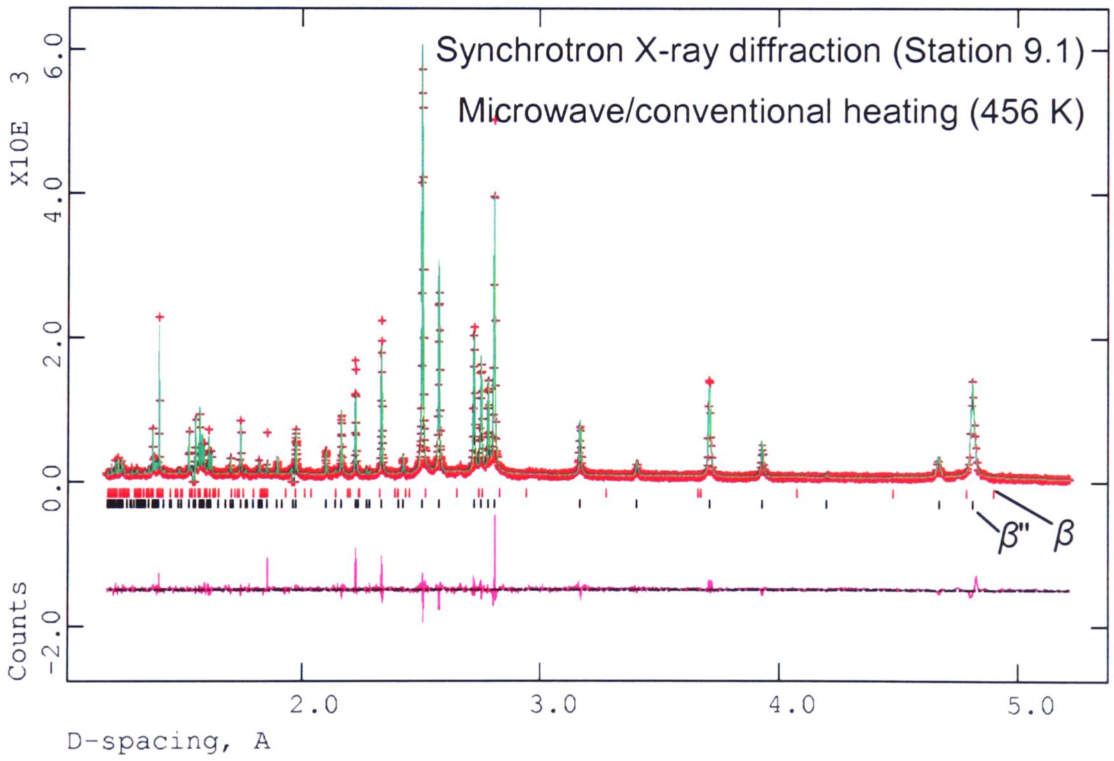

Figure 6.13 - Histogram for β"$_{Ag}$-alumina (synchrotron X-ray diffraction, 456 K by microwave/ conventional heating). Upper part of the diagram shows the collected data (crosses) and the fitted structural model (line through the points). Tick marks showing reflections for β"$_{Ag}$ and minority phase, β$_{Ag}$ are shown. The lower part shows the difference between the data and the fitted model.

Examination of the data in Table 6-5 and Table 6-6 shows little difference between the two forms of heating. This is illustrated graphically in Figure 6.14. Though not all of the atomic displacement parameters are within a single standard deviation (error bars) of each other, there does not appear to be a trend for which form of heating gives the larger value. For the majority of atoms in the spinel blocks, i.e. aluminium, magnesium and oxygen (1-4), the displacements parameters parallel to the plane of conduction (U^{11} and U^{22}) and perpendicular to the plane of conduction (U^{33}) are around the same value. The heaviest of these, the aluminium atoms, are more accurately defined (owing to their larger X-ray scattering cross-section) and tend to show the vibration perpendicular to the plane to be greater, whilst the atoms in the conduction slab, i.e. silver and the bridging oxygen (5) show much larger vibrations in the plane of conduction, as would be expected. It is noted that many of the ADP values are negative: a physical impossibility. This is most likely a result of correlation with the profile function and thus another variable compensates for this effect. Although not physically accurate, comparison of the ADPs is still valid, assuming constant values for the profile function coefficients, as in this case.

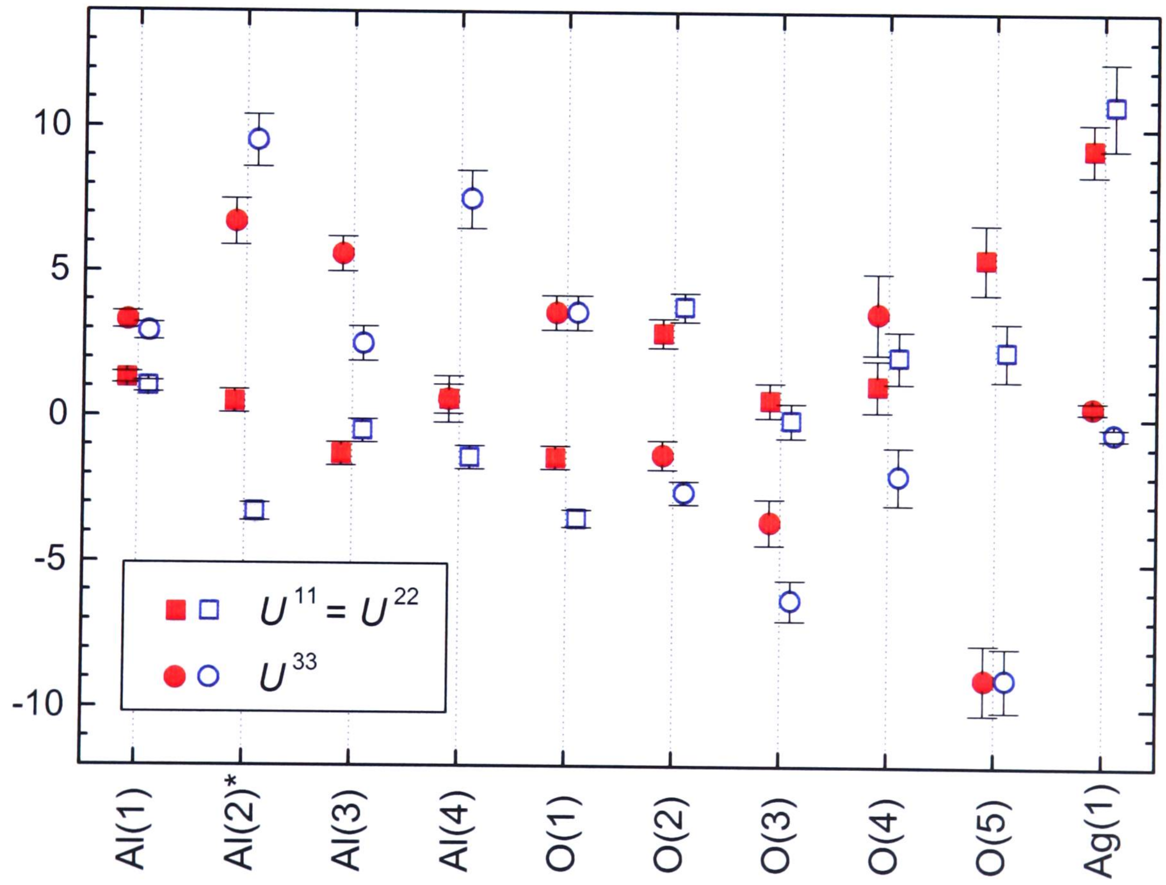

Figure 6.14 - Major atomic displacement parameters for β"$_{Ag}$-alumina for both conventional heating (solid) and microwave heating (open). U^{11} and U^{22} are the thermal parameters in the plane of conduction, U^{33} is perpendicular to the plane of conduction. The Al(2)* position is also the Mg(1) position.

6.4 Discussion

This experiment has shown no difference between heating with microwaves and heating by conventional methods. The reason for this may simply be that there are no differences to be observed. However, the enhanced mobility of ions has been seen in other materials[53] and the sensitivity of this technique is such that one might expect to observe the evidence. Another reason, therefore, may be that the experimental procedure is flawed.

The design of the applicator is slightly different from that used when heating silver iodide in the earlier experiment. The applicator diameter and volume are significantly greater, the antenna is shorter and is aligned perpendicular to the cylindrical axis of the applicator. The implications of these differences are several:

(i) The heated volume is increased (for conventional heating methods). For microwave dielectric heating, only the sample should be heated, however power is also lost at the applicator walls. The large surface area means the power at the sample is attenuated.

(ii) Several modes may operate in the applicator, resulting in the formation of a complex standing wave pattern and widely varying field amplitude inside the applicator. The result is that fine-tuning of the applicator to give rise to a field-strength maximum at the sample is difficult.

(iii) The shortened antenna is not aligned with the cylindrical applicator walls. This affects the efficiency of power transfer from the coaxial to the applicator.

This last point requires further explanation. For a coaxial system (a conductor within a hollow conducting tube) field lines are radial about the central conductor and normal to the surfaces of both inner and outer conductor. In this case, the field pattern is more complicated, however it remains true that field lines will be normal to both the antenna and the inner surface of the applicator. This is shown in Figure 6.15. Notice that the field intensity (how closely the lines are spaced) is relatively weak at the sample position and is much stronger near the base of the antenna, away from the sample position. Thus, due to an oversight in reactor design, the efficiency of heating is poor.

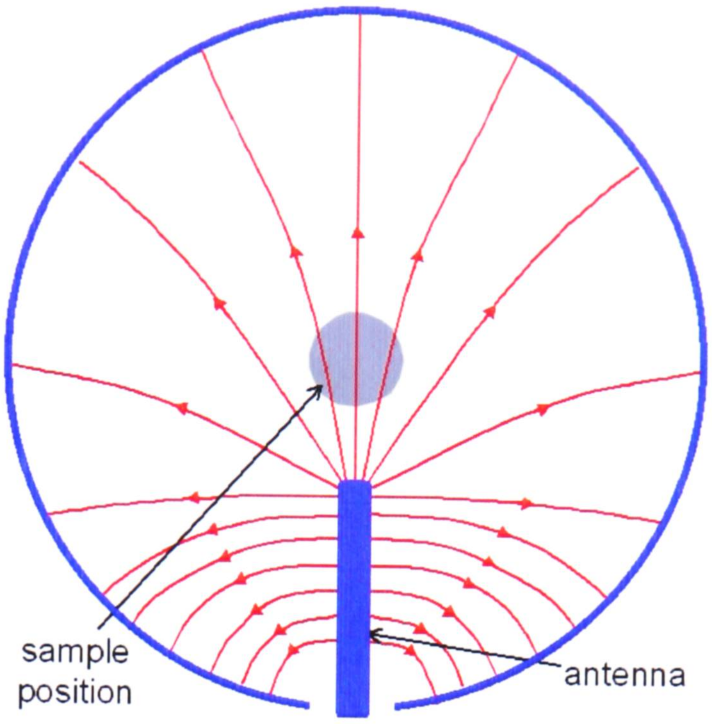

Figure 6.15 - Electric field lines at the sample position, taken as a cross-section through the applicator.

In addition, there are the problems associated with the use of coaxial lines. That is, that junctions, curves and other discontinuities are all points of poorer conductivity and result in quite severe I^2R heating at the high currents involved with microwave fields. The net result of all these characteristics is that power is seriously diminished in transmission and therefore the power at the sample is significantly less than the maximum 200 W generated. The fact that microwave power alone was insufficient to heat the samples to the desired temperature is an indication of this. The power dissipation is even more apparent when you consider that the same materials showed rapid heating (of the order of 10 Ks^{-1} at room temperature) in a domestic 800 W microwave oven.

7 Ferroelectric perovskites

In the previous chapters, the largest question hanging over the tentative conclusions presented there is: how accurate is the temperature measurement? Much could be easily explained without the presence of a specific microwave effect, particularly as regarding phase transformations, if it became clear that the actual temperature was much higher than recorded. Difference could arise not only from the different heating rates of different materials, but also localised heating can result in temperature gradients within the sample.[62] To this end an experiment was designed in which independent temperature measurement was intrinsic to the method. One of the fundamental properties of a solid material, expansion upon heating, was used as a measure of core sample temperature.

In order to be convinced that the 'temperature' deduced from the structure was accurate with sufficient time-resolution to be useful, high-quality diffraction data was required. However, previous experiments were unable to deliver the most accurate crystal structure data, such as atomic displacement parameters (ADPs) for the following reasons: the investigation of silver iodide had insufficient X-ray flux for full structure determination; whilst β''-alumina proved to have too complex a structure to achieve precise ADP values for the quantity of data we were able to record. In order to overcome these difficulties it was decided to use available time on a high-resolution powder neutron diffraction instrument to look at a class of functional materials with relatively simple structures: the ferroelectric perovskites. These are materials with ABO_3 stoichiometry (A is a main-group metal, B is a transition group metal), with ideal cubic structure as shown in Figure 7.1.

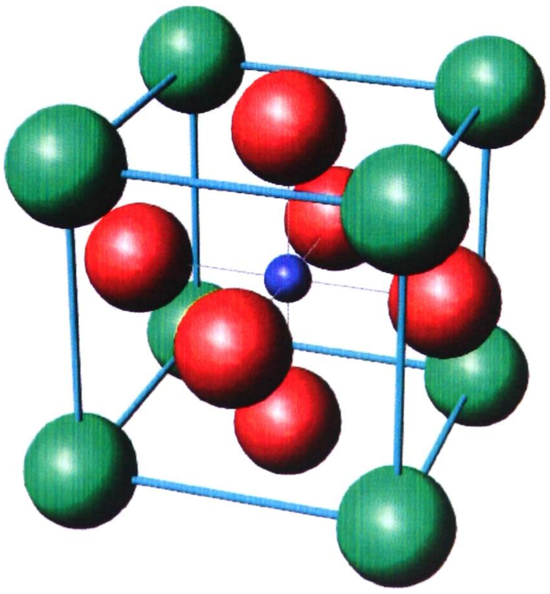

Figure 7.1 - Unit cell structure of idealised cubic perovskite, ABO_3 (A at cube vertices, B at the centre and Oxygen central on the cube faces).

For this study, two archetypal perovskite materials were chosen: barium titanate[†] ($BaTiO_3$) and potassium niobate ($KNbO_3$). Both have a high dielectric loss tangent with 2.45 GHz microwave radiation and an appreciable coefficient of linear expansion (so the heating and cooling of the structure may be observed).[117] The cubic structure (Figure 7.1) of these materials is paraelectric. Ferroelectricity is characterised by a shift of ions from their positions in the paraelectric state. The centres of gravity of the positive and negative ions do not coincide and a spontaneous electric polarisation is created, even without the application of an external electric field.

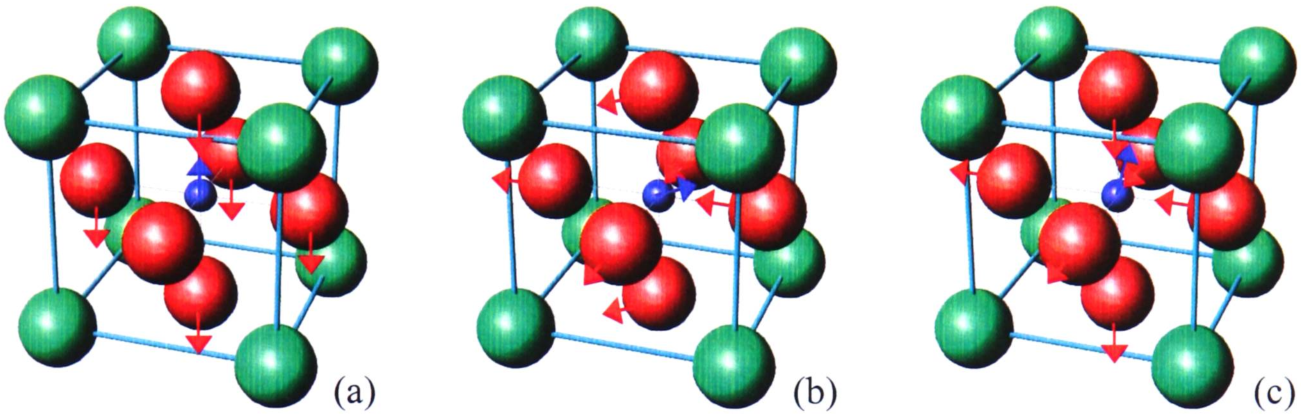

Figure 7.2 - Displacements of B and O ions from the original cubic to the (a) tetragonal, (b) orthorhombic, and (c) rhombohedral polymorphs.

In order to perform the transformation, the material must be cooled; polarisation occurs at temperatures below the Curie temperature (T_c). In the case of the chosen materials, polarisation occurs due to small displacements of atoms along the crystallographic z-axis, the [001] direction. Relative to the A atoms at the unit cell vertices, the central B atom is displaced along the [001] axis, whilst the oxygen atoms are displaced in the opposite direction. The result is a dipole moment parallel to the z-axis and a slight elongation of the unit cell to give a tetragonal phase. Further cooling results in subsequent phase transformation, a consequence of distortions along the [011] axis (orthorhombic phase) and [111] axis (rhombohedral phase). Both $BaTiO_3$ and $KNbO_3$ show the typical series of phase transformations on cooling, i.e. cubic (space group: $Pm3m$), tetragonal ($P4mm$), orthorhombic ($Amm2$) and rhombohedral ($R3m$), as shown in Figure 7.2. Both materials are

---

[†] Barium titanate is of particular interest as it is an important material in the electronics industry, finding applications in dynamic random access memory (DRAM) devices and mobile phone applications.

well studied and a wealth of information is available about their properties.[117-139] In particular, both materials have a thermally accessible phase transformation, i.e. of the order of 100 K above room temperature. $BaTiO_3$ undergoes the tetragonal to cubic phase change at ~393 K, whilst $KNbO_3$ transforms from orthorhombic to tetragonal at ~498 K.

7.1 Applicator Design

The investigation was performed on the HRPD (high resolution powder diffraction) station at the ISIS Facility. HRPD is unique amongst the instruments at ISIS in that it is set almost 100 m away from the spallation target, much further than the other instruments. The reason for this is to improve the resolution, $\Delta d/d$. Three factors affect the resolution: an angular uncertainty ($\Delta\theta$), a timing uncertainty (Δt) and a flight-path uncertainty (ΔL).

$$\Delta d/d = \left[\Delta\theta^2 \cot^2\theta + \left(\Delta t/t\right)^2 + \left(\Delta L/L\right)^2\right]^{1/2} \qquad \textbf{(7.1)}$$

The main contribution to Δt is the moderation time of the neutron. The mechanism of neutron production and moderation at a spallation source is a complicated process and thus it is not surprising that the pulse shape is of a complex nature. However, the finite time width of the initial neutron pulse is clearly independent of t; neutrons of a particular wavelength will propagate non-dispersively (because wavelength and hence velocity are constant) and so the ratio ($\Delta t/t$) is decreased simply by increasing the flight time or total neutron flight path. The error in flight path is similarly minimised and arises chiefly because of the finite moderator thickness (neutrons may be "born" from its front or back) and to a lesser extent due to finite sample and detector sizes. The uncertainty in scattering angle is a consequence of neutron beam divergence and is simply represented by the differentiation of Bragg's Law. In consequence it can be seen that resolution increases linearly with flight path with the maximum resolution obtained in back-scattering geometry with $\theta = 90°$, i.e. $\cot\theta \sim 0$.

The result is extremely high resolution, with $\Delta d/d$ up to $\sim 4\times10^{-4}$ (effectively constant over the wide d-spacing range available). A liquid methane cooled (100 K) moderator provides HRPD with an incident flux out to a maximum wavelength of some 10-12 Å. The highest resolution data may therefore be recorded out to *d*-spacing of some 5-6 Å. The high resolution can be used for very precise studies, including: refinement of complex molecules (bound in crystals), structure solution of simple unit cells from powder (normally requiring single crystals) and study of subtle phase transitions. It is therefore an ideal instrument for the study of phase changes in ferroelectric perovskites.

The sample ($BaTiO_3$ or $KNbO_3$, both 99.99% (metals basis), supplied by Alfa Aesar) was compressed into a cylindrical pellet (diameter 13 mm and height approximately 5 mm) with a force of 10 tonnes. Powder neutron diffraction patterns were taken on HRPD on the bank of back-scatter detectors (ZnS scintillator, 160°-176°), where the greatest resolution is to be attained. To provide a basis for comparison between conventional and microwave heating, the sample was first heated in a standard RAL vacuum furnace with Vanadium element and heat shields. The furnace temperatures were controlled and monitored using type-K, (Chromel/Alumel) thermocouples. Time of flight (TOF) patterns were recorded *in-situ,* between 30 and 130 ms, for a period of approximately 2 hours (collection rate of 18.0 μAh) at a series of temperatures, starting at room temperature (295 K) and rising to 873 K.

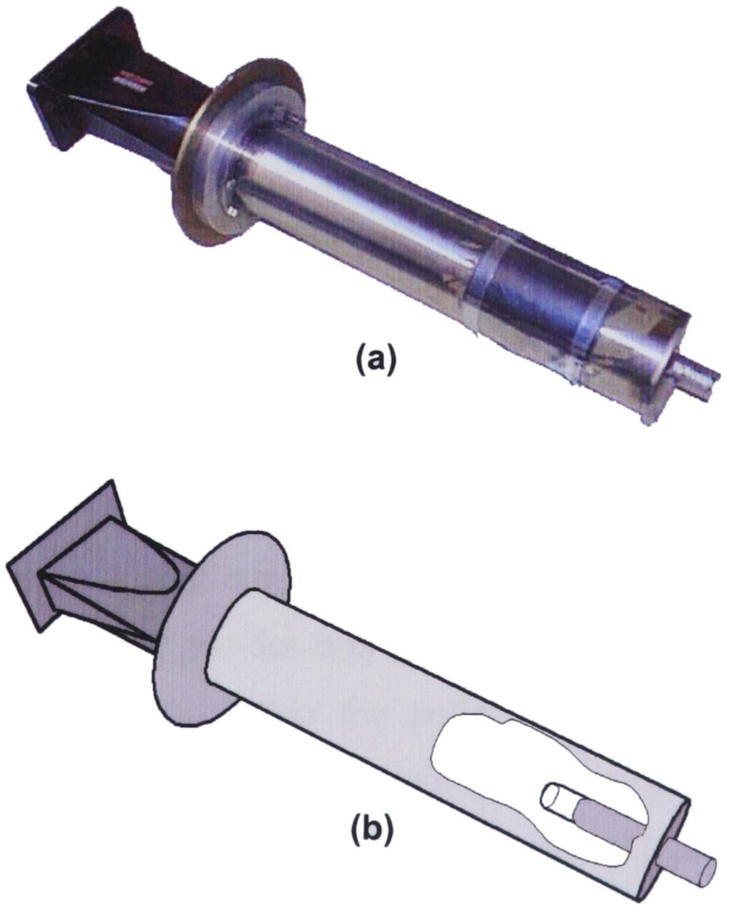

Figure 7.3 - Microwave applicator for HRPD experiment. (a) photo showing vanadium foil windows (right-hand end). (b) schematic showing sample position.

In order to perform similar measurements with microwave heating, a microwave applicator was constructed which was compatible with the requirements of HRPD and resulted in minimum disruption to normal experimental procedure. The applicator design was based on a cylindrical waveguide of diameter 81 mm and length ~420 mm, constructed from stainless steel (Figure 7.3). The sample was positioned a quarter wavelength from the terminating short-circuit of the waveguide, where the electric field strength was at a maximum. The diameter of the applicator is such that only the fundamental TE_{11} mode propagates: field intensity is a maximum at the centre of the circular cross-section (Figure 7.4). The waveguide fitted to the magnetron generator (ASTeX 5-1000, variable power source up to 1 kW) is rectangular and therefore a transition piece was required between the two different types, as shown in Figure 7.5. The distance of the sample from the rectangular to circular transition was sufficient to quench any extra modes thus excited.

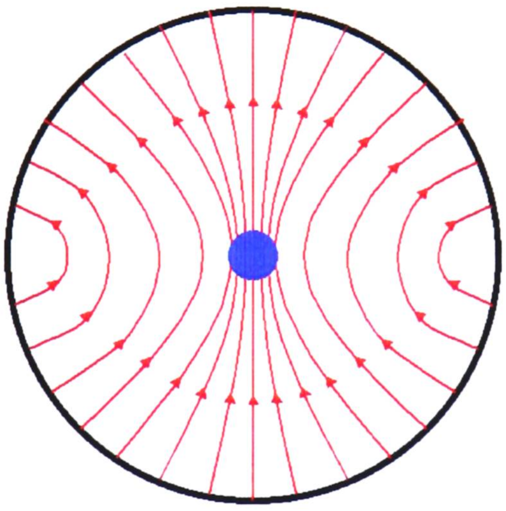

Figure 7.4 - Electric field lines for a cross-section of the cylindrical applicator.

The sample was a compressed pellet (the same as used in the conventionally heated experiment) surrounded by loose powder of the same material and contained in a thin-walled silica crucible, supported on a very low-loss, ceramic (Shapal™) support. The purpose of surrounding the sample in loose powder was to prevent significant surface cooling, thus minimising temperature gradients within the pellet (essentially the source of all the diffraction data). In microwave heating, materials with penetration depths larger than the sample size have an inverse temperature profile, where the surface is cooler than the bulk. Here the powder insulated the pellet, so the pellet itself had a more homogeneous temperature profile.

A hole was cut in the wall of the applicator and covered with vanadium foil (Figure 7.3). Vanadium is a good 'window' material as it has a low neutron-scattering cross-section. The window was edged with neutron-absorbing gadolinium sheet to minimise scattering from other components of the microwave heating system.

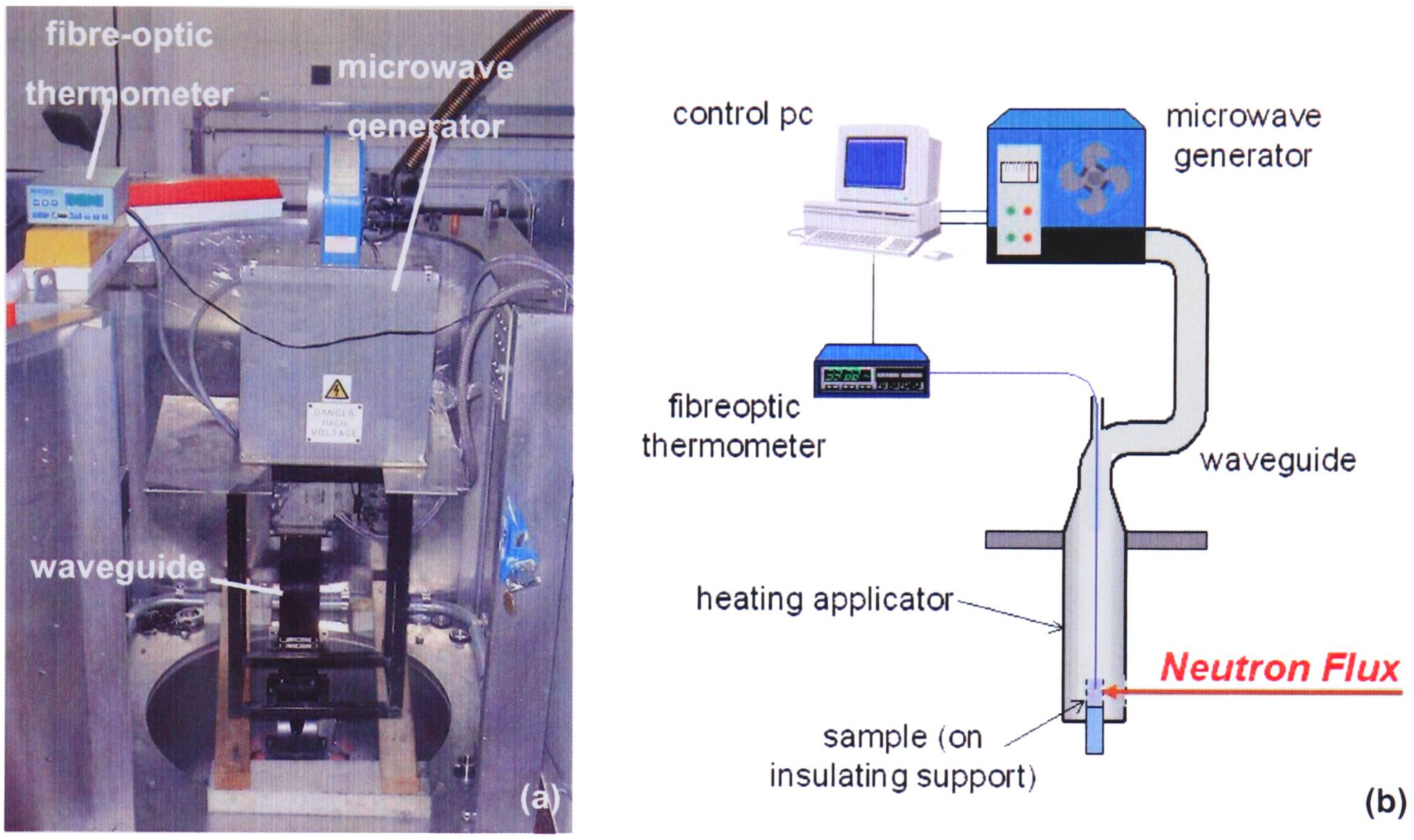

Figure 7.5 - Apparatus for diffraction experiment on HRPD, (a) in use, and (b) schematically.

7.2 Experimental

Temperature was monitored with a fluoro-optic temperature probe (Nortech Fibronic Inc, noEMI-TS series) with a precision of approximately 0.1 K. The thermometer had been previously calibrated by a co-worker (A. G. Whittaker). The output of this device was read by a PC, which in turn controls the power output of the microwave generator (Figure 7.5). In this way, a constant temperature was maintained for the duration of diffraction measurements. Small adjustments to the microwave field pattern were achieved using a 4-stub multi-screw tuner, enabling the position of the field maximum to be modified relative to the sample, if necessary.

During microwave heating, longer scan periods were employed (30-55 μAh) as there was concern that signal noise, due to increased scatter from the microwave cell, could be a problem. Diffraction patterns were recorded *in-situ* at 295 K (no microwaves – for a comparison against the conventional cell), and then at several temperatures with microwave heating. Microwave power level was varied throughout to maintain temperature to within ±1 K. Unfortunately, due to some equipment failure and consequent loss of beam time, data could only be taken at relatively few temperatures.

7.3 Results

Data were collected as a function of time of flight (TOF). Refinements were performed using the Rietveld method; on a desktop PC running the GSAS (Generalised Structure Analysis System) suite of programs,[92] with EXPGUI (MS Windows compatible interface).[93] HRPD has a well-defined peak shape, corresponding to the GSAS TOF profile function 3: a combination of terms describing Gaussian and Lorentzian broadening and a function describing the modulator pulse shape:

$$H(\Delta T) = \int E(\Delta T - t)[\eta L(t,\Gamma) + (1-\eta)G(t,\Gamma)]dt \tag{7.2}$$

where E is an exponential function, G is a Gaussian, L is a Lorentzian, Γ is a function of the peak width (FWHM) and η is the mixing factor. The invariance of the peak shape means that certain variables in the peak profile have well defined values. The only profile coefficients allowed to vary are those describing line broadening due to the sample. Line broadening related to the Gaussian line shape is described by σ terms. A complete explanation of how σ relates to $H(\Delta T)$ is beyond the scope of this discussion and I would refer the interested reader to the GSAS manual.[92] However, for a more simple function with no Lorentzian component (such as that described by the GSAS 'type 1' profile function) the relationship between σ and $H(\Delta T)$ is as shown in Equation (7.3).

$$G(\Delta T - t) = \frac{1}{\sqrt{2\pi\sigma^2}} \exp\left[\frac{-(\Delta T - t)^2}{2\sigma^2}\right] \tag{7.3}$$

Additional complications arising from the introduction of the Lorentian function do not alter this basic relationship. Broadening related to the Lorentzian line shape is described similarly by γ terms. Expansion of the terms σ^2 and γ^2 lead to a series of terms of which only the second and third are commonly used (the first having no physical relevance), e.g. Equations (7.4) and (7.5). The terms σ_1 and γ_1 describe particle strain, whilst σ_2 and γ_2 describe particle size. However in practice, all these terms are highly correlated during refinement. This is discussed in greater detail in the Appendix (page A2).

$$\sigma^2 = \sigma_0^2 + \sigma_1^2 d^2 + \sigma_2^2 d^4 \tag{7.4}$$

$$\gamma = \gamma_0 + \gamma_1 d + \gamma_2 d^2 + \left(\gamma_{1e} d + \gamma_{2e} d^2\right)\cos\phi + \gamma_L \tag{7.5}$$

7.3.1 Barium titanate

It is known that for non-strained samples of barium titanate the Curie temperature, T_c, is 393 K. Above this temperature, the structure has a cubic perovskite structure (space group *Pm*3*m*) and on cooling below this temperature the structure undergoes a distortion along the [001] axis to give a tetragonal structure (space group *P*4*mm*). Data were recorded at temperatures in the range 295 K to 873 K and refinement was performed using the appropriate phase for that temperature, yielding optimised values of cell parameters, atom displacement parameters (ADPs) and profile coefficients. It was discovered early in the process that a superior fit was achieved using a two-phase refinement, see Table 7-1 for a comparison of single and dual phase refinement.

Table 7-1 - Goodness of fit comparison for barium titanate heated conventionally to 873 K, fitted with either a single phase or two phases.

PARAMETER	SINGLE PHASE	TWO PHASE MAJOR (82.11%)	 MINOR (17.89%)
Space Group	*Pm*3*m*	*Pm*3*m*	*Pm*3*m*
a/Å	4.03207(6)	4.03200(5)	4.0530(5)
χ^2	2.050	1.249	
R_{wp}	0.0870	0.0679	
R_p	0.0722	0.00566	

The second phase fits to a cubic cell but the cell parameter is consistently about 0.017 Å longer than in the majority phase. Similar effects have been observed previously in barium titanate[118-121, 131] and similar materials.[140, 141] The cause is thought to be small particles stabilised in a pseudo-cubic phase through local strain. All data, including those in the tetragonal phase, show this minority cubic phase present at around 20% and consequently it was included in all refinements and its parameters were optimised separately.

An example of a diffraction pattern is shown in Figure 7.6 (note that some data at higher *d*-spacing has been excluded from the refinement; the missing data are anomalous and derives from the sample holder; the same data have been excised from all refinements). The final structure determinations for all data on barium titanate are summarised in Table 7-2.

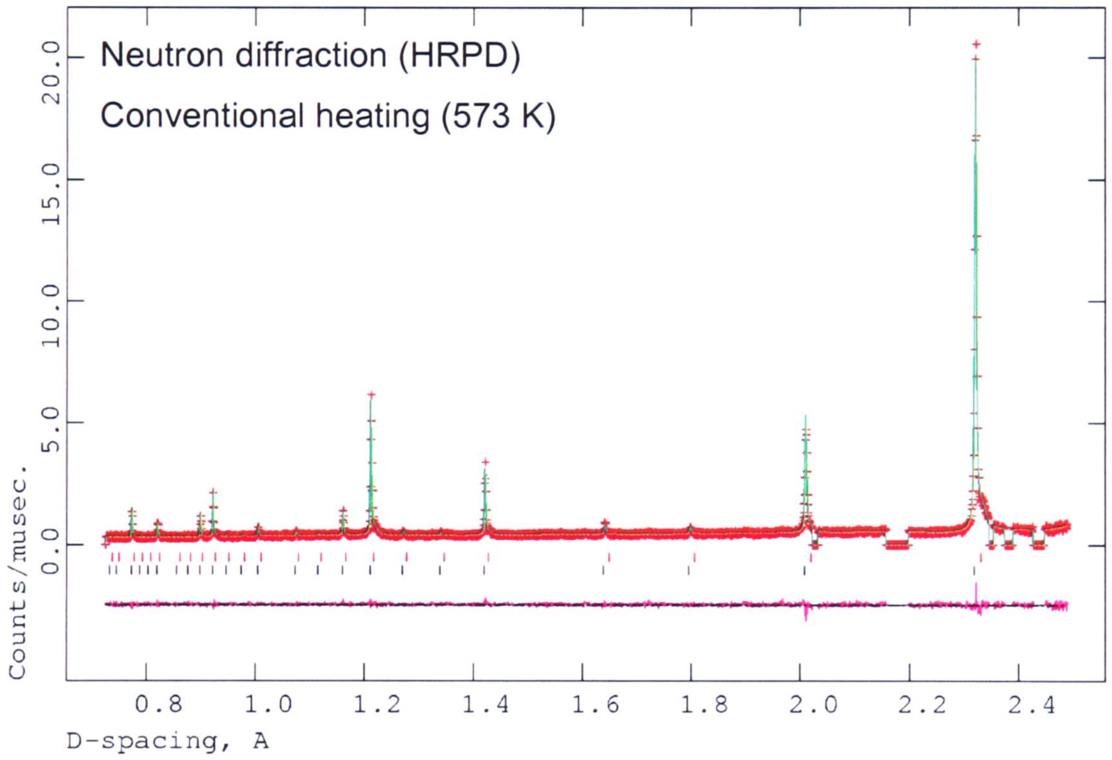

Figure 7.6 – Histogram for $BaTiO_3$ (neutron diffraction, 573 K by conventional heating). Upper part of diagram shows the collected data (crosses) and structural model (line through the points). Below is the difference between measured and fitted data. The tickmarks show the position of reflections from the two phases (lower set is the majority phase, upper set is the minority phase).

Table 7-2 - Crystallographic data for BaTiO3. ADPs are scaled by a factor of 100. The figures in brackets represent one standard deviation in the last decimal place(s).

	ELECTRIC FURNACE							MICROWAVE		
TEMPERATURE / K	295	423	473	573	673	773	873	295	383	473
Space Group	*P4mm*	*Pm3m*	*Pm3m*	*Pm3m*	*Pm3m*	*Pm3m*	*Pm3m*	*P4mm*	*Pm3m*	*Pm3m*
Phase Fraction (%)	75.66	78.79	79.26	79.34	80.03	80.75	82.11	81.23	80.07	81.17
σ_1	572(24)	448(14)	483(15)	462(14)	403(13)	397(13)	393(13)	598(19)	662(24)	692(17)
a / Å	3.99218(9)	4.01129(5)	4.01363(5)	4.01786(5)	4.02294(5)	4.02837(5)	4.03200(5)	3.99478(7)	4.01081(7)	4.01389(5)
c / Å	4.03448(12)							4.03420(9)		
V / Å^3	64.2996(29)	64.5433(14)	64.6565(14)	64.8612(13)	65.1072(14)	65.3713(13)	65.5485(14)	64.3786(22)	64.5204(20)	64.6689(14)
$V^{1/3}$ / Å	4.00623(18)							4.00787(14)		
Ba (0,0,0)										
$U^{11}=U^{22}$ / Å^2	0.30(19)	1.11(7)	1.20(7)	1.40(7)	1.44(7)	1.77(7)	1.76(7)	0.55(18)	0.89(11)	0.62(7)
U^{33} / Å^2	1.4(13)	1.11(7)	1.20(7)	1.40(7)	1.44(7)	1.77(7)	1.76(7)	1.1(21)	0.89(11)	0.62(7)
U^{eq} / Å^2	0.7(6)	1.11(7)	1.20(7)	1.40(7)	1.44(7)	1.77(7)	1.76(7)	0.7(8)	0.89(11)	0.62(7)
Ti (½,½,½+Δz_{Ti})										
Δz_{Ti}	-0.035 (5)							-0.009(33)		
$U^{11}=U^{22}$ / Å^2	0.73(21)	1.26(9)	1.31(9)	1.51(9)	1.61(9)	1.79(9)	1.75(9)	0.66(19)	0.83(12)	0.80(8)
U^{33} / Å^2	1(4)	1.26(9)	1.31(9)	1.51(9)	1.61(9)	1.79(9)	1.75(9)	2.2(27)	0.83(12)	0.80(8)
U^{eq} / Å^2	0.8(15)	1.26(9)	1.31(9)	1.51(9)	1.61(9)	1.79(9)	1.75(9)	1.2(11)	0.83(12)	0.80(8)
O1 (½,½,Δz_{O1})										
Δz_{O1}	0.021(4)							0.036(10)		
$U^{11}=U^{22}$ / Å^2	0.17(29)	1.14(7)	1.05(7)	1.24(7)	1.46(7)	1.72(7)	1.89(7)	0.30(27)	0.89(10)	0.74(7)
U^{33} / Å^2	1.0(23)	1.12(12)	1.32(12)	1.49(12)	1.66(12)	1.86(12)	1.93(13)	1.5(13)	0.84(10)	0.74(7)
U^{eq} / Å^2	0.5(10)	1.13(9)	1.14(9)	1.32(9)	1.53(9)	1.76(9)	1.90(9)	0.7(6)	0.87(10)	0.74(7)
O2 (½,0,½+Δz_{O2})										
Δz_{O2}	0.006(5)							0.026(12)		
U^{11} / Å^2	0.34(34)							0.28(28)		
U^{22} / Å^2	1.30(26)							0.64(22)		
U^{33} / Å^2	2.0(6)							1.6(4)		
U^{eq} / Å^2	1.2(4)							0.82(30)		
Minority Cubic Phase										
a / Å	4.0142(3)	4.0287(7)	4.0338(5)	4.0384(5)	4.0425(5)	4.0480(5)	4.0530(5)	4.01908(25)	4.0238(6)	4.0325(6)
V / Å^3	64.682(8)	65.389(18)	65.634(15)	65.861(14)	66.064(15)	66.330(15)	66.577(15)	64.920(7)	65.148(16)	65.572(18)
χ^2	1.855	1.422	1.41	1.321	1.402	1.275	1.249	2.958	2.478	1.65
R_{wp}	0.0551	0.0703	0.0684	0.0666	0.0708	0.0682	0.0679	0.0538	0.0657	0.0492
R_p	0.0449	0.06	0.0562	0.0542	0.059	0.0558	0.0566	0.0439	0.0554	0.0417

For both tetragonal and cubic phases only the diagonal elements of the ADP matrix (U^{11}, U^{22} and U^{33}) are non-zero and in the cubic phase thermal motion is anisotropic as a consequence of symmetry constraints, i.e. all U^{ij} components are equal. The non-zero ADPs are quoted for each majority phase, as is U^{eq}, the equivalent anisotropic atomic displacement parameter. This is calculated as the mean of the diagonal elements of the ADP tensor. In addition, to facilitate comparison between cubic and tetragonal phases, a pseudo-cubic cell parameter ($\equiv V^{1/3}$) is reported in Table 7-2.

It was found that the line width parameters, σ_1, σ_2, γ_1 and γ_2, were correlated with one another to the extent that refinement of all four was a meaningless exercise. Instead, three of the parameters were fixed at sensible values (σ_2=-38, γ_1=52 and γ_2=0) and only σ_1 was refined. This had the effect of slightly worsening the goodness of fit parameters (χ^2, R_{wp} and R_p), but gives a more physically meaningful model. The term σ_1 is the second in the expansion of σ, where σ^2 is the Gaussian variance (Equation (7.3)), but accounts for total variance here. σ_1 is thus the peak width parameter, with contributions from both instrumental resolution and isotropic strain broadening.

The most remarkable result from Table 7-2 is the ferro- to para-electric transition temperature (T_c). T_c, for unstrained samples of $BaTiO_3$, is accepted to occur in the immeadiate vicinity of 393 K. It is not unknown for this phase change temperature to be *higher*, indeed in the case of thin, strained films of $BaTiO_3$ grown on $SrTiO_3$, T_c may be as high as 800-1100 K.[122] Yet, it is clear from these data, that although the conventionally heated sample retains the expected behaviour, the microwave heated sample undergoes a phase transition at a temperature *lower* than 383 K.

In order to compare the data taken with microwave heating and with conventional heating more clearly, some of the important parameters have been plotted. Figure 7.7 shows a comparison of the unit cell parameter for the two forms of heating. As previously stated, the minority cubic phase has a consistently larger unit cell than the majority phase. Both the major and minor phases have an apparently linear increase with temperature.

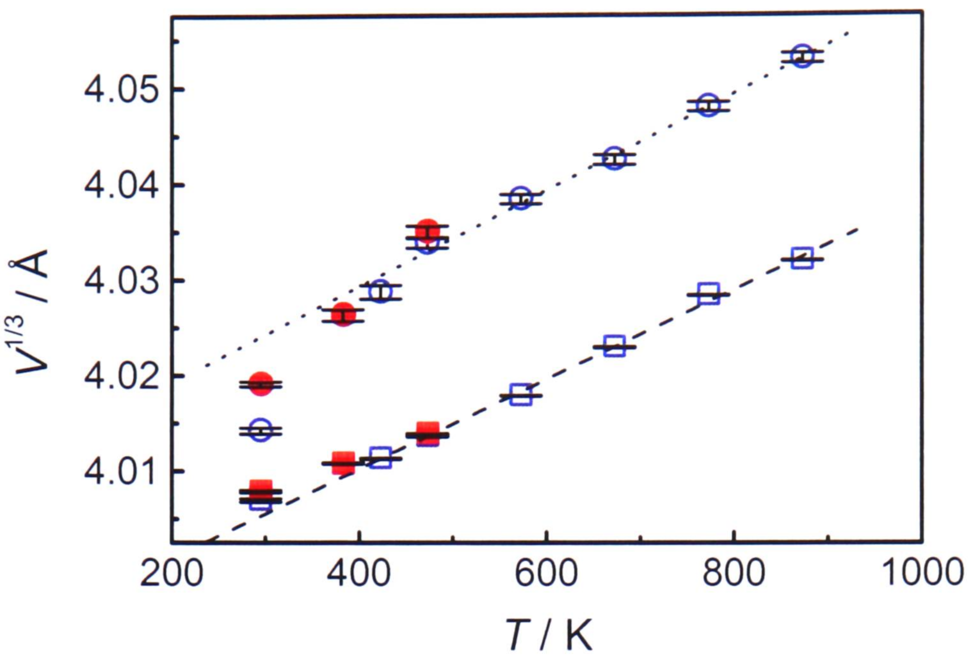

Figure 7.7 - Comparison of unit cell parameter, *a*, for $BaTiO_3$ with microwave (■,●) and conventional heating (□,○). Squares indicate the majority phase while circles correspond to the minority cubic phase. For the tetragonal phase the pseudo-cubic cell parameter is used. The lines through the points are merely guides to the eye.

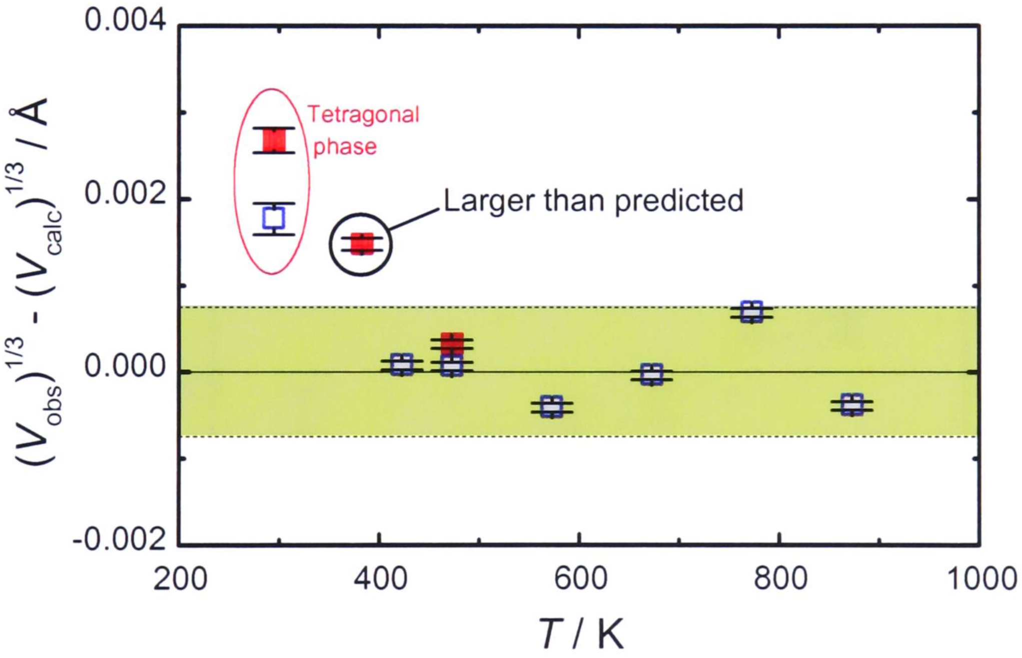

Figure 7.8 – Plotted residuals between observed unit-cell parameter and calculated trend line, for $BaTiO_3$ with microwave (■) and conventional heating (□). For the tetragonal phase the pseudo-cubic cell parameter is used. Dashed lines enclosing shaded region indicate the standard error in the calculated trend.

Figure 7.8 shows the same data (for the majority phase) as Figure 7.7, but as a difference against the linear trend line (calculated for cubic-phase data only). Examining the data clearly shows that though the values for microwave heating and conventional heating are close, there is a significant trend for the microwave heated samples to show a larger than expected cell parameter. The data for the tetragonal phase (T = 295 K) deviates from the trend in the cubic phase. The difference between the pseudo cell-parameter for the tetragonal phase under the two forms of heating is approximately two standard deviations and is therefore taken to be insignificant. This is to be expected, as neither sample is actually heated (no microwaves, no conventional heating), only the sample environments are different. The larger than expected cell expansion under microwave heating (especially for the sample at 383 K – difference is greater than five standard deviations) can be interpreted in an alternative way. The cell parameter corresponds to a temperature higher than that measured – between 10 K and 20 K higher if one extrapolates trend from the higher temperatures.

Contrast this with the measured atomic displacement parameters, as shown in Figure 7.9 - Figure 7.11. Though the errors in ADP values are proportionally much greater than for the cell parameter, it is clear that there are some distinct differences between microwave and conventional heating. Ignoring data in the tetragonal phase (which contains very large errors) all microwave data exhibits smaller than expected ADP values. This would correspond with smaller atomic vibrations and a *lower* apparent temperature; the opposite of what the cell-parameter data would indicate.

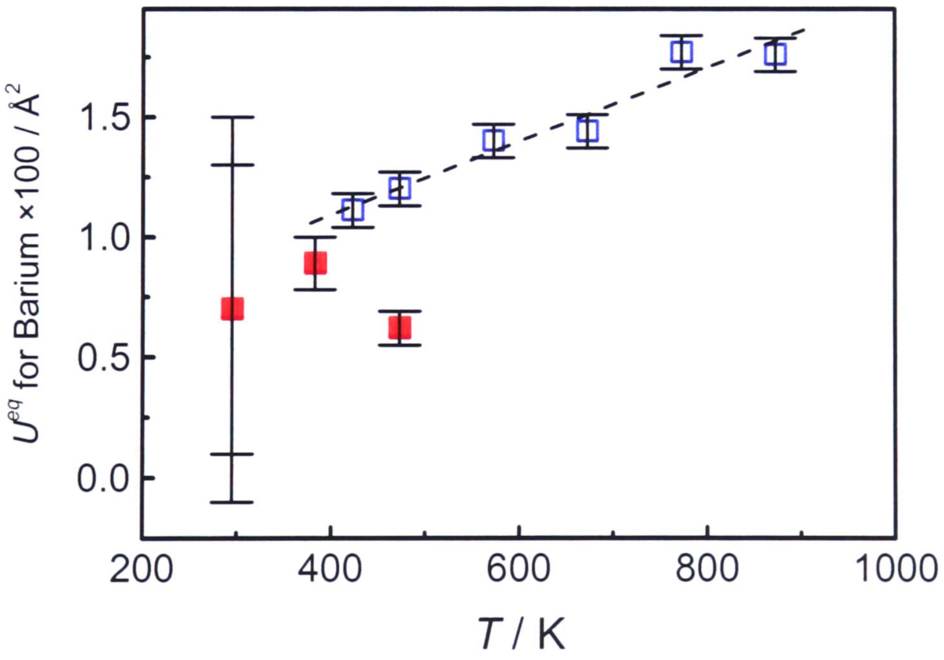

Figure 7.9 – Isotropic ADPs for barium in $BaTiO_3$ as a function of temperature for microwave heating (■) and conventional heating (□). The line through the points is merely a guide to the eye.

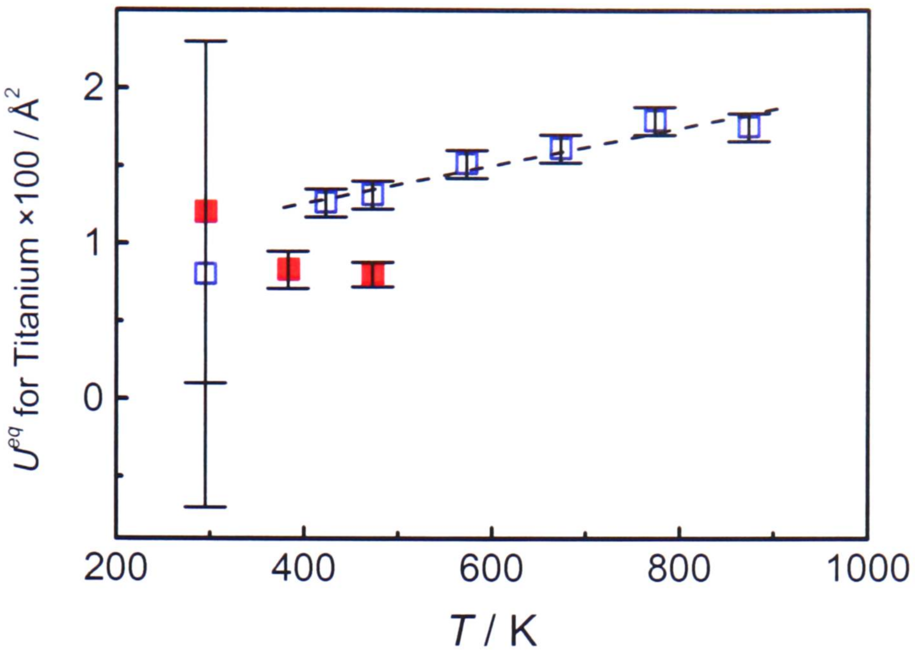

Figure 7.10 - Isotropic ADPs for titanium in $BaTiO_3$ as a function of temperature for microwave heating (■) and conventional heating (□). The line through the points is merely a guide to the eye.

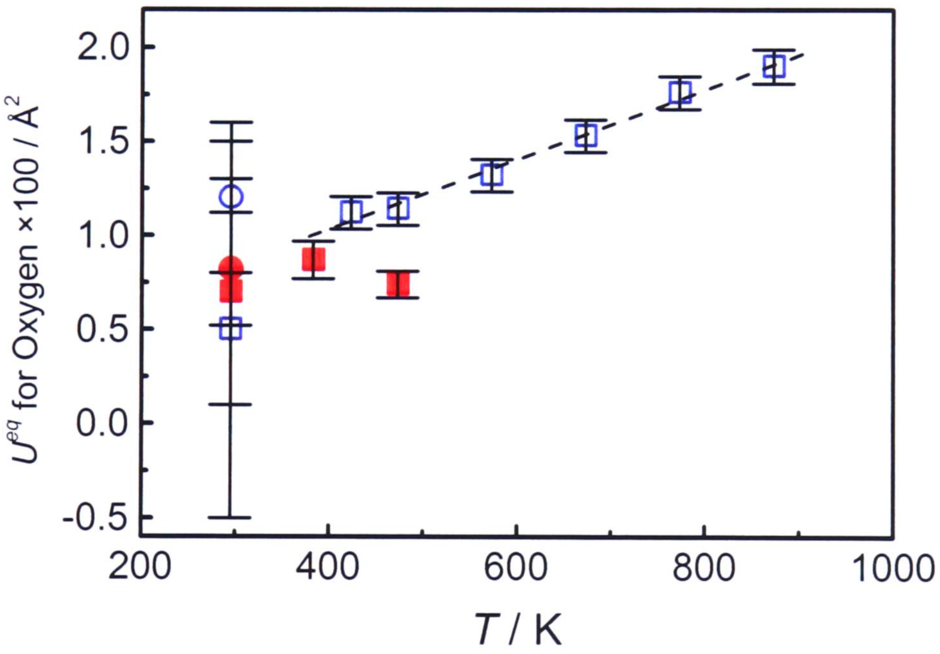

Figure 7.11 - Isotropic ADPs for oxygen in $BaTiO_3$ as a function of temperature for microwave heating (■,●) and conventional heating (□,○). In the lower temperature tetragonal phase, the data are in pairs for each mode of heating with symbols distinguishing the O1 (square) and O2 (circle) sites. The line through the points is merely a guide to the eye.

The final parameter to which we can attach some significance is the peak width parameter σ_1. Having fixed all other parameters, this single parameter accounts for all variation in peak width. These variations could be due to changes in particle size, stress and strain.

Comparison of the data for microwave and conventional heating (Figure 7.12) shows significant differences.

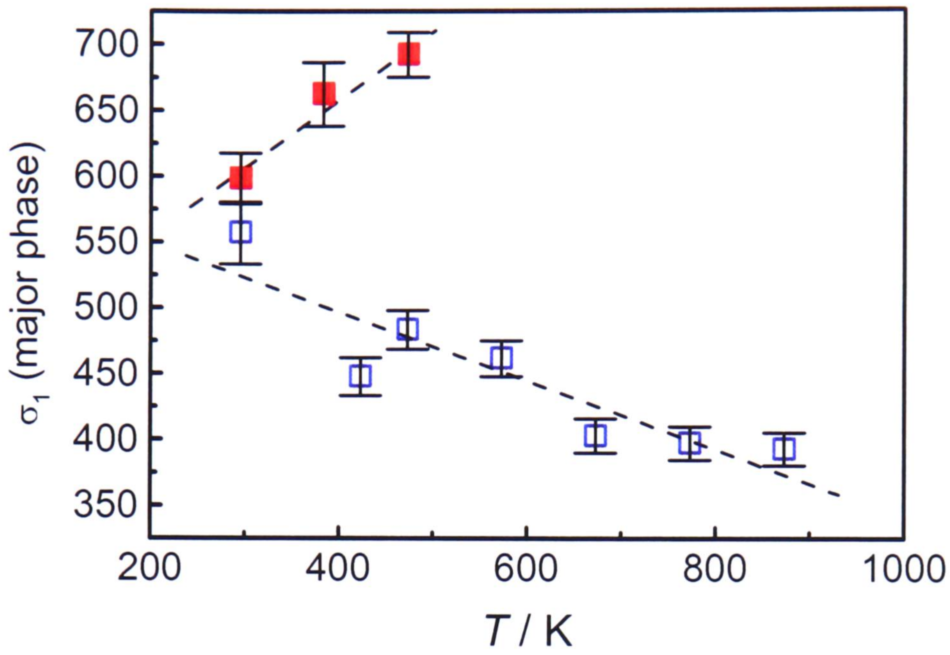

Figure 7.12 – Width parameter σ_1 for $BaTiO_3$ as a function of temperature for microwave heating (■) and conventional heating (□). The line through the points is merely a guide to the eye.

It should be noted that a strong correlation exists between several of the fitted parameters at 295 K, where the minority cubic phase and the majority tetragonal phase co-exist. This gives rise to very large standard deviations in the ADPs. It also results in, what appears to be, an anomalously small value for the minority phase cell parameter (most notable under conventional heating). This was found to be in correlation with the width parameter, σ_1. Concerned that this correlation may result in a physically unrealistic fit, the model was refined with certain fixed values of the minority-phase cell parameter in order to determine the effect this would have on the refinement of other parameters. The result can be seen in Figure 7.13 and shows that increasing the cell parameter up to that extrapolated from the higher temperature data significantly increases σ_1 and worsens the fit. Indeed, for the extrapolated value (a=4.02419 Å), χ^2 was optimised (3.381) when σ_1 was 738.9, whilst the unconstrained data were optimised (χ^2=2.83) with a cell parameter of 4.01416 Å and with a σ_1 value of 556.9. Comparison of these values with Figure 7.12 and consideration of χ^2 lead to the belief that the original value obtained when refinement was not constrained gives the most realistic model.

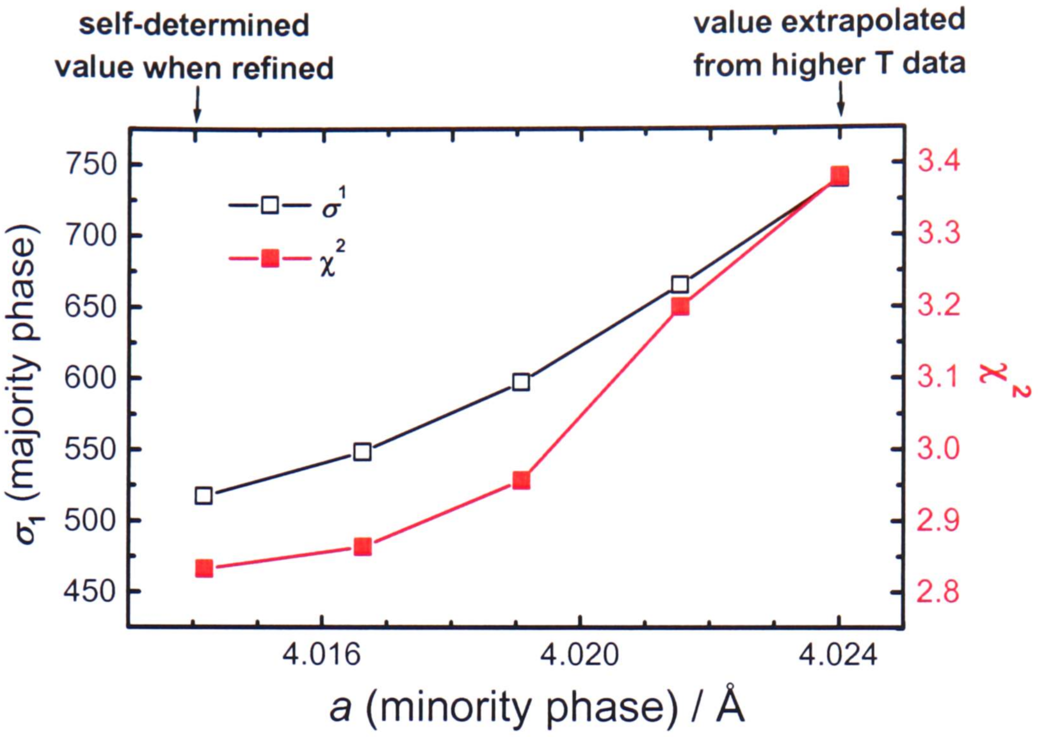

Figure 7.13 - Influence of the minority phase cell parameter on the width parameter σ^1 (□) and the goodness of fit parameter χ^2 (■) for $BaTiO_3$ at 295 K (in conventional furnace, but without heating).

7.3.2 Potassium niobate

Potassium niobate ($KNbO_3$) is found in an orthorhombic phase (*Amm*2) at room temperature and on heating under goes a phase transformation to a tetragonal phase (*P*4*mm*) at ~498 K. Rietveld refinement was again found to require a two-phase model for improved optimisation of parameters. In this instance, the second phase gave the best fit for a tetragonal phase. Also, as for $BaTiO_3$, the width parameters were found to be highly correlated and so all were fixed at sensible values, except σ_1, which was allowed to refine freely. Fixed parameters are $\sigma_2 = 100$, $\gamma_1 = 60$ and $\gamma_2 = 0$. Equipment breakdown resulted in limited time on the instrument with this sample. Data were taken between 300 K and 500 K and refinement was performed using the appropriate phase for that temperature, yielding optimised values of cell parameters, atom displacement parameters (ADPs) and profile coefficients. Details of the structure for three temperatures under conventional heating, and one under microwave heating are shown in Table 7-3. An example diffraction pattern for $KNbO_3$ is shown in Figure 7.1. Notice that again, as with $BaTiO_3$, some data have been excised from the refinement. This has been attributed to the sample environment and the same data have been removed from all refinements.

Table 7-3- Crystallographic data for $KNbO_3$ in orthorhombic (*Amm*2) and tetragonal (*P*4*mm*) phases. All ADPs are scaled by a factor of 100. The figures in brackets represent one standard deviation in the last decimal place(s) of the quoted figure.

	ELECTRIC FURNACE			MICROWAVE
TEMPERATURE / K	328	373	473	392
Space Group	*Amm*2	*Amm*2	*Amm*2	*P*4*mm*
Phase Fraction (%)	80.54	80.17	79.2	94.75
σ_l	256(17)	269(17)	282(19)	275*
a / Å	3.97475(7)	3.97676(7)	3.98290(8)	3.99729(9)
b / Å	5.69420(11)	5.69483(11)	5.69610(12)	*a*
c / Å	5.71840(11)	5.71836(11)	5.71757(12)	4.06373(11)
V / Å^3	129.425(4)	129.503(4)	129.714(5)	64.9315(28)
K				
Position Vector	{0,0,0}	{0,0,0}	{0,0,0}	{0,0,0}
U^{eq} / Å^2	1.1(3)	1.5(3)	1.3(3)	1.4(5)
Nb				
Position Vector	{½, 0, 0.511(3)}	{½, 0, 0.476(3)}	{½, 0, 0.468(3)}	{½, ½, 0.50(5)}
U^{eq} / Å^2	2.0(4)	1.14(15)	1.13(14)	1.1(7)
O1				
Position Vector	{0, 0, 0.543(2)}	{0, 0, 0.513(4)}	{0, 0, 0.505(3)}	{½, ½, 0.04(4)}
U^{eq} / Å^2	1.12(15)	1.2(2)	1.5(3)	1.3(3)
O2				
Position Vector	{½,0.248(1), 0.291(2)}	{½,0.249(1), 0.260(4)}	{½,0.246(2), 0.251(2)}	{½, 0, 0.53(4)}
U^{eq} / Å^2	1.30(10)	1.8(2)	2.16(17)	1.0(4)
MINORITY PHASE				
Space Group	*P*4*mm*	*P*4*mm*	*P*4*mm*	*Amm*2
a / Å	4.0085(5)	4.0077(5)	4.0096(4)	3.9840(4)
b / Å	*a*	*a*	*a*	5.7130(8)
c / Å	4.0442(10)	4.0464(10)	4.0500(8)	5.7024(9)
V / Å^3	64.983(20)	64.992(19)	65.112(17)	129.79(3)
χ^2	1.812	1.837	1.930	1.949
R_{wp}	0.0713	0.0733	0.0759	0.0705
R_p	0.0648	0.0654	0.0698	0.0610

* this value was fixed in the refinement (at a value extrapolated from the conventional data). If left to optimise independently the value became physically unrealistic. Though correlated with ADPs, the effect of fixing σ_l, to the final ADP values, is negligible.

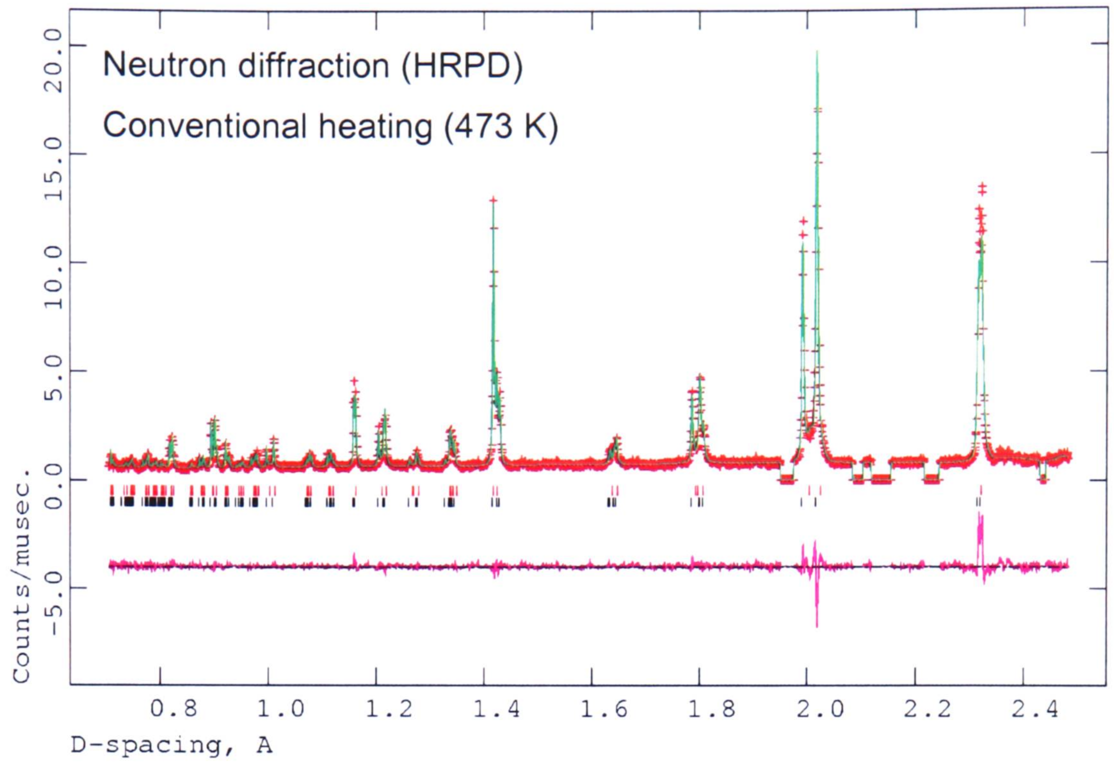

Figure 7.14 - Histogram for $KNbO_3$ (neutron diffraction, 473 K by conventional heating). Upper part of diagram shows the collected data (crosses) and structural model (line through the points). Below is the difference between measured and fitted data.

Owing to limited beam time, data were recorded at significantly fewer temperatures here than was possible for barium titanate. It was therefore much more difficult to find trends and anomalies in the data. However, what is clear is that the structure of the microwave heated sample is tetragonal at all temperatures measured, whilst the conventionally heated sample is orthorhombic at temperatures in the same range. The second phase for the refinement of the sample under microwave irradiation has been fitted to an orthorhombic structure. The identity of the majority and minority phases has therefore been inverted. The implication is that the sample is near T_c and hence much hotter (~100 K) than the 392 K measured temperature, for microwave heating.

In order to evaluate thermal expansion for the two different structures, a common sub-structure must be used. An orthorhombic unit cell contains exactly twice the number of atoms as a tetragonal cell. Thus both structures can be considered on an orthorhombic lattice and the unit cell volume compared between the two heating methods. This is shown in Figure 7.15.

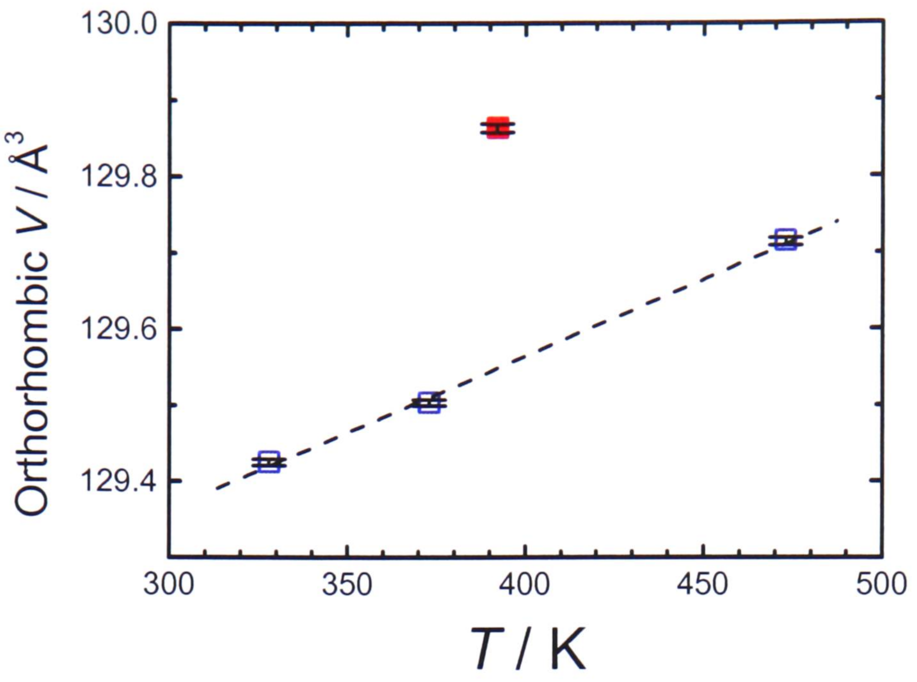

Figure 7.15 - Unit cell volume (as calculated from the orthorhombic lattice, equal to twice the volume of tetragonal unit cell) as a function of temperature for both microwave (■) and conventional heating (□).

It is clear from Figure 7.15 that the (orthorhombic) unit cell volume is significantly greater for the microwave heated sample than by conventional heating. Given that these are two different phases, this is hardly surprising. Some thought should be given, therefore, to the accuracy of the measured temperature. Any errors would be associated with thermal gradients in the sample rather than inaccurate equipment. Another indication of large thermal gradients in the sample would be increased peak width. Though unstable in the microwave refinement, σ_1 is comparable with the data measured in the absence of microwaves and χ^2 is also comparable. However, ADPs for the microwave refinement do show larger errors than for the conventional heating. This points to some fluctuations in their values across the sample. Nonetheless as the measurement is time averaged over the recording period, the recorded temperature does represent a good average, fluctuating by less than 10 K from the quoted value. To conclude, though there is likely to be a significant error in the quoted temperature, it is small relative to the apparent discrepancy indicated in Figure 7.15 and there is thus persuasive evidence that the sample undergoes phase transformation at a much lower temperature than the literature value when heated with microwaves.

7.4 Discussion

Though interesting, the results concerning potassium niobate are of limited value and generally serve only to confirm the trend observed for barium titanate. It is instructive therefore to limit the discussion here to barium titanate in the most part and assume that any conclusions can be generalised to other iso-structural materials with comparable electronic properties.

When bathed in microwaves, barium titanate showed a lowering of the Curie temperature, T_c, at which the ferro to paraelectric phase transition occurs. Silver iodide (Chapter 5) showed a similarly depressed phase transition temperature in the presence of microwave radiation. It was proposed, for silver iodide, that a low-lying lattice vibration is responsible for displacing ions from their mean positions and driving the displacive phase transition. Furthermore, the theory has been applied to binary oxides, such as BaO, with some success.[142] Barium titanate is more studied than silver iodide and the nature of the ferro to paraelectric phase transition itself has been the subject of much interest, owing to its importance in the dielectric behaviour of the material in relation to device applications.[123] However, the process is not yet fully understood, largely due to experimental difficulties in studying phonon behaviour.[124]

Two theories have been proposed to explain the observed ferroelectric behaviour. *Soft-mode theory*, based on the work of Slater[143] and Cochran,[130, 144] treats the phase transition as displacive. In the cubic phase there is a low-lying transverse-optic (TO) mode, which is associated with random displacement of the titanium ion about its mean position. On cooling to T_c this mode is frozen, resulting in a permanent displacement and a spontaneous polarisation along one of the original cubic axes.

Alternatively, *order-disorder theory*, based on the work of Comes *et al.*,[145] describes the cubic phase as a result of static disorder in the Ti position, rather than dynamic motion.[146] There are eight potential energy minima located a small distance from the central position and in the direction of the eight faces of the TiO_6 octahedral. The Ti ion is randomly displaced to one of these off-centre positions and the mean position, averaged over a macroscopic crystallite, is in the centre. On cooling to T_c the local field is altered and the eight degenerate positions are split; with four mutually adjacent positions becoming more favourable. The mean Ti position is then observed to be displaced from the centre along one of the original cubic axes.

Both theories have been shown to apply to various different members of the perovskite family. Inelastic neutron diffraction[147, 148] and Raman scattering[149, 150] have shown the validity of soft-mode theory as applied to $PbTiO_3$ and $SrTiO_3$; whilst diffuse X-ray scattering and electron diffraction have been used to confirm the order-disorder theory.[145] Yet, the behaviour of barium titanate has been difficult to ascribe: phonon damping making determination of the phonon behaviour near the phase transition difficult.[128]

7.4.1 Soft mode behaviour

If we were to suppose that the explanation for the reduced Curie temperature is the same as proposed for silver iodide, then soft-mode behaviour would be expected. If such a low-energy TO mode does exist for barium titanate, then it could be preferentially excited by the microwave field. As the Curie temperature is approached from below this mode may then be driven by the field at $T < T_c$. Thus the mode is unfrozen, polarisation is removed and the structure defaults to the cubic, paraelectric phase. In order to assess the validity of this theory it is necessary to ascertain whether such a TO mode does exist. Takeuchi and co-workers[128] have performed detailed density functional theory calculations on the frontier orbitals of $BaTiO_3$; orbital symmetry arguments indicate that transition density at the HOMO and LUMO give useful information on the preferred motion of the constituent ions in the phase transition. The calculations modelled the structure using only TiO_6 clusters (Ba ions are shown to produce bands far from the Fermi energy and therefore are inconsequential in such calculations). On all clusters for which they performed calculations, they found that the direct product of HOMO and LUMO gave the lattice distortion that was both optical and lead to the tetragonal phase (e.g. Figure 7.16). Thus, their calculations support the existence of a TO mode involved in the ferro to paraelectric phase transition.

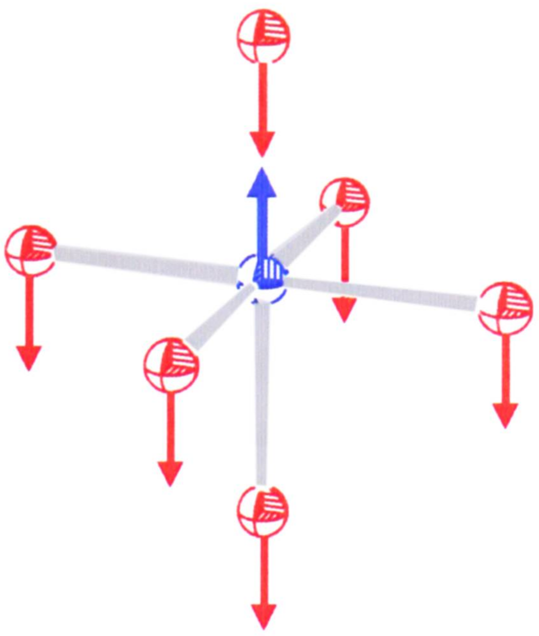

Figure 7.16 - Transverse optic vibrational mode calculated for TiO_6^{8-} cluster.

A theoretical treatment of an iso-structural system (strontium titanate) has been performed by Silverman,[151] treating the coupled motions of adjacent unit cells as an array of viscously damped harmonic oscillators of uniform density, N. The dielectric permittivity, ε^*, for such a system is given by:

$$\varepsilon^* = 1 + \left(\frac{Nq^2}{m}\right)\left(\frac{1}{\omega_0{}^2 - \omega^2 + i\omega\gamma}\right) \tag{7.6}$$

where q is the charge on the oscillator, m is the oscillator mass, ω_0 is the resonant frequency of the soft-mode driven by the microwave field of frequency ω, and γ is the damping constant. The frequency of the soft-mode is anomalously low compared with other non-paraelectric, crystalline materials, but still large compared to the field frequency. Once again considering only titanium and oxygen ions, the model treats coupled chains of Ti and O ions in the [100], [010] and [001] directions of the cubic unit cell to be uncoupled from each other. In other words, shear forces are neglected. This facilitates a one-dimensional strategy for modelling the system and only chains in the [100] direction need be considered. The k=0 mode has the correct behaviour for the TO mode of interest, driven by the microwave field, where the field is characterised by propagation vector, κ. The absolute value of κ is sufficiently small that the phase difference over a domain with dimensions large compared with the unit cell, but small compared with the sample, can be neglected. In Silverman's simple model, both anions and cations are treated as having equal mass and charge. The microwave field virtually excites a polarisation mode phonon (polaron) of frequency ω. This polaron is then destroyed with the simultaneous destruction of an acoustic phonon and the creation of an optical phonon.

The model is shown to correctly reproduce the microwave-frequency dependent behaviour of strontium titanate with damping of the induced polarisation mode a consequence of multi-phonon interactions: three and four wave mixing, as described in Section 1.1.1. The most significant obstacle with the model is that the separation of acoustic and optical branches for a diatomic chain is large: of the order of optical frequencies. However, the work of Cochran[152] suggests that the low-lying transverse optical branch crosses the longitudinal acoustic branch at some point within the Brillouin zone (Figure 7.17b). The origin of the damping is undetermined, though it is speculated that defects (intrinsic and extrinsic) may play a role.

7.4.2 Order-disorder behaviour

Though undeniably present, soft-mode theory cannot be used to explain all features of barium titanate. For example, Raman selection rules are violated in the cubic phase, suggesting the existence of disordered local distortions in the paraelectric phase.[153-155] The diffuse X-ray scattering measurements of Comes and co-workers[145] revealed phase-dependent streak patterns well above the ferroelectric transition temperature for both $KNbO_3$ and $BaTiO_3$. These they attribute to local ordering, in the form of static chains of ions. Furthermore, EXAFS (Extended X-ray Absorption Fine Structure) studies provided the position pair distribution function.[156-159] $BaTiO_3$, $KNbO_3$ and $PbTiO_3$ all show a double peaked distribution, even far above T_c, with a minimum at a distance corresponding to the ideal cubic structure. Notably, EXAFS measurements showed only a single peak for Ta and Ti ion positions in $KTaO_3$ and $SrTiO_3$ respectively.

A density functional theory study of $BaTiO_3$ reveals interesting behaviour of the potential energy surface along the O–Ti–O co-ordinate.[127, 136] For Ti displacements along this axis the calculations show a double minimum, approximately 0.02c either side of the central position, lending credence to the notion of static disorder. The study also shows a strengthening of the covalent Ti-O bonding along this axis as the cubic phase is cooled towards the Curie temperature, favouring ion correlation and local ordering. Experimental studies by high resolution neutron diffraction show similar results in a range of materials.[160]

Though difficult to measure, several workers have had success in calculating the phonon dispersion of both $KNbO_3$ and $BaTiO_3$.[129, 134, 139, 161, 162] Tinte and co-workers[134] use a full-potential linear muffin-tin orbital (LMTO) approach to calculate orbital mixing and appropriate energies for these materials. Each model correctly reproduced the experimental series of phase transformations accurately. The calculated phonon dispersion for the cubic phase is shown in Figure 7.17.

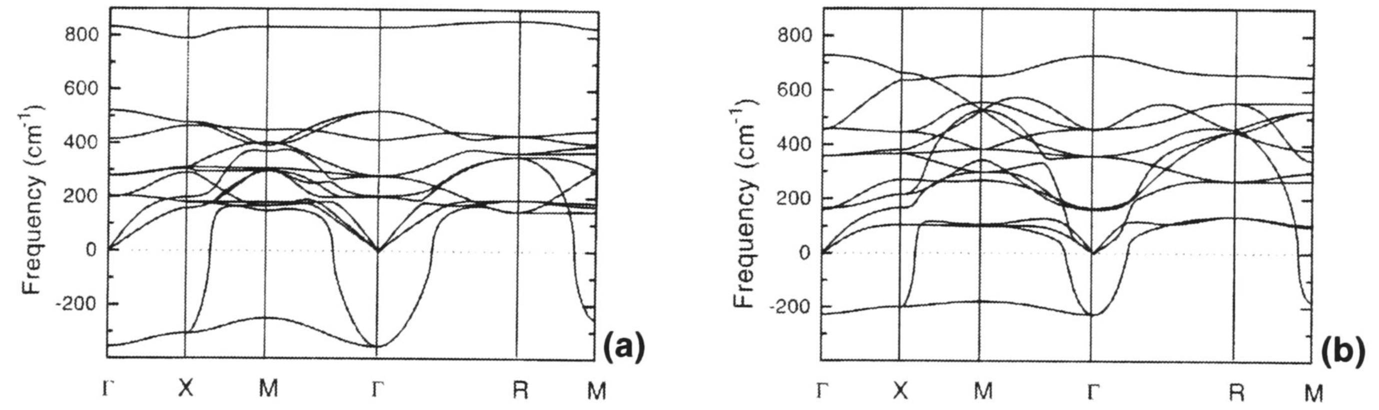

Figure 7.17 - Calculated phonon dispersions of (a) $KNbO_3$ and (b) $BaTiO_3$ in the cubic structure at the experimental lattice constant. Imaginary phonon frequencies are represented as negative values.[134]

Both (a) and (b) in Figure 7.17 show an unstable phonon with pronounced two-dimensional character. With reference to the labels in Figure 7.17, there is an imaginary frequency for Γ towards X and M, yet stiffening significantly towards R. The instability is thus confined to three quasi-two-dimensional 'slabs' of reciprocal space, intersecting at Γ. This is the fingerprint of a 'chainlike' unstable localised distortion of the Ti displacements in real space, as suggested by order-disorder theory.

Computational models of barium titanate have been attempted,[125] but have proven insufficiently detailed for our purposes. The behaviour of $KNbO_3$ has been successfully investigated using a molecular dynamics approach in order to try to rationalise the two theories and understand this unusual behaviour.[126] The resulting model correctly reproduced the sequence of phase changes and the diffuse X-ray scattering measurements, indicative of disorder above the Curie temperature. Furthermore, a softening of the unstable low-lying TO mode was observed on cooling to T_c, as suggested by soft-mode theory.

However, softening of this mode is not limited to k=0, but is observed over large regions of the Brillouin zone. They demonstrate that local order must exist, in the forms of correlated chains. Furthermore, they demonstrate that only dynamic chains can explain both the observed soft-mode and order-disorder behaviour. The simulations show that chain-like clusters are pre-formed well above T_c; the chains being defined by rows of distorted primitive cells oriented along the three cubic axes, with atomic displacement along the chains correlated with one another. The softening of modes, corresponding to the onset of coherence of families of chains, correlates with the sequence of phase transitions.

Hence a model can be formulated to unify both soft-mode and order-disorder theories. The random displacements of ions are correlated and form locally ordered chains. These chains are dynamic and their movement behaves as a soft-mode. Within the framework of this model, the microwave-induced lowering of T_c and the increased cell parameter can both be explained by the interaction of the microwave field and this low-lying TO mode. However, it cannot explain why the atomic displacement parameters (ADPs) are reduced. Common sense dictates that excitation of a phonon mode would enhance atomic vibrations and hence ADPs, whilst the static component is not directly affected. Another interaction must therefore be involved in order to explain these discrepancies.

7.4.3 Electron – phonon interactions

There is evidence of a connection between local ordering and phonon modes.[133, 163-165] A phenomenological model has been created by Girshberg and co-workers [133, 164] that may provide further insight into the behaviour of barium titanate. The model is based on the following three assumptions:

(i) The metal ions undergo spontaneous off-centre displacements (referred to as the pseudo-spin sub-system),

(ii) The system has a soft-mode, which could lead to a purely displacive transition, and

(iii) The off-centre displacements and the soft-mode interact with each other.

The method invokes electron-phonon interactions as a means of accomplishing (iii). In the interband theory of ferroelectricity[138] there is generally believed to be a strong interaction between electrons and transverse optical (TO) phonons. This is consistent with the microwave heating of solids where the microwave field polarises the electrons, exciting them into a vibrational mode (a polaron). The energy of this polaron is transferred to phonons through this interaction. The energy of a phonon and the polaron are used to create a new phonon of greater energy. Girshberg proposes that in addition to this there is a strong interaction between electrons and longitudinal optical (LO) phonons. This interaction leads to the creation of spontaneous local distortions in the paraelectric phase. It is known that this interaction is strong because of the large polaronic mobilities.

The physical picture that emerges from their calculations (which are complex and beyond the scope of this discussion) is that the mobile ions (mainly Ti in the case of barium titanate) are displaced to off-centre positions. This displacement is a vector (having magnitude and direction) and is represented by a new term: the 'pseudo-spin' of the ion. Displacements in different cells are in different directions and the average over a macroscopic crystallite is zero. The ions vibrate about these new positions and vibrations have both transverse and longitudinal branches. However, due to the fact that the energy is non-linear in the displacements, the Hamiltonian to describe the system has normal phonon terms, pseudo-spin terms and interactions between them.

As in the normal interband theory, the electron–TO phonon coupling leads to a softening of the TO mode and is the origin of ferroelectricity below T_c. The spin–phonon interaction is therefore large, creating an indirect spin-spin interaction. This interaction turns out to be much larger than the direct spin-spin interaction and accounts for observations of local ordering.

The phase transition occurs at T_c where the Ising-type model shows that the system undergoes an order-disorder phase transition. The soft-mode, rather than being directly involved (as in soft-mode theory) plays an unusual role as the interaction mediator: a spin-spin interaction due to the soft mode determines the spin ordering and the phase transition. The model shows good agreement with experimental observations for both $KNbO_3$ and $PbTiO_3$, despite the different properties of these materials.

As regards microwave heating, much of the explanation is as before: the microwave field excites a polaron, which interacts with a soft-mode phonon. Excitation of this phonon may induce phase transition to the paraelectric phase at $T < T_c$. Consequently, it would also result in the observed larger cell-parameter near T_c. In addition, as this soft-mode is the carrier for local-ordering interactions it is quite conceivable that the degree of ordering is affected by microwaves and could therefore show the anomalously small ADPs, observed for barium titanate. The hypothesis would therefore be that excitation of the mediating soft-mode increases the strength of the spin-spin interaction and increases the degree of order in the system, thus reducing the static disorder component of the ADPs, as observed experimentally.

On the atomic scale, this is the only description capable of explaining all the observations of microwave-irradiated barium titanate. However, on a larger scale size the microstructure, including crystallite size and formations of local domains may be important.

7.4.4 Microstructure

Ferroelectric barium titanate, i.e. below T_c, does not exist as a single continuous structure with all tetragonal distortions aligned uniformly. Rather the structure consists of micro-domains of set polarisation, arranged so that the net polarisation of the material is zero. It is the formation of these domains at T_c that allows the release of stresses induced in the crystal. Domains are arranged with either 90° or 180° boundaries (Figure 7.18). The 90° boundaries are more favourable energetically and this results in a typical 'banded' or 'herringbone' microstructure observed in samples of barium titanate[135] and similar materials.[166, 167]

The microstructure of single-crystal and polycrystalline barium titanate has been studied by SEM (scanning electron microscopy) and SFM (scanning force microscopy) in order to obtain clear pictures of these micro-domains. For particle sizes above 3 μm the microstructure is independent of the particle size and a series of banded domains is observed with domain widths of approximately 1 μm.[135] A small region of disorder exists between domains; the domain walls therefore have a finite thickness, observed to be between 0.03 μm and 0.15 μm, depending on grain size and preparation method.[132]

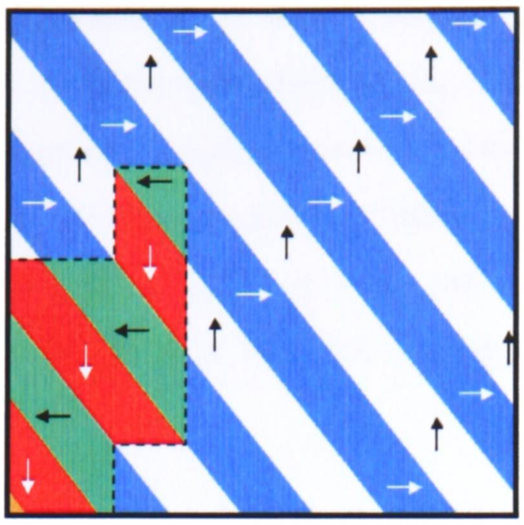

Figure 7.18 – Two-dimensional representation of domain microstructure found for barium titanate. Light-dark boundaries are at 90°, whilst dotted boundaries are at 180°. Arrows indicate orientation of polarisation.

The dynamics of the domain structure under the influence of electric fields have been studied by several authors,[137, 168-170] owing largely to the importance of ferroelectrics as technologically important materials. There are a number of different theories to describe the observed behaviour in barium titanate and similar materials. The theory of Kittel[171] is generally accepted and states that polarisation at the unit cell level 'flips' under the influence of an a.c. field, resulting in the movement of domain walls. This movement has an inertial component, resulting in a phase lag between field and polarisation at appropriate field frequencies (the origin of dielectric microwave heating). More recent work by Arlt and co-workers[172] point to gross shear of the 90° domains, with resonant frequency in the GHz (microwave) region. Therefore, under the influence of an electric field with microwave frequency domains will move dynamically with the field.

For longer term exposure Potter and co-workers[173] have performed a number of Monte Carlo simulations of the behaviour of a model two-dimensional ferroelectric under the influence of an applied alternating field. The model was shown to qualitatively model tetragonally-distorted ferroelectric materials and provide the experimentally observed response under a number of conditions. The effective frequency of the applied field was varied by altering the number of steps allowed for the system to attain equilibrium. Selection of a frequency such that polarisation lagged behind the field (as would be the case for microwave frequencies) produced an interesting result. The domain walls moved under the field's influence, as expected, and merged to produce fewer, larger domains. It is this action that may contribute to reduced atomic displacement parameters in barium titanate. As the domains grow and the number of domains is reduced, so is the proportion of the structure existing within domain walls. The structure is therefore more ordered and the static component of the ADPs is reduced. This clearly applies to the tetragonal phase, below T_c, but cannot be applied to the paraelectric cubic phase. However, it may serve to pre-order the structure so that on formation of the cubic phase local order is retained; a theory given some credence by the observations of Comes *et al.*[145]

Equally important may be the role of defects, such as ferroelectric domain walls, in phonon transport and redistribution. For barium titanate it can be shown that phonon scattering is controlled by domain walls.[174] If the effect of microwaves is to create larger domains then the processes of phonon scattering and the corresponding redistribution of energy through other phonons will be restrained. The result would be slower redistribution of energy and an increased probability of a non-equilibrium density of states.

7.4.5 Inhomogeneous heating

The final factor that must be considered in this system is temperature measurement. The technology used to measure temperature is very accurate. However, there is no guarantee that the measured temperature is necessarily representative of the sample as a whole. Nonetheless, the observations (larger cell-parameter *versus* smaller ADPs) are inconsistent with a sample where the bulk is either significantly hotter or cooler than the measured temperature.

However, the σ_l values (representative of stress in the sample) indicate that something unusual is occurring. With microwave heating, as the temperature increases the power necessary to attain that temperature also increases. It can be seen in Figure 7.12 that particle stress also increases with temperature, and thus microwave power. One source of stress would be inhomogeneous temperature distribution in the sample; the field being concentrated at inter-particle boundaries, for example. Thus the difference between conventional and microwave heating, in terms of σ_l, can be easily explained. Note that the same explanation cannot be applied to explain the other differences.

7.4.6 Conclusion

It is clear that some inhomogeneous heating of barium titanate does occur, but that the majority of observations cannot be accounted for by this process. The ferro to paraelectric phase transition has both displacive and order-disorder characteristics and a unified model describing the soft-mode behaviour of locally ordered chains in the paraelectric phase can be applied in order to explain both forms of behaviour. Excitation of a low-lying transverse optical mode (shown to be present for barium titanate) can provide a rationale for the lower value for the Curie temperature and anomalously large thermal expansion at approximately the same temperature. Extension of this model to describe the interactions of adjacent off-centre displacements, as mediated by a soft transverse optical mode, allows static disorder to be linked with excitation of particular phonons. This is a coherent framework in which to explain all observations made for barium titanate under the influence of a microwave field. Microscopic structure is important, not only for its role in inhomogeneous heating, but may also have a role in pre-ordering the structure below the Curie temperature, to create less static disorder in the paraelectric phase.

8 Improved equipment for future work

The preceding sections have shown that diffraction is an insightful technique for the observation of crystalline solids under the influence of microwave radiation. However, they have also demonstrated that the design of the applicator is the key to a good experiment. In order to be able to apply these techniques more widely it is necessary to adapt equipment for use on a commercially available X-ray diffractometer. As it is primarily powdered materials that are of interest, the Philips X'pert system (θ, 2θ geometry, Cu K_{α} source), to which we had ready access, is a suitable choice.

8.1 Applicator Design

The microwave applicator used previously on this instrument has several disadvantages, not least of which is poor efficiency of heating. The preceding experiments showed that the all-waveguide construction, as used with the HRPD station at ISIS, is the most effective and reliable applicator. Therefore, a new applicator was designed for use with the Philips X'pert system, incorporating many of the features of these other applicators. The criteria for design are therefore:

(i) Must be compatible with Philips X'pert system, i.e. the applicator will hold and rotate the sample in correct alignment, with θ, 2θ geometry, for recording of a diffraction pattern.
(ii) Has an aluminium foil window to allow passage of X-rays.
(iii) Based on circular waveguide of diameter sufficient to support the TE_{11} fundamental mode.
(iv) Sample positioned approximately a quarter wavelength from the waveguide termination, for maximum field intensity.
(v) The ability to vary the effective waveguide length by use of a sliding short-circuit termination.
(vi) Waveguides must be able to enter safety hutch without allowing X-rays to escape.

The reactor shown in Figure 8.1 was designed with these criteria in mind. This involved the manufacture not only of a new applicator, but also of an aligned sample stage so that the part projecting into the applicator was non-metallic. Another difficulty with this design was that the waveguide must come in from the top of the hutch (for safety and practicality), yet the applicator is aligned towards the front of the hutch. Clearly, a bend is required in order to resolve this situation. Bends with efficient transmission are based on large radius, rectangular cross-section waveguides, yet the applicator is circular in cross-section and there is insufficient space for a circular to rectangular transition piece. The solution is to construct a mitre bend from circular waveguide tubing (Figure 8.2). Though not perfect, adequate transmission is achieved.

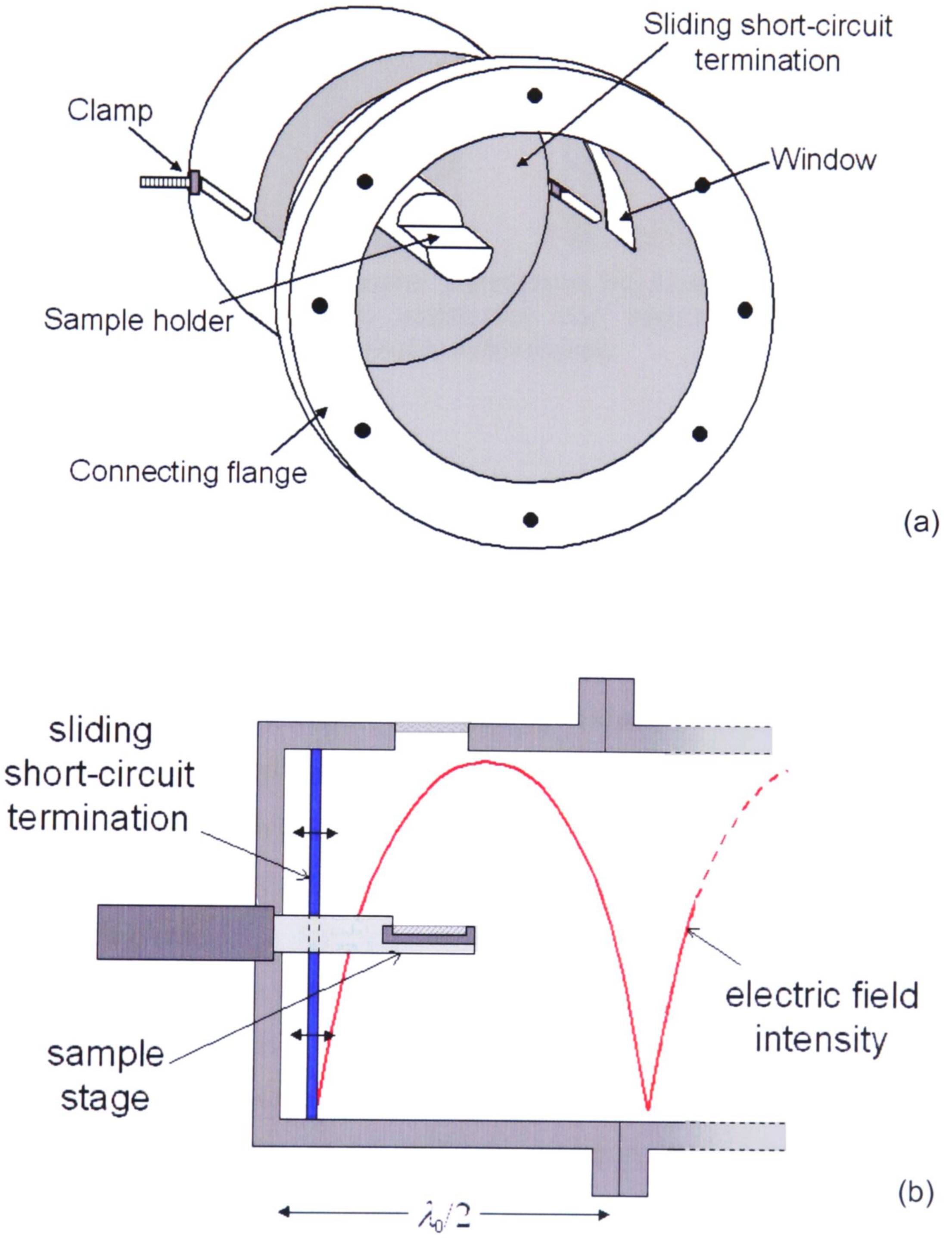

Figure 8.1 - The improved microwave applicator for use with the Philips X'pert instrument, (a) in perspective, (b) in cross-section.

The new applicator has several advantages over that used in Chapter 5: the power is limited by the magnetron, not the apparatus; the wavefunction can be adjusted to focus maximum power at the sample position; and lengthy experiments are possible without the danger of overheating.

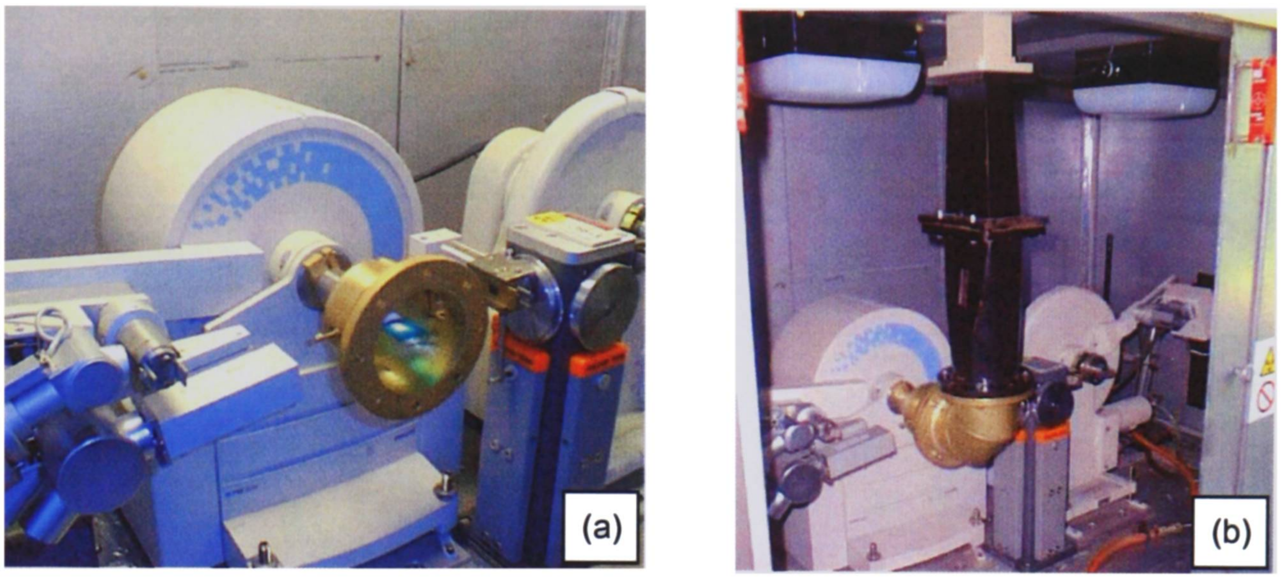

Figure 8.2 - Photographs of improved microwave applicator attached to Philips X'pert system diffractometer, (a) applicator and sample stage, (b) with all waveguide attachment connected (note, mitre bend).

8.2 Experimental

The first test of the apparatus was to ensure that it would heat efficiently. To this end, a small amount of charcoal powder (known to be extremely lossy) was placed on a glass slide, at the sample position. A fibre-optic thermometer (Nortech Fibronic NoEMI-TS series fluoroptic thermometer) was fed through one of the slots in the reactor wall (guides for the terminating short circuit) and to the sample. With microwave heating at 100 W, a rapid rise in temperature was observed of the order of 30 K per minute. Heating was stopped after a few minutes (having reached a temperature of 400 K). On inspection, the glass slide appeared to have melted. This could have been due to the heat generated in the charcoal, requiring the charcoal to reach a much higher temperature than 400 K. An alternative explanation is that the microwaves are coupling directly with relatively mobile ions in the glass. In either case, the ability of microwaves to heat at the sample position has been proven.

The next test of the applicator was to ensure that diffraction data of sufficient quality can be collected. Silver iodide (a material studied previously) was placed on a glass slide in the applicator and the diffraction pattern was taken without microwaves (unfortunately the complete apparatus was not ready for use at this stage). The structure was refined against the pattern using GSAS[92] and EXPGUI.[93] The fitted model (as fitted to β-AgI structure, with γ-AgI impurity) is shown in Figure 8.3.

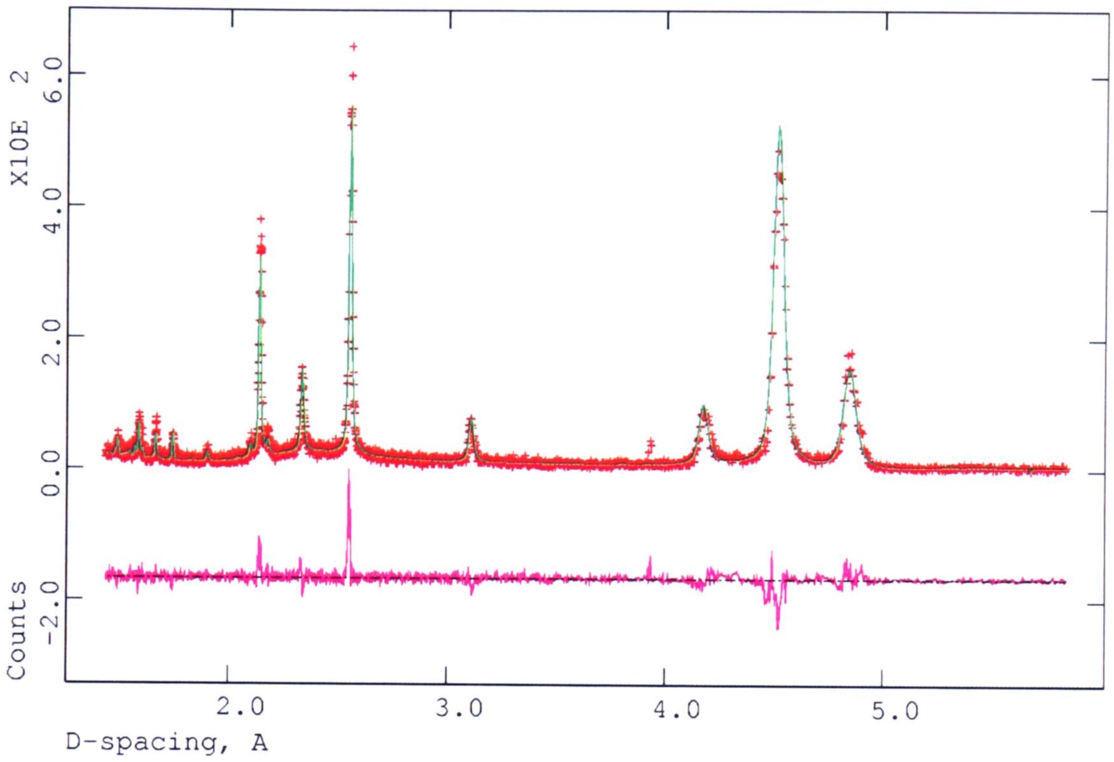

Figure 8.3 - Powder X-ray diffraction pattern of silver iodide at 300 K, using prototype applicator and conventional heating. In the upper part of the diagram, crosses show the experimental data and the line through the points is the refined structural model. Below is the line showing the calculated difference.

A good refinement is possible, as can be seen visually from Figure 8.3 and from Table 8-1. Table 8-1 also shows a comparison between this dataset and that taken for silver iodide using the previous microwave applicator (Section 5). It can be clearly seen that the diffraction measurement performed with the new applicator is superior. It also appears that the cell volume is larger in the waveguide applicator. However, it should be noted that the poorer fit for the coaxial applicator will tolerate more correlation between variables and so increase the likelihood of errors.

Table 8-1 - Comparison of diffraction data for silver iodide using coaxial-feed and waveguide-type *in-situ* applicators.

Experiment	Coaxial applicator at 353 K		Waveguide applicator at 298 K	
Phase	β-AgI	γ-AgI	β-AgI	γ-AgI
Space Group	$P63mc$	$F\bar{4}3m$	$P63mc$	$F\bar{4}3m$
Phase Fraction (%)	68.5(17)	31.5(17)	64.3(15)	35.7(15)
S_S	0		387(1)	
$a = b$ / Å	4.5983(9)	6.5094(12)	4.6726(6)	6.6008(7)
c / Å	7.526(2)	6.5094(12)	7.643(1)	6.6008(7)
V / Å^3	137.81(5)	275.82(9)	144.51(4)	287.60(5)
Ag *position vector*	{⅓, ⅔, 0}	{0, 0, 0}	{⅓, ⅔, 0}	{0, 0, 0}
U^{eq} / Å^2	-0.016(12)	-0.06(3)	0.028(8)	-0.004(8)
I *position vector*	{⅓, ⅔, 0.62(2)}	{¼, ¼, ¼}	{⅓, ⅔, 0.618(2)}	{¼, ¼, ¼}
U^{eq} / Å^2	-0.074(6)	-0.05(3)	-0.045(4)	-0.019(5)
χ^2	4.383		1.458	
R_{wp}	0.2780		0.1715	
R_p	0.2162		0.2207	

In order to fit these data a modified parameter set must be used. Normally, for measurements on samples without microwaves and not requiring a protective atmosphere, diffraction data is recorded with the sample on a plate positioned to be in alignment with the X-ray beam and the detector. This position is calibrated precisely and the vertical displacement of the sample relative to its ideal position is zero. However, having constructed a new sample holder, the alignment must be recalibrated. The form of the profile function is as described in Equations (8.1) - (8.3). It is a pseudo-Voigt function, i.e. a convolution of Gaussian (G) and Lorentzian (L) elements, as in Equation (8.2), where Γ and the mixing factor, η, are governed by the peak width. The modified 2θ difference, $\Delta T'$, has contributions from asymmetry, A_S, sample shift, S_S, and sample transparency, T_S. The sample position in this case is uncalibrated and consequently the sample-shift term is non-zero. In this fit, S_S is refined to a value of 386.8 ±0.6. The consequence of this is that intensity falls off at higher angle (i.e. lower d-spacing) more sharply than in previous refinements. The standard deviation quoted for the sample displacement is small and once the accurate value of S_S has been found, structure refinement is straightforward. It is therefore possible to perform diffraction measurements of sufficient quality for structure refinement, over long periods and at higher power levels than was possible for coaxial cables, without danger of the apparatus overheating.

$$H(\Delta T) = \sum_{i=1}^{n} g_i F(\Delta T') \tag{8.1}$$

$$F(\Delta T') = \eta L(\Delta T', \Gamma) + (1-\eta) G(\Delta T', \Gamma) \tag{8.2}$$

$$\Delta T' = \Delta T + \frac{f_i A_S}{\tan 2\theta} + S_S \cos\theta + T_S \sin 2\theta \tag{8.3}$$

For the first experiment using the new applicator, it was decided to look for a material with a simple crystal structure and which is known to be lossy. The material chosen was silicon. A slurry of the sample in acetone was made and a glass dropper was used to transfer some to a glass slide where the powder dried to the glass surface. A quick scan over a large angle range (10°<2θ<70°) revealed sharp Bragg reflections. It was decided to improve temperature resolution by concentrating on a single Bragg reflection. The most intense peak is the [111] reflection at ~29° 2θ.

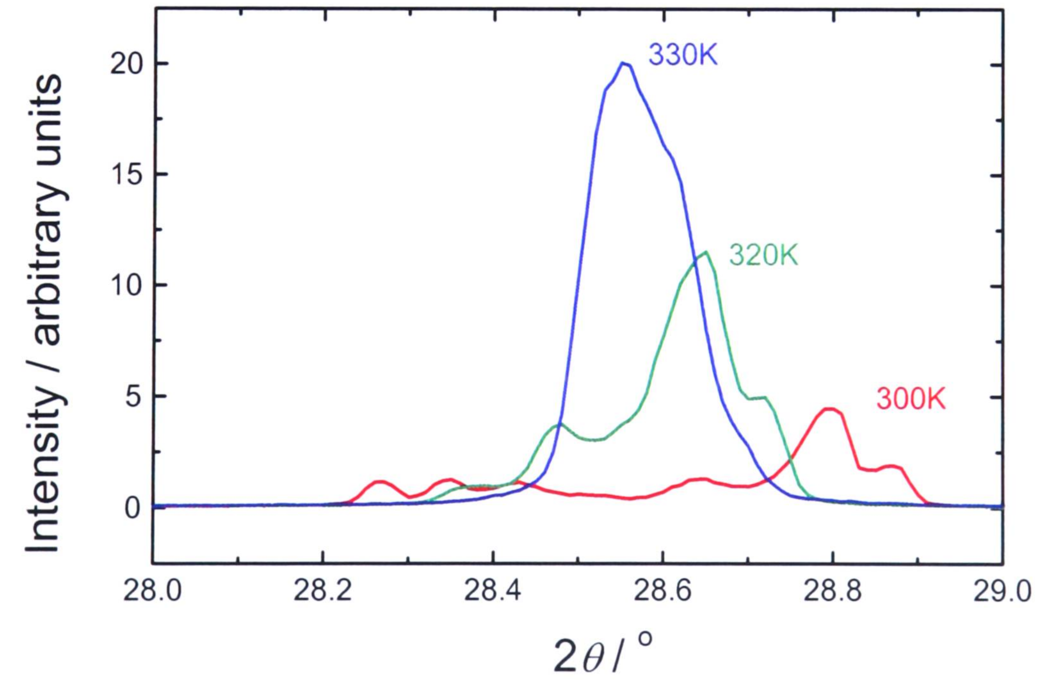

Figure 8.4 - Evolution of the silicon [111] reflection with temperature under microwave heating.

Figure 8.4 shows that heating of silicon results in a shift of the Bragg peak to lower angle, i.e. larger d-spacing, consistent with thermal expansion of the unit cell. Unfortunately, after the measurement at 330 K the peak disappeared from the scans. It appears that the glass slide, being used as a sample holder, had melted. This seems to be a case of thermal runaway: at room temperature the glass does not couple with the microwaves to a significant extent, but at higher temperatures the conduction levels populate and the glass begins to heat strongly, melting rapidly. Previous testing had failed to spot this problem, as the glass does not heat rapidly at ambient temperature.

For later experiments, it was proposed to use a square of polytetrafluoroethylene (PTFE) instead of a glass slide. PTFE does not interact with the microwave field. Furthermore, PTFE can be shaped and cut to allow practical incorporation of the temperature probe at the sample position. The PTFE square is thicker than the glass slide, so the sample shift parameter requires refinement for this new sample stage. This sample plate is shown in Figure 8.5. Note that a slot has been cut in the PTFE slide to accommodate the temperature probe and ensure that it is in intimate contact with the sample.

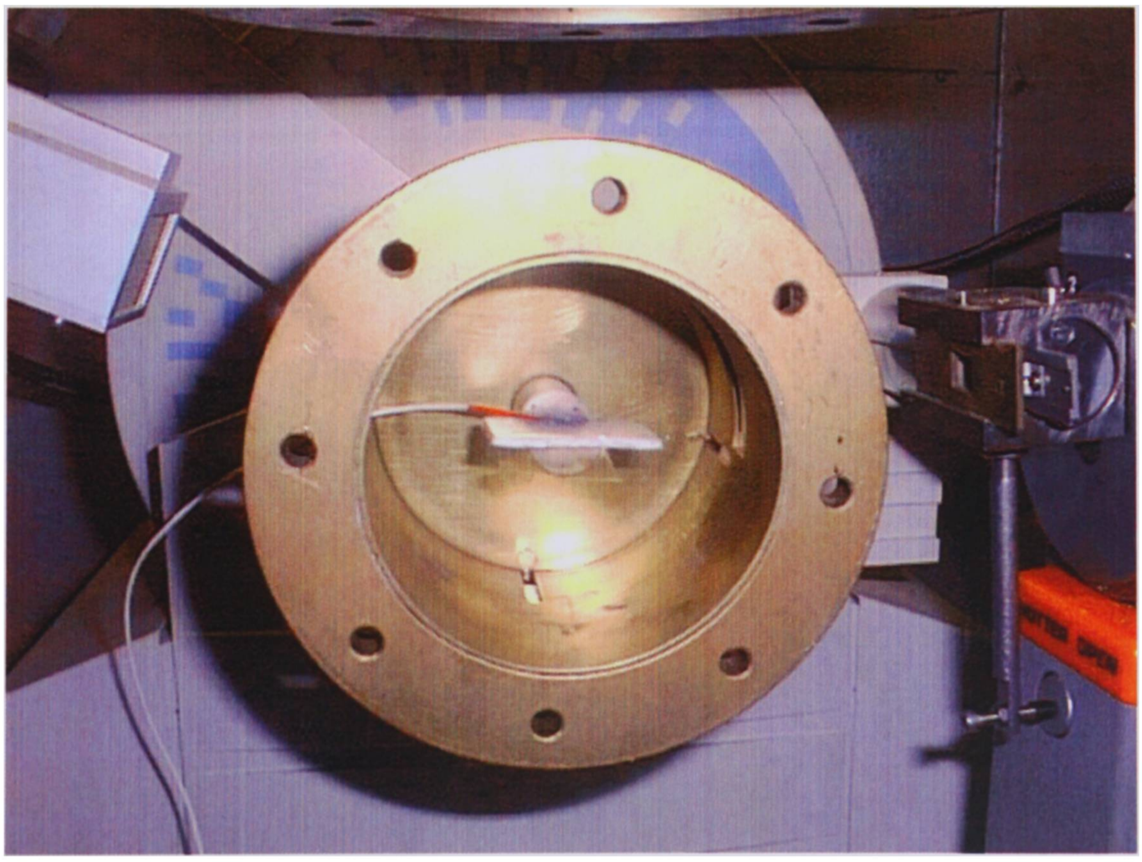

Figure 8.5 - Microwave applicator showing PTFE sample plate and temperature probe.

8.3 Discussion

The brief experiments performed with the new applicator act as proof of concept. It is now at a stage where full X-ray diffraction data may routinely be taken for a sample with and without microwave irradiation, in order to assess the effect of the microwave field on, amongst other things, thermal expansion and atomic displacement parameters. Unfortunately, the prototype was only completed in the last few months of my PhD and as such it falls to other students following on from my work to test the applicator in a real, *in-situ* monitoring experiment.

9 Nanoparticle synthesis using microwave induced plasmas

9.1 Nanoparticles

A potential application of microwave radiation, and particularly microwave-induced plasmas (introduced in Chapter 1), is the synthesis of *nanoparticles* – a form of matter with interesting and technologically very useful properties. Nanoparticles can be created from almost any solid material, crystalline or amorphous, with dimensions of the order of 1 to 100 nm. They have been found to be very interesting from a chemical perspective as they exhibit a range of intriguing physical and chemical attributes. Due to their small size they have a high surface to bulk atom ratio: surface effects cannot be ignored – as they can be with larger particles – and the material's properties are modified accordingly. Nanoparticle characteristics are therefore greatly affected by their size and they can thus be adapted for specific applications. Michael Faraday was one of the first to study this effect when preparing nanoparticles of gold and noticed that particle size altered the way they scattered light.[175] When suspended in water, particles with a diameter of 60 nm appear red, whilst particles with a diameter of 120 nm are blue. It is only in more recent years however that instrumentation has progressed to the point where these nanoparticles may be observed, examined and therefore better understood. Many more diverse applications have emerged as a consequence.[176]

9.1.1 Uses of nanoparticles

The manufacture of ceramics is one area where nanoparticles have been found to be advantageous. Traditionally ceramics have been made either from fine-powders, or by various sol-gel methods, employing an intimate mixture of the ceramic material. This powder is placed in an oven at high temperature (typically several hundred Kelvin) for several tens of hours to allow *sintering* (densification and amalgamation of particles) to take place. This process can be accelerated and improved dramatically by using nanoparticles instead of powder produced by grinding bulk material. Preparation methods for nanoparticles often result in a very narrow particle size distribution. This size uniformity allows the nanoparticles to pack more closely and the high proportion of surface atoms allows them to be deformed more easily.[176] Furthermore, as sintering and other reactions occur at the surface, the interfacial area for reaction is greater. Hence, sintering is much easier: sintering time is much less, and the process does not require such extreme temperatures. Furthermore the mechanical properties of the resulting ceramic are markedly improved, e.g. strength, hardness and durability.

Nanoparticles may also have very different electronic properties from the bulk material. Bulk silicon is a commonly used semiconductor and is useful in computer chips due to the size of its bandgap, its relatively low cost and the ease of fabricating devices based on silicon and its derivatives. However, the size and nature (i.e. indirect rather than direct) of the bandgap in silicon makes it useless for other applications and other semiconductors must be used instead, though they are much more expensive, e.g. when a different size of bandgap is required, or in small devices where a more-efficient, direct-bandgap semiconductor must be used. However, by using silicon nanoparticles of controlled size it is possible to tune the bandgap for a range of applications, see Figure 9.1. For example, light-emitting diodes could be made with material of pre-selected particle size and thus a selected bandgap to produce any colour desired. [176]

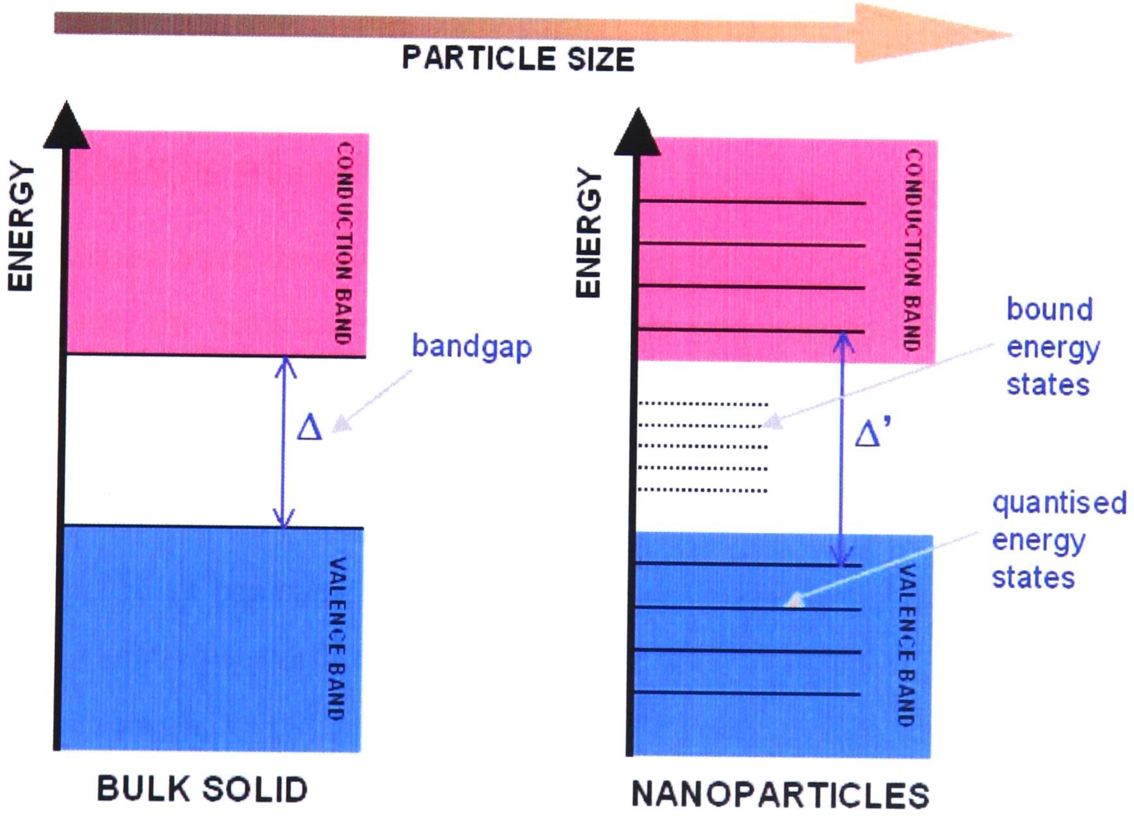

Figure 9.1 - Illustration of how the bandgap between valence and conduction bands varies as a function of the particle size. As particle size decreases energy becomes quantised, effectively increasing the bandgap energy between the lowest-energy conduction band state and highest-energy valance band state.

Magnetic nanoparticles can be extremely useful, in recording media and biology, amongst others. The uniformity associated with nanosized magnetic particles can give a much better specification with respect to the quality of recording media as they pack more evenly on the recording surface. Furthermore, needle-like particles used in recording give a more uniform magnetic response, improving the signal to noise ratio and prolonging the lifetime of the recording. The magnetic properties are greatly influenced by the particle size,[177] and so selection and synthesis of appropriate particle diameter is fundamental to improving recording characteristics and robustness of the recording medium. Wang *et al.*[178] have developed a straightforward, microwave-induced hydrothermal route to particles with needle-like geometry.

Similarly nanoparticles with a desired property can be grafted into polymer sheets or other materials to produce a plastic or other material with a specific colour, bandgap, optical or other property. One of the greatest challenges in the field of nanoparticles is producing uniform particles of the desired size, as the single most important factor in determining the size, and hence properties, of nanoparticles is the method of synthesis.

9.1.2 Synthesis of nanoparticles

Different techniques have been attempted, with varying degrees of success, to synthesise nanoparticles with the smallest possible dimension and highest possible purity. These techniques can be broadly classified either as solvothermal or as gas-phase condensation reactions.

The hydrothermal route has been highly successful in some cases. Forced hydrolysis of iron salts to give a rapid synthesis of hematite, maghemite or other related and mixed-metal oxides has been achieved with small particles (of the order of 100 nm), a small distribution of particle size and reasonable purity.[20, 179] The use of microwave heating can improve the quality of the product by speeding up the rate of nucleation and thereby limiting grain growth. The use of emulsions can be particularly beneficial when using microwave heating. Each emulsion droplet can act as a self-contained reactor producing a single particle and as all the emulsion droplets are of uniform size, so will be the particles. However, performing the reaction in solution has numerous problems associated with it, not least of which is the incorporation of solvent molecules into the nanoparticles. The size of these particles means that even a tiny amount of impurity can have a dramatic effect on the properties. This is especially important in ceramic manufacture where impurities result in weak, brittle products and dilution of desirable electromagnetic properties. A better way is to exclude, as much as possible, potential contaminants from the reaction. This can be done by performing the reaction in the gas phase.

Gas phase condensation reactions, a variation on typical chemical vapour deposition techniques, are a popular way of creating high-purity, nanosized particles. The technique requires a volatile precursor (or mixture of precursors), which is vaporised and then reacted in the gas phase to form the product. Some grain growth will occur (the amount being a function of the reactor temperature and characteristics) before the nanoparticle leaves the 'hot zone' and is collected on some surface. Often the collector is artificially cooled to quench any subsequent grain growth. The source of heat can have a huge effect on the size and properties of the nanoparticles formed in this way. Conventional heating is least effective, as it tends to heat the reactor walls most, encouraging deposition and degeneration of the product there. Direct pyrolysis, that is the use of a torch flame, has been employed in the past but is not much better as the flame chemistry can be quite complex. Furthermore, some fuel for the torch must be included into the carrier gas and will inevitably be incorporated into the products.

A novel technique, employed by Elihn *et al.*,[180] is the laser-assisted photolysis of ferrocene in the gas phase. Their method had the advantage of working under atmospheric pressure. By adjusting the pulse length and frequency of an ArF excimer laser they could obtain iron-containing particles with diameters between 3 and 100 nm. Though a relatively simple procedure, the short time-scale of reaction and relatively high pressure tend to produce impure nanoparticles.

A better way is to use an inert carrier gas, at low pressure, and heat the gas stream directly. This can be done by employing a plasma. The technique is particularly versatile, with many experimental variables that can be modified to produce the most desirable conditions for any given reaction. In this way films[181] and nanoscale particles of metals,[13] metal oxides,[12] chalcogenides,[14] ceramic,[45, 46] diamond,[4] crystalline and coated[182] materials may all be deposited uniformly. The synthesis of spherical particles with diameters from 100 nm down to 10 nm has been achieved in this way.[15]

Microwaves are not the only energy source used for plasmas. However, they do present some interesting properties, which are particularly useful in the production of nanoparticles. The main advantage is the relative temperature of the plasma itself. Microwave plasmas, especially in the afterglow region, are significantly cooler than other sources: grain growth is thus limited and smaller particles can be produced. Despite the lower temperature, the high-energy ions and neutral species present can be used to drive reactions at lower temperatures where they would otherwise be kinetically unfeasible.

Chou *et al.* carried out studies to investigate the effect of various experimental variables on the nanophase product.[13] They used ferrocene as the iron precursor, hoping to deposit iron nanoparticles. If the precursor was injected into the hot zone of the reactor it was found that relatively large particle sizes were common (ca. 50 nm), whilst much smaller (ca. 10 nm) particles were seen to result from injection into the cooler afterglow region. Another consideration is highlighted by their work: the choice of carrier gas. Only under reducing conditions, i.e. hydrogen gas, were iron nanoparticles observed. With all other gases – even inert species such as argon – iron oxide was the product (a result of trace impurity gases). Furthermore, the product in all cases was mixed with graphitic carbon, a bi-product of ferrocene breakdown. In order to manufacture a purer product it will be necessary to select 'cleaner' precursors.

Vollath *et al.* have improved on the technique and have successfully synthesised nano-crystalline particles of molybdenum and tungsten sulphides (ca 50-100 nm),[14] and maghemite (ca. 5-10 nm).[16] They used metal carbonyl and metal chloride precursors which fell apart easily in the plasma to yield the metal and carbon monoxide or chlorine gas. Consequently very little carbon or other impurity was deposited with the product. The only variable they found of any significance to the nature of their product was the plasma temperature, which notably affected particle size. This is a good example of a modern, clean, plasma reaction.

9.2 MIP pyrolysis of an aerosol

Microwave-induced plasma (MIP) pyrolysis is a convenient method of creating nanoparticles. The normal method is to heat a volatile precursor and, once in the gas phase, inject it into the active zone of the MIP where the high energy species present will decompose these molecules and form the desired product as nanoscale particles.

This method has been used with success, but is limited by the choice of starting material. Not all substances have a convenient, volatile precursor. Therefore, an alternative strategy is proposed by Wu *et al.*[183] where less volatile precursors can be used. An aqueous solution of an appropriate precursor is used to create an aerosol, either by spraying through a fine nozzle, or by using ultrasonic vibrations to create a fine mist. This is injected into the active zone of the MIP where the solvent is rapidly dried off, leaving small amounts of the precursor, which will then decompose in the heat to form nanoparticles of the product. The advantage of this method is that the precursors are easier to handle. However, solvent contamination of the product is possible. Furthermore, the drying process can result in the formation of hollow particles, which will shatter and give irregular particle morphology.

Ceramic nanoparticles and an easy route to their formation are of particular importance to industry. Therefore, it was decided that this would be a good choice of reaction to attempt. In order to facilitate the experiment a simple ceramic target material was chosen: alumina, i.e. aluminium oxide (Al_2O_3). The choice was made on the basis of availability of a suitable precursor and on the stability of the product. Aluminium nitrate ($Al(NO_3)_3(H_2O)_9$) is water soluble and is likely to decompose with heating to yield alumina.

9.2.1 Experimental

The microwave-induced plasma was created inside a quartz tube under dynamic vacuum (rotary pump) using an ASTeX S-1000 2.45 GHz power source (see Figure 9.2) and the waveform adjusted and focused on the tube using a tri-stub tuner. Tuning was performed to achieve maximum power to the sample, i.e. minimum reflected power. The power setting for the microwave generator could be varied, but an output of 300 W was used for most experiments. The aerosol mist was created using a pizo-electronic nebuliser, constructed inhouse. An electrostatic collector (potential difference of 8 kV between collector and earth) was placed downstream from the plasma to collect any solid product formed in the reaction. All connections on glass and metal were made airtight using Swagelok fittings, Cajon Ultra-Torr O-rings or vacuum wax. The quartz tube was surrounded by a wire mesh cage to prevent any microwave radiation leakage.

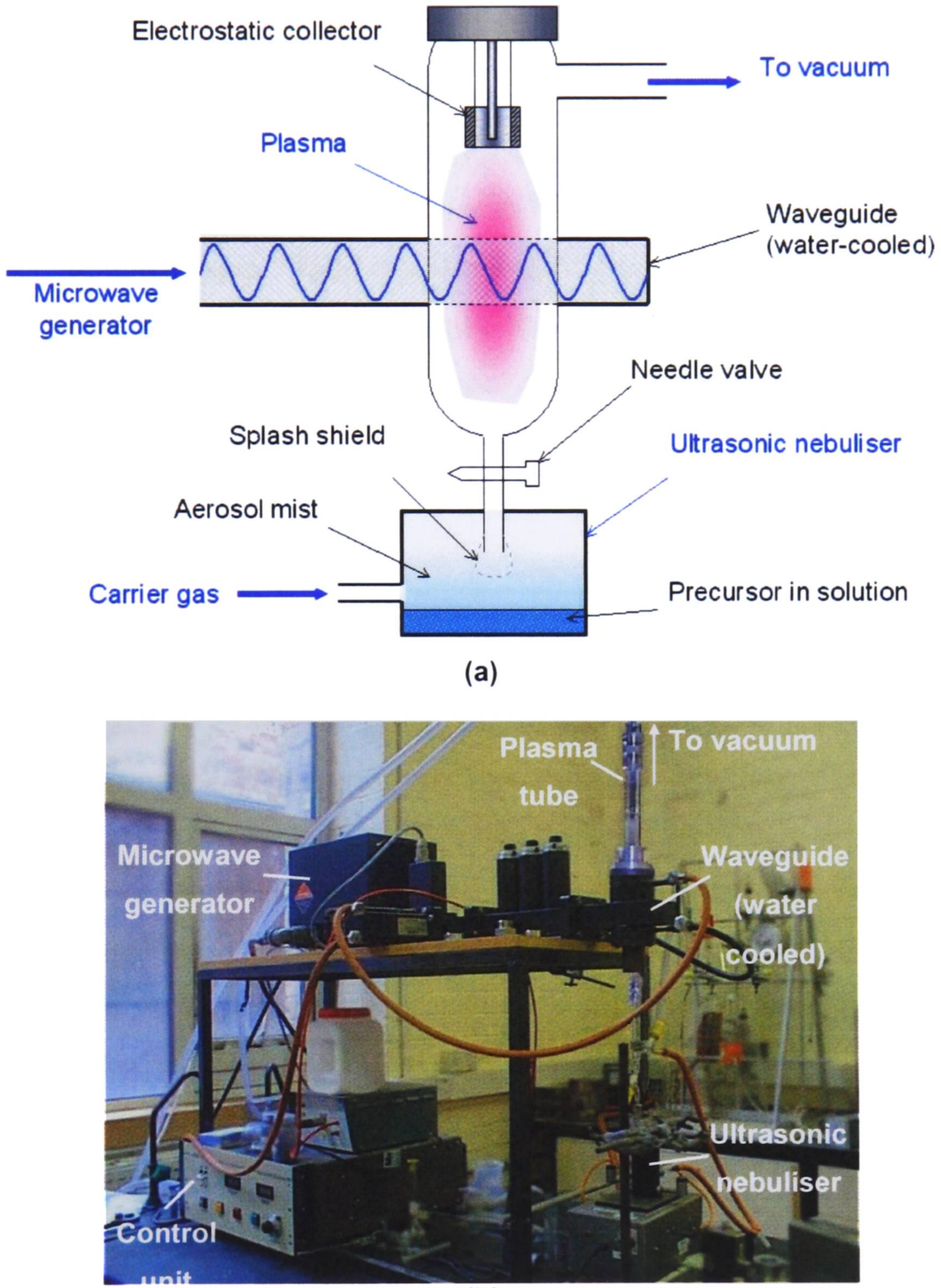

(a)

(b)

Figure 9.2 – (a) Schematic, and (b) photograph of apparatus used in microwave-induced plasma pyrolysis of aerosol experiments.

Before any work was done with the MIP it was necessary to verify that alumina was the decomposition product when aluminium nitrate solution is heated. This was done using a simple sol-gel technique. 100 cm^3 of a 0.1 mol dm^{-3} solution of aluminium nitrate in deionised water was placed in an evaporating basin and left in an oven at 373 K overnight. The water evaporated from the sample leaving a white powder, found to be amorphous by Powder X-ray Diffraction (PXRD). Measurements were performed using a Phillips PW 1730 powder diffractometer. Crystal structure refinement was performed using the GSAS suite of programmes[92] with EXPGUI interface.[93] Half this sample was then heated in the oven for 24 hours at 773 K. PXRD of the sample revealed that the sample remained amorphous. A further 24 hours heating at 1273 K was performed. The white powder product was examined using PXRD and found to be crystalline. Phillips' pattern matching software compared this pattern with those in its database and it was found to match that of α-alumina. Hence, decomposition of aluminium nitrate in the MIP should also result in the formation of alumina.

The apparatus as shown (Figure 9.2) represents considerable modification from the first experiments, which used the same arrangement as had been employed in previous studies using volatile precursors.[184] All modifications were made in order to solve problems encountered in these initial investigations. The ultrasonic nebuliser was the source of initial experimental difficulties. The quartz tube had originally been mounted in the vertically-inverted position from that shown above. It was decided that in order to prevent bulk liquid reaching the plasma reactor the quartz tube should be turned upside down relative to the position shown in Figure 9.2 – this made no significant difference to the plasma as the particles involved are too small to be significantly affected by gravity. Unfortunately, the apparatus still clogged with liquid even after this modification. After examination of the action of the nebuliser this was put down to splashing of the solution up into the output tube, caused by the action of the nebuliser and of the input stream of gas. This was resolved by using a small strip of aluminium foil as a protective shield over the output pipe, as shown in Figure 9.3. This blocks the direct line between solution and output, preventing splashes from entering the output tube, but allows the aerosol mist to take a indirect route and exit the chamber easily through the tube. This successfully prevented bulk solution from clogging the gas lines and allowed experiments to be carried out successfully.

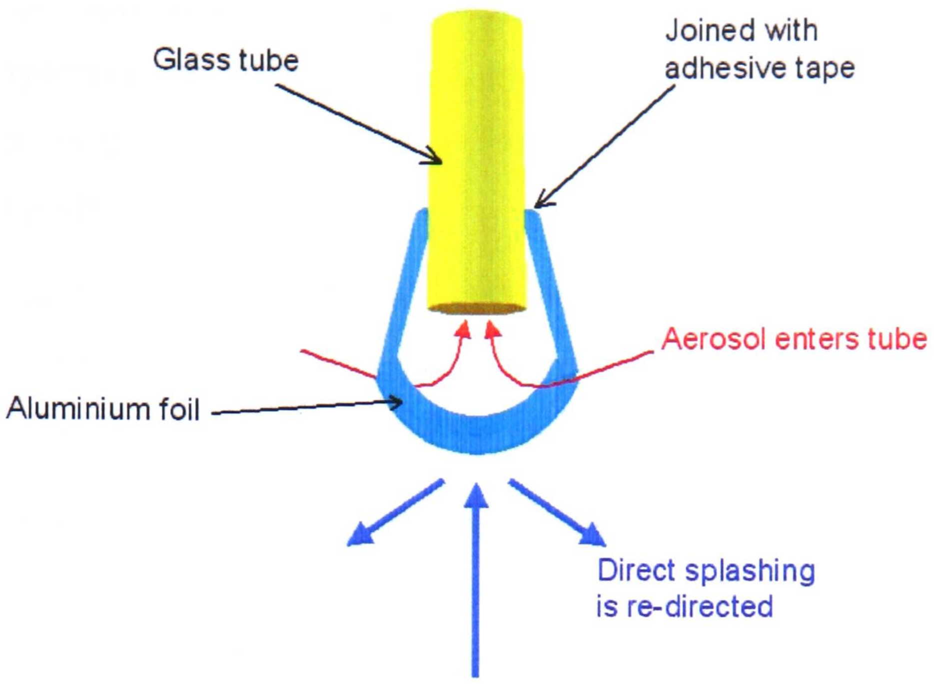

Figure 9.3 - Illustration showing in detail the splash shield used to prevent bulk solution reaching plasma.

It was found that continued operation resulted in excessive heating of metal parts, particularly those close to the source of the plasma. O-ring joints were badly affected by this heat and began to melt. A water-cooled head was added to the apparatus to counter this problem. This makes reaction times of over an hour possible. The final modification was the addition of heating tape wrapped round the connecting tubing between the nebuliser and the quartz tube. This prevented re-condensation of the aerosol on the sides of this tubing, delivering the majority of it cleanly into the MIP.

When performing aerosol pyrolysis experiments with a MIP, there are a number of variables to be taken into consideration. Optimisation of these is important in achieving a good yield and small particle size of the desired product. Relevant variables are:

1. The power output from the microwave generator. It was possible to vary this between 50 and 1000 W.
2. The reflected power, i.e. the energy not employed in the plasma and absorbed by the buffer tank of water. This is displayed on the generator control panel and throughout all experiments the tri-stub tuner was used to minimise its value. Ideally <10 W was achieved.

3. The carrier gas. Several different gases were at our disposal, including argon, nitrogen, air, oxygen, hydrogen and ammonia. Furthermore, mixtures of these gases were possible, as were small proportions of volatile liquids (achieved by bubbling the carrier gas through the liquid).
4. The pressure and flow rate of the gas could be controlled. However, in practice the needle valve controlled both these factors. The cylinder head pressure was generally set to 0.3 bar, though no effect was observed by varying this.
5. The vacuum strength. It proved extremely difficult to measure the pressure inside the quartz tube (under dynamic vacuum) due to the presence of reactive species that may damage sensitive pressure-measuring equipment. Increases in pressure, brought about by opening the input needle valve, significantly reduced the extent of the plasma region. Hence, as high a vacuum as possible was maintained throughout experiments – obtained by setting the needle valve to the minimum, practical opening.
6. The precursor solution concentration could be controlled. Concentrations up to 1.00 mol dm^{-3} of aluminium nitrate were used.

Any product formed in the plasma was collected, both from the collector and from the walls of the tube, by removal with a spatula and ultimately using an ultrasonic bath (Dawe Instruments 1160) to loosen any material and collect it in a beaker of acetone (from where the particles were subsequently dried). The product was examined using PXRD, SEM and EDX. Microanalysis (SEM and EDX) was conducted on a Cameca Camebax Microbeam electron probe, equipped with facilities for measuring secondary and back-scattered electrons, and X-rays using an Oxford Instruments Isis 300 energy dispersive analyser. For greater definition of SEM image, gold-coating of samples was employed (approximately 100 Å thickness with the default applied voltage bias, with the coating being added after EDX analysis). EDX analysis was performed at a working distance of 10 mm. Samples were prepared for microanalysis by creating a suspension of the sample in acetone. A few drops of this solution were allowed to dry on a carbon ‘sticky’ disc, set on top of a silicon wafer, on top of the aluminium microanalysis stub. The silicon wafer is necessary to increase the distance between sample and stub so that aluminium from the stub will not be observed in the EDX.

9.2.2 Results and discussion

Several experiments were completed. Only a few of these results shall be mentioned here as many were simply repeats of other experiments and provide no new insight. The experiments of most interest are detailed in Table 9-1.

Table 9-1 - Experimental conditions for aerosol pyrolysis utilising a MIP.

NO.	$[Al(NO_3)_3]$ / mol dm^{-3}	CARRIER GAS	POWER / W	DURATION / min	PRODUCT
1	1.00	Argon	~300	~60	large quantity of white powder collected
2	1.00	Oxygen	~300	~120	white amorphous solid on tube walls
3	0.50	Oxygen	~300	~60	white powder formed on tube walls
4	0.10	Argon	~100	~40	tiny quantity deposited directly on collector

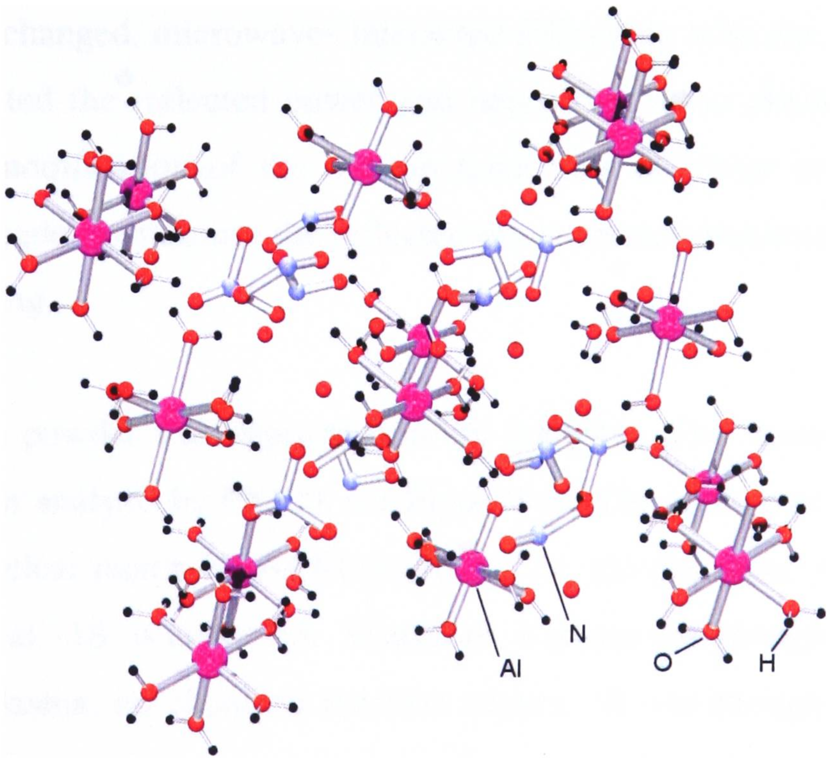

Figure 9.4 - Unit cell structure of aluminium nitrate hydrate. Atom types as shown.

Powder X-ray diffraction measurements were performed using the Philips PW1730 generator and X'pert diffractometer. Analysis was by the Rietveld method using the GSAS suite of programs with the EXPGUI interface. The fitted model of aluminium nitrate hydrate was that established by Lazar *et al.*[185] as shown in Figure 9.4. A 'type 2' profile function and 24 background parameters were used.

Experiment 1

The power was turned on and the plasma was lit with the spark from a tesla coil. The argon plasma gave off a strong violet light. A power setting of approximately 300 W was used in this (and adopted for all subsequent) experiment as it was deemed a good compromise: giving a bright plasma but not causing significant overheating of the apparatus. Higher power settings (400+ W) did not produce a significantly brighter plasma, but melting of the rubber in one O-ring connection did occur. It should be noted that exact values for the power are not quoted, as the effective power reaching the plasma is unknown - the effective power depending on the reflected power.

$$P_{effectice} = P_{source} - P_{reflected} \qquad \textbf{(9.1)}$$

As the temperature changed, microwaves interacted differently with the plasma. Changes in the waveform affected the reflected power and hence the power absorbed by the plasma. Constant, manual modification of the tri-stub tuner was therefore necessary throughout. Adjustments were made to minimise the reflected power, hence maximising the efficiency of the microwave heating.

A quantity of white powder was deposited on the collector. This material was scraped off and ground finely for analysis by PXRD, see Figure 9.5. The histogram in Figure 9.5 shows that the pattern is a clear match for $Al(NO_3)_3(H_2O)_9$, i.e. the precursor, though the source of the anomalous peak at ~18° is unknown. Therefore, it seems that though the aerosol droplets were dried in the plasma, no chemical reaction occurs. It was thought that a contributing factor to the experiment's failure may have been that the needle valve became clogged with a thick fluid of the precursor solution, blocking the gas flow. The effect of this was that some larger droplets of material may have been held back, then injected into the plasma. These droplets, being too large to completely dry out pass through the plasma and are spattered onto the collector, where they dry under the dynamic vacuum.

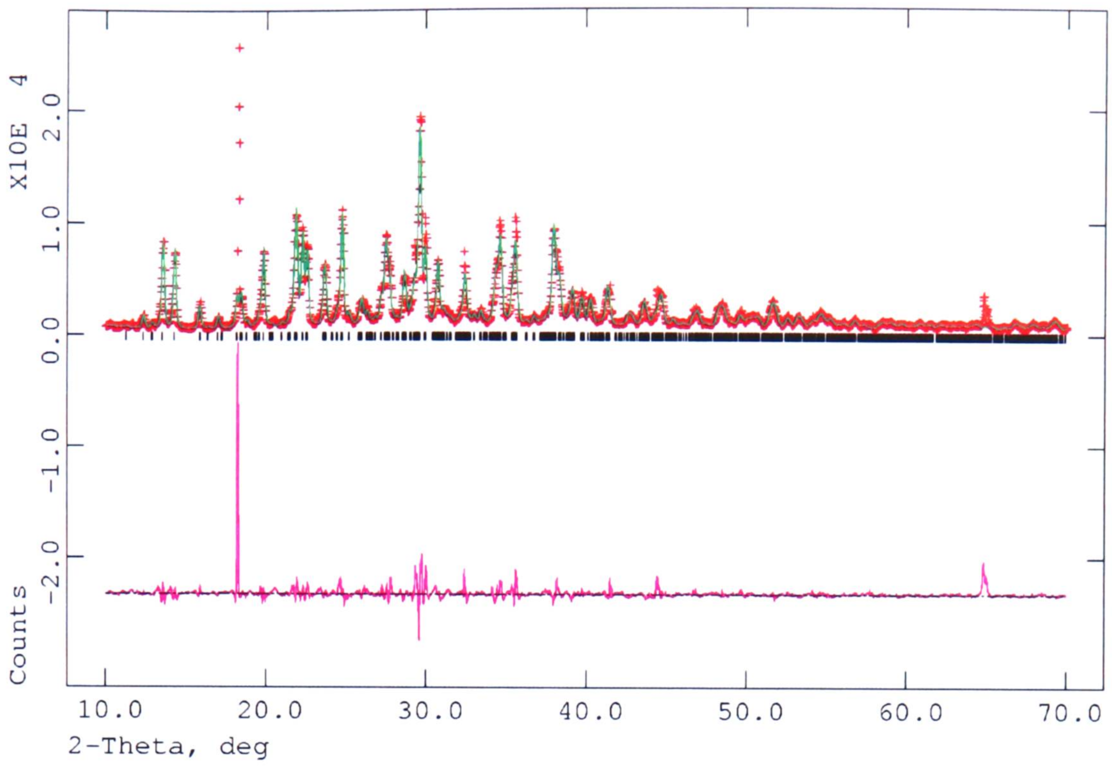

Figure 9.5 - Histogram for experiment 1 product. Upper part of diagram shows the collected data (crosses) and structural model for aluminium nitrate (line). Below is the difference between the model and experiment. Pattern taken with a step size of 0.02° and time per step was 4 seconds. χ^2=23.43, R_p=0.0847 and R_{wp}=0.1101.

Experiment 2

One consideration when trying to improve the experimental technique was that in such a water-rich atmosphere, the kinetically favoured route may be simply for the nitrate and aluminium ions to re-hydrate and then re-combine to yield the reactant. A more oxygen-rich atmosphere, however, may be useful in successfully decomposing aluminium nitrate to the oxide product. Therefore the next experiment employed oxygen plasma rather than argon in order to achieve this condition. The plasma produced was a deeper red colour than previously. Furthermore, the plasma was quite difficult to light and, once lit, remained relatively dull and small in volume. This is attributable to the fact that oxygen has a much higher electron affinity than argon – hence producing a 'colder' plasma (less energetic ions), but poor vacuum may also contribute.

In order to maximise the yield, a precursor solution of 1.00 mol dm^{-3} was once again used to form the aerosol. The process was left to run for an extended period of time, but after 2 hours the reaction was halted as deposited solid had blocked the tube, extinguishing the plasma. After this length of time the apparatus had heated somewhat and was allowed to cool before continuing. Unfortunately, on returning to the cooled apparatus, it was found that condensation had formed within the tube (due to action of the water-cooled head), turning the solid powder that had been produced into slurry. The quartz tube containing the product was removed and the slurry dried out. The solid material was collected and stored in a sealed vessel.

As the sample would have to be ground to a fine powder before PXRD analysis, it was decided to perform SEM and EDX analyses first. These techniques require only a very small amount of sample. The images taken by SEM are shown in Figure 9.6.

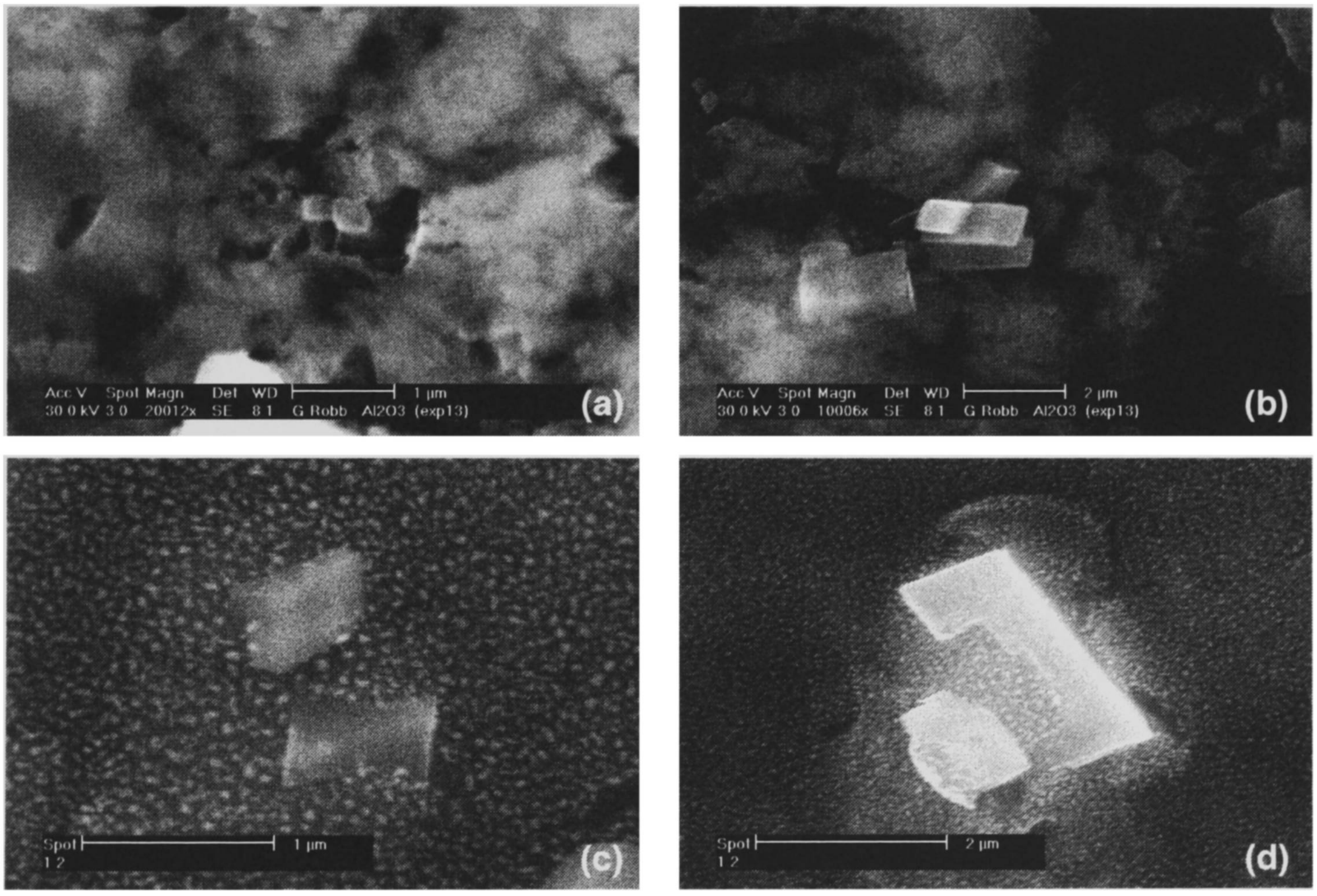

Figure 9.6 - Micrographs of product from experiment 2. (a) and (b) show SEM images with no sample preparation. (c) and (d) show images after gold coating of the sample. The dappled effect present in (c) and (d) is an artifact of the viewing process and is not a structural feature. A largely amorphous region is shown in (a), whereas cyrstallites are clearly visable in (b-d).

The image shown in Figure 9.6(a) is typical of the sample as a whole: generally the sample is amorphous. However a few crystals are present, as shown in (b) and more clearly in (c) and (d). The longest dimension of these crystals varies between ca. 600 nm and 2 μm. The few crystals that have been observed are not completely clear. It seems that one face is quite close to rectangular. However, almost certainly there are angles present that are neither 90° nor 120°. From this information, the crystal could be any of a range of shapes, but most likely is monoclinic. α-alumina (corundum) crystals are trigonal/hexagonal (space group = *R*3*c*). γ-alumina crystals, formation of which has been reported in the nanophase,[182] are cubic (space group = *Fm*3*m*), whilst aluminium nitrate hydrate crystals are monoclinic (space group = *P*121/*c*1), with $\beta = 95.51°$, i.e. close to a right angle.[185] The images (Figure 9.6) do not present sufficient information to make a confident identification, though monoclinic aluminium nitrate is a distinct possibility. EDX spectroscopy (carried out before gold coating) revealed no more information. The presence of aluminium was confirmed, but the spectrometer is not sensitive enough to clearly discriminate between lighter elements such as nitrogen and oxygen. In order to more accurately determine the identity of the product, it is necessary to use another technique: PXRD.

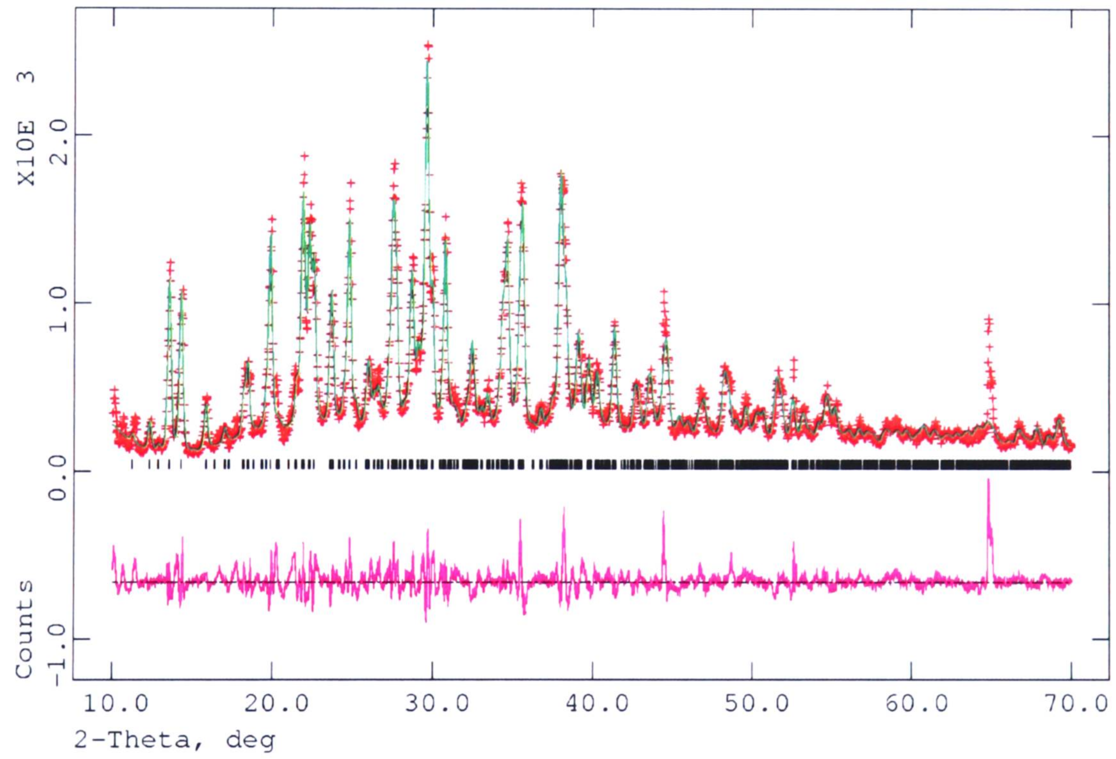

Figure 9.7 - Histogram for experiment 2 product. Upper part of diagram shows the collected data (crosses) and structural model for aluminium nitrate (line). Below is the difference between the model and experiment. Pattern taken with a step size of 0.02° and 2.5 seconds per step. $\chi^2=7.384$, $R_p=0.0979$ and $R_{wp}=0.1320$.

Again, the diffraction pattern of the product (Figure 9.7) seems to indicate the presence of crystalline aluminium nitrate hydrate, i.e. the starting material. However, examination of the pattern reveals clear discrepancies between the experimental data and the model pattern:

several sharp lines are observed in the difference plot, at approximately 35°, 38°, 44°, and 52°, all of which are present in the pattern of corundum (α-alumina),[186] as shown in Figure 9.8. However, not all lines are present and hence all that can be said is that some alumina product may be present in a distorted form of the α-alumina structure. This is consistent with the formation of nanoparticles where the small crystallite size would create a stressed structure, dominated by surface, rather than bulk, interactions. An additional line at 65° (also present for experiment 1, see Figure 9.5) is not part of the corundum pattern and is most likely due to the aluminium sample plate used in PXRD measurements. Nonetheless, most of the collected powder turned out to be due to the reactant and methods to improve the yield of the desired product are necessary.

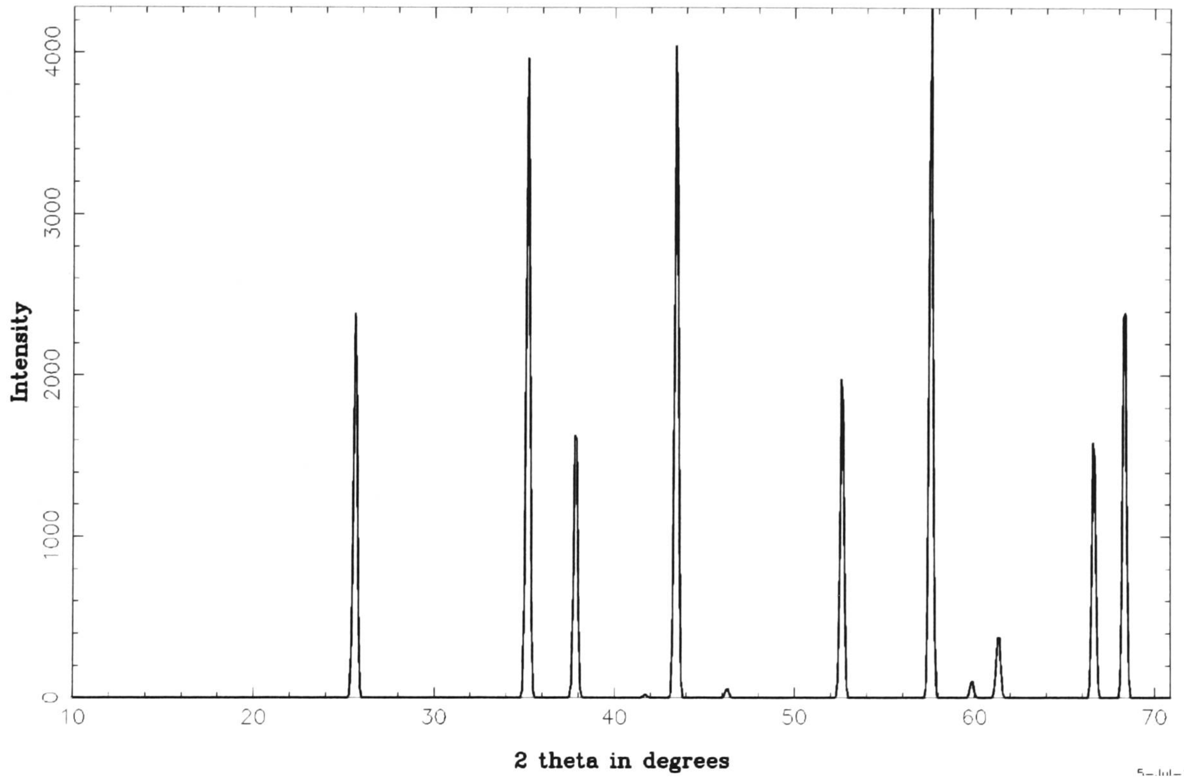

Figure 9.8 - Sample diffraction pattern for corundum using Cu K_α wavelength X-rays.[186]

Experiment 3

This experiment was essentially a repeat of experiment 2, with the purpose of obtaining a better quality of product. The experiment was also only run for half as long and only half the concentration of precursor was used (0.50 mol dm^{-3}) so as to avert the blocking of the tube with deposited solid. After an hour, the experiment was stopped and white powder was observed to be deposited on the tube walls. The apparatus was dismantled whilst still warm to prevent the formation of condensation and the tube examined. The particle size of the powder seemed to vary along the length of the tube: a rough demarcation occurring around the point in the tube where the plasma was focused. Two samplings were taken: from upstream and downstream of the plasma focus, and analysed separately.

Upstream deposit

Again SEM was used to examine the particle morphology. The upstream deposit was observed with the naked eye to be made from larger particles. However, on preparation for microanalysis the particles seemed to partially dissolve in the acetone. The images showed the resulting sample to be completely amorphous, see Figure 9.9.

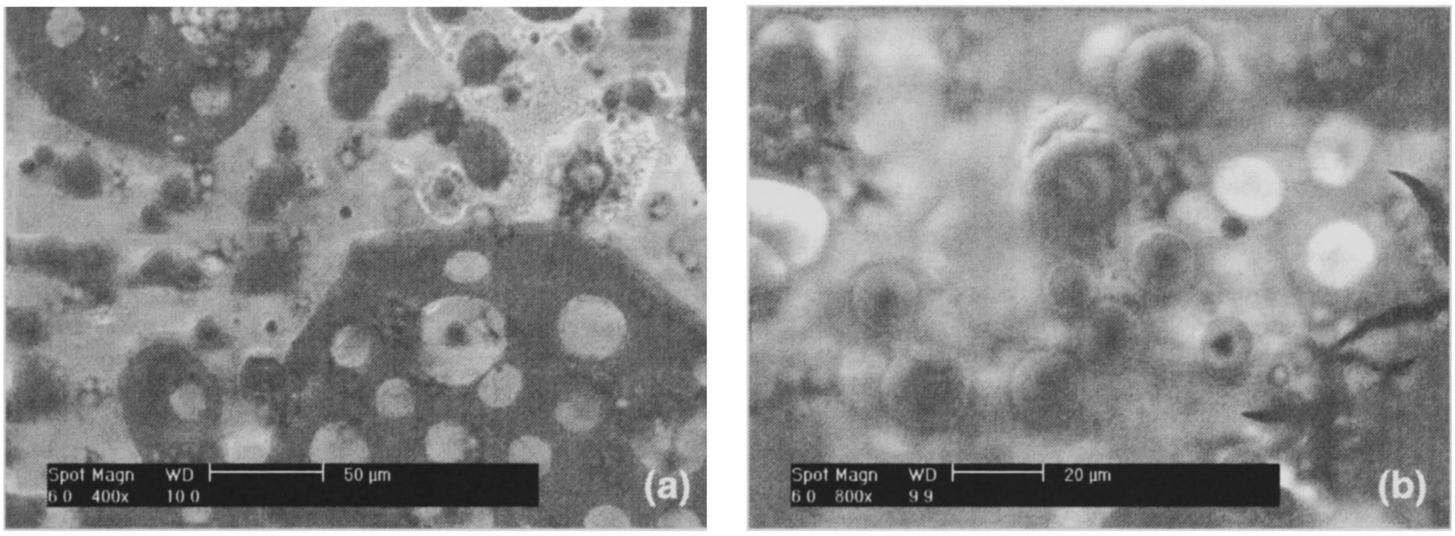

Figure 9.9 - Micrographs of upstream product from experiment 3. Both (a) and (b) show amorphous blobs and bubbles of various sizes.

The amorphous particles are between 10 and 20 µm in diameter, much larger than the nanometre scale particles that were intended. Furthermore, deterioration of the sample was apparent in the electron beam, indicating that the 'blobs' are in fact bubbles of amorphous material trapped on the surface. It is interesting that some dissolution in acetone occurred with this sample. This did not happen with the product from experiment 1 or the downstream product from experiment 2. It shall be investigated whether some material is present here that is not present in the other samples.

EDX spectroscopy was employed to help clarify the product's identity, see Figure 9.10. Note, carbon and sodium are present in the carbon disc that the sample sits on. These peaks are present in all EDX spectra prepared in this way.

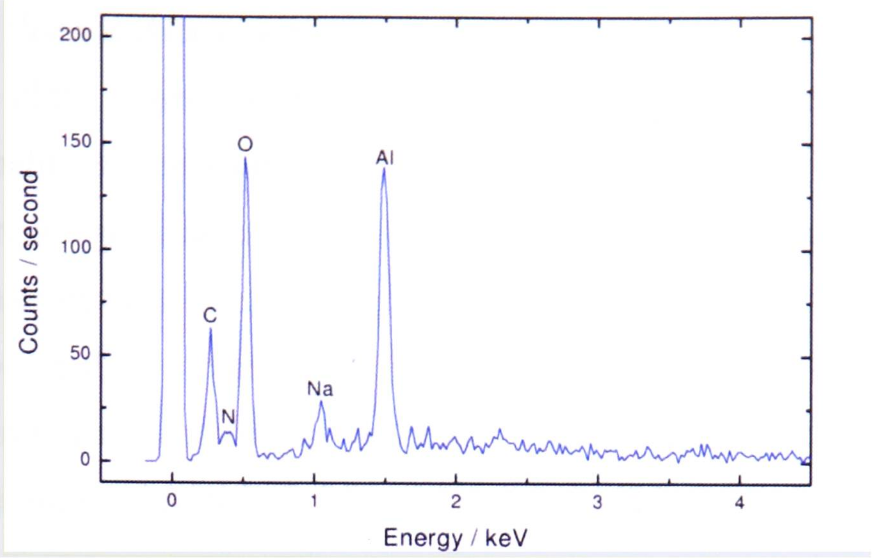

Figure 9.10 - EDX spectrum for upstream product of experiment 3.

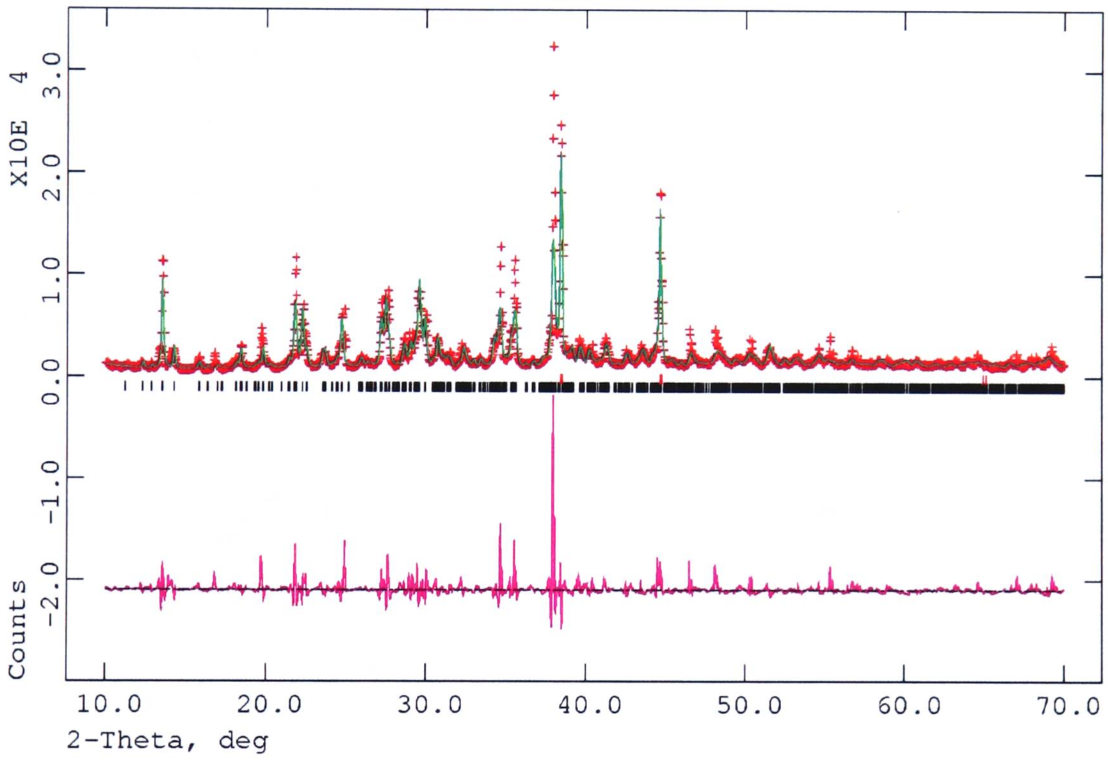

Figure 9.11 - Histogram for experiment 3 upstream product. Upper part of diagram shows the collected data (crosses) and structural model for aluminium nitrate (line). Below is the difference between the model and experiment. Pattern taken with a step size of 0.02° and 2.5 seconds per step. χ^2=78.40, R_p=0.1503 and R_{wp}=0.2016.

The EDX spectrum, when viewed at higher resolution, shows peaks for aluminium, oxygen and nitrogen (though peak heights are unrelated to concentrations). This goes some way to confirming the presence of the nitrate hydrate. However, the technique is unreliable for elements lighter than fluorine and on its own is insufficient evidence. PXRD analysis was therefore undertaken. Figure 9.11 shows the resulting diffraction pattern compared with that for aluminium nitrate hydrate.

Figure 9.11 shows that the data is a good match for aluminium nitrate, the reactant, plus the aluminium sample plate. There are few features in the difference plot other than the large peak at ~38° (probably due to aluminium). The pattern is notably different from previous experiments (Figure 9.5 and Figure 9.7) despite being fitting to the same structural model. It is thought that microstructure, e.g. sample size, stress and strain, may play a role in determining how ordered the structure is. Figure 9.11 shows sharp peaks and no 'hump' (due to diffuse scattering from amorphous material). It is likely that this sample is more crystalline than previous experiments.

Downstream deposit

The downstream deposit was formed in the afterglow of the plasma, further down the quartz tube from the plasma focus. Less of this sample was collected from the quartz tube and care had to be taken with initial analysis in order to provide sufficient sample for later PXRD. The sample was initially studied by SEM. Prior to gold coating, some evidence of nanoparticle formation was observed. However, the sensitivity of the instrument was insufficient to obtain a good image. The imaging was significantly improved by the addition of a fine gold coating to the sample. The images produced are shown in Figure 9.12.

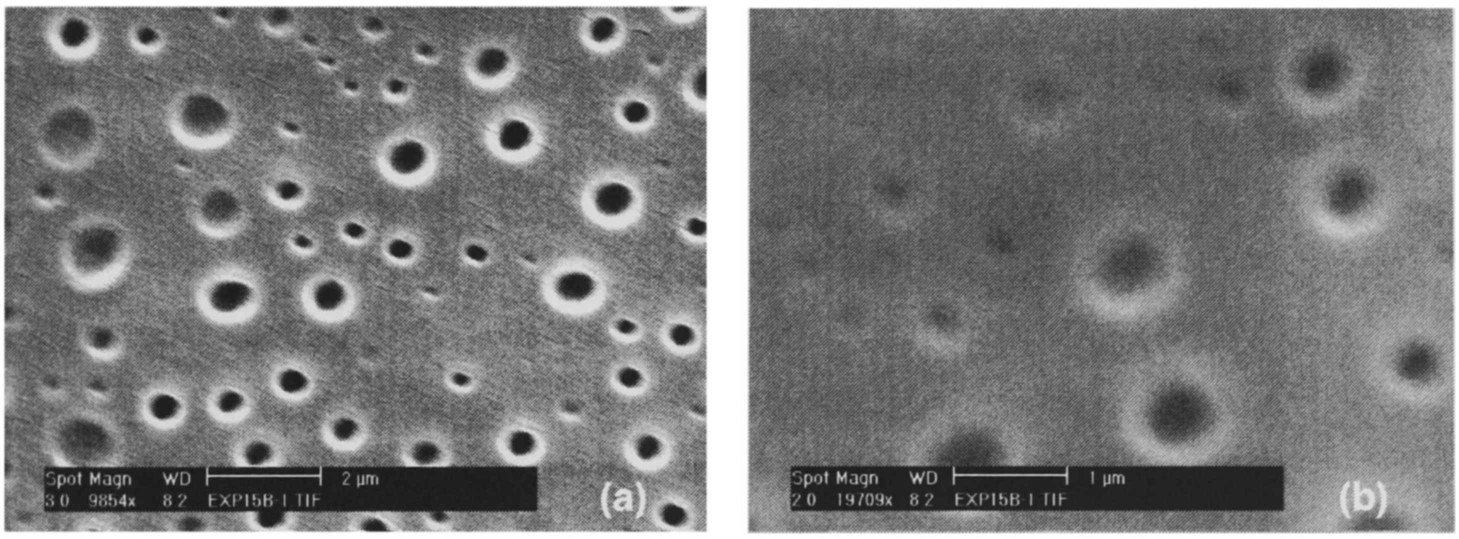

Figure 9.12 - Scanning electron micrographs of afterglow deposit from experiment 3. Images show spherical particles with diameter in the range 400-1000 nm. Particles are relatively uniform in shape and have a narrow size distribution.

Figure 9.12 clearly shows an array of sub-micron scale spherical particles, with a few small enough to be described as nanoparticles. The particles are of relatively uniform size, suggesting either rapid nucleation in the gas phase followed by relatively slow particle growth, or that the particle size is limited by the amount of material in each aerosol droplet. The most obvious thing about these images is the bright halo around the dark centre of each particle. This is probably because the particles are hollow. This implies that the particle size is determined by the size of the aerosol. The precursor in solution congregates at the droplet interface as the MIP dries off the solvent. Once all the solvent is driven off, a hollow shell of the precursor remains. It would be expected that smaller fragments, due to shattering of these hollow particles, are also present in the sample. Whether hollow shells of precursor compound are the final product, as seen in Figure 9.12, or whether they undergoes a further transformation in the MIP remains to be seen.

EDX analysis of the sample (prior to gold coating) was carried out. The results are shown in Figure 9.13. Oxygen and aluminium are both shown to be present, and there is no discernible peak due to nitrogen. The other peaks are due to the carbon 'sticky' disc and it should be noted that these peaks are larger, relative to the sample peaks than for the upstream product Figure 9.10), indicating that there is less sample on the slide and larger gaps between the particles. The evidence available supports the conclusion that aluminium oxide has been formed here, though what form it is in (amorphous, α-alumina, γ-alumina, etc) is unclear and PXRD analysis will be required to differentiate.

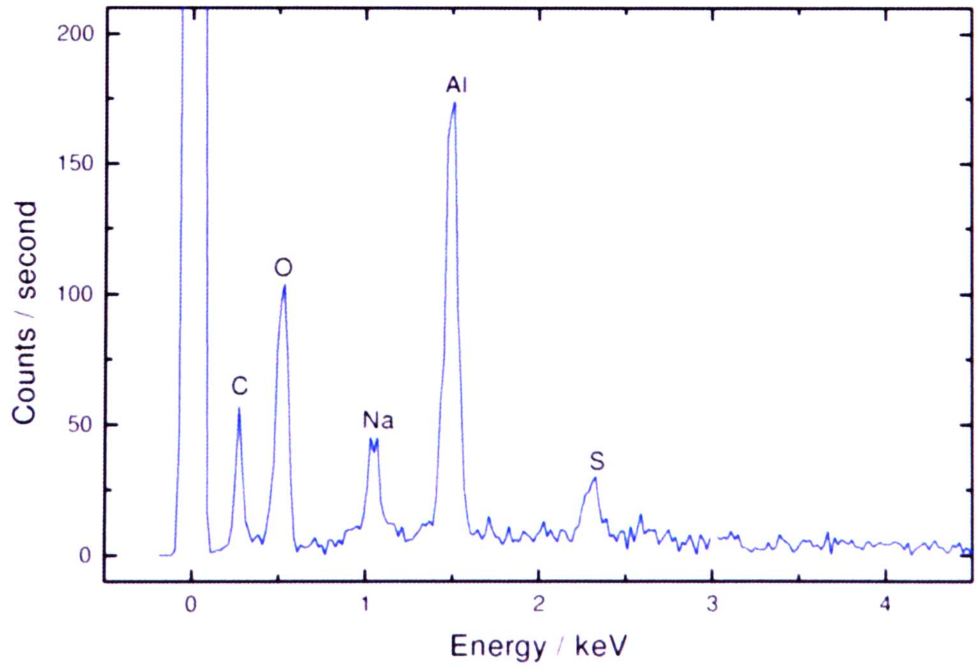

Figure 9.13 - EDX spectrum for afterglow product of experiment 7.

The diffraction pattern shown in Figure 9.14 is quite different for those of previous products (Figure 9.5, Figure 9.7 and Figure 9.11). However, much of the pattern corresponds to the structure of aluminium nitrate. The fit is less good than for previous patterns and there are many anomalous peaks, indicated clearly on the difference curve. These include approximately 34°, 38°, 44°, 56° and 64°, all of which are close to the pattern of corundum, as shown in Figure 9.8 (though note that some of these also correspond to aluminium). The lines do not all match up exactly, however, and it is thought that a distorted version of the α-alumina structure is present, consistent with the formation of sub-micron or nano-particles. Missing lines may therefore be masked or crystal distortions may significantly reduce the line intensity.

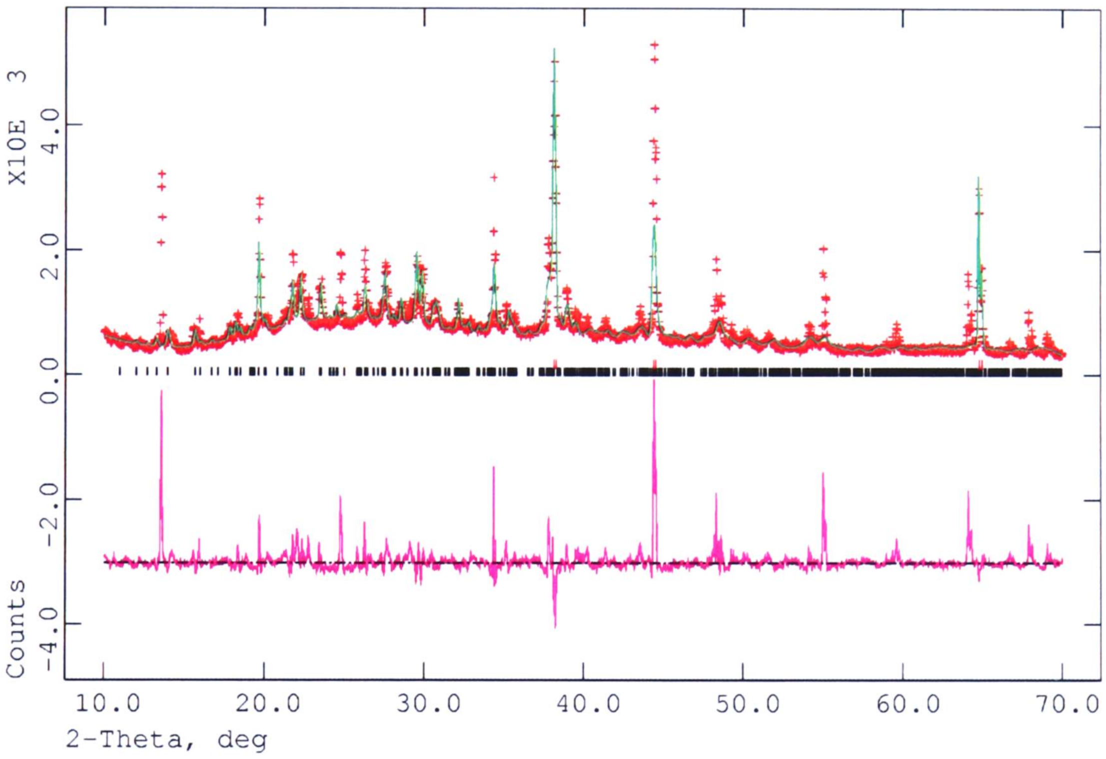

Figure 9.14 - Histogram for experiment 3 afterglow product. Upper part of diagram shows the collected data (crosses) and structural model for aluminium nitrate (line). Below is the difference between the model and experiment. Pattern taken with a step size of 0.02° and 2.5 seconds per step. χ^2=21.98, R_p=0.1180 and R_{wp}=0.1733.

Another aspect of Figure 9.14 is the very broad, low hump at low angles. This is indicative of amorphous material present in the sample. In order to better investigate the product it may be possible to re-crystallise this material and analyse it by powder X-ray diffraction. However, care would have to be taken to avoid chemical transformation of the sample, i.e. aluminium nitrate can decompose to alumina on heating.

Therefore, experiment 3, though ineffective at the focus of the plasma, does create small (400-1000 nm diameter), spherical, alumina-containing particles with a relatively small distribution range, in the afterglow region. However, the particles are impure, containing at least some of the starting material and probably also some amorphous material.

Experiment 4

All experiments to this point seem to have had trouble maintaining a particularly bright plasma. The largest obstacle has been maintaining a sufficiently good vacuum, whilst allowing the aerosol into the plasma chamber. Additionally, the needle valve is not ideal for this purpose as its narrow bore can become blocked easily. In order to overcome these difficulties a new piece of glassware was designed to introduce the aerosol into the reactor, as shown in Figure 9.15.

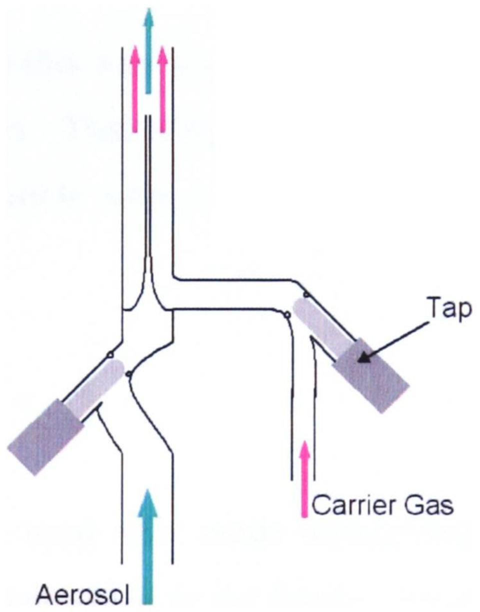

Figure 9.15 - New glassware for introduction of aerosol into MIP with a greater degree of control.

The new injector assembly is not only far less likely to leak, but has distinct advantages in terms of gas or vapour flow. There are now two separate gas streams: the aerosol and the carrier, allowing separate adjustment of the flow of each and therefore permitting the flow of aerosol into the reactor to be pulsed – useful for shorter, high concentration experiments. Furthermore, the narrow injector for the aerosol is place at the centre of the carrier gas stream, keeping the aerosol away from the reactor walls and producing a non-turbulent spray jet.

Unfortunately, there was only opportunity for some initial testing and very little product was collected: insufficient for PXRD or SEM analysis. However, it should be noted that tests were highly successful with a bright plasma achievable for a power setting of only 100 W (*c.f.* 300 W for previous experiments). When pulsed, a jet of 'misty' aerosol vapour was clearly seen. Future work with the apparatus may be able to successfully produce nanoparticles by this method.

9.2.3 Conclusion

Aerosol pyrolysis using a microwave-induced plasma has been shown to be possible using the apparatus described. However, the nature of the product is highly dependent upon the reaction conditions and much more work would need to be done in order to maximise the yield of desirable product from this system.

The size of particle produced in this way is generally dependent upon the size of the aerosol droplets rather than other factors. This being the case, the creation of particles smaller than those produced would be impossible without using a different device to create the aerosol in the first place.

9.2.4 Further work

Improvements to the apparatus used were made throughout these experiments and further modifications will need to be undertaken in the future. Ideally, the goal of this would be to control particle size through either the concentration of the precursor solution or the size of individual aerosol droplets.

10 Conclusions

The majority of the work of this thesis has been in the design and manufacture of microwave applicators for the heating or non-thermal irradiation of various inorganic materials. The fact that several previously unforeseen problems were encountered in using the microwave applicators described here points to the difficulties inherent in such a process. Through a series of iterative steps the design and heating efficiency of a microwave applicator compatible with the requirements of *in-situ* diffraction measurements has been improved and implemented. Similarly, the apparatus for microwave induced plasma (MIP) pyrolysis of an aerosol has been advanced and the ability to produce sub-micron scale particles has been demonstrated. These steps represent the conception and first prototypes in the design process and it is the intention here to provide sufficient information in order that interested parties may continue from this point to improve further upon these designs.

One of the key points illustrated in the experiments described is the difficulty in temperature determination in a microwave field. Normal methods, such as cryogenic gas used to cool a crystalline material, such as aspirin, are not always sufficient as these rely on temperature equilibrium occurring so that surroundings and sample are at the same temperature. Unfortunately, the specific nature of microwave heating can mean that a sample can be much hotter than its surroundings. Worse still, for a large sample the core of a material may be much hotter than its surface. This work has shown that accurate structure resolution by *in-situ* diffraction may be used as a reliable means of temperature determination for the bulk (interior) of the sample. The thermal expansion of the studied material, barium titanate, varied in a predictable way with conventional-oven temperature (away from phase transition points) and was thus an accurate, non-contact means of determining sample temperature during microwave irradiation.

The experiments using *in-situ* diffraction as an incisive tool for monitoring microwave-driven reactions have shown that microwaves can have specific effects on certain materials. These effects are particular not only to the chemical nature of the material, but also to its physical form. For example, a single crystal of aspirin demonstrated some heating with microwaves, but no anisotropic, non-thermal effects that could be attributed to the microwave field, whereas powdered silver iodide, as well as heating significantly, showed that the phase transition temperature may be strongly affected by the presence of a microwave field.

One of the aims of this thesis was to test for the existence of microwave-specific effect, and in the examples covered such effects have been shown to occur in certain materials, most obviously around their phase transition temperatures. These phase transitions were shown to involve the excitation of a 'soft-mode' vibration. The hypothesis of this thesis is that microwaves can interact with a low-lying phonon associated with the soft-mode, pumping energy into it at a rate sufficient to drive the phase transition at a temperature lower than is possible for conventional forms of heating. This is a kinetic effect as it is the result of energy being put into this mode faster than it can be redistributed. If equilibrium were allowed to take place then no microwave effect would be observed. The magnitude of the effect, therefore, should correspond to the microwave field intensity. This theory has been discussed at length regarding silver iodide, barium titanate and potassium niobate.

Curiously, though silver iodide and β''-alumina are both low-temperature ionic conductors, only silver iodide exhibits any specific effect in the microwave field. In light of my findings, it is likely that this is because β''-alumina does not possess a low-lying, soft-mode phonon. The sudden onset of conductance with heating in silver iodide is accompanied by a phase change involving such a mode. Conversely, the more gradual onset of conductivity in β''-alumina has no such activation mechanism. The delocalisation of metal ions in β''-alumina (i.e. sodium or silver in the cases studied) will increase as microwaves heat the material, however such a chaotic motion cannot be monitored by *in-situ* powder diffraction. Clearly, in retrospect β''-alumina was not an ideal material to study, though in finding this out, it helped in the formulation of the hypothesis explaining the observations for other materials.

The nature of the material barium titanate has been scrutinised closely. It is commonly believed that in the paramagnetic phase the structure is truly cubic with only temporal displacement of atoms about their mean positions. However, the results here support the hypothesis that the ion positions are not randomly disordered about their cubic positions, but rather the mean positions of the Titanium ions are themselves displaced to off-centre positions. The direction of these displacements is randomised over a bulk crystal, thus giving the net cubic structure. However, the displacements of adjacent ions *are* indirectly linked by a low-lying phonon mode (capable of being excited by microwave irradiation), allowing a degree of localised ordering. Thus, excitation of a low-lying mode (shown to be present for barium titanate) can provide a rationale not only for the lower value for the phase transition temperature (the same phenomenon as observed for silver iodide), but also the anomalously large thermal expansion observed for barium titanate at approximately the same temperature. This is thus a coherent framework in which to explain all observations made for barium titanate under the influence of a microwave field.

In summary, this work has shown evidence for the existence of a microwave effect and rationalised these observations in terms of solid-state theory and the interaction of microwave energy with low-lying vibrations via electron-phonon interactions.

11 Bibliography

1. Gabriel, C., et al., *Chemical Society Reviews*, 1998, **27** (3), 213-223.
2. Mingos, D.M.P. and A.G. Whittaker, *Microwave dielectric heating effects in chemical synthesis*, in *Chemistry under extreme or non-classical conditions*, R. van Eldik and C.D. Hubbard, Editors. 1997, John Wiley and Sons Inc.: New York. p. 479-514.
3. Meredith, R., *Engineers' Handbook of Industrial Microwave Heating*. 1998, London: The Institution of Electrical Engineers.
4. Kotaki, T., et al., *Diamond and Related Materials*, 1993, **2** (2-4), 342-346.
5. Bykov, Y.V., K.I. Rybakov, and V.E. Semenov, *Journal of Physics D: Applied Physics*, 2001, **34**, R55-R75.
6. Meng, B.S., et al., *Physical Review B: Condensed Matter*, 1996, **53** (19), 12777-12785.
7. Agrawal, D.K., *Current Opinion in Solid State & Materials Science*, 1998, **3** (5), 480-485.
8. Bergman, D.J. and D. Stroud, *Solid state physics: advances in research and applications*, in *Solid state physics: advances in research and applications vol 46*, H. Ehrenreich and D. Turnbull, Editors. 1992, Academic: New York. p. 147-269.
9. Hamon, B.V., *Australian Journal of Physics*, 1953, **6**, 304.
10. Junck, K.L. and W.D. Getty, *Journal of Vacuum Science & Technology A: Vacuum Surfaces and Films*, 1994, **12** (3), 760-768.
11. Diamy, A.M., et al., *Chemical Physics Letters*, 1997, **269** (3-4), 327-332.
12. Sugiyama, K., et al., *Journal of Materials Chemistry*, 1994, **4** (9), 1497-1501.
13. Chou, C.H. and J. Phillips, *Journal of Materials Research*, 1992, **7** (8), 2107-2113.
14. Vollath, D. and D.V. Szabo, *Materials Letters*, 1998, **35** (3-4), 236-244.
15. Brenner, J.R., et al., *Nanostructured Materials*, 1997, **8** (1), 1-17.
16. Vollath, D., et al., *Journal of Materials Research*, 1997, **12** (8), 2175-2182.

17. Kumada, N., N. Kinomura, and S. Komarneni, *Materials Research Bulletin*, 1998, **33** (9), 1411-1414.

18. Whittingham, M.S., *Current Opinion in Solid State & Materials Science*, 1996, **1** (2), 227-232.

19. Whittaker, G., *New Scientist*, 1998, **157** (2123), 34-37.

20. Li, Q. and Y. Wei, *Materials Research Bulletin*, 1998, **33** (5), 779-782.

21. Mingos, D.M.P. and D.R. Baghurst, *Chemical Society Reviews*, 1991, **20** (1), 1-47.

22. Gedye, R., F. Smith, and K. Westaway, *Journal of Microwave Power and Electromagnetic Energy*, 1991, **26** (1), 3-17.

23. Gedye, R.N. and J.B. Wei, *Canadian Journal of Chemistry-Revue Canadienne De Chimie*, 1998, **76** (5), 525-532.

24. Peng, J.H., J. Binner, and S. Bradshaw, *Journal of Materials Synthesis and Processing*, 2001, **9** (6), 363-368.

25. Jacob, J., L.H.L. Chia, and F.Y.C. Boey, *Journal of Materials Science*, 1995, **30** (21), 5321-5327.

26. Furlan, R.L.E., E.G. Mata, and O.Z. Mascaretti, *Tetrahedron Letters*, 1996, **37** (30), 5229-5232.

27. Chen, S.T., et al., *Journal of the Chinese Chemical Society*, 1991, **38** (1), 85-91.

28. Chemat, F., et al., *Journal of Microwave Power and Electromagnetic Energy*, 1998, **33** (2), 88-94.

29. Hajek, M., *Collection of Czechoslovak Chemical Communications*, 1997, **62** (2), 347-354.

30. Bond, G., R.B. Moyes, and D.A. Whan, *Catalysis Today*, 1993, **17** (3), 427-437.

31. Pere, C., E. Rodier, and O. Louisnard, *Drying Technology*, 2001, **19** (6), 1005-1022.

32. Pabst, W., et al., *Euro Ceramics Vii, Pt 1-3*, 2002, **206-2**, 373-376.

33. Sizgek, E. and G.D. Sizgek, *Chemical Engineering & Technology*, 2002, **25** (3), 287-292.

34. Pere, C. and E. Rodier, *Chemical Engineering and Processing*, 2002, **41** (5), 427-436.

35. Blanco, C. and S.M. Auerbach, *Journal of the American Chemical Society*, 2002, **124** (22), 6250-6251.

36. Diaz-Ortiz, A., et al., *Green Chemistry*, 2002, **4** (4), 339-343.

37. Yang, H.J., et al., *Synthetic Communications*, 2002, **32** (15), 2395-2402.

38. Bai, Y.J., et al., *Synthetic Communications*, 2002, **32** (16), 2549-2553.

39. Mojtahedi, M.M., et al., *Journal of Chemical Research-S*, 2002 (6), 286-287.

40. Kaboudin, B. and R. Nazari, *Journal of Chemical Research-S*, 2002 (6), 291-292.

41. Lee, J.C., H.J. Park, and J.Y. Park, *Tetrahedron Letters*, 2002, **43** (32), 5661-5663.

42. Rao, K.J., et al., *Chemistry of Materials*, 1999, **11** (4), 882-895.

43. Zhang, J.S., et al., *Journal of Materials Science & Technology*, 1999, **15** (5), 419-422.

44. Peng, J.H., et al., *Journal of Materials Science & Technology*, 1998, **14** (2), 173-175.

45. Vollath, D. and K.E. Sickafus, *Journal of Materials Science*, 1993, **28** (21), 5943-5948.

46. Vollath, D. and K.E. Sickafus, *Journal of Materials Research*, 1993, **8** (11), 2978-2984.

47. Gibbons, K.E., et al., *Chemical Communications*, 2000 (2), 159-160.

48. Ostorero, J., M. Gasgnier, and A. Petit, *Journal of Alloys and Compounds*, 1997, **262**, 275-280.

49. Vaidhyanathan, B., K. Balaji, and K.J. Rao, *Chemistry of Materials*, 1998, **10** (11), 3400-3404.

50. Booske, J.H., R.F. Cooper, and I. Dobson, *Journal of Materials Research*, 1992, **7** (2), 495-501.

51. Birnboim, A., J.P. Calame, and Y. Carmel, *Journal of Applied Physics*, 1999, **85** (1), 478-482.

52. Booske, J.H., et al., *Physics of Plasmas*, 1998, **5** (5), 1664-1670.

53. Rybakov, K.I., et al., *Physical Review B: Condensed Matter*, 1997, **55** (6), 3559-3567.

54. Whittaker, A.G. and L. Cronin. *The effects of microwave radiation on solid state ion diffusion.* in *Proceedings of the Second International Conference on Microwave Chemistry*. 2000. Antibes - Juan-les-pins: AMPERE.

55. Freeman, S.A., J.H. Booske, and R.F. Cooper, *Journal of Applied Physics*, 1998, **83** (11), 5761-5772.

56. Bryan, J.E. and J. Seyed-Yagoobi, *Journal of Heat Transfer-Transactions of the Asme*, 2000, **122** (2), 266-277.

57. Stewart, W., *Mobile Phones and Health: a report of the Independent Expert Group on Mobile Phones*. 2000, Chilton: National Radiation Protection Board.

58. de Pomerai, D.I., et al., *Nature*, 2000, **405**, 417-418.

59. de Pomerai, D.I., et al., *Enzyme and Microbial Technology*, 2002, **30**, 73-79.

60. Leszczynski, D., et al., *Differentiation*, 2002, **70**, 120-129.

61. French, P.W., et al., *Differentiation*, 2000, **67**, 93-97.

62. Stuerga, D. and P. Gaillard, *Tetrahedron*, 1996, **52** (15), 5505-5510.

63. Parkes, G.M.B., et al., *Thermochimica Acta*, 2000, **356** (1-2), 85-96.

64. Parkes, G.M.B., et al., *Review of Scientific Instruments*, 2000, **71** (1), 168-175.

65. Orrling, K., et al., *Chemical Communications*, 2004, 790-791.

66. Mukhopadhyay, A.K., et al., *Bulletin of Material Science*, 2001, **24** (2), 125-128.

67. Naitoh, K., T. Takizawa, and T. Matsuse, *Japanese Journal of Applied Physics Part 2-Letters*, 1999, **38** (7A), L724-L726.

68. Deka, N. and J.C. Sarma, *Journal of Organic Chemistry*, 2001, **66**, 1947-1948.

69. Panneerselvam, M. and K.J. Rao, *Bulletin of Material Science*, 2002, **25** (7), 593-598.

70. Zhang, X., D.O. Hayward, and D.M.P. Mingos, *Industrial and Engineering Chemistry Research*, 2001, **40** (13), 2810-2817.

71. Wang, S., J. Tang, and F. Younce, *Temperature Measurement*, in *Encyclopaedia of Agricultural, Food, and Biological Engineering*. 2003, Marcel Dekker: New York.

72. Dally, J.W., W.F. Riley, and K.G. McConnell, *Instrumentation for Engineering Measurements*. 2nd ed. 1993, New York: John Wiley and Sons.

73. Nuchter, M., et al., *Green Chemistry*, 2004, **6**, 128-141.

74. Pert, E., et al., *Journal of the American Ceramic Society*, 2001, **84** (9), 1981.

75. Chein, T.-H., J. Wei, and Y. Tzeng, *Diamond and Related Materials*, 1999, **8**, 1686-1696.

76. Balmer, R.S. and T. Martin, *Journal of Crystal Growth*, 2003, **248**, 216-221.

77. Bond, G., et al., *Measurement Science & Technology*, 1991, **2** (6), 571-572.

78. Roland, U., et al., *Sensor Letters*, 2003, **1**, 93-98.

79. Ladd, M.F.C. and R.A. Palmer, *Structure Determination by Crystallography*. 3rd ed. 1993, New York: Plenum.

80. Schwarzenbach, D., *Crystallography*. 1996, New York: Wiley.

81. Hook, J.R. and H.E. Hall, *Solid State Physics*. 1991, New York: Wiley.

82. Kittel, C., *Introduction to Solid State Physics*. 1995, New York: Wiley.

83. Bührer, W., R.M. Nicklow, and P. Brüesch, *Physical Review B: Condensed Matter*, 1978, **17** (8), 3362-3370.

84. Margaritondo, G., *Elements of Synchrotron Light: For Biology, Chemistry and Medical Research*. 2002, London: Oxford University Press.

85. Duke, P., *Synchrotron Radiation: Production and Properties*. 2000, London: Clarendon Press.

86. ISIS, *ISIS Facility Annual Report 2000-2001*, 2001, **RAL-TR-2001-050**.

87. Young, R.A., *The Rietveld Method.* 1993, Oxford: University Press.

88. Rietveld, H.M., *Acta Crystallographica*, 1967, **22**, 151.

89. Rietveld, H.M., *Acta Crystallographica*, 1966, **20**, 508.

90. Rietveld, H.M., *Journal of Applied Crystallography*, 1969, **2**, 65.

91. Howard, J., *Journal of Applied Crystallography*, 1982, **15**, 615.

92. Larsen, A.C. and R.B. Von Dreele, *Los Alamos National Laboratory Report*, 2000, LAUR 86-748.

93. Toby, B.H., *Journal of Applied Crystallography*, 2001, **34**, 210-213.

94. Goldstein, J.I. and H. Yakowitz, *Practical Scanning Electron Microscopy.* Practical Scanning Electron Microscopy. 1975, London: Plenum Press.

95. Kim, Y. and K. Machida, *Chemical & Pharmaceutical Bulletin*, 1986, **34** (8), 3087-3096.

96. Wilson, C.C., *Chemical Physics Letters*, 2001, **335** (1-2), 57-63.

97. Wilson, C.C., *Journal of Chemical Physics*, 2002, submitted.

98. Wilson, C.C. and H. Nowell, *New Journal of Chemistry*, 2000, **24** (12), 1063-1066.

99. Wilson, C.C., *Zeitschrift Fur Kristallographie*, 2000, **215** (11), 693-701.

100. Youngson, I.D., *Thesis*, in *Chemistry*. 2002, University of Edinburgh: Edinburgh.

101. Wilson, C.C., *Journal of Molecular Structure*, 1997, **405** (2-3), 207-217.

102. Slack, G.A., et al., *Journal of Physics and Chemistry of Solids*, 1987, **48**, 641.

103. Sheldrick, G.M., *SHELXL97.* 1997, Germany: University of Göttingen.

104. Wilson, C.C., *Journal of Applied Crystallography*, 1997, **30**, 184-189.

105. Maskasky, J.E., *Physical Review B: Condensed Matter*, 1991, **43** (7), 5769-5772.

106. Rains, C.A., J.R. Ray, and P. Vashishta, *Physical Review B: Condensed Matter*, 1991, **44** (17), 9228-9239.

107. Tallon, J.L., *Physical Review B: Condensed Matter*, 1988, **38** (13), 9069-9079.

108. Yoshiasa, A., et al., *Acta Crystallographica*, 1987, **B43**, 434-440.

109. Cava, R.J. and E.A. Rietman, *Physical Review B: Condensed Matter*, 1984, **30** (12), 6896-6902.

110. Boilot, J.P., et al., *Physical Review B: Condensed Matter*, 1980, **22** (12), 5912-5923.

111. Yamagushi, G. and K. Suzuki, *Bulletin of the Chemical Society of Japan*, 1968, **41**, 93.

112. Boilot, J.P., et al., *Solid State Communications*, 1981, **38** (12), 1171-1174.

113. Kahn, A., P. Colomban, and J.P. Boilot, *Journal of Solid State Chemistry*, 1980, **33**, 149-151.

114. England, W.A., A.J. Jacobson, and B.C. Tofield, *Solid State Ionics*, 1982, **6** (1), 21-27.

115. Boilot, J.P., et al., *Physical Review Letters*, 1979, **42** (12), 785-787.

116. Roth, W.L., *Journal of Solid State Chemistry*, 1972, **4**, 60-75.

117. Maglione, M., et al., *Physical Review B: Condensed Matter*, 1989, **40** (16), 11441-11444.

118. Takeuchi, T., et al., *Solid State Ionics*, 1995, **79**, 325.

119. Valot, C., et al., *Journal De Physique IV*, 1996, **6** (C4), 71-89.

120. Floquet, N., et al., *Journal De Physique III*, 1997, **7** (6), 1105-1128.

121. Christen, H.M., et al., *Journal of Electroceramics*, 2000, **4** (2-3), 279-287.

122. Li, C.L., et al., *Journal of Applied Physics*, 1999, **86** (8), 4555-4558.

123. Meyerhofer, D., *Physical Review*, 1958, **112** (2), 413-423.

124. Berglund, C.N. and W.S. Baer, *Physical Review*, 1967, **157** (2), 358-366.

125. Zhong, W., D. Vanderbilt, and K.M. Rabe, *Physical Review Letters*, 1994, **73** (13), 1861-1864.

126. Krakauer, H., et al., *Journal of Physics: Condensed Matter*, 1999, **11** (18), 3779-3787.

127. Chen, Z.X., et al., *Chemical Physics*, 2001, **270** (2), 253-261.

128. Takeuchi, T., et al., *Journal of Materials Chemistry*, 1997, **7** (6), 969-975.

129. Tinte, S., et al., *Journal of Physics: Condensed Matter*, 1999, **11** (48), 9679-9690.

130. Shirane, G., et al., *Physical Review Letters*, 1967, **19** (5), 234-235.

131. Hirata, Y., et al., *Materials Letters*, 1996, **29** (4-6), 229-234.

132. Sarrazin, P., B. Thierry, and J.C. Niepce, *Journal of the European Ceramic Society*, 1995, **15** (7), 623-629.

133. Girshberg, Y. and Y. Yacoby, *Journal of Physics: Condensed Matter*, 2001, **13** (39), 8817-8830.

134. Tinte, S., et al., *Zeitschrift Fur Physik B: Condensed Matter*, 1997, **104** (4), 721-724.

135. Zivkovic, L.M., et al., *Journal of the European Ceramic Society*, 1999, **19** (6-7), 1085-1087.

136. Chen, Z.X., Y. Chen, and Y.S. Jiang, *Journal of Physical Chemistry B*, 2001, **105** (24), 5766-5771.

137. McNeal, M.P., S.J. Jang, and R.E. Newnham, *Journal of Applied Physics*, 1998, **83** (6), 3288-3297.

138. Saha, S., T.P. Sinha, and A. Mookerjee, *Physical Review B*, 2000, **62** (13), 8828-8834.

139. Ghosez, P., et al., *Physical Review B*, 1999, **60** (2), 836-843.

140. Sastry, P.U.M., et al., *Journal of Physics: Condensed Matter*, 1996, **8** (16), 2905-2913.

141. Bedoya, C., et al., *Journal of Physics: Condensed Matter*, 2001, **13** (30), 6453-6470.

142. Wu, E.J. and G. Ceder, *Journal of Applied Physics*, 2001, **89** (10), 5630-5636.

143. Slater, J.C., *Physical Review*, 1950, **78**, 748.

144. Cochran, W., *Physical Review Letters*, 1959, **3**, 412.

145. Comes, R., M. Lambert, and A. Guinier, *Solid State Communications*, 1968, **6**, 715.

146. Muller, C., et al., *Acta Crystallographica, Section B: Structural Science*, 2000, **56**, 27-38.

147. Shirane, G., et al., *Physical Review B: Condensed Matter*, 1970, **2**, 155.

148. Cowley, R.A., *Physical Review A*, 1973, **134**, 981.

149. Burns, G. and B.A. Scott, *Physical Review B: Condensed Matter*, 1973, **7**, 3088.

150. Fleury, P.A. and J.M. Worlock, *Physical Review*, 1968, **174**, 613.

151. Silverman, B.D., *Physical Review*, 1962, **125** (6), 1921-1929.

152. Cochran, W., *Physical Review Letters*, 1959, **3**, 412.

153. Quittet, A.M. and M. Lambert, *Solid State Communications*, 1973, **12**, 1053.

154. Yacoby, Y. and S. Just, *Solid State Communications*, 1974, **15**, 715.

155. Yacoby, Y., *Zeitschrift Fur Physik B: Condensed Matter*, 1978, **31**, 275.

156. Sicron, N., et al., *Physical Review B*, 1994, **50** (18), 13168-13180.

157. De Mathan, N., et al., *Journal of Physics-Condensed Matter*, 1993, **5** (9), 1261-1270.

158. Hanske-Petitpierre, O., et al., *Physical Review B*, 1991, **44** (13), 6700-6707.

159. Kim, K.H., et al., *Physical Review B*, 1990, **42** (16), 10724-10726.

160. Kiat, J.M., et al., *Journal of Physics: Condensed Matter*, 2000, **12** (39), 8411-8425.

161. Khalal, A., D. Khatib, and B. Jannot, *Physica B*, 1999, **271** (1-4), 343-347.

162. Khalal, A., D. Khatib, and B. Jannot, *Annales De Chimie-Science Des Materiaux*, 1999, **24** (7), 471-480.

163. Rousseau, M., et al., *Physica B*, 1997, **234**, 139-141.

164. Girshberg, Y. and Y. Yacoby, *Journal of Physics: Condensed Matter*, 1999, **11** (48), 9807-9822.

165. Elissalde, C. and J. Ravez, *Journal of Materials Chemistry*, 2001, **11** (8), 1957-1967.

166. Chou, C.C. and C.S. Chen, *Ceramics International*, 2000, **26** (7), 693-697.

167. Zhu, X.H., et al., *Journal of Applied Physics*, 2001, **89** (9), 5079-5082.

168. Bell, A.J., *Journal of Applied Physics*, 2001, **89** (7), 3907-3914.

169. Eng, L.M., et al., *Applied Physics Letters*, 1999, **74** (2), 233-235.

170. Damjanovic, D. and M. Demartin, *Journal of Physics: Condensed Matter*, 1997, **9** (23), 4943-4953.

171. Kittel, C., *Physical Review*, 1951, **83**, 458.

172. Arlt, G., U. Bottger, and S. Witte, *Applied Physics Letters*, 1993, **63** (5), 602-604.

173. Potter, B.G., V. Tikare, and B.A. Tuttle, *Journal of Applied Physics*, 2000, **87** (9), 4415-4424.

174. Ivanov, S.N., et al., *Physica B*, 1999, **263**, 784-787.

175. Faraday, M., *Annals of Physics*, 1857, **101**, 383.

176. Walker, G., *New Scientist*, 1995, **147** (1994), 28-31.

177. Zhang, D.J., et al., *Physical Review B: Condensed Matter*, 1998, **58** (21), 14167-14170.

178. Wang, G.H., et al., *Materials Research Bulletin*, 1998, **33** (11), 1571-1579.

179. Komarneni, S., et al., *Journal of the American Ceramic Society*, 1998, **81** (11), 3041-3043.

180. Elihn, K., et al., *Nanostructured Materials*, 1999, **12** (1-4), 79-82.

181. Sung, S.L., et al., *Japanese Journal of Applied Physics Part 2-Letters*, 1998, **37** (2A), L148-L150.

182. Vollath, D., D.V. Szabo, and J. Hausselt, *Journal of the European Ceramic Society*, 1997, **17** (11), 1317-1324.

183. Wu, M.K., et al., *Aerosol Science and Technology*, 1993, **19** (4), 527-548.

184. Whittaker, A.G. and A. Harrison, *unpublished work*,.

185. Lazar, D., B. Ribar, and B. Prelesnik, *Acta Crystallographica, Section C: Crystal Structure Communications*, 1991, **47**, 2282-2285.

186. Ishizawa, N., et al., *Acta Crystallographica, Section B: Structural Science*, 1980, **36**, 228-230.

12 Appendix

I. Diffraction Profile Functions

Diffraction data recorded over the course of this work was generated at one of three sources: a Philips X'pert system, located in the School of Chemistry at the University of Edinburgh; Station 9.1 at the Synchrotron Radiation Source, Daresbury Laboratory; or the HRPD station at ISIS, the Rutherford Appleton Laboratory. In first two cases, the diffracting radiation is X-rays, and in both cases the same profile function was used to refine the structural model to the data. This function is for constant wavelength data and is termed a 'CW type 2' function by GSAS. In the last case, data were recorded as a function of time of flight. A different function, termed a 'TOF type 3' function in GSAS, was used to refine the structural model in these cases. A complete description, including citations for the mathematical functions employed, can be found in the GSAS manual.[92]

Constant Wavelength – function 2

This function employs a multi-term Simpson's rule integration of the pseudo-Voight function, F(ΔT).

$$\mathrm{H}(\Delta \mathrm{T}) = \sum_{i=1}^{n} g_i \, \mathrm{F}(\Delta \mathrm{T}')$$

$$\mathrm{F}(\Delta \mathrm{T}') = \eta \mathrm{L}(\Delta \mathrm{T}', \Gamma) + (1-\eta) \mathrm{G}(\Delta \mathrm{T}', \Gamma)$$

where L and G represent Lorentzian and Gaussian functions respectively. The mixing factor, η, is a function of the total FWHM (full-width-half-max), Γ, and the Lorentzian coefficient, γ. Γ is itself a function of the Gaussian FWHM, Γ_g, and γ.

$$\eta = 1.36603(\gamma/\Gamma) - 0.47719(\gamma/\Gamma)^2 + 0.11116(\gamma/\Gamma)^3$$

$$\Gamma = \sqrt[5]{\Gamma_g^5 + 2.69269\Gamma_g^4\gamma + 2.42843\Gamma_g^3\gamma^2 + 4.47163\Gamma_g^2\gamma^3 + 0.07842\Gamma_g\gamma^4 + \gamma^5}$$

$$\Gamma_g = \sqrt{(8ln2)\sigma^2}$$

The 2θ difference modified for asymmetry, A_S, and sample shift, S_S, is:

$$\Delta T' = \Delta T + \frac{f_i A_S}{\tan 2\theta} + S_S \cos\theta + T_S \sin 2\theta$$

where the number of terms in the sum depends on the size of A_S. The corresponding Simpson's rule coefficients, g_i and f_i, depend on the number of terms in the summation. In the case of Bragg-Brentano geometry for x-ray powder diffraction (as in all examples here), the sample shift can be interpreted as a physical shift of the sample, s, from the diffractometer axis.

$$s = \frac{-\pi R S_S}{36000}$$

where R is the diffractometer radius. In a similar way, the effective sample absorption can be obtained from the transparency coefficient, T_S, by:

$$\mu_{eff} = \frac{-9000}{\pi R T_S}$$

The variance of the peak, σ^2, varies with 2θ as:

$$\sigma^2 = U\tan^2\theta + V\tan\theta + W + P/\cos^2\theta$$

where U, V and W are the profile coefficients and P is the Scherrer coefficient for Gaussian broadening. The Lorentzian coefficient, γ, varies as:

$$\gamma = \frac{X + X_e\cos\phi}{\cos\theta} + (Y + Y_e\cos\phi + \gamma_L d^2)\tan\theta$$

The first term is the Lorentzian Scherrer broadening ad includes an anisotropy coefficient, X_e. The second term describes strain broadening and also includes an anisotropy coefficient. If a sublattice is defined by use of "stacking fault vectors", then the above function only is applied to the reflections that are part of the sublattice. All other reflections have their Lorentzian broadening defined by (note the change from X_e to X_s):

$$\gamma = \frac{X + X_e \cos\phi}{\cos\theta} + (Y + Y_e \cos\phi + \gamma_L d^2)\tan\theta$$

This means that one set of reflections has a different particle size anisotropy than the other set. This effect is seen when the sample contains stacking faults that will broaden some reflections leaving a sublattice of sharp reflections that correspond to the substructure that continues unmodified through the stacking fault. Generally, X_e will be much larger than X_s. The γ_L term in these two expressions are an empirical extension of the microstrain anisotropy by:

$$\gamma_L = \gamma_{11}h^2 + \gamma_{22}k^2 + \gamma_{33}l^2 + 2\gamma_{12}hk + 2\gamma_{13}hl + 2\gamma_{23}kl$$

This function gives a good fit to asymmetric profiles and shows less correlation with lattice parameters than some simpler functions. It does less well treating the reflection asymmetry due to axial divergence at low angles ($2\theta < 10°$).

Time of Flight – function 3

This function is a convolution of back-to-back exponentials with a pseudo-Voigt function.

$$\mathrm{H}(\Delta\mathrm{T}) = \int \mathrm{E}(\Delta\mathrm{T} - t)\,\mathrm{P}(t)\,\mathrm{d}t$$

$$\mathrm{H}(\Delta\mathrm{T}) = (1-\eta)N\left[e^{u}\operatorname{erfc} y + e^{v}\operatorname{erfc} z\right] - \frac{2N\eta}{\pi}\left\{\mathrm{Im}\left[\exp(p\mathrm{E}_1\, p)\right] + \mathrm{Im}\left[\exp(q\mathrm{E}_1\, q)\right]\right\}$$

where η, N, u, v, y, z, p and q are defined:

$$\eta = 1.36603(\gamma/\Gamma) - 0.47719(\gamma/\Gamma)^2 + 0.11116(\gamma/\Gamma)^3$$

$$N = \frac{\alpha\beta}{2(\alpha+\beta)}$$

$$u = \frac{\alpha}{2}\left(\alpha\sigma^2 + 2\Delta \mathrm{T}\right) \qquad v = \frac{\beta}{2}\left(\beta\sigma^2 - 2\Delta \mathrm{T}\right)$$

$$y = \frac{\alpha\sigma^2 + \Delta \mathrm{T}}{\sqrt{2\sigma^2}} \qquad z = \frac{\beta\sigma^2 - \Delta T}{\sqrt{2\sigma^2}}$$

$$p = -\alpha\Delta \mathrm{T} + \frac{i\alpha\gamma}{2} \qquad q = -\beta\Delta \mathrm{T} + \frac{i\beta\gamma}{2}$$

The terms α, β, and σ are defined in terms of the d-spacing.

$$\alpha = \frac{\alpha_1}{d} \qquad \beta = \beta_0 + \frac{\beta_1}{d^4} \qquad \sigma^2 = \sigma_0^2 + \sigma_1^2 d^2 + \sigma_2^2 d^4$$

For the γ profile coefficient an additional type of broadening is introduced where two classes of reflections can be defined. Those that fall on sublattice (as defined by three vectors and includes the origin) have the following expression for the γ coefficient:

$$\gamma = \gamma_0 + \gamma_1 d + \gamma_2 d^2 + \left(\gamma_{1e} d + \gamma_{2e} d^2\right)\cos\phi + \gamma_L$$

while the rest have the following equation (note the difference in the final coefficient in parentheses):

$$\gamma = \gamma_0 + \gamma_1 d + \gamma_2 d^2 + \left(\gamma_{1e} d + \gamma_{2s} d^2\right)\cos\phi + \gamma_L$$

This means that, like the CW function above, one set of reflections has a different particle size anisotropy than the other set. This effect is seen when the sample contains stacking faults that will broaden some reflections leaving a sublattice of sharp reflections that correspond to the substructure that continues unmodified through the stacking fault. Generally, γ_{2s} will be much larger than γ_{2e}. The final term in both these expressions of γ is an empirical extension of the microstrain anisotropy (similar to the CW function above) by:

$$\gamma_L = \gamma_{11}h^2 + \gamma_{22}k^2 + \gamma_{33}l^2 + 2\gamma_{12}hk + 2\gamma_{13}hl + 2\gamma_{23}kl$$

In the data following, taken at HRPD, many of the coefficients are well-defined for the instrument, leading to greater accuracy in the subsequent refinements.

II. Experimental Diffraction Data

Title

Silver iodide powder at 353 K, using *in-situ* microwave adapter and convection heating. Diffraction by Cu Kα radiation form Philips X'pert system, Edinburgh University.	
Main text reference	p100

Phase 1

Title	β- silver iodide				
Space Group	$P6_3mc$		Proportion/%	86.0(13)	
a/Å	4.5983(9)	b/Å	4.5983(9)	c/Å	7.5260(18)
α/°	90	β/°	90	γ/°	120
Atom	x	y	z	F	U^{eq}/Å^2
Ag (1)	⅓	⅔	0	1	-0.016(12)
I (1)	⅓	⅔	0.6157(22)	1	-0.074(6)
Profile type	CW type 2	GU	6.3(8)E+03	GV	-5.7(6)E+03
GW	1.48(12)E+03	LX	0	LY	0
trans	0	asym	0	shft	0

Phase 2

Title	γ- silver iodide				
Space Group	$F\bar{4}3m$		Proportion/%	24.0(13)	
a/Å	6.5094(12)	b/Å	6.5094(12)	c/Å	6.5094(12)
α/°	90	β/°	90	γ/°	90
Atom	x	y	z	F	U^{eq}/Å^2
Ag (1)	0	0	0	1	-0.060(29)
I (1)	¼	¼	¼	1	-0.054(27)
Profile type	CW type 2	GU	1.57(12)E+04	GV	-9.8(7)E+03
GW	1.65(10)E+03	LX	0	LY	0
trans	0	asym	0	shft	0

Instrument Parameters

Min 2θ/°	20.00	Max 2θ/°	60.00	Step 2θ/°	0.01
λ/Å	1.5405600, 1.5443900 (Cu Kα)			ratio	0.5
Zero	-6.5(6)	POLA	0.55	Scale	0.75(3)
Background	Type 2 (Cosine Fourier series)			terms	24

Goodness of Fit

χ^2	4.383	R_{wp}	0.2780	R_p	0.2162

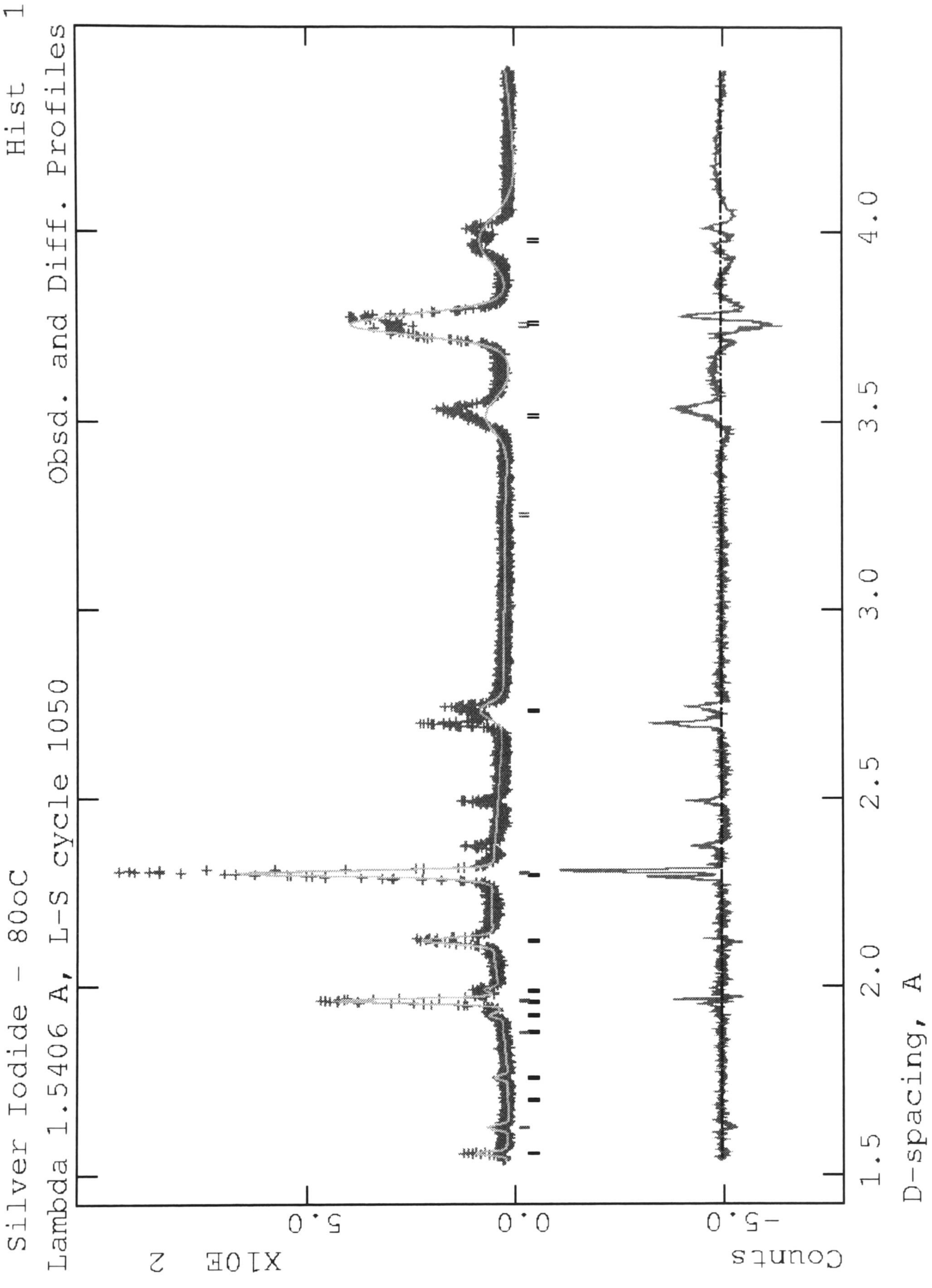
Silver Iodide - 80oC
Lambda 1.5406 A, L-S cycle 1050
Hist 1
Obsd. and Diff. Profiles
X10E 2
Counts
5.0
0.0
-5.0
1.5
2.0
2.5
3.0
3.5
4.0
D-spacing, A

Title

Sodium β” alumina at 523 K, using *in-situ* microwave adapter and conventional heating. Diffraction by synchrotron radiation at Station 9.1 at SRS, Daresbury laboratory.	
Main text reference	p119

Phase 1

Title	Sodium β” alumina				
Space Group	$R\bar{3}m$		Proportion/%	81.4(12)	
a/Å	5.61018(9)	b/Å	5.61018(9)	c/Å	33.4767(6)
α/°	90	β/°	90	γ/°	120

Atom	x	y	z	F	U^{eq}/Å^2
Al (1)	0.1666(4)	0.3331(8)	0.92918(8)	1	0.0491
Al (2)	0	0	0.34864(17)	0.6725	0.0662
Mg (1)	0	0	0.34864(17)	0.3275	0.0662
Al (3)	0	0	0.45013(14)	1	0.0420
Al (4)	0	0	0	1	0.0415
O (1)	0.1708(6)	0.3417(13)	0.23476(17)	1	0.0474
O (2)	0.1470(5)	0.2939(11)	0.03491(13)	1	0.0436
O (3)	0	0	0.09510(24)	1	0.0510
O (4)	0	0	0.29494(27)	1	0.0332
O (5)	0	0	½	1	0.0423
Na (1)	0	0	0.7868(47)	0.3400	0.7961
Na (2)	0.0606(25)	0.121(5)	0.8292(6)	0.1616	0.0921

Atom	U^{11}/Å^2	U^{22}/Å^2	U^{33}/Å^2	U^{12}/Å^2	U^{13}/Å^2	U^{23}/Å^2
Al (1)	0.0485(16)	0.0589(21)	0.0386(18)	0.0295(10)	-0.0011(11)	-0.0023(21)
Al (2)	0.0473(28)	0.0473(28)	0.0869(66)	0.0111(14)	0	0
Mg (1)	0.0473(28)	0.0473(28)	0.0869(66)	0.0111(14)	0	0
Al (3)	0.0404(26)	0.0404(26)	0.0443(45)	0.0202(13)	0	0
Al (4)	0.0422(29)	0.0422(29)	0.0390(53)	0.0211(15)	0	0
O (1)	0.0375(26)	0.026(4)	0.0782(43)	0.0130(18)	-0.0083(21)	-0.017(4)
O (2)	0.0471(29)	0.065(4)	0.0171(35)	0.0326(21)	0.0110(19)	0.022(4)
O (3)	0.0748(42)	0.075(4)	0.0018(67)	0.0374(21)	0	0
O (4)	0.0187(50)	0.019(5)	0.0617(82)	0.0093(25)	0	0
O (5)	0.0896(79)	0.090(8)	-0.0543(83)	0.0448(40)	0	0
Na (1)	0.80(14)	0.80(14)	0.77(25)	0.40(7)	0	0
Na (2)	0.042(16)	0.24(5)	-0.024(8)	0.106(27)	0.036(10)	0.073(21)

Profile type	CW type 2	GU	30.00	GV	-5.42
GW	2.50	LX	0.90	LY	10.20
trans	0	asym	0	shft	0

(continued)

Phase 2

Title	Sodium β alumina				
Space Group	$P6_3mmc$		Proportion/%	18.6(12)	
a/Å	5.638(6)	b/Å	5.638(6)	c/Å	22.00(4)
α/°	90	β/°	90	γ/°	120
Atom	x	y	z	F	U^{eq}/Å^2
Al (1)	0.811(4)	0.622(8)	0.1066(22)	1	0.1887
Al (2)	⅓	⅔	0.013(13)	1	0.5579
Al (3)	⅓	⅔	0.178(20)	1	0.6655
Al (4)	0	0	0	1	-0.0504
O (1)	0.1339(26)	0.268(5)	0.0526(11)	1	-0.0614
O (2)	0.496(13)	0.991(27)	0.1818(142)	1	0.4984
O (3)	⅔	⅓	0.0809(74)	1	0.1733
O (4)	0	0	0.1489(26)	1	-0.0378
O (5)	0.195(16)	0.390(33)	¼	1	0.8000
Na (1)	0.593(6)	0.186(13)	¼	0.2333	-0.0900
Na (2)	0.927(6)	0.854(12)	¼	0.2333	-0.0900
Profile type	CW type 2	GU	5E+04	GV	-1.5E+04
GW	2E+03	LX	0	LY	0
trans	0	asym	0	shft	0

Instrument Parameters

Min 2θ/°	11.00	Max 2θ/°	50.00	Step 2θ/°	0.01
λ/Å	1.000 (synchrotron radiation)				
Zero	-1.15(4)	POLA	0.95000	Scale	23.10(23)
Background	Type 2 (Cosine Fourier series)			terms	24

Goodness of Fit

χ^2	5.021	R_{wp}	0.1318	R_p	0.1001

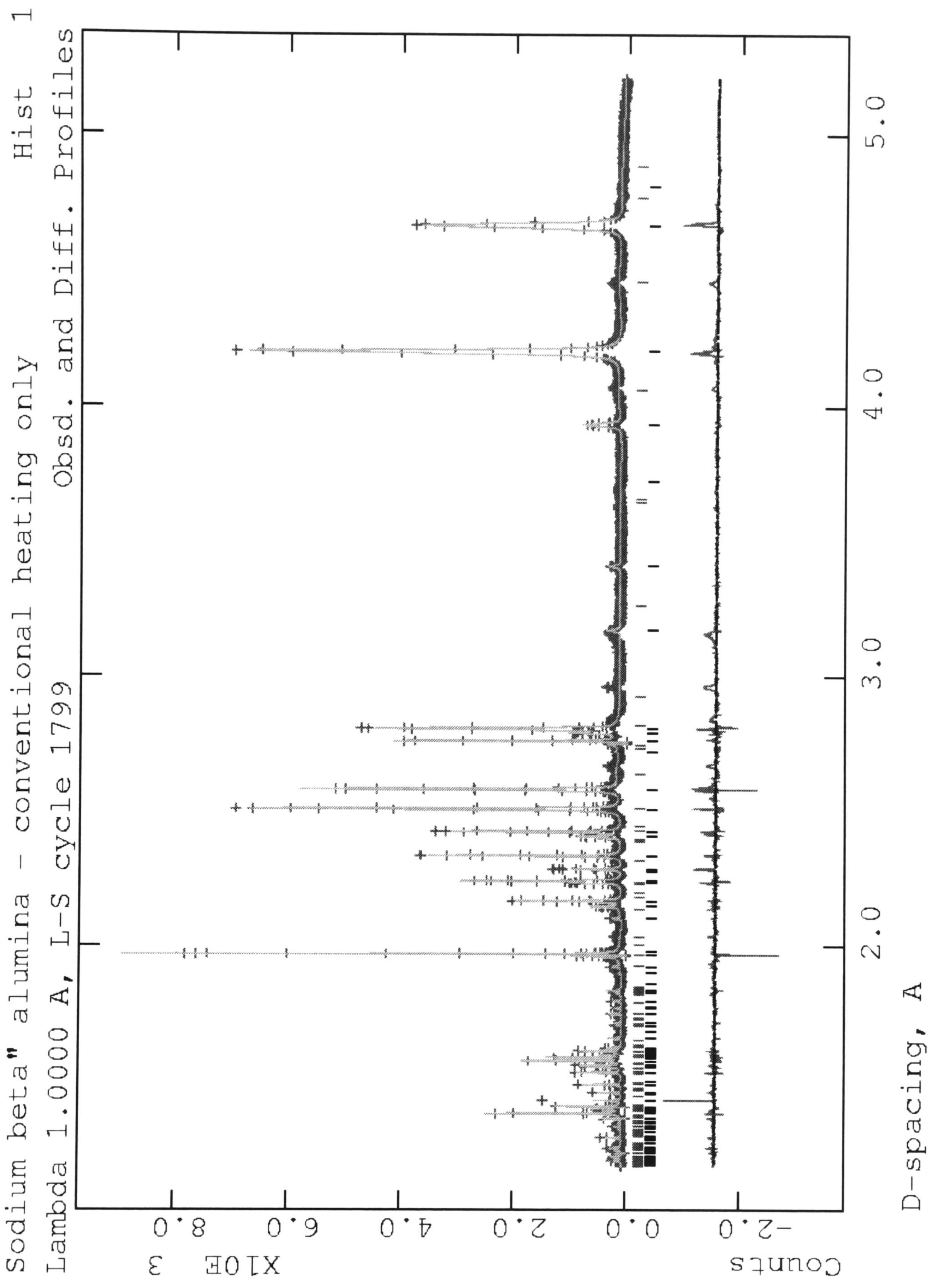
Sodium beta" alumina - conventional heating only Hist 1
Lambda 1.0000 A, L-S cycle 1799 Obsd. and Diff. Profiles
Counts X10E 3
8.0
6.0
4.0
2.0
0.0
-2.0
D-spacing, A
2.0
3.0
4.0
5.0

Title

Sodium β" alumina at 523 K, using *in-situ* microwave adapter and combined microwave/conventional heating. Diffraction by synchrotron radiation at Station 9.1 at SRS, Daresbury laboratory.	
Main text reference	p120

Phase 1

Title	Sodium β" alumina				
Space Group	$R\bar{3}m$		Proportion/%	78.7(11)	
a/Å	5.61029(9)	b/Å	5.61029(9)	c/Å	33.4722(6)
α/°	90	β/°	90	γ/°	120

Atom	*x*	*y*	*z*	*F*	U^{eq}/Å^2
Al (1)	0.1664(4)	0.3327(8)	0.92905(8)	1	0.0477
Al (2)	0	0	0.34892(18)	0.6725	0.0643
Mg (1)	0	0	0.34892(18)	0.3275	0.0643
Al (3)	0	0	0.45017(14)	1	0.0410
Al (4)	0	0	0	1	0.0388
O (1)	0.1709(7)	0.3417(13)	0.23489(17)	1	0.0468
O (2)	0.1469(6)	0.2938(11)	0.03493(13)	1	0.0400
O (3)	0	0	0.09487(26)	1	0.0533
O (4)	0	0	0.29496(27)	1	0.0303
O (5)	0	0	½	1	0.0440
Na (1)	0	0	0.7890(48)	0.3400	0.7842
Na (2)	0.0614(24)	0.123(5)	0.8291(6)	0.1616	0.0867

Atom	U^{11}/Å^2	U^{22}/Å^2	U^{33}/Å^2	U^{12}/Å^2	U^{13}/Å^2	U^{23}/Å^2
Al (1)	0.0475(16)	0.0584(21)	0.0360(18)	0.0292(11)	-0.0013(11)	-0.0027(22)
Al (2)	0.0450(27)	0.0450(27)	0.0857(67)	0.0100(14)	0	0
Mg (1)	0.0450(27)	0.0450(27)	0.0857(67)	0.0100(14)	0	0
Al (3)	0.0417(27)	0.0417(27)	0.0389(47)	0.0208(14)	0	0
Al (4)	0.0364(29)	0.0364(29)	0.0428(57)	0.0182(15)	0	0
O (1)	0.0392(27)	0.030(4)	0.070(4)	0.0150(19)	-0.0121(21)	-0.024(4)
O (2)	0.0458(29)	0.060(4)	0.013(4)	0.0300(20)	0.0100(19)	0.020(4)
O (3)	0.0736(43)	0.074(4)	0.011(7)	0.0368(22)	0	0
O (4)	0.0173(50)	0.017(5)	0.056(8)	0.0086(25)	0	0
O (5)	0.0907(83)	0.091(8)	-0.051(9)	0.0454(42)	0	0
Na (1)	0.80(14)	0.80(14)	0.74(24)	0.40(7)	0	0
Na (2)	0.045(17)	0.23(5)	-0.036(8)	0.102(27)	0.026(9)	0.052(18)

Profile type	CW type 2	GU	30.00	GV	-5.42
GW	2.50	LX	0.90	LY	10.20
trans	0	asym	0	shft	0

(continued)

Phase 2

Title	Sodium β alumina				
Space Group	$P6_3/mmc$		Proportion/%	21.3(11)	
a/Å	5.643(6)	b/Å	5.643(6)	c/Å	21.983(35)
α/°	90	β/°	90	γ/°	120
Atom	x	y	z	F	U^{eq}/Å^2
Al (1)	0.815(4)	0.631(8)	0.1045(21)	1	0.2108
Al (2)	⅓	⅔	0.011(9)	1	0.4818
Al (3)	⅓	⅔	0.179(17)	1	0.7245
Al (4)	0	0	0	1	-0.0445
O (1)	0.1371(26)	0.274(6)	0.0524(12)	1	-0.0480
O (2)	0.500(11)	0.000(22)	0.180(12)	1	0.4728
O (3)	⅔	⅓	0.0845(66)	1	0.1619
O (4)	0	0	0.1518(26)	1	-0.0350
O (5)	0.201(15)	0.401(29)	¼	1	0.8000
Na (1)	0.593(6)	0.185(11)	¼	0.2333	-0.0900
Na (2)	0.928(5)	0.856(11)	¼	0.2333	-0.0900
Profile type	CW type 2	GU	5E+04	GV	-1.5E+04
GW	2E+03	LX	0	LY	0
trans	0	asym	0	shft	0

Instrument Parameters

Min 2θ/°	11.00	Max 2θ/°	50.00	Step 2θ/°	0.01
λ/Å	1.000 (synchrotron radiation)				
Zero	-1.30(4)	POLA	0.95000	Scale	18.434
Background	Type 2 (Cosine Fourier series)			terms	24

Goodness of Fit

χ^2	4.294	R_{wp}	0.1423	R_p	0.1036

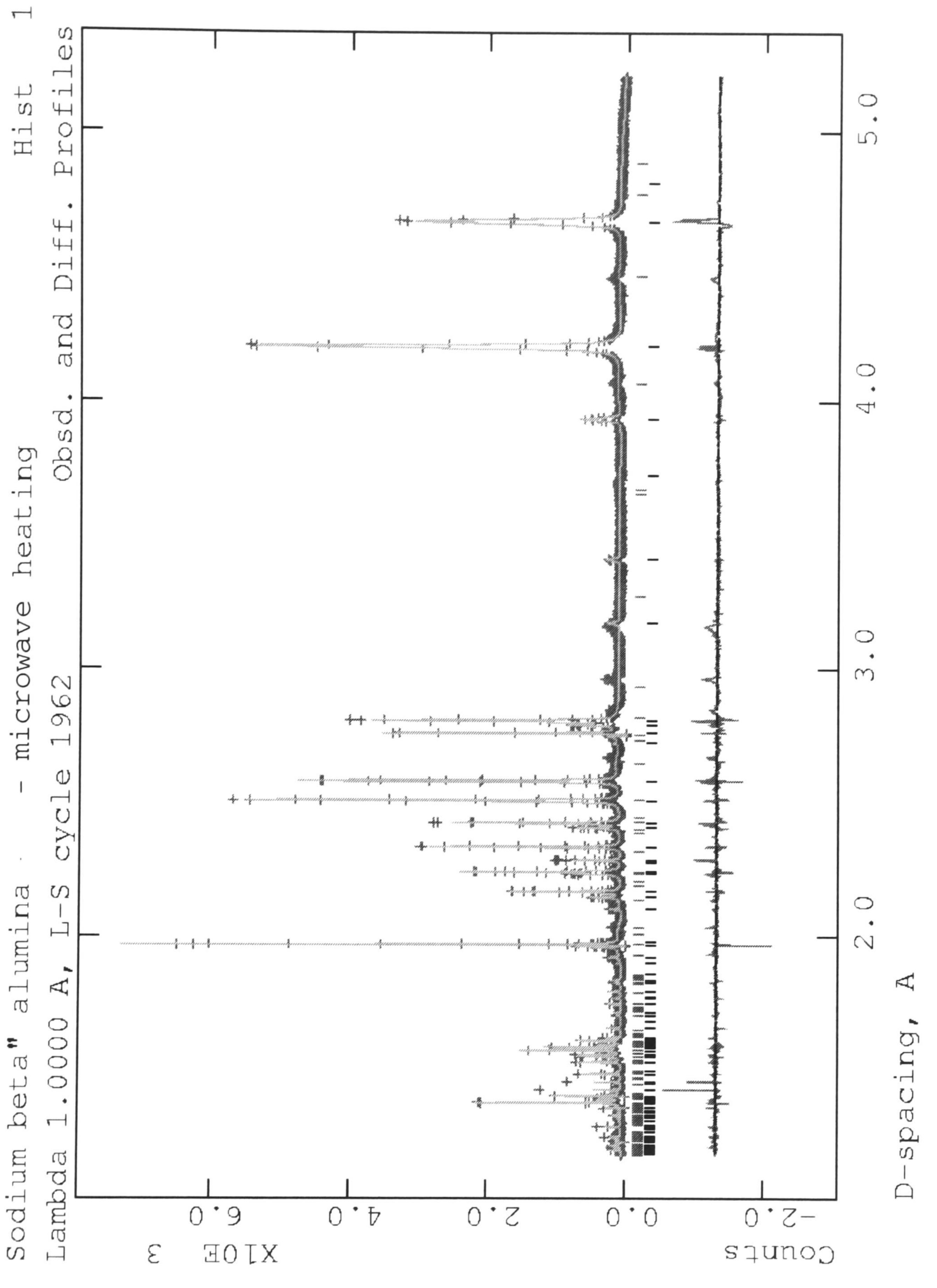
Sodium beta" alumina - microwave heating
Lambda 1.0000 A, L-S cycle 1962
Hist 1
Obsd. and Diff. Profiles
X10E 3
Counts
6.0
4.0
2.0
0.0
-2.0
2.0
3.0
4.0
5.0
D-spacing, A

Title

Silver β" alumina at 456 K, using *in-situ* microwave adapter and conventional heating. Diffraction by synchrotron radiation at Station 9.1 at SRS, Daresbury laboratory.	
Main text reference	p124

Phase 1

Title	Silver β" alumina				
Space Group	$R\bar{3}m$		Proportion/%	89.1(14)	
a/Å	5.61351(8)	b/Å	5.61351(8)	c/Å	33.3795(6)
α/°	90	β/°	90	γ/°	120

Atom	x	y	z	F	U^{eq}/Å^2
Al (1)	0.1656(6)	0.8344(6)	0.92817(11)	1	0.0206
Al (2)	0	0	0.35101(24)	0.633(9)	0.0309
Mg (1)	0	0	0.35101(24)	0.367(9)	0.0309
Al (3)	0	0	0.45137(22)	1	0.0102
Al (4)	0	0	0	1	0.0062
O (1)	0.1658(8)	0.8342(8)	0.23524(18)	1	0.0061
O (2)	0.1541(8)	0.8459(8)	0.03482(16)	1	0.0148
O (3)	0	0	0.10099(28)	1	-0.0082
O (4)	0	0	0.29801(41)	1	0.0195
O (5)	0	0	½	1	0.0070
Ag (1)	0.021(7)	0.979(7)	0.83087(11)	0.289(3)	0.0754

Atom	U^{11}/Å^2	U^{22}/Å^2	U^{33}/Å^2	U^{12}/Å^2	U^{13}/Å^2	U^{23}/Å^2
Al (1)	0.0134(24)	0.0134(24)	0.033(3)	0.0057(24)	0.0088(14)	-0.0088(14)
Al (2)	0.0046(43)	0.0046(43)	0.067(8)	-0.010(2)	0	0
Mg (1)	0.0046(43)	0.0046(43)	0.067(8)	-0.010(2)	0	0
Al (3)	-0.0125(37)	-0.0125(37)	0.056(6)	-0.0062(18)	0	0
Al (4)	0.0061(48)	0.0061(48)	0.006(7)	0.0031(24)	0	0
O (1)	-0.014(4)	-0.014(4)	0.036(6)	-0.015(4)	0.002(3)	-0.002(3)
O (2)	0.029(5)	0.029(5)	-0.013(5)	0.015(4)	-0.013(2)	0.013(2)
O (3)	0.006(6)	0.006(6)	-0.036(8)	0.003(3)	0	0
O (4)	0.011(9)	0.011(9)	0.036(14)	0.006(4)	0	0
O (5)	0.055(12)	0.055(12)	-0.090(12)	0.028(6)	0	0
Ag (1)	0.093(9)	0.093(9)	0.0042(21)	0.020(13)	0.013(7)	-0.013(7)

Profile type	CW type 2	GU	37.00	GV	-5.00
GW	1.30	LX	1.50	LY	9.00
trans	0	asym	0	shft	0

(continued)

Phase 2

Title	Silver β alumina				
Space Group	$P6_3/mmc$		Proportion/%	10.9(14)	
a/Å	5.671(7)	b/Å	5.671(7)	c/Å	21.96(4)
α/°	90	β/°	90	γ/°	120
Atom	*x*	*y*	*z*	*F*	U^{eq}/Å^2
Al (1)	0.855(8)	0.709(15)	0.1144(22)	1	-0.0444
Al (2)	⅓	⅔	0.0118(40)	1	-0.0562
Al (3)	⅓	⅔	0.1741(94)	1	0.226
Al (4)	0	0	0	1	-0.0375
O (1)	0.140(10)	0.280(19)	0.045(4)	1	-0.0363
O (2)	0.512(4)	0.025(8)	0.172(4)	1	-0.0840
O (3)	⅔	⅓	0.101(13)	1	-0.135
O (4)	0	0	0.167(79)	1	0.635
O (5)	0.122(50)	0.245(100)	¼	⅓	-0.0900
Ag (1)	0.711(11)	0.423(22)	¼	⅓	-0.0148
Ag (2)	0.940(6)	0.880(12)	¼	0.16667	-0.0900
Profile type	CW type 2	GU	5E+04	GV	-1.5E+04
GW	2E+03	LX	0	LY	0
trans	0	asym	0	shft	0

Instrument Parameters

Min 2θ/°	11.00	Max 2θ/°	50.00	Step 2θ/°	0.01
λ/Å	1.000 (synchrotron radiation)				
Zero	0.51(3)	POLA	0.95	Scale	5.08(9)
Background	Type 2 (Cosine Fourier series)			terms	24

Goodness of Fit

χ^2	2.574	R_{wp}	0.1059	R_p	0.0813

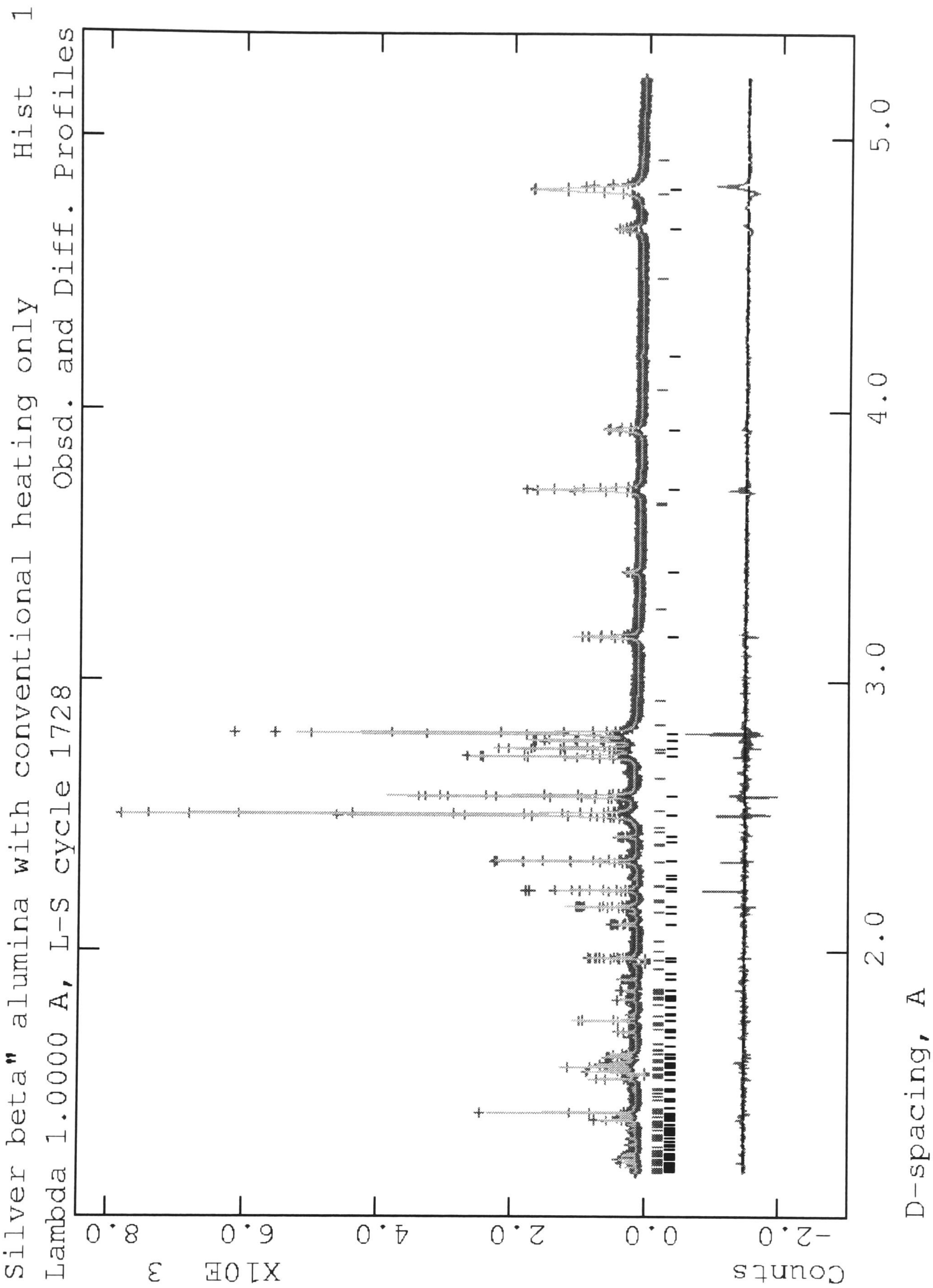
Silver beta" alumina with conventional heating only Hist 1
Lambda 1.0000 A, L-S cycle 1728 Obsd. and Diff. Profiles
X10E 3
Counts
8.0
6.0
4.0
2.0
0.0
-2.0
2.0
3.0
4.0
5.0
D-spacing, A

Title

Silver β" alumina at 456 K, using *in-situ* microwave adapter and combined conventional/microwave heating. Diffraction by synchrotron radiation at Station 9.1 at SRS, Daresbury laboratory.	
Main text reference	p124

Phase 1

Title	Silver β" alumina				
Space Group	$R\bar{3}m$		Proportion/%	85.9(13)	
a/Å	5.61307(8)	b/Å	5.61307(8)	c/Å	33.3754(6)
α/°	90	β/°	90	γ/°	120

Atom	*x*	*y*	*z*	*F*	U^{eq}/Å^2
Al (1)	0.1585(5)	0.8415(5)	0.92830(11)	1	0.0150
Al (2)	0	0	0.34872(26)	0.633(9)	0.0149
Mg (1)	0	0	0.34872(26)	0.367(9)	0.0149
Al (3)	0	0	0.45029(21)	1	0.0052
Al (4)	0	0	0	1	0.0158
O (1)	0.1624(7)	0.8376(7)	0.23541(17)	1	-0.0034
O (2)	0.1613(7)	0.8387(7)	0.03381(15)	1	0.0039
O (3)	0	0	0.10220(25)	1	-0.0218
O (4)	0	0	0.29434(38)	1	0.0078
O (5)	0	0	½	1	0.0145
Ag (1)	0.029(5)	0.971(5)	0.83128(10)	0.289(3)	0.0705

Atom	U^{11}/Å^2	U^{22}/Å^2	U^{33}/Å^2	U^{12}/Å^2	U^{13}/Å^2	U^{23}/Å^2
Al (1)	0.0100(22)	0.0100(22)	0.0286(32)	0.0079(24)	-0.0036(15)	0.0036(15)
Al (2)	-0.0328(31)	-0.0328(31)	0.0948(86)	-0.0289(16)	0	0
Mg (1)	-0.0328(31)	-0.0328(31)	0.0948(86)	-0.0289(16)	0	0
Al (3)	-0.0048(36)	-0.0048(36)	0.0251(59)	-0.0024(18)	0	0
Al (4)	-0.0136(44)	-0.0136(44)	0.075(10)	-0.0068(22)	0	0
O (1)	-0.0351(30)	-0.0351(30)	0.036(6)	-0.0368(34)	0.0067(31)	-0.0067(31)
O (2)	0.0376(46)	0.0376(46)	-0.026(4)	0.0479(49)	-0.0150(24)	0.0150(24)
O (3)	-0.0014(58)	-0.0014(58)	-0.063(7)	-0.0007(29)	0	0
O (4)	0.0214(86)	0.0214(86)	-0.020(10)	0.0107(43)	0	0
O (5)	0.023(10)	0.023(10)	-0.090(11)	0.0115(50)	0	0
Ag (1)	0.108(15)	0.108(15)	0.0049(23)	0.056(5)	0.018(5)	-0.018(5)

Profile type	CW type 2	GU	37.00	GV	-5.00
GW	1.30	LX	1.50	LY	9.00
trans	0	asym	0	shft	0

(continued)

Phase 2

Title	Silver β alumina				
Space Group	$P6_3/mmc$		Proportion/%	14.1(13)	
a/Å	5.655(7)	b/Å	5.655(7)	c/Å	22.04(5)
α/°	90	β/°	90	γ/°	120
Atom	*x*	*y*	*z*	*F*	U^{eq}/Å^2
Al (1)	0.845(7)	0.689(15)	0.1140(32)	1	0.0107
Al (2)	⅓	⅔	0.0191(40)	1	-0.0398
Al (3)	⅓	⅔	0.1863(92)	1	0.0750
Al (4)	0	0	0	1	0.0334
O (1)	0.142(10)	0.285(21)	0.0446(33)	1	-0.0670
O (2)	0.524(7)	0.047(13)	0.1703(54)	1	-0.0758
O (3)	⅔	⅓	0.1009(643)	1	0.6384
O (4)	0	0	0.3288(335)	1	0.2518
O (5)	0.188(57)	0.375(113)	¼	⅓	0.0707
Ag (1)	0.707(12)	0.414(24)	¼	⅓	0.0776
Ag (2)	0.057(9)	1.114(18)	¼	0.16667	-0.0633
Profile type	CW type 2	GU	5E+04	GV	-1.5E+04
GW	2E+03	LX	0	LY	0
trans	0	asym	0	shft	0

Instrument Parameters

Min 2θ/°	11.00	Max 2θ/°	50.00	Step 2θ/°	0.01
λ/Å	1.000 (synchrotron radiation)				
Zero	-0.30(4)	POLA	0.95	Scale	4.09(6)
Background	Type 2 (Cosine Fourier series)			terms	24

Goodness of Fit

χ^2	2.406	R_{wp}	0.1121	R_p	0.0855

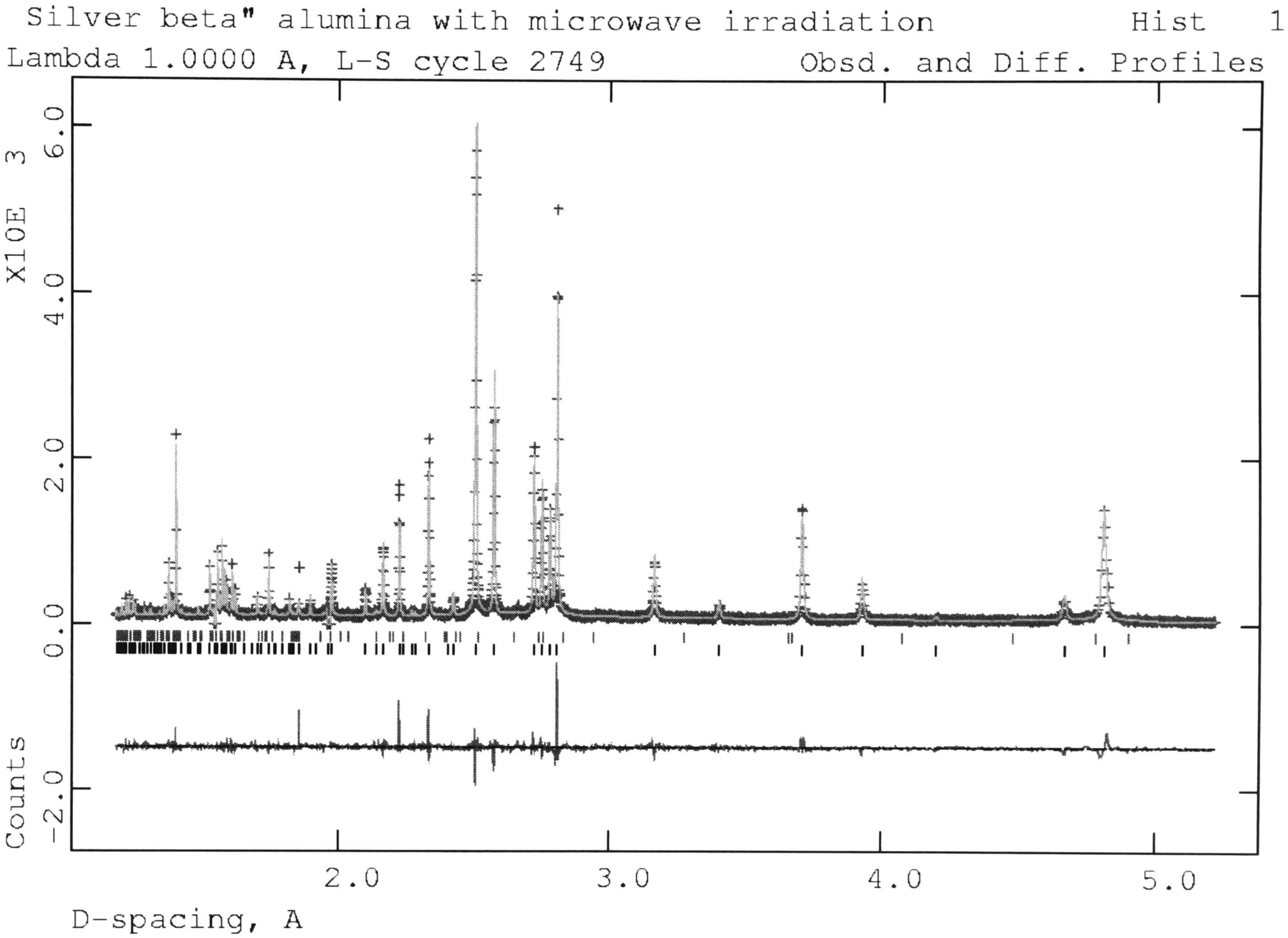
Silver beta" alumina with microwave irradiation
Hist 1
Lambda 1.0000 A, L-S cycle 2749
Obsd. and Diff. Profiles
X10E 3
Counts
6.0
4.0
2.0
0.0
-2.0
2.0
3.0
4.0
5.0
D-spacing, A

Title

Sodium β" alumina at 473 K, using electric furnace heating and vanadium sample holder. Diffraction by neutron radiation at HRPD instrument, ISIS, Rutherford Appleton Laboratory.	
Main text reference	p117

Phase 1

Title	Sodium β" alumina				
Space Group	$R\bar{3}m$		Proportion/%	99.05(33)	
a/Å	5.61727(13)	b/Å	5.61727(13)	c/Å	33.5113(9)
α/°	90	β/°	90	γ/°	120
Atom	x	y	z	F	U^{eq}/Å^2
Al (1)	0.1601(18)	0.320(4)	0.9293(5)	1	0.0152
Al (2)	0	0	0.3517(9)	0.6725	0.0320
Mg (1)	0	0	0.3502(9)	0.3275	0.0320
Al (3)	0	0	0.4506(5)	1	-0.0098
Al (4)	0	0	0	1	0.0296
O (1)	0.1629(14)	0.3258(28)	0.23426(26)	1	0.0099
O (2)	0.1597(11)	0.3194(23)	0.03475(22)	1	0.0137
O (3)	0	0	0.09847(54)	1	0.0178
O (4)	0	0	0.29495(38)	1	-0.0008
O (5)	0	0	½	1	0.0287
Na (1)	0	0	0.7973(27)	0.3400	0.1023
Na (2)	0.986(33)	0.97(7)	0.8303(20)	0.1616	0.3454

Atom	U^{11}/Å^2	U^{22}/Å^2	U^{33}/Å^2	U^{12}/Å^2	U^{13}/Å^2	U^{23}/Å^2
Al (1)	-0.005(3)	-0.002(5)	0.053(7)	-0.001(3)	-0.006(4)	-0.013(9)
Al (2)	0.013(5)	0.013(5)	0.054(17)	-0.006(3)	0	0
Mg (1)	0.013(5)	0.013(5)	0.054(17)	-0.006(3)	0	0
Al (3)	-0.006(4)	-0.006(4)	-0.016(8)	-0.003(2)	0	0
Al (4)	-0.017(8)	-0.017(8)	0.12(4)	-0.008(4)	0	0
O (1)	-0.0014(21)	0.4(4)	0.028(4)	0.0018(18)	0.002(2)	0.004(4)
O (2)	0.013(3)	0.024(6)	0.003(3)	0.012(3)	-0.006(3)	-0.012(5)
O (3)	0.018(5)	0.018(5)	0.018(10)	0.009(2)	0	0
O (4)	0.0005(47)	0.001(5)	-0.003(7)	0.000(2)	0	0
O (5)	0.041(9)	0.041(9)	0.003(13)	0.021(5)	0	0
Na (1)	0.15(7)	0.15(7)	0.01(5)	0.07(3)	0	0
Na (2)	0.27(10)	0.8(5)	-0.05(3)	0.4(2)	0.05(6)	0.10(12)

Profile type	TOF type 3	α	1.529E-01	β-0	2.125E-02
β-1	1.093E-02	σ-0	0	σ-1	1.07(35)E+02
σ-2	0	γ-0	0	γ-1	6.57(16)E+01
γ-2	0				

(continued)

Phase 2

Title	Sodium β alumina				
Space Group	$P6_3/mmc$		Proportion/%	0.95(33)	
a/Å	5.6452(19)	b/Å	5.6452(19)	c/Å	22.092(11)
α/°	90	β/°	90	γ/°	120
Atom	*x*	*y*	*z*	*F*	U^{eq}/Å^2
Al (1)	0.822(10)	0.643(20)	0.1396(50)	1	-0.0513
Al (2)	⅓	⅔	0.0373(75)	1	-0.0596
Al (3)	⅓	⅔	0.1761(33)	1	-0.0816
Al (4)	0	0	0	1	0.8
O (1)	0.132(6)	0.264(12)	0.0491(20)	1	-0.0630
O (2)	0.53(11)	0.039(26)	0.1272(72)	1	0.0181
O (3)	⅔	⅓	0.933(22)	1	0.0107
O (4)	0	0	0.153(15)	1	-0.0063
O (5)	0.243(10)	0.486(20)	¼	1	-0.0466
Na (1)	0.464(25)	0.93(5)	¼	0.2333	-0.0846
Na (2)	0.909(82)	0.82(16)	¼	0.2333	-0.0378
Profile type	TOF type 3	α	1.529E-01	β-0	2.125E-02
β-1	1.093E-02	σ-0	0	σ-1	8.14(18)E+02
σ-2	0	γ-0	0	γ-1	4(8)E+01
γ-2	0				

Instrument Parameters

Min TOF/μs	34.00		Max TOF/μs	118.00	
DIFA	48233.41	DIFC	0.70	Scale	35.4(5)
Zero	6.8(15)	Background	Type 1	terms	24

Goodness of Fit

χ^2	1.272	R_{wp}	0.0574	R_p	0.0464

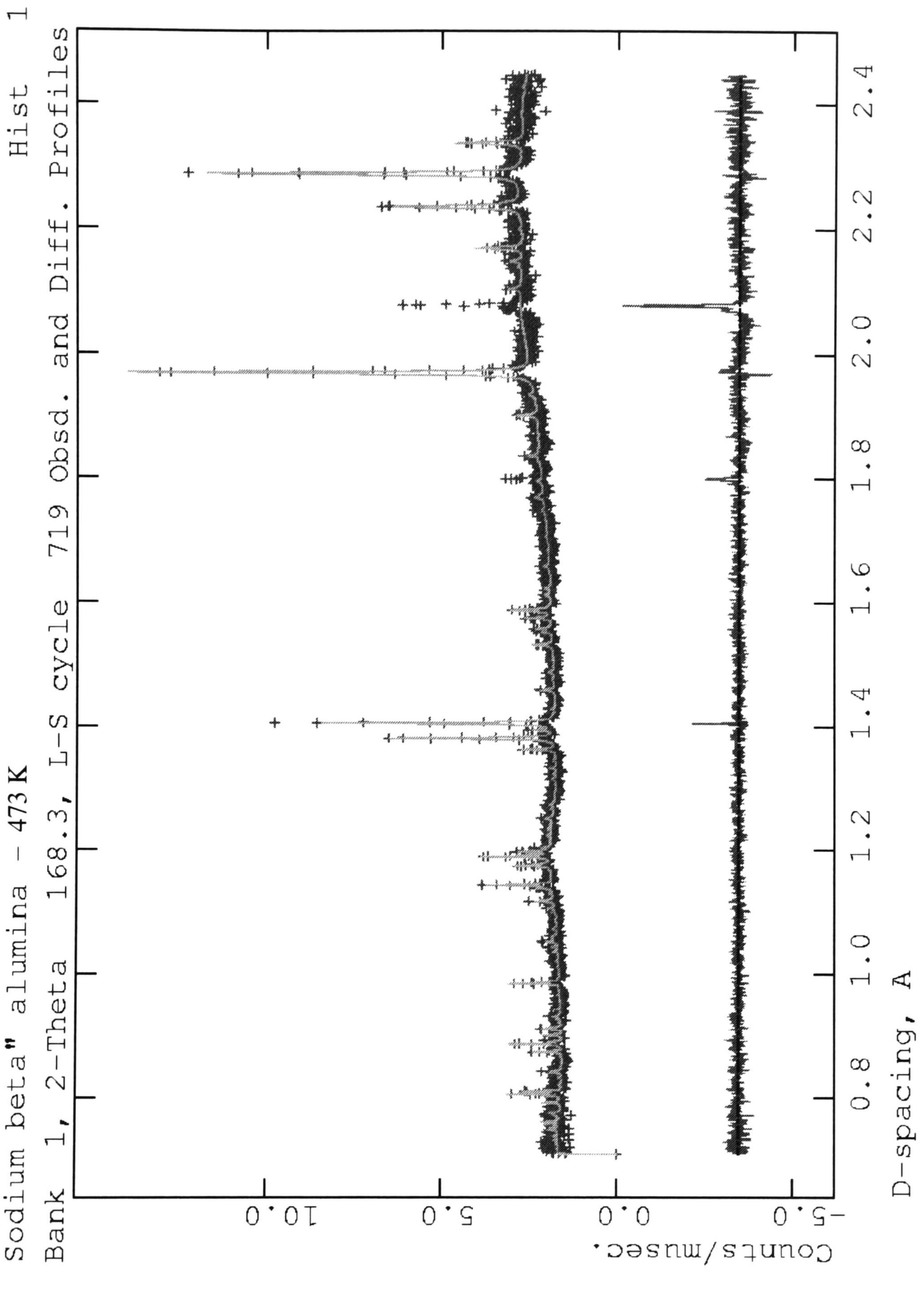
Sodium beta" alumina - 473 K
Bank 1, 2-Theta 168.3, L-S cycle 719 Obsd. and Diff. Profiles
Hist 1
Counts/musec.
10.0
5.0
0.0
-5.0
D-spacing, A
0.8
1.0
1.2
1.4
1.6
1.8
2.0
2.2
2.4

Title

Barium titanate at 295 K, no heating, with sample in vanadium can. Diffraction using neutron radiation at HRPD instrument, ISIS, Rutherford Appleton Laboratory.	
Main text reference	p139

Phase 1

Title	Tetragonal $BaTiO_3$				
Space Group	*P4mm*		Proportion/%	75.7(5)	
a/Å	3.99218(9)	b/Å	3.99218(9)	c/Å	4.03448(12)
α/°	90	β/°	90	γ/°	90

Atom	*x*	*y*	*z*	*F*	U^{eq}/Å^2
Ba (1)	0	0	0	1	0.007(6)
Ti (1)	½	½	0.465(5)	1	0.008(15)
O (1)	½	½	0.021(4)	1	0.005(10)
O (2)	½	0	0.506(5)	1	0.012(4)

Atom	U^{11}/Å^2	U^{22}/Å^2	U^{33}/Å^2	U^{12}/Å^2	U^{13}/Å^2	U^{23}/Å^2
Ba (1)	0.0030(19)	0.0030(19)	0.014(13)	0	0	0
Ti (1)	0.0073(21)	0.0073(21)	0.01(4)	0	0	0
O (1)	0.0017(29)	0.0017(29)	0.010(23)	0	0	0
O (2)	0.0034(34)	0.0130(26)	0.020(6)	0	0	0

Profile type	TOF type 3	α	1.529E-01	β-0	2.125E-02
β-1	1.093E-02	σ-0	0	σ-1	5.72(24)E+02
σ-2	-3.8E+01	γ-0	0	γ-1	5.2E+01
γ-2	0				

Phase 2

Title	Cubic $BaTiO_3$				
Space Group	*Pm*3*m*		Proportion/%	24.3(5)	
a/Å	4.0142(3)	b/Å	4.0142(3)	c/Å	4.0142(3)
α/°	90	β/°	90	γ/°	90

Atom	*x*	*y*	*z*	*F*	U^{eq}/Å^2
Ba (1)	0	0	0	1	-0.0056(30)
Ti (1)	½	½	½	1	-0.0046(28)
O (1)	½	½	0	1	0.0018(15)

Profile type	TOF type 3	α	1.529E-01	β-0	2.125E-02
β-1	1.093E-02	σ-0	0	σ-1	3.0E+04
σ-2	-4.3E+01	γ-0	0	γ-1	5.6E+01
γ-2	0				

Instrument Parameters

Min TOF/μs	34.00		Max TOF/μs	118.00	
DIFA	48233.41	DIFC	0.70	Scale	35.4(5)
Zero	6.8(15)	Background	Type 1	terms	24

Goodness of Fit

χ^2	1.855	R_{wp}	0.0551	R_p	0.0449

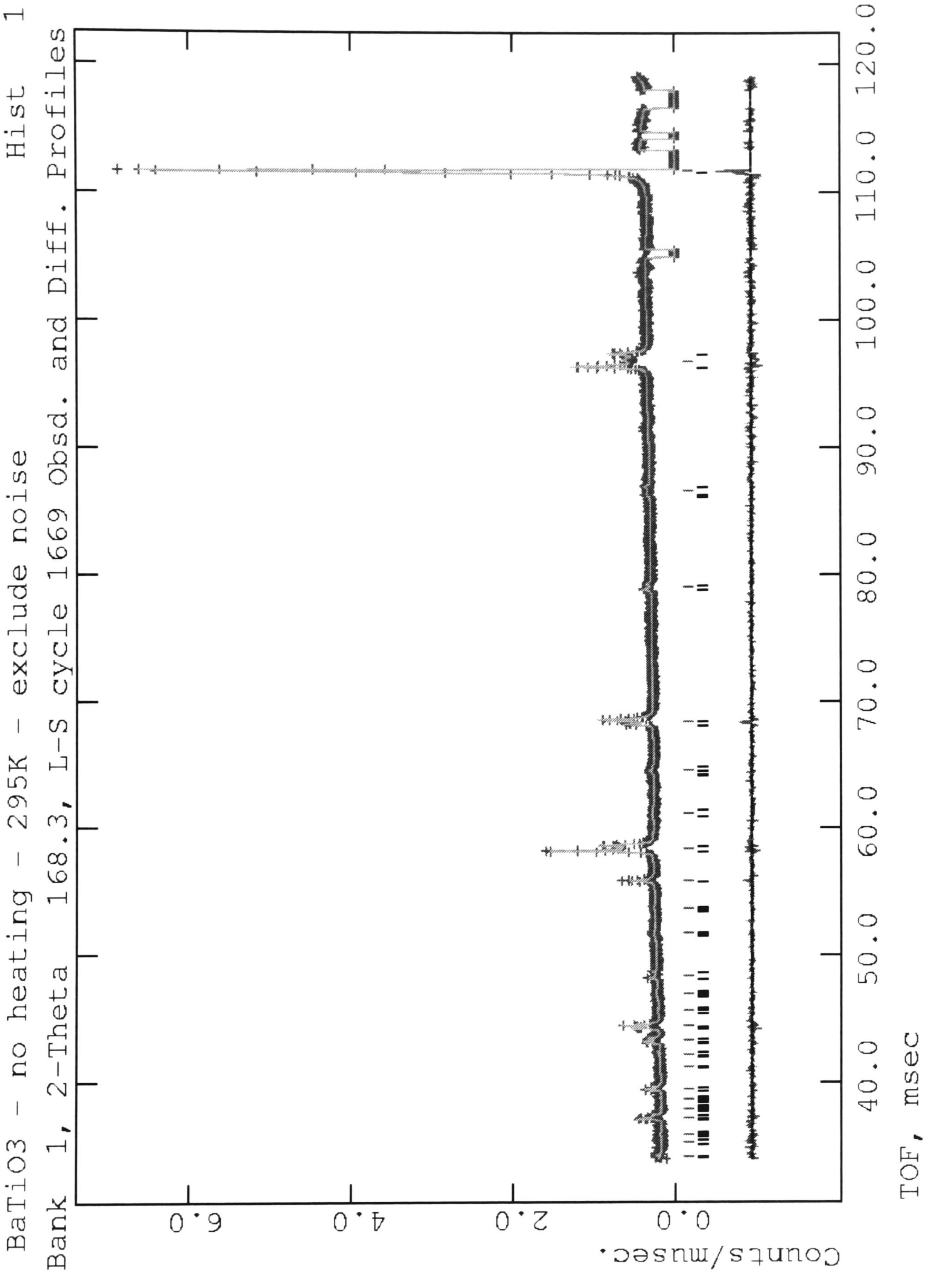
BaTiO3 - no heating - 295K - exclude noise
Hist 1
Bank 1, 2-Theta 168.3, L-S cycle 1669 Obsd. and Diff. Profiles
Counts/musec.
6.0
4.0
2.0
0.0
TOF, msec
40.0
50.0
60.0
70.0
80.0
90.0
100.0
110.0
120.0

Title

Barium titanate at 423 K, electric furnace, with sample in vanadium can. Diffraction using neutron radiation at HRPD instrument, ISIS, Rutherford Appleton Laboratory.	
Main text reference	p139

Phase 1

Title	Cubic $BaTiO_3$				
Space Group	*Pm*3*m*		Proportion/%	78.8(13)	
a/Å	4.01129(5)	b/Å	4.01129(5)	c/Å	4.01129(5)
α/°	90	β/°	90	γ/°	90
Atom	*x*	*y*	*z*	*F*	U^{eq}/Å^2
Ba (1)	0	0	0	1	0.0111(7)
Ti (1)	½	½	½	1	0.0126(9)
O (1)	½	½	0	1	0.0114(7)
Profile type	TOF type 3	α	1.529E-01	β-0	2.125E-02
β-1	1.093E-02	σ-0	0	σ-1	4.48(14)E+02
σ-2	-3.8E+01	γ-0	0	γ-1	5.2E+01
γ-2	0				

Phase 2

Title	Cubic $BaTiO_3$				
Space Group	*Pm*3*m*		Proportion/%	21.6(13)	
a/Å	4.0287(7)	b/Å	4.0287(7)	c/Å	4.0287(7)
α/°	90	β/°	90	γ/°	90
Atom	*x*	*y*	*z*	*F*	U^{eq}/Å^2
Ba (1)	0	0	0	1	-0.017(4)
Ti (1)	½	½	½	1	0.011(5)
O (1)	½	½	0	1	0.0122(24)
Profile type	TOF type 3	α	1.529E-01	β-0	2.125E-02
β-1	1.093E-02	σ-0	0	σ-1	3.7E+04
σ-2	-9.2E+03	γ-0	0	γ-1	4.0E+02
γ-2	0				

Instrument Parameters

Min TOF/μs	34.00		Max TOF/μs	118.00	
DIFA	48233.41	DIFC	0.70	Scale	252(2)
Zero	11.0(8)	Background	Type 1	terms	24

Goodness of Fit

χ^2	1.422	R_{wp}	0.0703	R_p	0.0600

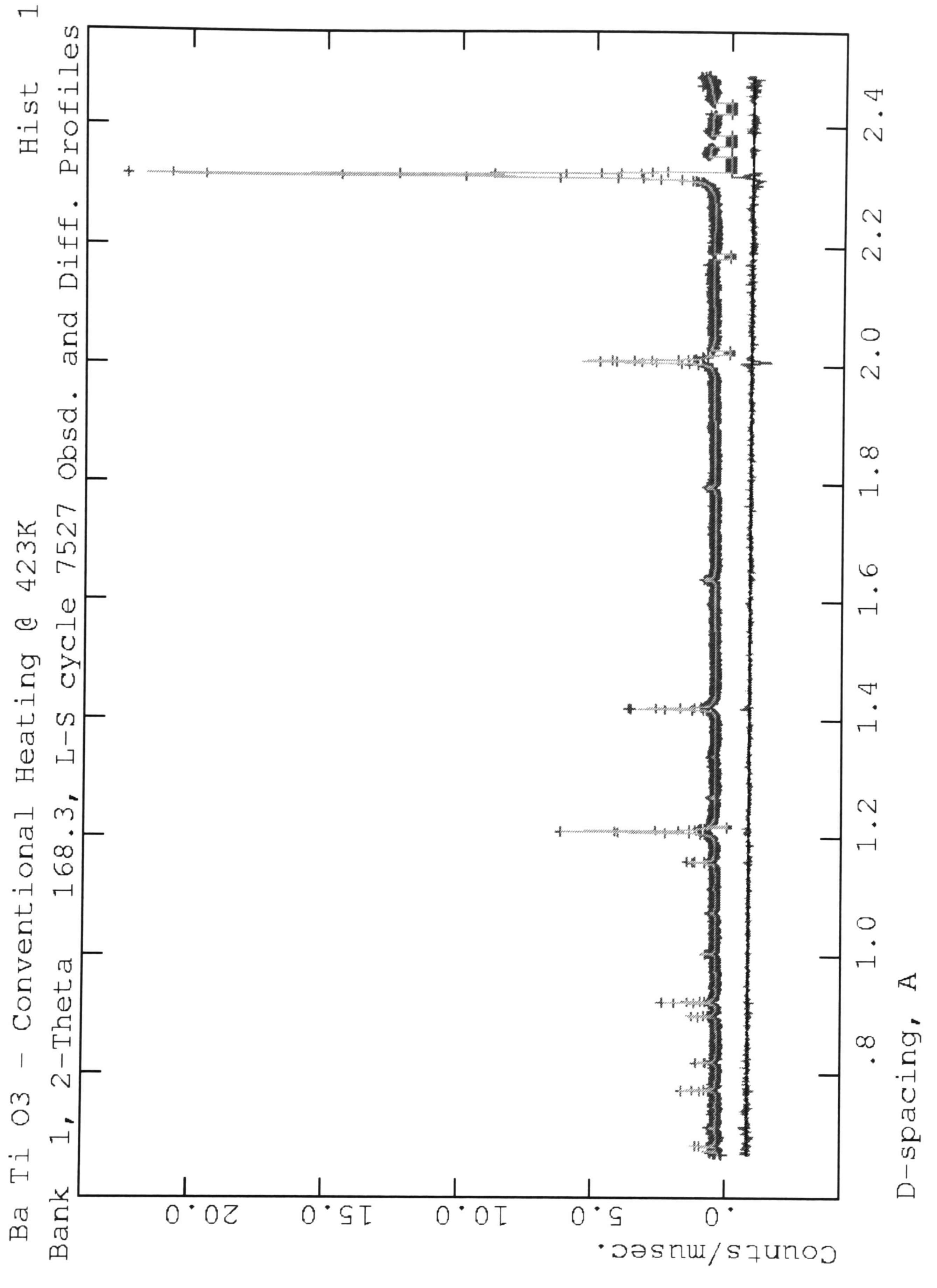
Ba Ti O3 - Conventional Heating @ 423K
Hist 1
Bank 1, 2-Theta 168.3, L-S cycle 7527 Obsd. and Diff. Profiles
Counts/musec.
.0
5.0
10.0
15.0
20.0
D-spacing, A
.8
1.0
1.2
1.4
1.6
1.8
2.0
2.2
2.4

Title

Barium titanate at 473 K, electric furnace, with sample in vanadium can. Diffraction using neutron radiation at HRPD instrument, ISIS, Rutherford Appleton Laboratory.	
Main text reference	p139

Phase 1

Title	Cubic BaTiO$_3$				
Space Group	*Pm*3*m*		Proportion/%	79.3(10)	
a/Å	4.01363(5)	b/Å	4.01363(5)	c/Å	4.01363(5)
α/°	90	β/°	90	γ/°	90
Atom	*x*	*y*	*z*	*F*	U^{eq}/Å^2
Ba (1)	0	0	0	1	0.0120(7)
Ti (1)	½	½	½	1	0.0131(9)
O (1)	½	½	0	1	0.0105(7)
Profile type	TOF type 3	α	1.529E-01	β-0	2.125E-02
β-1	1.093E-02	σ-0	0	σ-1	4.83(15)E+02
σ-2	-3.8E+01	γ-0	0	γ-1	5.2E+01
γ-2	0				

Phase 2

Title	Cubic BaTiO$_3$				
Space Group	*Pm*3*m*		Proportion/%	20.7(10)	
a/Å	4.0338(5)	b/Å	4.0338(5)	c/Å	4.0338(5)
α/°	90	β/°	90	γ/°	90
Atom	*x*	*y*	*z*	*F*	U^{eq}/Å^2
Ba (1)	0	0	0	1	-0.0083(3)
Ti (1)	½	½	½	1	-0.003(4)
O (1)	½	½	0	1	0.0136(21)
Profile type	TOF type 3	α	1.529E-01	β-0	2.125E-02
β-1	1.093E-02	σ-0	0	σ-1	4.8E+03
σ-2	-8.8E+02	γ-0	0	γ-1	4.3E+02
γ-2	0				

Instrument Parameters

Min TOF/μs	34.00		Max TOF/μs	118.00	
DIFA	48233.41	DIFC	0.70	Scale	91.5(7)
Zero	10.2(8)	Background	Type 1	terms	24

Goodness of Fit

χ^2	1.422	R_{wp}	0.0703	R_p	0.0600

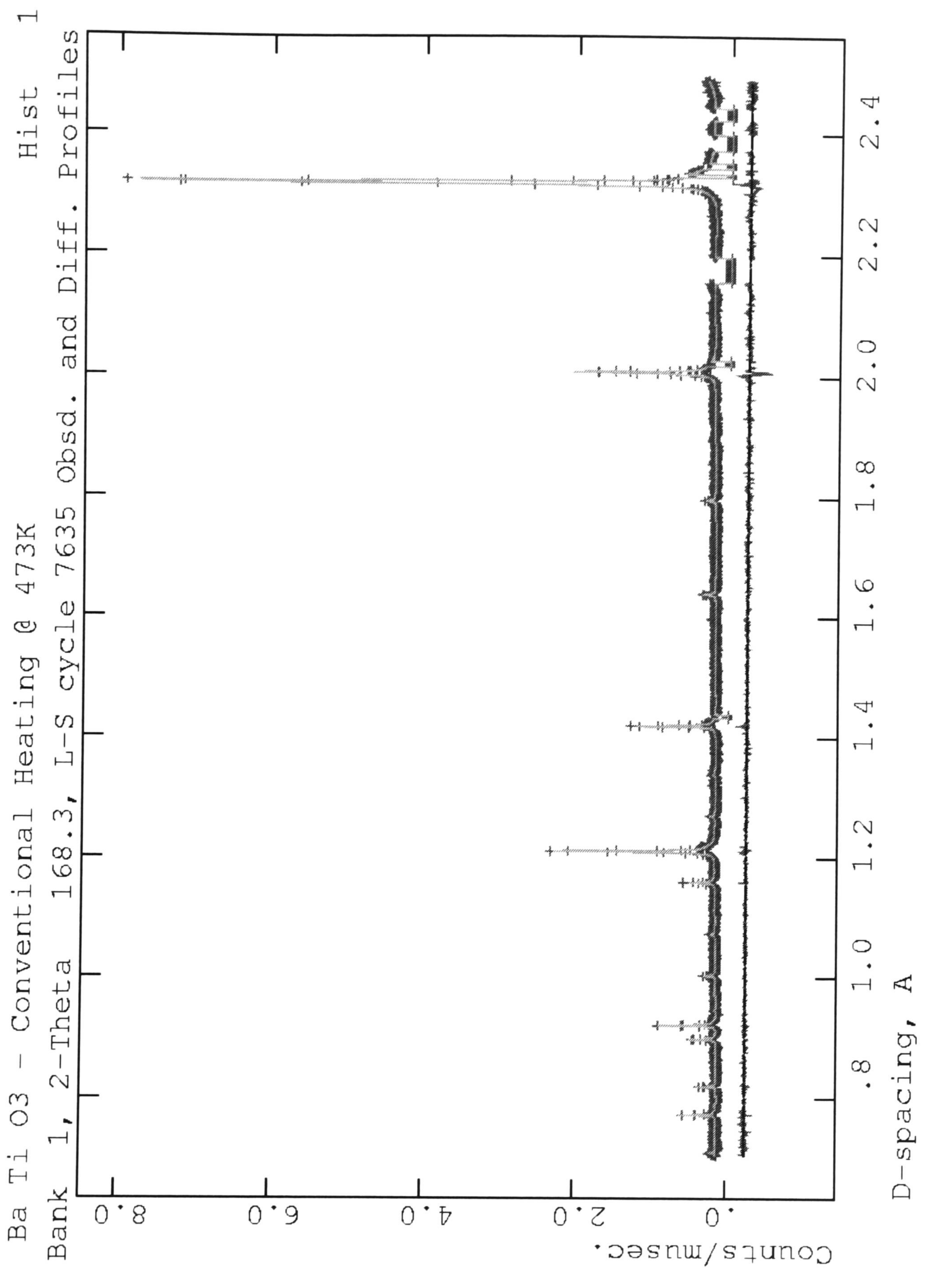
Ba Ti O3 - Conventional Heating @ 473K
Hist 1
Bank 1, 2-Theta 168.3, L-S cycle 7635 Obsd. and Diff. Profiles
Counts/musec.
8.0
6.0
4.0
2.0
.0
.8
1.0
1.2
1.4
1.6
1.8
2.0
2.2
2.4
D-spacing, A

Title

Barium titanate at 573 K, electric furnace, with sample in vanadium can. Diffraction using neutron radiation at HRPD instrument, ISIS, Rutherford Appleton Laboratory.	
Main text reference	p139

Phase 1

Title	Cubic $BaTiO_3$				
Space Group	*Pm*3*m*		Proportion/%	79.3(6)	
a/Å	4.01786(5)	b/Å	4.01786(5)	c/Å	4.01786(5)
α/°	90	β/°	90	γ/°	90
Atom	*x*	*y*	*z*	*F*	U^{eq}/Å^2
Ba (1)	0	0	0	1	0.0140(7)
Ti (1)	½	½	½	1	0.0151(9)
O (1)	½	½	0	1	0.0132(9)
Profile type	TOF type 3	α	1.529E-01	β-0	2.125E-02
β-1	1.093E-02	σ-0	0	σ-1	4.62(14)E+02
σ-2	-3.8E+01	γ-0	0	γ-1	5.2E+01
γ-2	0				

Phase 2

Title	Cubic $BaTiO_3$				
Space Group	*Pm*3*m*		Proportion/%	20.7(6)	
a/Å	4.0384(5)	b/Å	4.0384(5)	c/Å	4.0384(5)
α/°	90	β/°	90	γ/°	90
Atom	*x*	*y*	*z*	*F*	U^{eq}/Å^2
Ba (1)	0	0	0	1	-0.006(4)
Ti (1)	½	½	½	1	-0.002(4)
O (1)	½	½	0	1	0.020(2)
Profile type	TOF type 3	α	1.529E-01	β-0	2.125E-02
β-1	1.093E-02	σ-0	0	σ-1	4.9E+03
σ-2	-1.2E+3	γ-0	0	γ-1	4.1E+02
γ-2	0				

Instrument Parameters

Min TOF/μs	34.00		Max TOF/μs	118.00	
DIFA	48233.41	DIFC	0.70	Scale	243.7
Zero	12.54	Background	Type 1	terms	24

Goodness of Fit

χ^2	1.321	R_{wp}	0.0666	R_p	0.0542

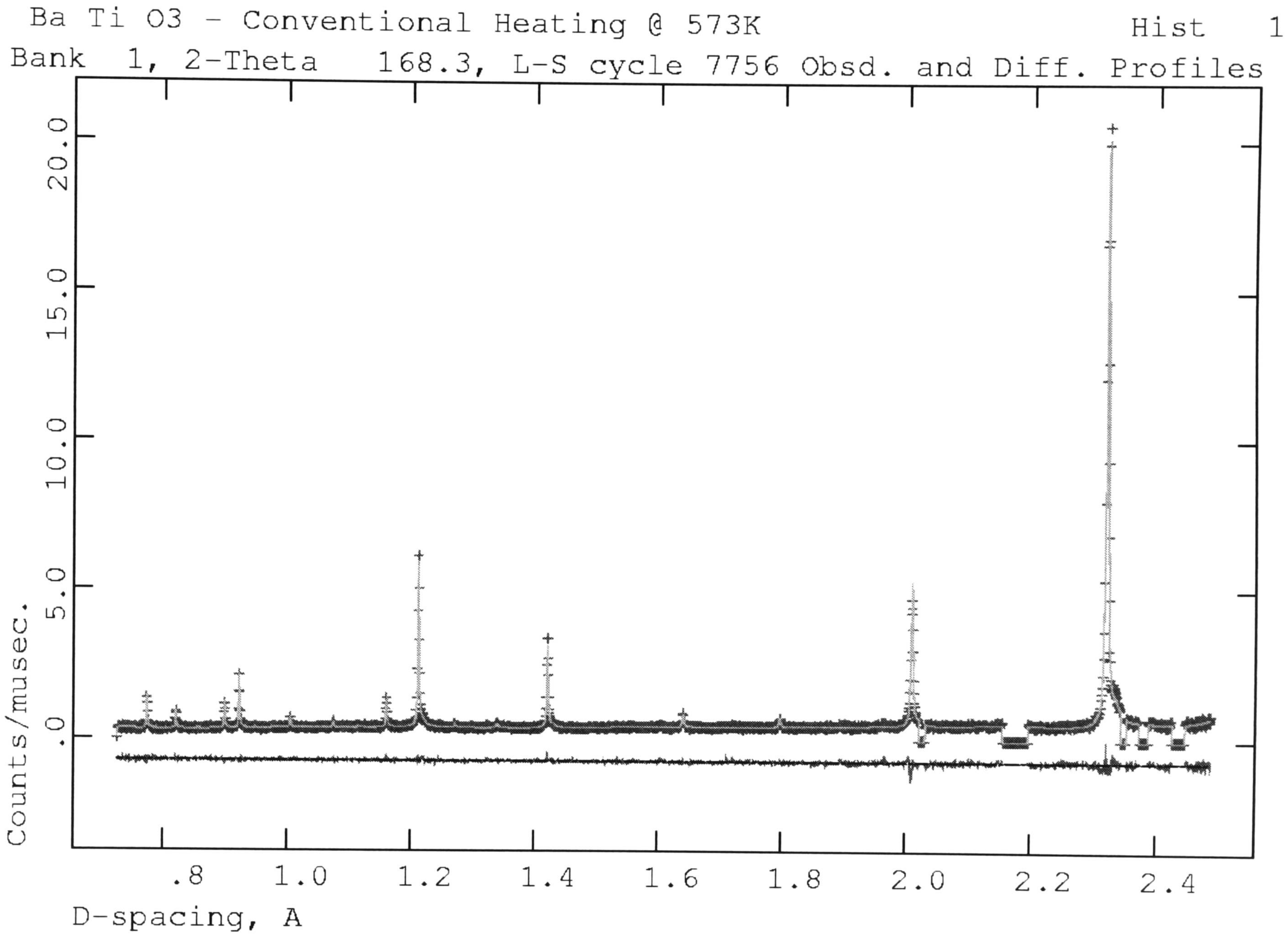
Ba Ti O3 - Conventional Heating @ 573K
Hist 1
Bank 1, 2-Theta 168.3, L-S cycle 7756 Obsd. and Diff. Profiles
20.0
15.0
10.0
5.0
.0
Counts/musec.
.8
1.0
1.2
1.4
1.6
1.8
2.0
2.2
2.4
D-spacing, A

Title

Barium titanate at 673 K, electric furnace, with sample in vanadium can. Diffraction using neutron radiation at HRPD instrument, ISIS, Rutherford Appleton Laboratory.	
Main text reference	p139

Phase 1

Title	Cubic $BaTiO_3$				
Space Group	*Pm*3*m*		Proportion/%	80.0(7)	
a/Å	4.02294(5)	b/Å	4.02294(5)	c/Å	4.02294(5)
α/°	90	β/°	90	γ/°	90
Atom	*x*	*y*	*z*	*F*	U^{eq}/Å^2
Ba (1)	0	0	0	1	0.0144(7)
Ti (1)	½	½	½	1	0.0161(9)
O (1)	½	½	0	1	0.0153(9)
Profile type	TOF type 3	α	1.529E-01	β-0	2.125E-02
β-1	1.093E-02	σ-0	0	σ-1	4.03(13)E+02
σ-2	-3.8E+01	γ-0	0	γ-1	5.2E+01
γ-2	0				

Phase 2

Title	Cubic $BaTiO_3$				
Space Group	*Pm*3*m*		Proportion/%	20.0(7)	
a/Å	4.0425(5)	b/Å	4.0425(5)	c/Å	4.0425(5)
α/°	90	β/°	90	γ/°	90
Atom	*x*	*y*	*z*	*F*	U^{eq}/Å^2
Ba (1)	0	0	0	1	0.000(5)
Ti (1)	½	½	½	1	0.010(5)
O (1)	½	½	0	1	0.024(3)
Profile type	TOF type 3	α	1.529E-01	β-0	2.125E-02
β-1	1.093E-02	σ-0	0	σ-1	1.8E+03
σ-2	-8.7E+02	γ-0	0	γ-1	4.0E+02
γ-2	0				

Instrument Parameters

Min TOF/μs	34.00		Max TOF/μs	118.00	
DIFA	48233.41	DIFC	0.70	Scale	113.56
Zero	14.66	Background	Type 1	terms	24

Goodness of Fit

χ^2	1.402	R_{wp}	0.0708	R_p	0.0590

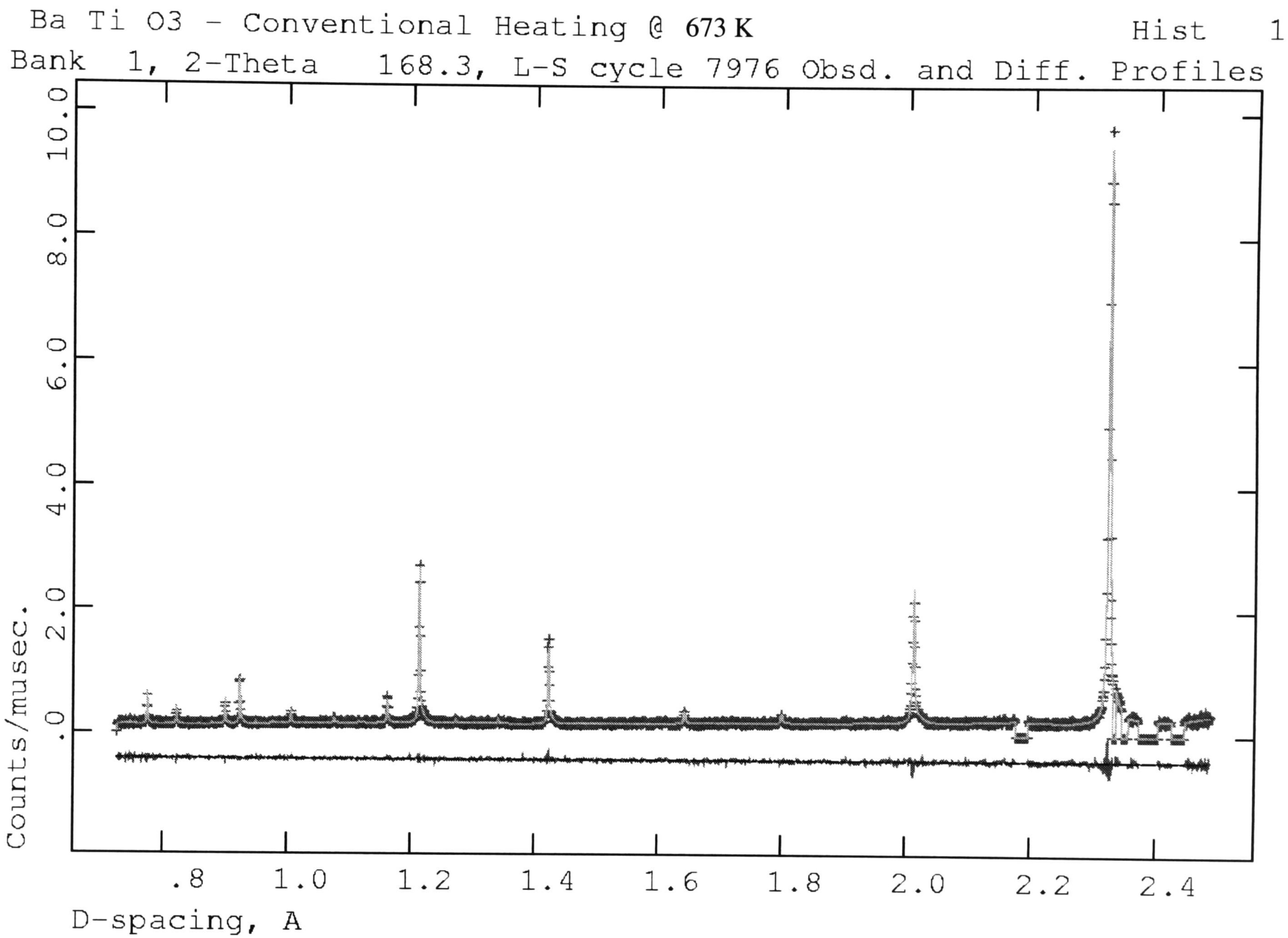
Ba Ti O3 - Conventional Heating @ 673 K
Hist 1
Bank 1, 2-Theta 168.3, L-S cycle 7976 Obsd. and Diff. Profiles
Counts/musec.
10.0
8.0
6.0
4.0
2.0
.0
.8
1.0
1.2
1.4
1.6
1.8
2.0
2.2
2.4
D-spacing, A

Title

Barium titanate at 773 K, electric furnace, with sample in vanadium can. Diffraction using neutron radiation at HRPD instrument, ISIS, Rutherford Appleton Laboratory.	
Main text reference	p139

Phase 1

Title	Cubic $BaTiO_3$				
Space Group	*Pm*3*m*		Proportion/%	80.8(10)	
a/Å	4.02837(5)	b/Å	4.02837(5)	c/Å	4.02837(5)
α/°	90	β/°	90	γ/°	90
Atom	*x*	*y*	*z*	*F*	$U^{eq}/Å^2$
Ba (1)	0	0	0	1	0.0177(7)
Ti (1)	½	½	½	1	0.0179(9)
O (1)	½	½	0	1	0.0176(9)
Profile type	TOF type 3	α	1.529E-01	β-0	2.125E-02
β-1	1.093E-02	σ-0	0	σ-1	3.97(13)E+02
σ-2	-3.8E+01	γ-0	0	γ-1	5.2E+01
γ-2	0				

Phase 2

Title	Cubic $BaTiO_3$				
Space Group	*Pm*3*m*		Proportion/%	19.2(10)	
a/Å	4.0480(5)	b/Å	4.0480(5)	c/Å	4.0480(5)
α/°	90	β/°	90	γ/°	90
Atom	*x*	*y*	*z*	*F*	$U^{eq}/Å^2$
Ba (1)	0	0	0	1	-0.002(4)
Ti (1)	½	½	½	1	0.002(5)
O (1)	½	½	0	1	0.028(3)
Profile type	TOF type 3	α	1.529E-01	β-0	2.125E-02
β-1	1.093E-02	σ-0	0	σ-1	2.0E+01
σ-2	-1.0E+03	γ-0	0	γ-1	3.9E+02
γ-2	0				

Instrument Parameters

Min TOF/μs	34.00		Max TOF/μs	118.00	
DIFA	48233.41	DIFC	0.70	Scale	96.7
Zero	14.00	Background	Type 1	terms	24

Goodness of Fit

χ^2	1.275	R_{wp}	0.0682	R_p	0.0558

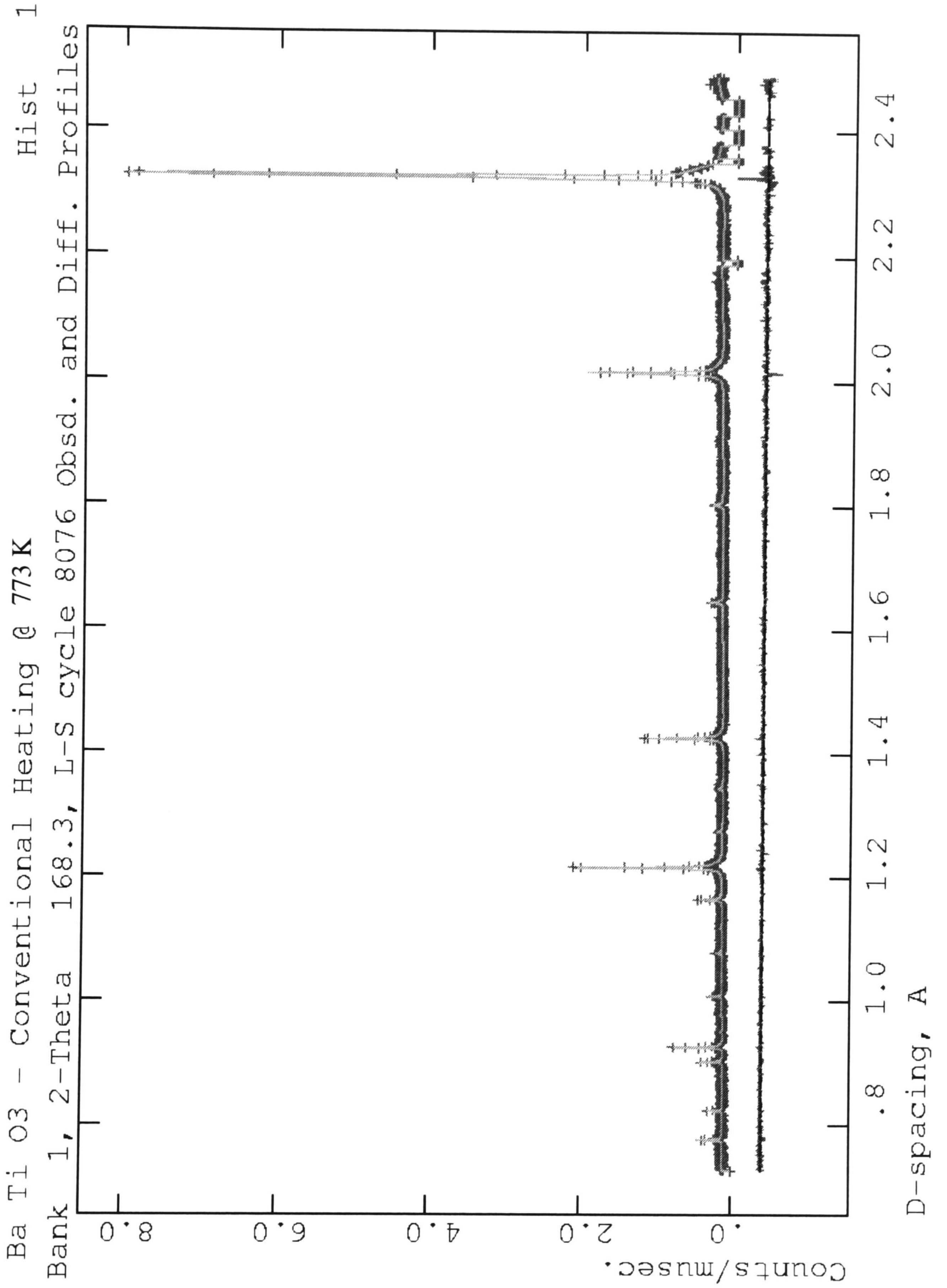
Ba Ti O3 - Conventional Heating @ 773 K
Hist 1
Bank 1, 2-Theta 168.3, L-S cycle 8076 Obsd. and Diff. Profiles
8.0
6.0
4.0
2.0
.0
Counts/musec.
.8
1.0
1.2
1.4
1.6
1.8
2.0
2.2
2.4
D-spacing, A

Title

Barium titanate at 873 K, electric furnace, with sample in vanadium can. Diffraction using neutron radiation at HRPD instrument, ISIS, Rutherford Appleton Laboratory.	
Main text reference	p139

Phase 1

Title	Cubic BaTiO$_3$				
Space Group	*Pm*3*m*		Proportion/%	82.1(11)	
a/Å	4.03200(5)	b/Å	4.03200(5)	c/Å	4.03200(5)
α/°	90	β/°	90	γ/°	90
Atom	x	y	z	F	U^{eq}/Å^2
Ba (1)	0	0	0	1	0.0176(7)
Ti (1)	½	½	½	1	0.0175(9)
O (1)	½	½	0	1	0.0190(9)
Profile type	TOF type 3	α	1.529E-01	β-0	2.125E-02
β-1	1.093E-02	σ-0	0	σ-1	3.93(13)E+02
σ-2	-3.8E+01	γ-0	0	γ-1	5.2E+01
γ-2	0				

Phase 2

Title	Cubic BaTiO$_3$				
Space Group	*Pm*3*m*		Proportion/%	17.9(11)	
a/Å	4.0530(5)	b/Å	4.0530(5)	c/Å	4.0530(5)
α/°	90	β/°	90	γ/°	90
Atom	x	y	z	F	U^{eq}/Å^2
Ba (1)	0	0	0	1	0.011(5)
Ti (1)	½	½	½	1	-0.006(4)
O (1)	½	½	0	1	0.026(3)
Profile type	TOF type 3	α	1.529E-01	β-0	2.125E-02
β-1	1.093E-02	σ-0	0	σ-1	7.3E+02
σ-2	-1.5E+03	γ-0	0	γ-1	3.9E+02
γ-2	0				

Instrument Parameters

Min TOF/μs	34.00		Max TOF/μs	118.00	
DIFA	48233.41	DIFC	0.70	Scale	261.07
Zero	14.09	Background	Type 1	terms	24

Goodness of Fit

χ^2	1.249	R_{wp}	0.0679	R_p	0.0566

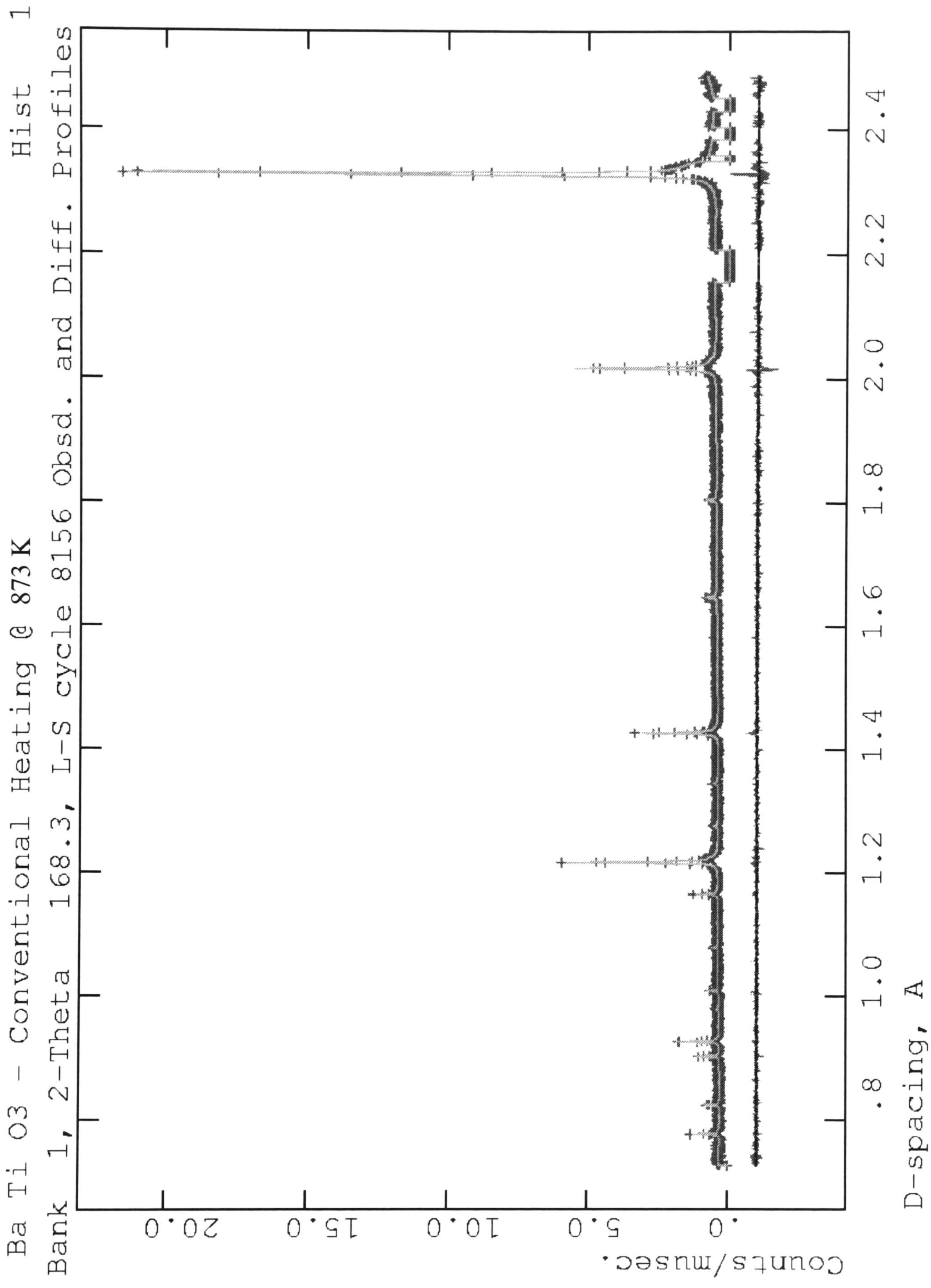
Ba Ti O3 - Conventional Heating @ 873 K
Hist 1
Bank 1, 2-Theta 168.3, L-S cycle 8156 Obsd. and Diff. Profiles
Counts/musec.
20.0
15.0
10.0
5.0
.0
D-spacing, A
.8
1.0
1.2
1.4
1.6
1.8
2.0
2.2
2.4

Title

Barium titanate at 295 K, microwave heating, with sample on ceramic support. Diffraction using neutron radiation at HRPD instrument, ISIS, Rutherford Appleton Laboratory.	
Main text reference	p139

Phase 1

Title	Tetragonal BaTiO$_3$				
Space Group	*P*4*mm*		Proportion/%	81.2(6)	
a/Å	3.99478(7)	b/Å	3.99478(7)	c/Å	4.03420(9)
α/°	90	β/°	90	γ/°	90
Atom	*x*	*y*	*z*	*F*	U^{eq}/Å^2
Ba (1)	0	0	0	1	0.007(8)
Ti (1)	½	½	0.491(33)	1	0.012(11)
O (1)	½	½	0.036(10)	1	0.007(6)
O2	½	0	0.526(12)	1	0.008(3)

Atom	U^{11}/Å^2	U^{22}/Å^2	U^{33}/Å^2	U^{12}/Å^2	U^{13}/Å^2	U^{23}/Å^2
Ba (1)	0.0055(18)	0.0055(18)	0.011(21)	0	0	0
Ti (1)	0.0066(19)	0.0066(19)	0.022(27)	0	0	0
O (1)	0.0030(27)	0.0030(27)	0.015(13)	0	0	0
O (2)	0.0028(28)	0.0064(22)	0.016(4)	0	0	0

Profile type	TOF type 3	α	1.529E-01	β-0	2.125E-02
β-1	1.093E-02	σ-0	0	σ-1	5.98(19)E+02
σ-2	-3.8E+01	γ-0	0	γ-1	5.2E+01
γ-2	0				

Phase 2

Title	Cubic BaTiO$_3$				
Space Group	*Pm*3*m*		Proportion/%	18.8(6)	
a/Å	4.01908(25)	b/Å	4.01908(25)	c/Å	4.01908(25)
α/°	90	β/°	90	γ/°	90
Atom	*x*	*y*	*z*	*F*	U^{eq}/Å^2
Ba (1)	0	0	0	1	-0.001(5)
Ti (1)	½	½	½	1	-0.008(4)
O (1)	½	½	0	1	-0.004(2)
Profile type	TOF type 3	α	1.529E-01	β-0	2.125E-02
β-1	1.093E-02	σ-0	0	σ-1	1.9E+04
σ-2	3.2E+03	γ-0	0	γ-1	0
γ-2	0				

Instrument Parameters

Min TOF/μs	34.00		Max TOF/μs	118.00	
DIFA	48233.41	DIFC	0.70	Scale	319.79
Zero	6.14	Background	Type 1	terms	24

Goodness of Fit

χ^2	2.958	R_{wp}	0.0538	R_p	0.0439

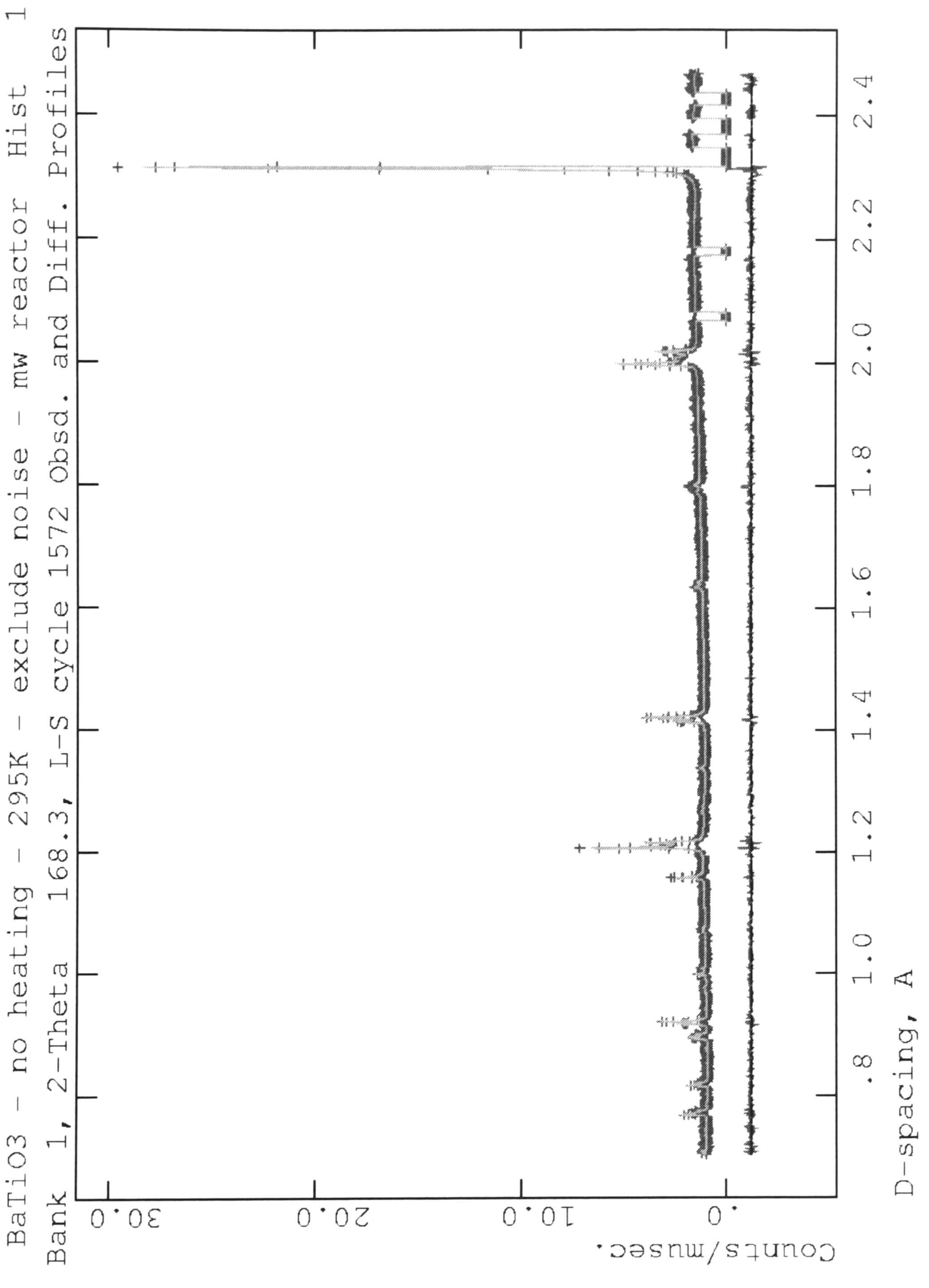
BaTiO3 - no heating - 295K - exclude noise - mw reactor Hist 1
Bank 1, 2-Theta 168.3, L-S cycle 1572 Obsd. and Diff. Profiles
Counts/musec.
30.0
20.0
10.0
.0
.8
1.0
1.2
1.4
1.6
1.8
2.0
2.2
2.4
D-spacing, A

Title

Barium titanate at 383 K, microwave heating, with sample on ceramic support. Diffraction using neutron radiation at HRPD instrument, ISIS, Rutherford Appleton Laboratory.	
Main text reference	p139

Phase 1

Title	Cubic $BaTiO_3$				
Space Group	*Pm*3*m*		Proportion/%	80.1(18)	
a/Å	4.01081(7)	b/Å	4.01081(7)	c/Å	4.01081(7)
α/°	90	β/°	90	γ/°	90
Atom	*x*	*y*	*z*	*F*	U^{eq}/Å^2
Ba (1)	0	0	0	1	0.0089(11)
Ti (1)	½	½	½	1	0.0083(12)
O (1)	½	½	0	1	0.0087(10)
Profile type	TOF type 3	α	1.529E-01	β-0	2.125E-02
β-1	1.093E-02	σ-0	0	σ-1	6.62(24)E+02
σ-2	-3.8E+01	γ-0	0	γ-1	5.2E+01
γ-2	0				

Phase 2

Title	Cubic $BaTiO_3$				
Space Group	*Pm*3*m*		Proportion/%	19.9(18)	
a/Å	4.0238(6)	b/Å	4.0238(6)	c/Å	4.0238(6)
α/°	90	β/°	90	γ/°	90
Atom	*x*	*y*	*z*	*F*	U^{eq}/Å^2
Ba (1)	0	0	0	1	-0.010(5)
Ti (1)	½	½	½	1	-0.004(5)
O (1)	½	½	0	1	0.001(3)
Profile type	TOF type 3	α	1.529E-01	β-0	2.125E-02
β-1	1.093E-02	σ-0	0	σ-1	1.4E+04
σ-2	1.8E+03	γ-0	0	γ-1	1.9E+02
γ-2	0				

Instrument Parameters

Min TOF/μs	34.00		Max TOF/μs	118.00	
DIFA	48233.41	DIFC	0.70	Scale	247.9
Zero	6.59	Background	Type 1	terms	24

Goodness of Fit

χ^2	2.478	R_{wp}	0.0657	R_p	0.0554

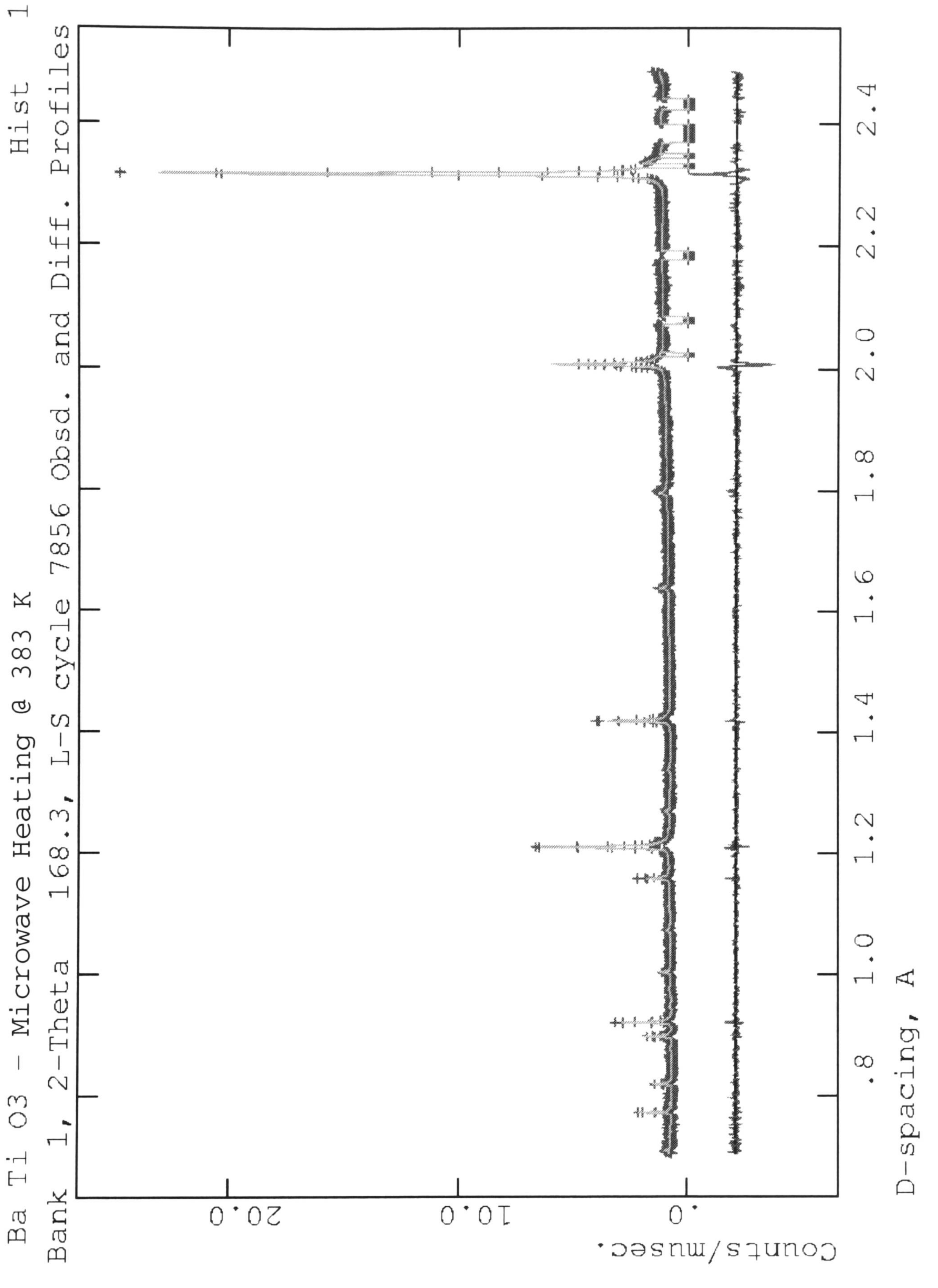
Ba Ti O3 - Microwave Heating @ 383 K
Hist 1
Bank 1, 2-Theta 168.3, L-S cycle 7856 Obsd. and Diff. Profiles
Counts/musec.
20.0
10.0
.0
D-spacing, A
.8
1.0
1.2
1.4
1.6
1.8
2.0
2.2
2.4

Title

Barium titanate at 473 K, microwave heating, with sample on ceramic support. Diffraction using neutron radiation at HRPD instrument, ISIS, Rutherford Appleton Laboratory.	
Main text reference	p139

Phase 1

Title	Cubic BaTiO$_3$				
Space Group	*Pm*3*m*		Proportion/%	81.2(17)	
a/Å	4.01389(5)	b/Å	4.01389(5)	c/Å	4.01389(5)
α/°	90	β/°	90	γ/°	90
Atom	*x*	*y*	*z*	*F*	U^{eq}/Å^2
Ba (1)	0	0	0	1	0.0062(7)
Ti (1)	½	½	½	1	0.0080(8)
O (1)	½	½	0	1	0.0074(7)
Profile type	TOF type 3	α	1.529E-01	β-0	2.125E-02
β-1	1.093E-02	σ-0	0	σ-1	6.92(17)E+02
σ-2	-3.8E+01	γ-0	0	γ-1	5.2E+01
γ-2	0				

Phase 2

Title	Cubic BaTiO$_3$				
Space Group	*Pm*3*m*		Proportion/%	18.8(17)	
a/Å	4.0325(6)	b/Å	4.0325(6)	c/Å	4.0325(6)
α/°	90	β/°	90	γ/°	90
Atom	*x*	*y*	*z*	*F*	U^{eq}/Å^2
Ba (1)	0	0	0	1	-0.001(5)
Ti (1)	½	½	½	1	-0.002(5)
O (1)	½	½	0	1	0.007(3)
Profile type	TOF type 3	α	1.529E-01	β-0	2.125E-02
β-1	1.093E-02	σ-0	0	σ-1	1.4E+04
σ-2	-4.3E+02	γ-0	0	γ-1	3.0E+02
γ-2	0				

Instrument Parameters

Min TOF/µs	34.00		Max TOF/µs	118.00	
DIFA	48233.41	DIFC	0.70	Scale	297.2
Zero	17.41	Background	Type 1	terms	24

Goodness of Fit

χ^2	1.650	R_{wp}	0.0492	R_p	0.0417

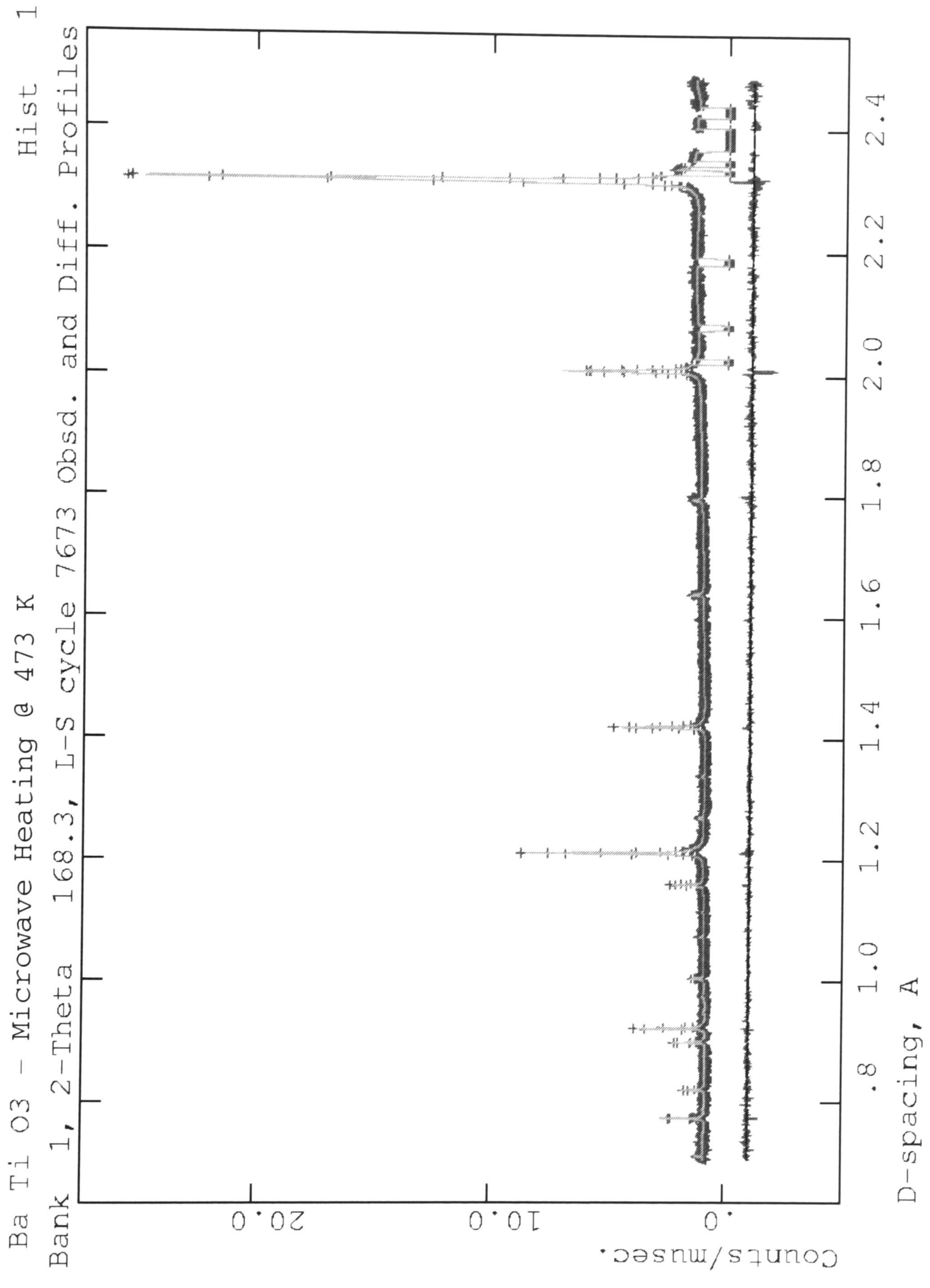
Ba Ti O3 - Microwave Heating @ 473 K
Hist 1
Bank 1, 2-Theta 168.3, L-S cycle 7673 Obsd. and Diff. Profiles
Counts/musec.
20.0
10.0
.0
.8
1.0
1.2
1.4
1.6
1.8
2.0
2.2
2.4
D-spacing, A

Title

Potassium niobate at 323 K, electric furnace, with sample in vanadium can. Diffraction using neutron radiation at HRPD instrument, ISIS, Rutherford Appleton Laboratory.	
Main text reference	p146

Phase 1

Title	Orthorhombic KNbO$_3$				
Space Group	*Amm*2		Proportion/%	80.5(10)	
a/Å	3.97475(7)	b/Å	5.69420(11)	c/Å	5.71840(11)
α/°	90	β/°	90	γ/°	90
Atom	*x*	*y*	*z*	*F*	U^{eq}/Å^2
K (1)	0	0	0	1	0.011(3)
Nb (1)	½	0	0.511(3)	1	0.020(4)
O (1)	0	0	0.543(2)	1	0.0112(15)
O (2)	½	0.248(1)	0.291(2)	1	0.0130(10)
Profile type	TOF type 3	α	1.529E-01	β-0	2.125E-02
β-1	1.093E-02	σ-0	0	σ-1	2.56(17)E+02
σ-2	1E+02	γ-0	0	γ-1	6E+01
γ-2	0				

Phase 2

Title	Tetragonal KNbO$_3$				
Space Group	*P*4*mm*		Proportion/%	19.5(10)	
a/Å	4.0085(5)	b/Å	4.0085(5)	c/Å	4.0442(10)
α/°	90	β/°	90	γ/°	90
Atom	*x*	*y*	*z*	*F*	U^{eq}/Å^2
K (1)	0	0	0	1	-0.003(5)
Nb (1)	½	½	0.49(3)	1	0.008(4)
O (1)	½	½	0.02(3)	1	-0.016(3)
O (2)	½	0	0.50(4)	1	0.026(4)
Profile type	TOF type 3	α	1.529E-01	β-0	2.125E-02
β-1	1.093E-02	σ-0	0	σ-1	2.6E+04
σ-2	0	γ-0	0	γ-1	0
γ-2	0				

Instrument Parameters

Min TOF/μs	34.00		Max TOF/μs	118.00	
DIFA	48233.41	DIFC	0.70	Scale	463.8
Zero	15.70	Background	Type 1	terms	24

Goodness of Fit

χ^2	1.812	R_{wp}	0.0733	R_p	0.0648

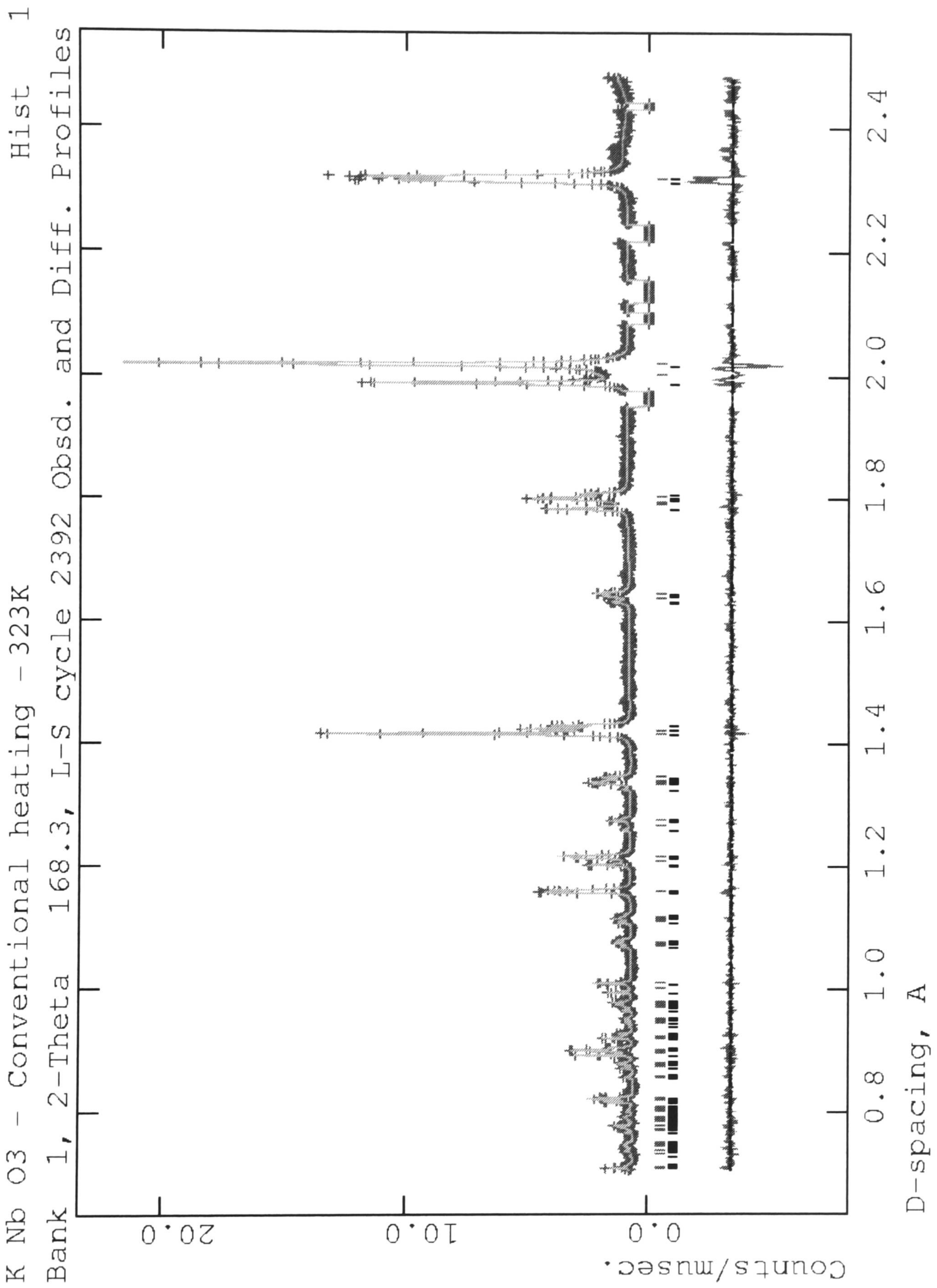
K Nb O3 - Conventional heating - 323K
Hist 1
Bank 1, 2-Theta 168.3, L-S cycle 2392 Obsd. and Diff. Profiles
Counts/musec.
0.0
10.0
20.0
D-spacing, A
0.8
1.0
1.2
1.4
1.6
1.8
2.0
2.2
2.4

Title

Potassium niobate at 373 K, electric furnace, with sample in vanadium can. Diffraction using neutron radiation at HRPD instrument, ISIS, Rutherford Appleton Laboratory.	
Main text reference	p146

Phase 1

Title	Orthorhombic KNbO$_3$				
Space Group	*Amm*2		Proportion/%	80.2(11)	
a/Å	3.97676(7)	b/Å	5.69483(11)	c/Å	5.71836(11)
α/°	90	β/°	90	γ/°	90
Atom	*x*	*y*	*z*	*F*	U^{eq}/Å^2
K (1)	0	0	0	1	0.015(3)
Nb (1)	½	0	0.476(3)	1	0.0114(15)
O (1)	0	0	0.513(4)	1	0.012(2)
O (2)	½	0.249(1)	0.260(4)	1	0.018(2)
Profile type	TOF type 3	α	1.529E-01	β-0	2.125E-02
β-1	1.093E-02	σ-0	0	σ-1	2.69(17)E+02
σ-2	1E+02	γ-0	0	γ-1	6E+01
γ-2	0				

Phase 2

Title	Tetrahedral KNbO$_3$				
Space Group	*P*4*mm*		Proportion/%	19.8(11)	
a/Å	4.0077(5)	b/Å	4.0077(5)	c/Å	4.0464(10)
α/°	90	β/°	90	γ/°	90
Atom	*x*	*y*	*z*	*F*	U^{eq}/Å^2
K (1)	0	0	0	1	0.000(6)
Nb (1)	½	½	0.48(3)	1	0.014(5)
O (1)	½	½	0.01(3)	1	-0.016(3)
O (2)	½	0	0.50(3)	1	0.032(5)
Profile type	TOF type 3	α	1.529E-01	β-0	2.125E-02
β-1	1.093E-02	σ-0	0	σ-1	2.5E+04
σ-2	0	γ-0	0	γ-1	0
γ-2	0				

Instrument Parameters

Min TOF/μs	34.00		Max TOF/μs	118.00	
DIFA	48233.41	DIFC	0.70	Scale	463.1
Zero	15.44	Background	Type 1	terms	24

Goodness of Fit

χ^2	1.837	R_{wp}	0.0733	R_p	0.0654

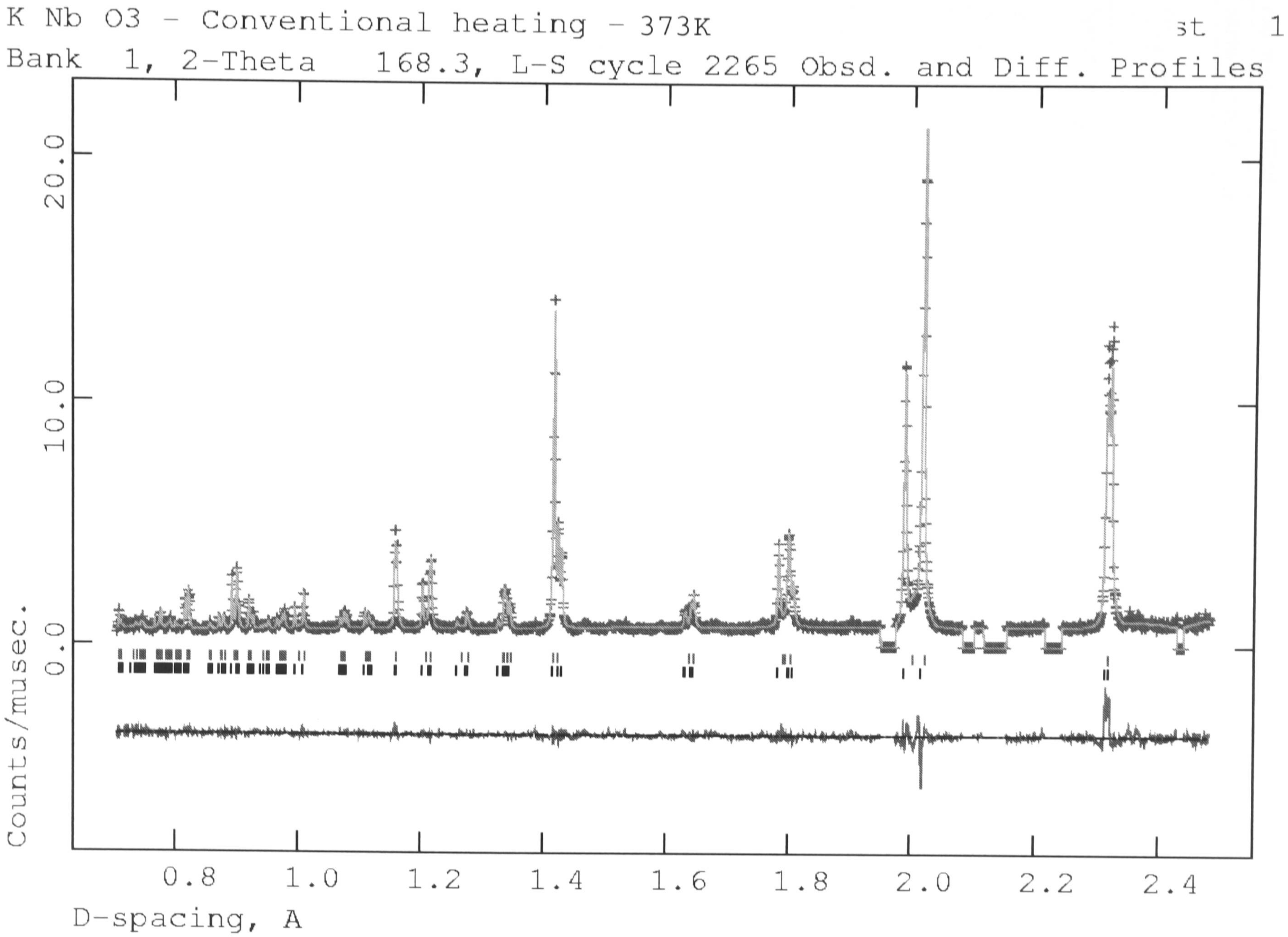
K Nb O3 - Conventional heating - 373K
st 1
Bank 1, 2-Theta 168.3, L-S cycle 2265 Obsd. and Diff. Profiles
Counts/musec.
0.0
10.0
20.0
0.8
1.0
1.2
1.4
1.6
1.8
2.0
2.2
2.4
D-spacing, A

Title

Potassium niobate at 473 K, electric furnace, with sample in vanadium can. Diffraction using neutron radiation at HRPD instrument, ISIS, Rutherford Appleton Laboratory.	
Main text reference	p146

Phase 1

Title	Orthorhombic KNbO$_3$				
Space Group	*Amm*2		Proportion/%	79.2(11)	
a/Å	3.98290(8)	b/Å	5.69610(12)	c/Å	5.71757(12)
α/°	90	β/°	90	γ/°	90
Atom	*x*	*y*	*z*	*F*	U^{eq}/Å^2
K (1)	0	0	0	1	0.013(3)
Nb (1)	½	0	0.468(3)	1	0.0113(14)
O (1)	0	0	0.505(3)	1	0.015(3)
O (2)	½	0.246(2)	0.251(2)	1	0.0216(17)
Profile type	TOF type 3	α	1.529E-01	β-0	2.125E-02
β-1	1.093E-02	σ-0	0	σ-1	2.82E+02
σ-2	1E+02	γ-0	0	γ-1	6E+01
γ-2	0				

Phase 2

Title	Tetragonal KNbO$_3$				
Space Group	*P*4*mm*		Proportion/%	20.8(11)	
a/Å	4.0096(4)	b/Å	4.0096(4)	c/Å	4.0500(8)
α/°	90	β/°	90	γ/°	90
Atom	*x*	*y*	*z*	*F*	U^{eq}/Å^2
K (1)	0	0	0	1	0.002(6)
Nb (1)	½	½	0.48(3)	1	0.008(4)
O (1)	½	½	0.01(3)	1	-0.008(5)
O (2)	½	0	0.50(4)	1	0.021(4)
Profile type	TOF type 3	α	1.529E-01	β-0	2.125E-02
β-1	1.093E-02	σ-0	0	σ-1	2.0E+04
σ-2	0	γ-0	0	γ-1	0
γ-2	0				

Instrument Parameters

Min TOF/μs	34.00		Max TOF/μs	118.00	
DIFA	48233.41	DIFC	0.70	Scale	445.1
Zero	13.55	Background	Type 1	terms	24

Goodness of Fit

χ^2	1.930	R_{wp}	0.0759	R_p	0.0610

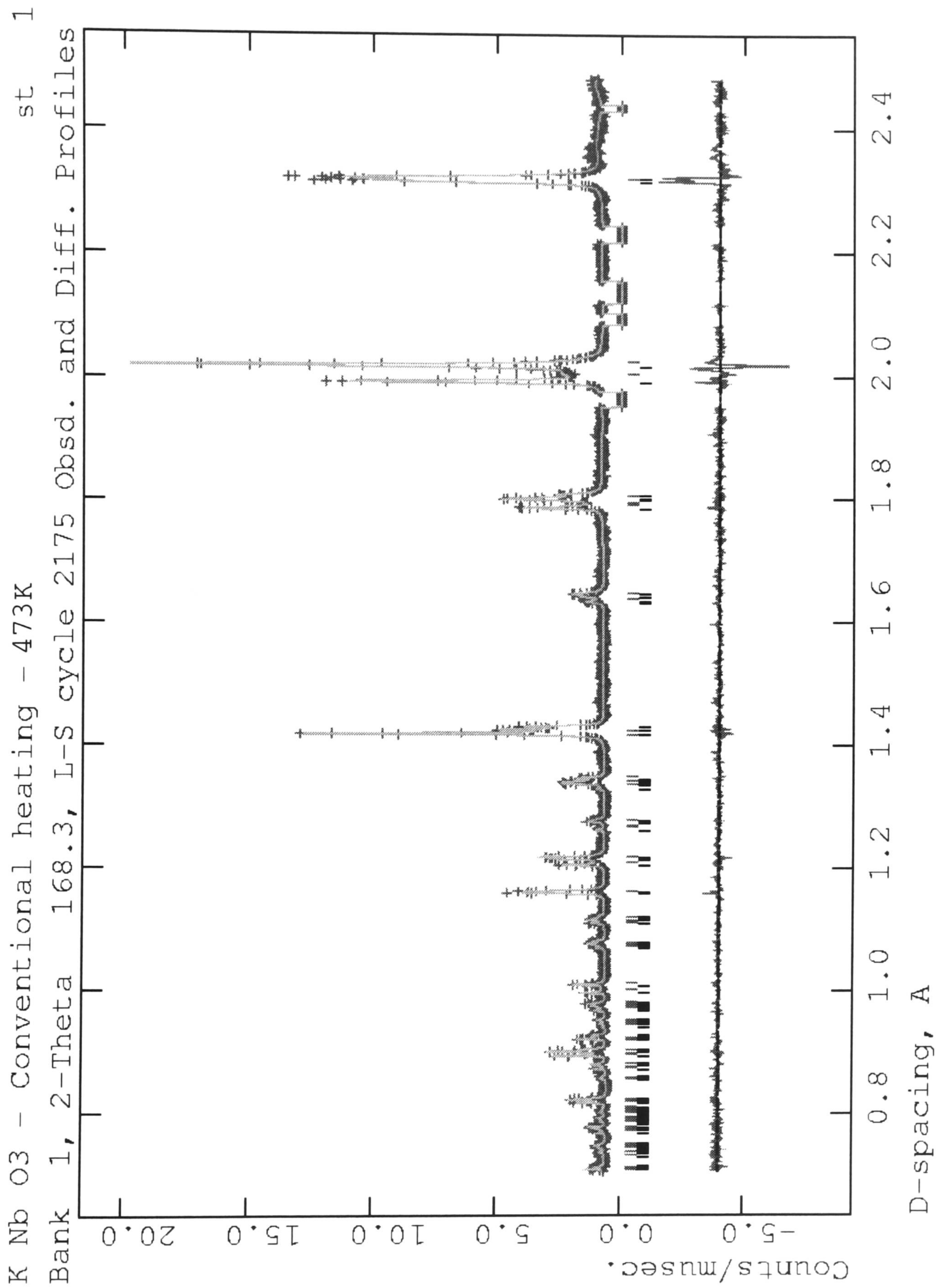
K Nb O3 - Conventional heating - 473K
st 1
Bank 1, 2-Theta 168.3, L-S cycle 2175 Obsd. and Diff. Profiles
Counts/musec.
20.0
15.0
10.0
5.0
0.0
-5.0
D-spacing, A
0.8
1.0
1.2
1.4
1.6
1.8
2.0
2.2
2.4

Title

Potassium niobate at 392 K, microwave heating, with sample on ceramic support. Diffraction using neutron radiation at HRPD instrument, ISIS, Rutherford Appleton Laboratory.	
Main text reference	p146

Phase 1

Title	Tetragonal $KNbO_3$				
Space Group	*P4mm*		Proportion/%	94.8(12)	
a/Å	3.99729(9)	b/Å	3.99729(9)	c/Å	4.06373(11)
α/°	90	β/°	90	γ/°	90
Atom	*x*	*y*	*z*	*F*	U^{eq}/Å^2
K (1)	0	0	0	1	0.014(5)
Nb (1)	½	½	0.50(5)	1	0.011(7)
O (1)	½	½	0.04(4)	1	0.013(3)
O (2)	½	0	0.53(4)	1	0.010(4)
Profile type	TOF type 3	A	1.529E-01	β-0	2.125E-02
β-1	1.093E-02	σ-0	0	σ-1	2.75E+02
σ-2	1E+02	γ-0	0	γ-1	6E+01
γ-2	0				

Phase 2

Title	Orthrhombic $KNbO_3$				
Space Group	*Amm*2		Proportion/%	5.2(12)	
a/Å	3.9840(4)	b/Å	5.7130(8)	c/Å	5.7024(9)
α/°	90	β/°	90	γ/°	90
Atom	*x*	*y*	*z*	*F*	U^{eq}/Å^2
K (1)	0	0	0	1	0.015(19)
Nb (1)	½	0	0.44(3)	1	0.09(2)
O (1)	0	0	0.03(19)	1	0.4(4)
O (2)	½	0.257(10)	0.208(17)	1	0.012(7)
Profile type	TOF type 3	α	1.529E-01	β-0	2.125E-02
β-1	1.093E-02	σ-0	0	σ-1	8.4E+02
σ-2	0	γ-0	0	γ-1	0
γ-2	0				

Instrument Parameters

Min TOF/μs	34.00		Max TOF/μs	118.00	
DIFA	48233.41	DIFC	0.70	Scale	435.9
Zero	13.28	Background	Type 1	terms	24

Goodness of Fit

χ^2	1.949	R_{wp}	0.0705	R_p	0.0610

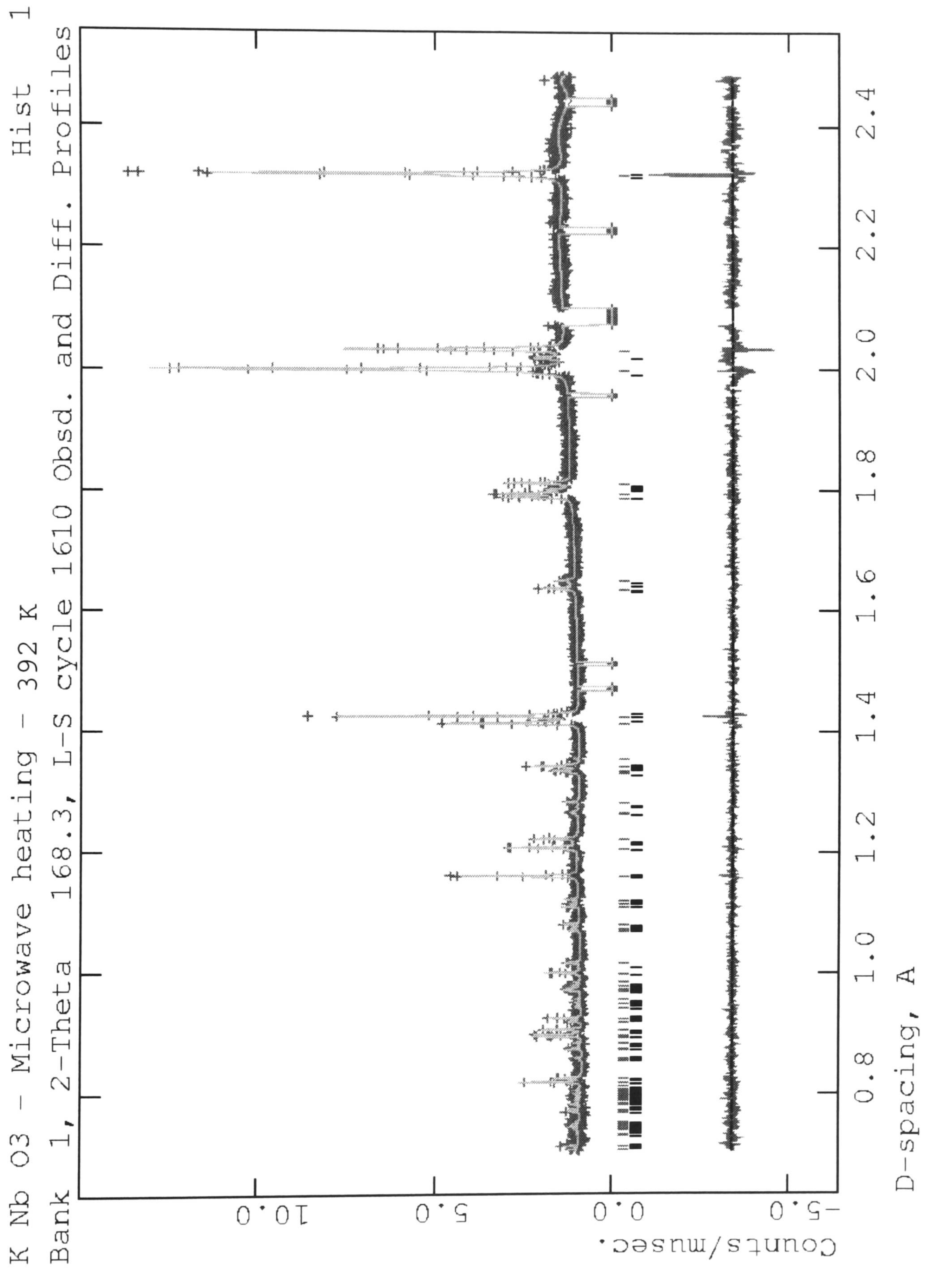
K Nb O3 - Microwave heating - 392 K
Hist 1
Bank 1, 2-Theta 168.3, L-S cycle 1610 Obsd. and Diff. Profiles
10.0
5.0
0.0
-5.0
Counts/musec.
0.8
1.0
1.2
1.4
1.6
1.8
2.0
2.2
2.4
D-spacing, A